

**Alma Mater Studiorum - Università degli studi di Bologna**

---

DIPARTIMENTO DI FISICA ED ASTRONOMIA

Corso di Dottorato di Ricerca in Astronomia

CICLO XXVI

**Development of new tools and devices for  
CMB and foreground data analysis  
and future experiments**

Dottorando:

**Molinari Diego**

Relatore:

**Dott. Carlo Burigana**

Chiar.mo Prof. **Daniele Dallacasa**

Chiar.mo Prof. **Andrea Fratalocchi**

Chiar.mo Prof. **Paolo De Bernardis**

Coordinatore:

Chiar.mo Prof. **Lauro Moscardini**

Esame finale anno 2014

---

SCUOLA DI DOTTORATO IN SCIENZE MATEMATICHE, FISICHE E ASTRONOMICHE

Settore Concorsuale: 02/C1 - Astronomia, Astrofisica, Fisica della Terra e dei Pianeti

Settore Scientifico-Disciplinare: FIS/05 - Astronomia e Astrofisica

*Seconda stella a destra  
questo è il cammino  
e poi dritto, fino al mattino  
poi la strada la trovi da te  
porta all'isola che non c'è.*

*(da "L'isola che non c'è" di Edoardo Bennato)*

# Contents

<b>Introduction</b>	<b>1</b>
<b>1 The Cosmic Microwave Background</b>	<b>7</b>
1.1 Introduction . . . . .	7
1.2 The Big Bang theory . . . . .	9
1.2.1 The inflationary solution . . . . .	11
1.3 The CMB anisotropies . . . . .	14
1.3.1 Temperature anisotropies . . . . .	16
1.3.2 Polarization anisotropies . . . . .	23
1.3.3 New polarization results: PLANCK perspective . . . . .	27
1.4 LFI Polarization Data acquiring methodology: the Ortho- Mode Transducer . . . . .	29
1.5 Future expectation: CORE, PRISM and other projects . . . . .	34
1.5.1 The research for new device . . . . .	38
<b>2 Microwave Foregrounds</b>	<b>39</b>
2.1 The Foregrounds . . . . .	43
2.1.1 Diffuse foreground . . . . .	44
2.1.2 Extragalactic Discrete Foreground . . . . .	51
2.1.3 The Cosmic Infrared Background . . . . .	56
2.2 The Galactic Synchrotron Emission . . . . .	57
2.2.1 Temperature Synchrotron Emission . . . . .	58
2.2.2 Polarized Synchrotron Emission . . . . .	63
2.2.3 The Synchrotron APS . . . . .	65

---

2.2.4	The 408 MHz and 1.4 GHz surveys . . . . .	66
<b>3</b>	<b>Data analysis</b>	<b>69</b>
3.1	The pixelization problem . . . . .	72
3.1.1	The HEALPix package . . . . .	75
3.2	The effect of the change of coordinates . . . . .	78
3.2.1	Change of coordinates in pixel space . . . . .	78
3.2.2	Change of coordinates in harmonic space . . . . .	80
3.2.3	Results on pure CMB simulated maps . . . . .	82
3.2.4	CMB maps with beam . . . . .	95
3.2.5	Application to WMAP maps . . . . .	97
3.3	Angular Power Spectrum estimators . . . . .	102
3.3.1	The Cromaster code . . . . .	103
3.3.2	The BolPol code . . . . .	106
3.4	Comparison between pseudo- $C_\ell$ and QML estimators at large scales . . . . .	109
3.4.1	Details of the simulations . . . . .	110
3.4.2	Figure of Merit . . . . .	112
3.4.3	Results . . . . .	114
3.4.4	Applications . . . . .	115
3.5	The aliasing effect in maps degradation . . . . .	117
3.5.1	Details of the simulation . . . . .	120
3.5.2	Results . . . . .	122
<b>4</b>	<b>The CMB large scales analysis</b>	<b>125</b>
4.1	The origin of the large scales signal . . . . .	127
4.2	Planck and WMAP9 results: the large scales APS . . . . .	129
4.3	The large scales anomalies . . . . .	131
4.4	Low variance at large scales of WMAP 9 year data . . . . .	138
4.4.1	Data sets and estimators used . . . . .	138
4.4.2	Results . . . . .	140

---

4.4.3	Impact of the smoothing procedure in the temperature analysis . . . . .	142
4.4.4	Polarization analysis . . . . .	143
4.4.5	Discussion . . . . .	144
4.5	Quest for an explanation to the anomalies . . . . .	145
<b>5</b>	<b>The Galactic Synchrotron emission</b>	<b>149</b>
5.1	Introduction . . . . .	149
5.2	The patch determination . . . . .	151
5.3	The Total Intensity results . . . . .	156
<b>6</b>	<b>Future observation: the development of new devices</b>	<b>163</b>
6.1	Photonic Crystals . . . . .	165
6.1.1	The reciprocal lattice and the Brillouin zone . . . . .	167
6.1.2	Waves in a periodic medium . . . . .	169
6.1.3	2D photonic crystals: TE and TM modes . . . . .	172
6.1.4	Photonic cavities and waveguides . . . . .	173
6.2	Ab-initio numerical simulations: the FDTD method . . . . .	176
6.2.1	The Yee algorithm . . . . .	178
6.2.2	Numerical stability . . . . .	181
6.2.3	Electromagnetic sources in the FDTD code . . . . .	183
6.2.4	Absorbing boundary conditions . . . . .	186
6.3	Multimode interference . . . . .	187
6.4	Chaotic resonator to enhance the energy harvesting . . . . .	192
6.5	The polarization splitter device . . . . .	200
	<b>Conclusions</b>	<b>209</b>
	<b>Acknowledgements</b>	<b>215</b>
	<b>Bibliography</b>	<b>217</b>



# Introduction

The discovery of the Cosmic Microwave Background (CMB) radiation [1] and the determination of its cosmological origin in 1965 [2] set a fundamental milestone for the confirmation of the Big Bang theory which basic concepts were proposed in 1948 [3]. The theory states that the Universe was initially in a hot and dense phase from which it started to expand and cool up to its present status, undergoing a series of phase transitions in the early stages of its evolution. In particular, during the recombination, free electrons and protons of the primordial plasma started to form neutral atoms. Thanks to this process, the photons previously interacting with charged particles could propagate across the Universe and arrive to us today as the CMB radiation. The possibility of measuring this relic radiation coming directly from the early Universe drove huge efforts in both the theoretical and the experimental side. The NASA satellite COsmic Background Explorer (COBE) opened the era of precision cosmology. It determined that the CMB is well approximated by a thermal black body spectrum with a mean temperature of  $T_0 = (2.725 \pm 0.002)$  [4] and confirmed the presence of temperature fluctuations (the CMB anisotropies) at a level of  $\Delta T/T \sim 10^{-5}$  for angular distances of  $\Delta\theta \gtrsim 7^\circ$  [5]. COBE results were improved by many experiments at small angular scales and in particular by the Balloon Observations Of Millimetric Extragalactic Radiation and Geophysics (BOOMERanG) [6] and then by the Wilkinson Microwave Anisotropy Probe (WMAP), the 2<sup>nd</sup> generation of satellite missions [7], dedicated to the measurement with unprecedented accuracy of the CMB anisotropies. The data collected allowed to

constrain the parameters of the standard cosmological model that describes the anisotropies as the footprints of primordial cosmological perturbations which generated the large scale structures we observe nowadays and are directly related to the geometrical and physical properties of the Universe since its early stages. Recently, the 3<sup>rd</sup> generation of satellite mission, called *Planck*, released its temperature results\* [8]. The excellent accuracy of its maps set a new challenge for the cosmologists in the data analysis processes and in their interpretation. The results confirmed the validity of the standard cosmological model and put tighter constraints to its parameters.

In this context, this PhD thesis deals with several aspects and useful tools of the data analysis, focusing on their optimization in order to have a complete exploitation of the *Planck* data and contribute to the final published results.

The tool chosen by the *Planck* collaboration to project the satellite data into 2D maps is the HEALPix package. It is suitable for fast and accurate statistical and astrophysical data analyses. Inside the HEALPix package there is a routine that performs the change of coordinates. A full sky or patch map is typically provided in Ecliptic, Galactic or Equatorial coordinates. Maps obtained by telescopes like WMAP and *Planck* are usually provided in Galactic coordinates, whereas ground based or balloons ones are in Equatorial (or Ecliptic) coordinates. The possibility of changing the coordinates is very useful in order to compare the data obtained with different instruments and eventually to combine them achieving better results. Therefore, an accurate change of coordinates of the maps is crucial for the analysis of multiple datasets.

A very useful way to analyse the full sky maps generated, goes through the extraction of the Angular Power Spectrum (APS). On intermediate and small angular scales, the APS extracted from the maps are used by the likelihood functions dedicated to explore the parameter space of the considered cosmological model. On large angular scales, the likelihood function works

---

\*Polarization data will be published in 2014.

directly at map level, but also in this case, the APS is very useful to test the results obtained. The APS extraction is commonly used also to check for the presence of some kinds of anomalies in the CMB anisotropy pattern. The analysis of the resulting APS helps to determine if the anomalies have a cosmological origin, leading for example to violations of the standard cosmological model or of the standard inflationary mechanisms, or if they are due to non CMB signals that can origin from systematics, data analysis artefacts or residual foregrounds. This thesis will deeply study two tools, called BolPol and Cromaster, that use different methods to extract the APS from the maps. The qualities of the tools are compared and, subsequently, they are applied to the maps in order to extract the *Planck* CMB APS on large angular scales and focusing on the analysis of few large angular scale anomalies. For these results the maps have been downgraded to lower resolution. There are different methods to downgrade the maps. Using the APS extracted with BolPol, the performances of the methods have been analysed in order to define which is the best one to downgrade the resolution of the maps.

The maps generated by CMB missions collect all the signals in the microwaves including Galactic and extragalactic emissions that for CMB studies are considered as foregrounds to be studied and removed from the maps. The APS is an useful tool to study the characteristics of the foregrounds and to detect possible residuals in the cleaned maps. In this thesis, we studied the Galactic synchrotron emission focusing on the APS analysis of selected portions of the sky associated to interesting features far from the Galactic plane, aiming also at improving the cleaning process of the CMB maps.

*Planck* polarization results are expected to be even more interesting. They will set also the scene for a 4<sup>th</sup> generation satellite mission dedicated to the polarization measurement with the aim of shedding a light on the still open questions about the early stages of the Universe, such as for example the details of inflationary mechanism. The new requirements define a new challenges to develop new technologies that will improve the instrument perfor-

mances in order to achieve better quality data with higher resolution and sensitivity. One important aspect for precise polarization measurements is the need for a correct and clean separation of the two polarization signals, fundamental to reach the required accuracy in the data. In this thesis we deeply analysed the technology of the Photonic Crystals. A Photonic Crystals is a dielectric periodic media that uses its periodicity properties in order to manipulate the radiation motion at certain frequencies. Here, this technology has been exploited in order to develop a polarization splitter device. Ab-initio simulations have been performed in order to optimize the device with the aim of reaching very competitive results.

Summarizing, the thesis is organized as follows:

- The first chapter will review some basic concepts of cosmology, in particular of the Big Bang theory and the CMB origin. We will review cosmological perturbations evolution in the standard cosmological model and the major aspects of CMB anisotropy analysis. A section is dedicated to present the *Planck* results, its technology used to separate the polarizations and to describe the on-going and future experiments.
- The second chapter is dedicated to a review of the foreground emissions in the microwaves focusing on the Galactic synchrotron signal and the main data set used for its analysis. Two radio survey maps at 408 MHz and 1.42 GHz are also introduced.
- The third chapter focuses on the results of this thesis about some data analysis aspects and APS estimators. The HEALPix pixelization technique is introduced and the accuracy of its routines to change the coordinates of a map are analysed. We will quantify the errors that affect the maps after the change of coordinates and will compare them with the sensitivities of WMAP, *Planck* and future missions. We will also describe two APS estimators (BolPol and Cromaster) and we will compare their performances focusing on the large scales. Using BolPol, we

will study the various methods proposed for generating low resolution maps in order to identify the most accurate one.

- The fourth chapter is dedicated to the large scale analyses of the CMB cleaned maps. We will present the results of the CMB APS extracted from the *Planck* data using BolPol. Moreover, we will introduce the most important anomalies and we will deeply analyse two of them: the Parity asymmetry and the Low Variance.
- The fifth chapter describes the analysis of the radio surveys at 408 MHz and 1.42 GHz based on the APS extraction for selected regions of the sky in order to derive the properties of the synchrotron emission.
- The sixth chapter is dedicated to introduce the Photonic Crystal technology, to describe the polarization splitter device and its qualities based on ab-initio simulations.

Finally, the main results achieved in this thesis and the future perspectives will be resumed in the Conclusions.



# Chapter 1

## The Cosmic Microwave Background

### 1.1 Introduction

When Arno Penzias and Robert Woodrow Wilson studied the data collected by the new horn antenna of the Bell Labs in 1964 [1], they were not expecting to find anything special. They were looking for the signal coming from radio waves bounced off the Echo balloon satellites. Independently from the direction, they observed an excess in the intensity of the signal described as a low, steady, mysterious noise persisting in their receiver. This excess remained even after their hard work to eliminate all recognizable interference from their receiver.

At the same time Robert H. Dicke and his group were preparing to search for microwave radiation in the same region of the electromagnetic spectrum. Their idea was that the Big Bang, thought as the "explosion" after which the Universe was generated, must have filled the entire Universe with a relic radiation with a black body spectrum since the beginning of its existence. With the proper instrumentation, this radiation should have been detectable in the microwave range [2].

By looking for possible explanations of their extra signal, Penzias and

Wilson discovered that the characteristics of the radiation detected fit exactly the radiation predicted by Dicke [1]: it was the first detection of the Cosmic Microwave Background (CMB). For this result they were awarded the Nobel Prize for Physics in 1978. This detection, in combination with the discovery of the expansion of the Universe and the measurement of primordial element abundances, is a fundamental milestone supporting the Big Bang theory.

After the discovery, a large number of observational campaigns have been carried out aimed at measuring the black body spectrum of the Big Bang microwave emission [9–13], and testing its isotropy all over the sky [14–16] with great precision. The first measurement of the CMB dipole was published in 1992 [17]. With the same motivation in 1989 the NASA’s Cosmic Background Explorer (COBE) was launched. It measured with great precision the black-body form of the CMB confirming its cosmological origin [4] and detected for the first time its temperature anisotropies [5], imprints of the fluctuations in the early Universe. Mather and Smoot were awarded the Nobel Prize for Physics in 2006.

After COBE a great number of ground-based observations (e.g. DASI), balloon-borne experiments (e.g. Boomerang, MAXIMA) and satellite missions (WMAP, *Planck*) were performed. Their results confirmed the predictions of the Big Bang theory and opened the so-called era of precision cosmology. Their results allowed the scientists to reach unprecedented knowledge of the early stages of our Universe, to test the assumptions associated with the cosmological model, that should describe the properties of our Universe, and to shed new light on the inflation mechanism, that should have generated the fluctuations that led to the generation of all the structures visible today. Nevertheless, scientists are always looking for new and more precise data, so they are developing new missions with a new generation of devices that will provide us an unprecedented knowledge of the Universe in which we live. The golden age of cosmology is still going on.

## 1.2 The Big Bang theory

The Big Bang theory states that the Universe was initially in a hot and dense state from which it started to expand and cool up to its present status, undergoing a series of phase transitions in the early phases of its evolution. Three of the fundamental milestones of observational cosmology coincided with the three proofs in support of the Big Bang theory: the discovery of the expansion of the universe, the measurements of primordial element abundances predicted by the Big Bang nucleosynthesis and the discovery of the CMB radiation.

The expansion of the Universe is known since the 1920s, when Lemaitre and Friedmann independently derived the solutions of the Einstein general relativity equations for an isotropic and homogeneous Universe [18,19]. Surprisingly, these solutions describe an evolving Universe and predict that it had undergone an expanding and cooling phase in the past. The first clues about an expanding Universe were collected by Slipher [20] in 1912. He observed a systematic redshift in the spectra of non-local galaxies, but at that time the knowledge on galaxies was still too poor to allow a cosmological interpretation of this effect. It was only in 1929 that Edwin Hubble associated this redshift with a general recession of galaxies one from the others, confirming what had been predicted by Lemaitre few years earlier [21]. In particular, the recession velocity is directly proportional to the distance of the galaxy through the Hubble parameter,  $H$ . Today we confirmed that this recession is almost due to the rate of the Universe expansion. Also the distance is related to the characteristics of this expansion that depends on time. Recent measurements of supernovae distances demonstrated, for the first time, that, in this epoch, the Universe is not only expanding, but its expansion is accelerated [22,23].

The basic concepts of the Big Bang theory were formulated by Gamow and Alpher [3] in 1948, also, in order to find an answer to the chemical abundances of light elements observed in very old stars. They introduced the Big Bang nucleosynthesis that describes how all these abundances were

generated in the first seconds while the Universe was cooling and expanding, thanks to the hot and dense state of the plasma. In fact, at the beginning protons and neutrons were kept in thermal equilibrium at temperature above 1 MeV by weak interactions as



While the temperature is dropping off and reaches values around  $T \sim 1$  MeV, the interactions above are no longer efficient enough and the relative abundances of neutrons and protons are frozen. From that time, neutrons and neutrinos fall out of thermal equilibrium. A small amount of deuterium can be formed at those temperatures through the interaction



When temperature decreased below 86 KeV, although more deuterium nuclei could form from free neutrons and protons, they combine to give  $He^4$  depending the rate on the baryon abundance. Also a small amount of  $He^3$  and lithium was produced. The abundances observed in the Universe are in agreement with the ones predicted by the nucleosynthesis: 75% hydrogen, 23% helium and 2% metals (everything that is not hydrogen or helium), and their measurements were considered the most important proof in support of the Big Bang theory until 1964 when the CMB radiation was discovered.

The CMB is an isotropic relic radiation predicted by the Big Bang theory. It represents a picture of the Universe when it was only about 380,000 years old corresponding to a redshift  $z \sim 1090$ . Earlier than that time, the temperature of the plasma was high enough to keep photons and electrons strongly interacting mainly via Thompson scattering. As the Universe expands and temperature falls off, protons and electrons could combine forming the first atoms (recombination epoch). The lower number of charged particles caused

the drop of the efficiency of Compton interaction. The mean free path of the photons became larger than the Universe and they could propagate until the present time carrying the physical properties of the last scattering with matter. In this way the Universe became transparent to radiation. The virtual surface where the photons are scattered by electrons for the last time is called *last scattering surface* (LSS) and can be considered a virtual emission surface of the CMB photons. The radiation observed by Penzias and Wilson and then measured by COBE is this CMB diffuse radiation shifted to the microwaves by the Universe expansion and it is observed today at a temperature of 2.725 K [4]. Also, the CMB is very isotropic with a level of fluctuations measured by COBE of the order of  $\Delta T/T = 10^{-5}$  on the angular scale of 7 degrees. From the analyses of the properties of the CMB photons, scientists can extract the properties of the Universe such as the matter density distribution at the LSS and infer models that can describe how they have been generated.

The Big Bang theory was a great success for cosmology, but some problems raised in this scenario. The most important are the cosmological horizon, the flatness and the magnetic monopoles.

### 1.2.1 The inflationary solution

In every Big Bang model we can define the cosmological horizon for a given particle,  $r_H$ . defined as:

$$r_H(t) = a(t) \int_0^t \frac{dt'}{a(t')} \quad . \quad (1.3)$$

It determines regions which are in causal connection and depends on time. Regions separated by a distance larger than the cosmological horizon should not have exactly the same properties. Cosmological observations are in agreement with a Big Bang model in which, at the LSS epoch, the cosmological horizon was much smaller than the size of the Universe. Despite this, the observations measured an exceptional level of isotropy of the order

of  $\Delta T/T \sim 10^{-5}$  even between regions not causally connected. In the light of this observations, Big Bang model alone is not sufficient to describe the CMB isotropy.

The flatness problem has a statistical nature. The Universe has a spatial curvature that can be positive, negative or null depending on its total energy density,  $\rho(t)$ . It can be also parametrized by  $\Omega = \rho/\rho_{cr}$ , time dependent, which is the ratio between the total energy density at a certain time and the critical density,  $\rho_{cr}$  defined as:

$$\rho_{cr} = \frac{3H_0^2}{8\pi G} \quad (1.4)$$

where  $H_0$  is the Hubble parameter value today (at  $t = 0$ ) and  $G$  is the gravitational constant. The critical density is associated to a flat Universe, values of  $\Omega < 1$  (that is,  $\rho < \rho_{cr}$ ) describe an open Universe with negative curvature, while values of  $\Omega > 1$  (that is,  $\rho > \rho_{cr}$ ) are associated to a closed Universe with positive curvature. The standard cosmological model predicts that any initial difference between  $\rho$  and  $\rho_{cr}$  grows with time. The hypothesis of a flat Universe in the present days, recently confirmed by cosmological data, therefore, requires an initial value of the total energy density very close to the critical one ( $\rho/\rho_{cr} \ll 10^{-60}$ ). This fine tuned initial conditions are statistically very unlikely.

The magnetic monopoles are a monodimensional relic defects introduced by the Grand Unification Theory (GUT) that should unify the electroweak theory and the strong interaction. The theory predicts that at the GUT phase transition, occurred at  $t = 10^{-35}$  sec, there has been the production of very massive magnetic monopoles ( $m \sim 10^{16} GeV$ ). With such a high mass, accordingly to the Big Bang theory, the monopoles should have been the dominant component in the Universe with a matter density parameter  $\Omega_M \sim 10^{16}$ . The lower total density parameter and the lack of positive detections mean that, indeed, the magnetic monopoles have a very low density.

The solution to these problems was found by Guth [24] and Starobinsky [25] when in 1980 developed the theory of inflation.

In the theory they predict an inflation phase that occurred just after the GUT phase transition and in which the Universe experienced an exponential expansion:

$$a(t) \propto e^{\int H(t') dt'} \quad , \quad (1.5)$$

where the Hubble parameter is nearly constant during this phase and the horizon grew much slower than the scale factor ( $a$ ). Regions with the same properties at the beginning, because they were in causal contact, during the inflation were separated to a scale by many orders of magnitude larger, becoming not causally connected on the CMB surface. This mechanism can explain the high level of isotropy of the CMB. Also, according to the theory, the density parameter during the inflation evolves as:

$$\Omega - 1 = \frac{K}{(aH)^2} \quad , \quad (1.6)$$

where the spatial parameter  $K$  represents the geometry of the 4-dimensional hypersurface where the Universe expands. As the time increases, the right-side of Eq. 1.6 goes to zero and the total density of the Universe becomes equal to one independently from its starting value. Last, the magnetic monopoles were created before inflation and therefore their density was diluted by the exponential expansion up to a point when their contribution to the cosmological fluid is irrelevant and, therefore, it is extremely unlikely to observe them.

Today there are several different models of inflation (for a review we refer the reader to [26]), that predict different properties of the CMB, in particular its anisotropies that are described in the next section. A correct and deep analysis of the observational results will allow to test these models, to understand the inflation mechanism and to shed new light to the early stages of the Universe.

### 1.3 The CMB anisotropies

The statistical analysis of the CMB anisotropies is one of the main topics of this thesis. Before presenting them, we need to introduce some fundamental concepts used to describe and understand the nature of CMB radiation.

The intensity field ( $I$ ) in a 2-dimensional plane perpendicular to the direction of photon propagation can be decomposed in:

$$I = \begin{pmatrix} T + Q & U \\ U & T - Q \end{pmatrix} , \quad (1.7)$$

where  $T$  is the temperature and  $Q$  and  $U$  are the usual Stokes parameters for the linear polarization description [27]. No circular polarization is taken into account since we do not expect Compton scattering to produce it at leading order.  $Q$  and  $U$  depend on the reference frame chosen in the plane perpendicular to the propagation direction, but it is possible to define a combination of them that is invariant under rotation of the polarization plane described by  $P = (Q^2 + U^2)^{1/2}$  called polarization amplitude.

In the observer frame, CMB photons appear as incoming radiation from any direction of the sky,  $\hat{n}$ , from the LSS towards the observer. The statistical analysis of CMB temperature and polarization anisotropies is fundamental to understand the properties of the primordial Universe. The analysis goes through the definition of the Angular Power Spectrum.

Temperature is a scalar quantity and does not depend on the reference frame. We can write the temperature field as the sum of its zeroth-order (the mean value) and the anisotropies,  $\Delta T = \delta T/T$ :

$$T(\hat{n}) = T(1 + \Delta T(\hat{n})) . \quad (1.8)$$

For the analysis of the anisotropies it is useful to expand them using spherical harmonics ( $Y_{\ell m}$ ) as orthonormal basis:

$$\Delta T(\hat{n}) = \sum_{\ell=1}^{\infty} \sum_{m=-\ell}^{\ell} a_{T,\ell m} Y_{\ell m}(\hat{n}) , \quad (1.9)$$

where  $a_{T,\ell m}$  are the coefficients of the expansion. From the observational point of view, the multipole  $\ell$  is approximately related to the angular distance,  $\theta$ , between two objects in the sky as:

$$\ell \sim \frac{180^\circ}{\theta(\text{deg})} \quad (1.10)$$

Following this definition, *large scales* (large values of  $\theta$ ) refer to small multipoles ( $\ell \leq 100$ ). Instead, *small scales* refer to large values of  $\ell$ . The integer  $m$  can assume all the values inside the range  $[-\ell, \ell]$  and defines all the independent spherical harmonics for a given value of  $\ell$ .

Instead, Q and U are spin-2 objects and depends on the orientation of the system. It is more useful to expand a combination of them in spin-2 spherical harmonics ( ${}_{\pm 2}Y_{\ell m}$ ):

$$(Q \pm iU)(\hat{n}) = \sum_{\ell=2}^{\infty} \sum_{m=-\ell}^{\ell} a_{\pm 2, \ell m \pm 2} Y_{\ell m}(\hat{n}) \quad , \quad (1.11)$$

again the  $a_{\pm 2, \ell m}$  are the coefficients of the expansion. However, the object on the left-side of Eq. 1.11 is not conserved under parity transformation. For this motivation, we introduce other coefficients obtained as the linear combination of the above:

$$\begin{aligned} a_{E, \ell m} &= -(a_{2, \ell m} + a_{-2, \ell m})/2 \\ a_{B, \ell m} &= i(a_{2, \ell m} - a_{-2, \ell m})/2 \quad . \end{aligned} \quad (1.12)$$

It turns out that  $a_{E, \ell m}$  and  $a_{B, \ell m}$  are the harmonic coefficients of non local (because constructed in harmonic space, not in real space) quantities, E and B, which transform under parity as scalar and pseudo-scalar respectively. In particular, B-modes change sign under parity transformation and are insensitive to linear scalar perturbation.

For any particular object  $X=(T,E,B)$ , it results that the mean over  $m$  of the  $a_{\ell m}$  distribution is zero ( $\langle a_{\ell m} \rangle = 0$ ) and therefore the first significant statistical moment of the anisotropy distribution is its variance. The variance

of the  $a_{\ell m}$ , called  $C_\ell$ , is the anisotropy Angular Power Spectrum (APS) and if the anisotropies are Gaussian it is the only non-zero statistical moment and incorporates all the information on the anisotropies. The CMB anisotropy APS is defined as:

$$C_\ell^{XX'} = \frac{1}{2\ell + 1} \sum_{m=-\ell}^{\ell} \langle a_{\ell m}^{*X'} a_{\ell m}^X \rangle \quad , \quad (1.13)$$

which implies together with  $\langle a_{\ell m} \rangle = 0$  that:

$$\langle a_{\ell m} a_{\ell' m'} \rangle = \delta_{\ell\ell'} \delta_{mm'} C_\ell \quad , \quad (1.14)$$

From the definition in Eq. 1.13, Temperature, E-modes and B-modes autocorrelations are defined by  $C_\ell^{TT}$ ,  $C_\ell^{EE}$  and  $C_\ell^{BB}$ , in the following named TT, EE and BB angular power spectra, while their cross-correlations are defined by  $C_\ell^{TE}$ ,  $C_\ell^{TB}$  and  $C_\ell^{EB}$ , in the following named TE, TB and EB angular power spectra.

For an all-sky observation, a statistical analysis of CMB anisotropies is affected by cosmic variance, which is the uncertainty related to the fact that we are applying a statistical analysis to one single realization: the only sky we observe. Since  $m$  varies in the range  $[-\ell, \ell]$ , for each multipole we have  $2\ell + 1$  coefficients to draw the underlying distribution. Therefore for high multipoles we have a large information to draw the distribution while for low multipoles we have only very few information available. The cosmic variance is defined as:

$$\frac{\Delta C_\ell}{C_\ell} = \sqrt{\frac{2}{2\ell + 1}} \quad . \quad (1.15)$$

and it is particularly relevant at low multipoles.

### 1.3.1 Temperature anisotropies

The CMB is a diffuse radiation observed today at an average temperature of 2.725 K. CMB is very isotropic with small fluctuations of the order of

$\delta T/T \sim 10^{-5}$  at an angular scale of 7 degree. These fluctuations are known as *anisotropies*. The anisotropies are related to the perturbations in the plasma density. The perturbations are supposed to be adiabatic, that is they evolve conserving the total entropy of the plasma. During the entire history of the Universe, the matter density perturbations grew under the effect of the gravity forming all the large structures observable today (i.e galaxies and cluster of galaxies). The study of the anisotropies is fundamental for the understanding of the generation mechanism and the evolution of the large structures up today.

They can be divided in two different components: the primary anisotropies that emerged at the time of the recombination, and the secondary ones that were subsequently imprinted on the CMB photons, such as, for example, those produced by Compton scattering between CMB photons and hot free electrons in cluster of galaxies along the line of sight, known as the Sunyaev-Zel'dovich (SZ) effect. This thesis focuses on the primary anisotropies. Since the inflation stretched all the primordial perturbations on scales larger than the Hubble radius and they remained frozen until the Universe expanded up to their sizes, we can classify the effects responsible for the anisotropies that we observe on the CMB in three different categories:

- Gravitational perturbations [28]: they produce the dominant large-scale effect arising from gravitational potential perturbations  $\delta\Phi$  at last scattering that cause a change in frequency of the CMB photons. There are two contributions opposed in sign: photons that climb out of a potential well generated by an overdensity region cools the background  $\Delta T/T = \delta\Phi/c^2$  (*gravitational redshift*). At the same time, while they are climbing out, the Universe is expanding slower compared to the surrounding regions because of the overdensity, giving another contribution of  $\Delta T/T = -\frac{2}{3}\delta\Phi/c^2$ . The net effect gives a temperature fluctuation of the order of:

$$\frac{\Delta T}{T} = \frac{1}{3} \frac{\delta\Phi}{c^2} . \quad (1.16)$$

- Velocity (Doppler) perturbations: the plasma has a non-zero velocity at recombination, leading to Doppler shifts in frequency and hence in brightness temperature. If  $\vec{v}$  is the velocity of the moving plasma as seen by the photons propagating in the direction  $\hat{r}$ , we have:

$$\frac{\Delta T}{T} = -\frac{\delta(\vec{v} \cdot \hat{r})}{c} . \quad (1.17)$$

- Acoustic perturbations: before the recombination, matter and photons are coupled. Within the horizon the gravitational collapse is opposed by radiation pressure. This creates an oscillatory behaviour of the baryon-photon plasma between an underdensity and an overdensity state. This is reflected in an higher temperature of the photons in the overdensities and a lower temperature in the underdensities.

All these effects operate at the epoch of recombination and affect the temperature of the photons we collect with our experiments about 13 billions of years later. The strongest contribution to the observed map of the CMB are the monopole that describes the mean temperature of the CMB and the dipole that is due to the combined rotation of the satellite around itself, its rotation around the Sun, the motion of the Sun in our Galaxy and the motion of our Galaxy in our local system. Once these contributions are removed, the results is the map of the CMB anisotropies that are the most impressive picture of the entire Universe. The recent WMAP 9 year and *Planck* temperature maps are the most precise full sky maps ever produced (Fig. 1.1).

From the analysis of these kinds of maps through the harmonic expansion of the data introduced in the previous section, we can derive the Temperature Angular Power Spectrum of the CMB. An example of APS is shown in Fig. 1.2. In the figure we can observe three characteristic scale ranges.

The large scale anisotropies,  $\ell < 100$ , represent perturbations which were on super-Hubble scales at recombination, where the only active force was the gravity. This part of the spectrum is called Sachs-Wolfe plateau from the

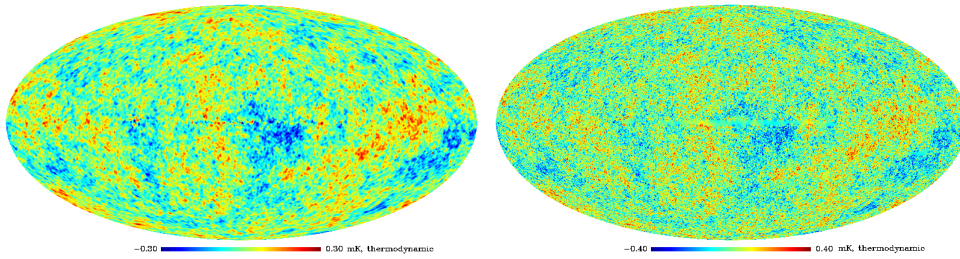


Figure 1.1: The most recent Cosmic Microwave Background maps. On the left the WMAP ILC 9 year map smoothed to 1 degree. On the right the *Planck* Smica nominal mission map with the resolution of 5 arcmin. The red (blue) points represents the points hotter (colder) than the average temperature by about a part over  $10^4$ .

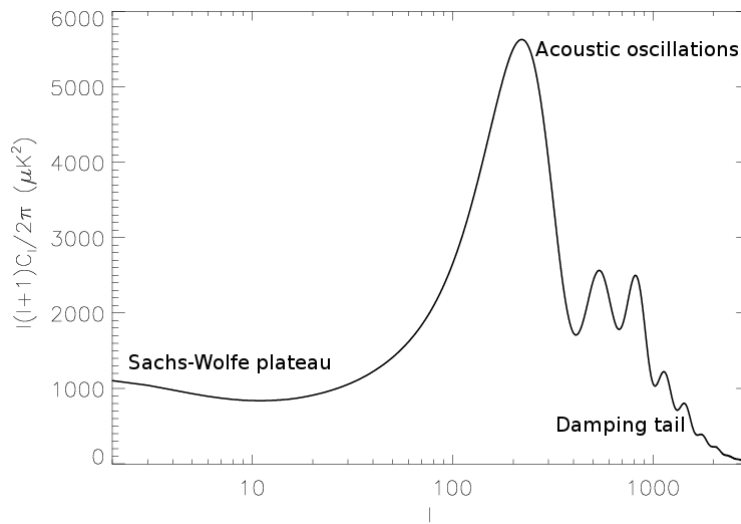


Figure 1.2: An example of Angular Power Spectrum divided in the three most important scale regions because of the different physical effects that generated the CMB signal.

scientists who formalized the gravitational perturbation for the first time [28]. The second range is where acoustic oscillations are present ( $100 < \ell < 1500$ ). On this intermediate range the perturbations are inside the Hubble radius at recombination. Inside the horizon the pressure starts to play its role causing the oscillation of the fluid between cold and hot regions. In this range of the angular spectrum we can see a series of acoustic peaks which represent the acoustic oscillations of the fluid. The third range corresponds to the very small angular scales ( $\ell > 1500$ ). At these scales the mean free path of the photons is larger than the scale of the cosmological perturbations that, for this reason, are destroyed by the pressure of the fluid. This effect is called Silk damping [29] and in this region the angular spectrum shows a damping tail.

Since the first experiments, scientists tried to extract the APS from the data. The first detection of the low- $\ell$  CMB APS was made by COBE-DMR [5], but the most impressive results came from the Boomerang data [6] later confirmed and refined by the WMAP first year mission [7] as shown in Figure 1.3.

From the properties extracted from the APS, scientists confirmed the results obtained by the measurements of type Ia supernovae distances implying a Universe with a flat geometry ( $\Omega_0 = 1$ ) and being 13,4 billion of years old. These results strongly contributed to define the parameters of the standard cosmological model of the Universe which turned to be constituted by about 5% of baryons, 20% of dark matter and 75% of Dark Energy. In order to explain the data scientists had to invoke the presence of the Dark Energy in the Universe moving from a Cold Dark Matter (CDM) cosmological model to a  $\Lambda$ CDM cosmological model with the introduction in the model of the cosmological constant  $\Lambda$ .

In the last years WMAP collected high quality data refining its early results. Moreover, *Planck* Collaboration released its temperature anisotropy results based on the data coming from the satellite and with an unprecedented resolution and sensitivity. In Fig. 1.4 we show the APS released by

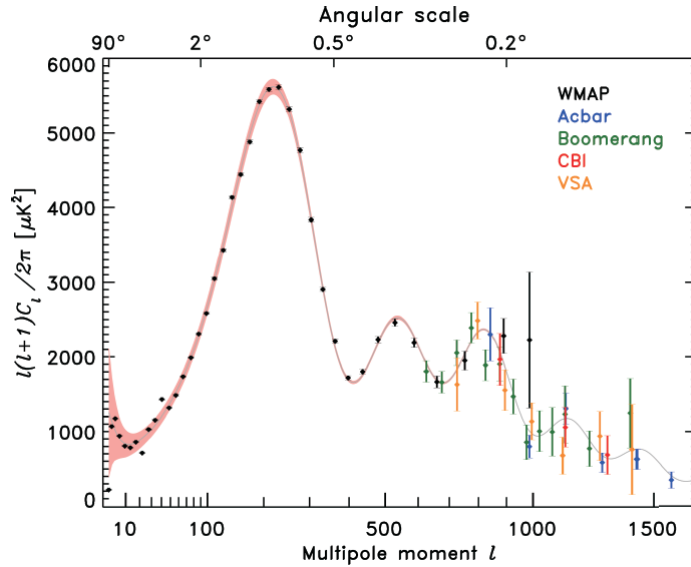


Figure 1.3: All the main Temperature CMB APS results before the *Planck* data arrival. With different uncertainties the points are all compatible with the  $\Lambda$ CDM model that describes the properties of the Universe [30].

WMAP and *Planck* at the beginning of 2013 [8,31]. At the same time, a new generation of ground-based experiments mapped the CMB anisotropies at small scales with very high resolution. The main projects are the Atacama Cosmology Telescope (ACT) [32] and the South Pole Telescope (SPT) [33].

Thanks to the *Planck* data scientists could extract a wealth of information about the early stages of the Universe that confirmed and refined the standard  $\Lambda$ CDM cosmological model by setting strong constraints to its parameters. By exploring the cosmological parameter space with a Markov Chain MonteCarlo (MCMC) technique, it is found that the spatial curvature is close to zero; the Universe total density is divided in  $\sim 5\%$  baryonic matter,  $\sim 26.5\%$  Cold Dark Matter and  $\sim 68.5\%$  cosmic density in the form of Dark Energy. The power spectrum of the primordial density perturbations is usually parametrized as a power law with  $P(k) \propto k^{n_s-1}$  where  $n_s$  is the spectral index of the primordial perturbations. A scale invariant power spectrum is determined by  $n_s = 1$ . *Planck* measured an highly significant deviation from scale invariance of the primordial power spectrum with the

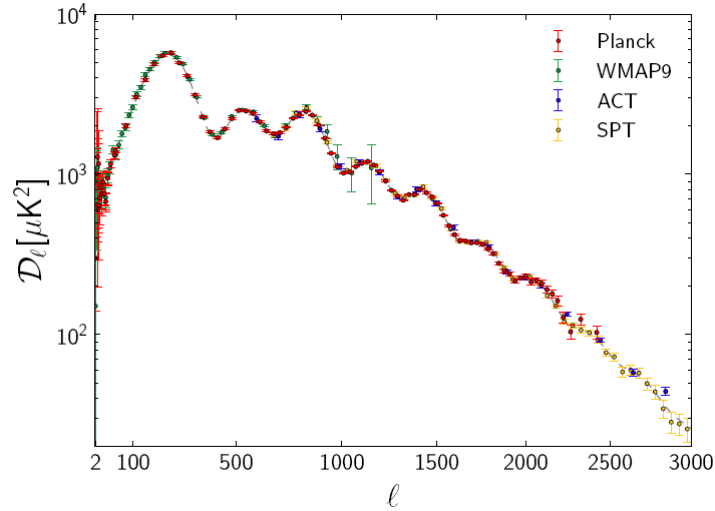


Figure 1.4: The Angular Power Spectrum measured by the four main CMB experiments collected in one single plot: *Planck* (red), WMAP 9 year (green), ACT (blue), SPT (yellow). The error bars contain the Cosmic Variance. All the results are in good agreement with the *Planck* best fit up to  $\ell = 2000$  [8].

parameter  $n_s$  that is lower than the unity by more than 3 sigma [34], a firm probe of the existence of an inflationary phase. From the same data, *Planck* set new limits on the number  $N_{eff}$  and mass  $m_\nu$  of neutrinos. It found no significant evidence for extra relativistic species, beyond the three species of (almost) massless neutrinos, although the value of  $N_{eff} = 3.30 \pm 0.27$  higher than 3 provoked a strong debate about the total number of neutrinos [35]. Also *Planck* data put new constraints to the sum of the masses of the neutrinos to be  $\sum m_\nu < 0.66 eV (95\%CL)$ . CMB fluctuations were supposed to be perturbed by gravitational lensing, primarily generated by the structures of the Universe on very large scales and at around redshift  $z \sim 2$ . *Planck* detected gravitational lensing of CMB anisotropies at  $25\sigma$  [36] and performed a measurement of the lensing potential with very high accuracy. Three of the fundamental assumptions of the standard cosmological model are that the initial fluctuations are adiabatic, statistically isotropic and Gaussian. *Planck* confirmed the adiabatic nature of the perturbations by putting strong constraint to the amount of non-adiabatic perturbations. Also, *Planck* results

do not show strong evidence for the presence of non-Gaussianity in the CMB Temperature APS [37]. Instead, deviations from isotropy have been found in the data, confirming and strengthening the previous WMAP results [38]. These anomalies are mainly located at large scales. An analysis of the large scale anomalies is presented in Chapter 4.

*Planck* data are also very useful for the study of astrophysical processes. In fact, the original *Planck* maps are the results of the superposition of CMB signal and the radiation of all the astrophysical processes that emit in the microwave range. This second part is called foreground emission and must be wiped out in order to have cleaned CMB maps to be analysed. The most important foregrounds are Galactic and extragalactic point sources, emissions from the Solar System, SZ effect, Galactic synchrotron, free-free, spinning and thermal dust emission. *Planck* data revealed the presence of an important emission from the CO molecule [39] and confirmed the WMAP results [40] about an anomalous emission localized around the Galactic center called "haze" [41].

A deep analysis of all these emission sources is fundamental in order to grow our knowledge about the physical processes generating the emissions and also to clean the CMB data in order to obtain cleaned full sky CMB maps to be analysed. In this thesis Chapter 2 is dedicated to a theoretical introduction of the foregrounds with a particular focus on the synchrotron emission while Chapter 5 is dedicated to present the results from the synchrotron analyses.

### 1.3.2 Polarization anisotropies

The CMB radiation is predicted to be linearly polarized with a polarization fraction of about 5% [42]. The polarised signal mainly arises from the Thompson scattering of CMB photons with free electrons in the plasma at the LSS. If the incident radiation were isotropic or had only a dipole variation, the scattered radiation would have no net polarization. However, if the incident radiation from perpendicular directions (separated by  $90^\circ$ ) had

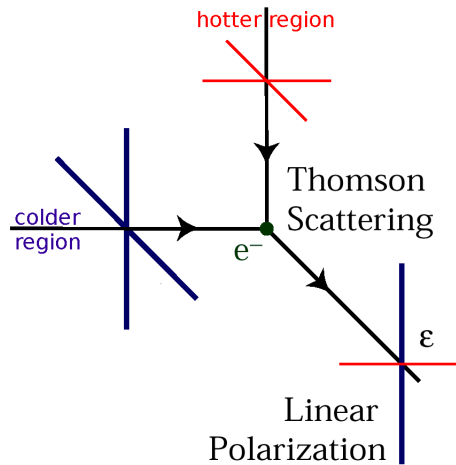


Figure 1.5: Thomson scattering of radiation with quadrupole anisotropy generates linear polarization. In the rest frame of the electron, red lines represent hotter radiation, while blue lines represent colder radiation resulting in a quadrupole anisotropy of the incident radiation.

different intensities, such as in the example of Figure 1.5, a net linear polarization would result. Such anisotropy is called "quadrupole" because the poles of anisotropy are  $90^\circ$  apart.

The sources of quadrupole anisotropy are mainly of two kinds: scalar and tensor perturbations. Scalar perturbations are due to the velocity gradient of the photons in the plasma density fluctuations. At the recombination, photons are flowing from the cold underdensities to the hot overdensities. This mechanism generates a gradient in the velocity distribution of the photons and so a scalar quadrupole anisotropy. Tensor perturbations at the recombination are generated by residual gravitational waves generated during the inflation. This tensor effect has been predicted by the inflationary theory, but it has still not been detected, consequently the predictions about its amplitude and its contribution to the linear polarization signal depend on the considered model. The amplitude of tensor perturbations is usually related to the intensity of the scalar perturbations through the so-called Tensor-to-Scalar ratio ( $r$ ). Recent data collected by WMAP and *Planck* satellite set an upper limit to  $r$  of 0.12 (95% CL).

Polarization signal is parametrized by two quantities called electric and magnetic modes (*E-modes* and *B-modes*) along the direction ( $\hat{n}$ ) and defined as:

$$\begin{aligned} E(\hat{n}) &= \sum_{\ell,m} a_{E,\ell m} Y_{\ell m}(\hat{n}) \\ B(\hat{n}) &= \sum_{\ell,m} a_{B,\ell m} Y_{\ell m}(\hat{n}) \quad . \end{aligned} \tag{1.18}$$

where the  $Y_{\ell m}$  are the spherical harmonics in which the modes have been expanded and the  $a_{E/B,\ell m}$  are the coefficients of the expansion, related by Eq. 1.12 to the Q and U Stokes parameter maps measured by CMB experiments. The introduction of the E (scalar) and B (pseudo-scalar) modes is not only due to a simplification of the mathematics, but also to the physical origins of the effects that generate the linearly polarized signal. E-modes are generated both by scalar and tensor perturbations, while B-modes arise only from tensor perturbations. Consequently, a firm proof of the presence of a primordial stochastic background of gravitational waves and of the inflationary predictions can come from a detection of primordial (large scales) B-modes in CMB polarization anisotropies at the LSS epoch.

There are other cosmological/astrophysical contributions that can generate E and B modes. The most important are the reionization and the weak lensing effect. At the very early stages of structure formations, photons emitted by the first stars had the effect to reionize the matter in the Universe. This epoch is called reionization and the large number of free electrons in the Universe, by interacting with the CMB photons, affected the CMB radiation. This effect is principally visible at the very large scales ( $\ell < 20$ ) in the EE angular spectrum. The peak in that range of multipoles is known as the reionization peak. Galaxies and clusters of galaxies perturb the space-time causing a deflection of the photons path which pass near these objects. The weak gravitational lensing effect is the sum of many small deflections which the CMB photons undergo, passing through galaxies and cluster of galaxies between us and the LSS. This deflection is a tensor effect since it is caused

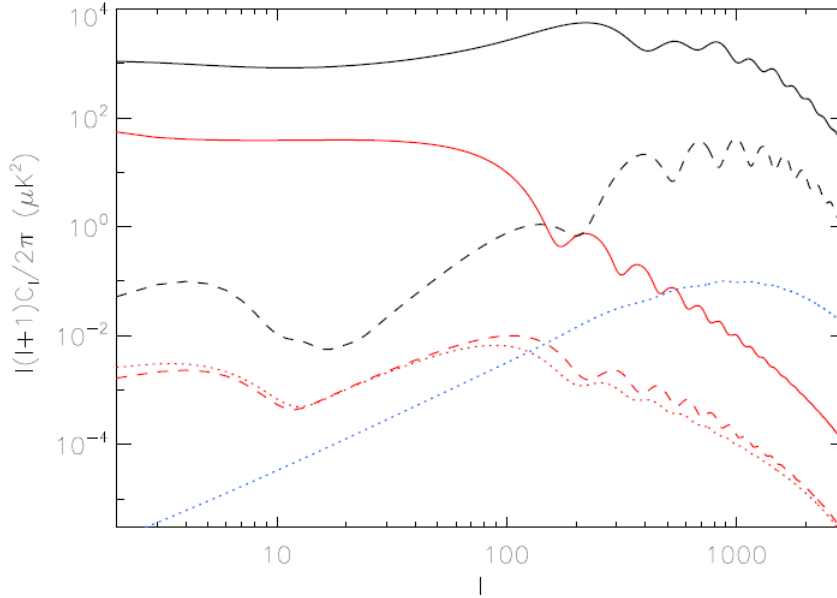


Figure 1.6: Theoretical APS of the different scalar (black) and tensor (red) CMB contributions to TT (solid line), EE (dashed line) and BB (dotted line) power spectra. The lensing effect of the matter structure in the Universe after the reioniation gives a contribution to the B modes (blue dotted line).

by the presence of a gravitational field. It is particular important in polarization because it generates non primordial B-modes through a distortion of the E-modes. Consequently, at the level of APS this effect causes an additional contribution to the BB spectrum proportional to the EE spectrum. This is a second order effect dominant in the BB angular spectrum at small scales because of the higher level of E polarization. The peak of BB spectrum at  $\ell \sim 1000$  due to this effect has been recently measured by SPT [43]. Fig. 1.6 shows the level of the contributions of scalar and tensor perturbations to the power spectra. In the Figure has been considered a Tensor to Scalar ratio of  $r = 0.1$ .

Waiting for *Planck* polarization data that should be released in 2014, the most recent and detailed full sky polarization maps come from WMAP [31]. From the analysis of the data, WMAP team extracted the TE and EE

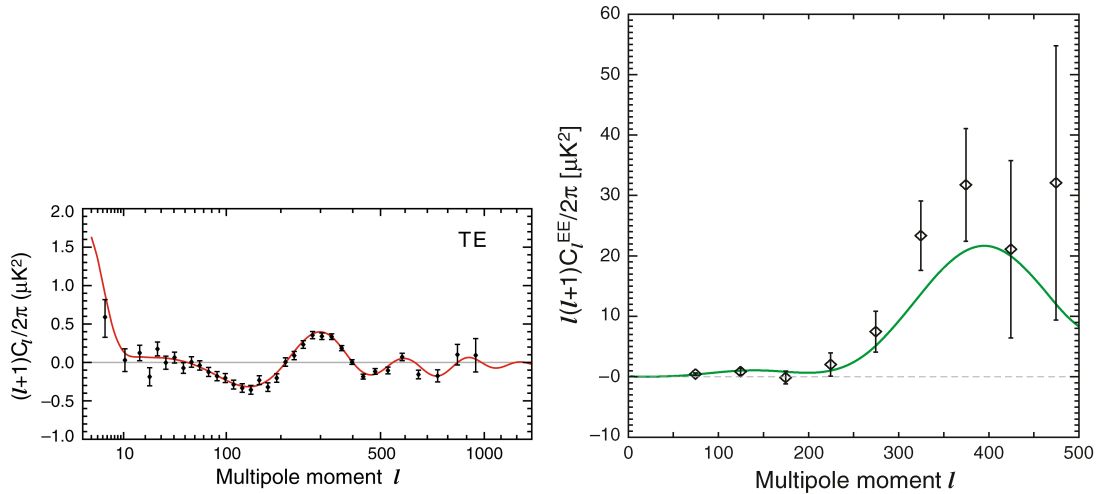


Figure 1.7: The TE (left) and EE (right) angular power spectra of the WMAP mission. The red and green curves are the theory fit to the data including the TT angular power spectrum data [44].

angular spectra shown in Fig. 1.7. In the figure red and green lines are the WMAP 9 yr best fit curves. WMAP data measured the parameters of the standard cosmological model to unprecedented level of precision, confirming the flatness geometry of the Universe, characterising the optical depth of reionization ( $\tau \sim 0.089$ ) and constraining the Tensor to Scalar ratio to be  $r < 0.13$  (95% CL).

The values of the most important parameters of the standard cosmological model are reported in Table 1.1. Columns 2 and 3 report the best fit and mean values obtained by *Planck* data complemented with the WMAP polarization data. Columns 4 and 5 has been obtained by WMAP 7 years data combined with SPT high  $\ell$  data in order to reach a larger range of multipoles in which performing the parameters analysis [34]. These set of data can be also combined together in order to achieve better results.

### 1.3.3 New polarization results: PLANCK perspective

A new release of *Planck* data is expected in 2014 with the full temperature data acquired by the satellite and, for the first time, the polarization

Parameter	Planck+WP+highL		WMAP-7+SPT	
	Best Fit	68% limit	Best Fit	68% limit
$100\Omega_b h^2$	2.207	$2.207 \pm 0.027$	2.223	$2.229 \pm 0.037$
$\Omega_c h^2$	0.1203	$0.1198 \pm 0.0026$	0.1097	$0.1093 \pm 0.0040$
$10^9 A_s$	2.211	$2.198 \pm 0.056$	2.143	$2.142 \pm 0.061$
$n_s$	0.958	$0.959 \pm 0.007$	0.963	$0.962 \pm 0.010$
$\tau$	0.093	$0.091 \pm 0.014$	0.083	$0.083 \pm 0.014$
$100\Theta_*$	1.0415	$1.0415 \pm 0.0006$	1.0425	$1.0429 \pm 0.0010$
$\Omega_\Lambda$	0.683	$0.685 \pm 0.017$	0.747	$0.750 \pm 0.020$
$H_0$	67.2	$67.3 \pm 1.2$	72.3	$72.5 \pm 1.9$

Table 1.1: The six fundamental parameters of the standard cosmological model as measured by *Planck* plus the WMAP polarization data and WMAP 7 year data plus data coming from SPT to reach a larger range of multipoles in which performing the parameters analysis [34].

results. *Planck* has been designed to observe the CMB polarization with unprecedented precision.

Fig. 1.8 shows the TE and EE angular power spectra, the blue bars representing the uncertainties expected from the *Planck* results [45]. The comparison with the results of Fig 1.7 clearly shows the great sensitivity of these new data, that will improve our knowledge of the early phases of the Universe.

The wide range of important scientific topics includes the perspectives in improving substantially the measures and the constraints to the parameters of the standard cosmological model, especially the optical depth  $\tau$ , the spectral index,  $n_s$ , and the Tensor to Scalar ratio,  $r$ . A clear detection of the reionization peak will allow to better understand the mechanism of reionization [46]. There is a possibility to detect for the first time the signal from the B-modes generated by the presence of a stochastic background of primordial gravitational waves.

In the standard scenario, the coefficients of the spherical harmonic ex-

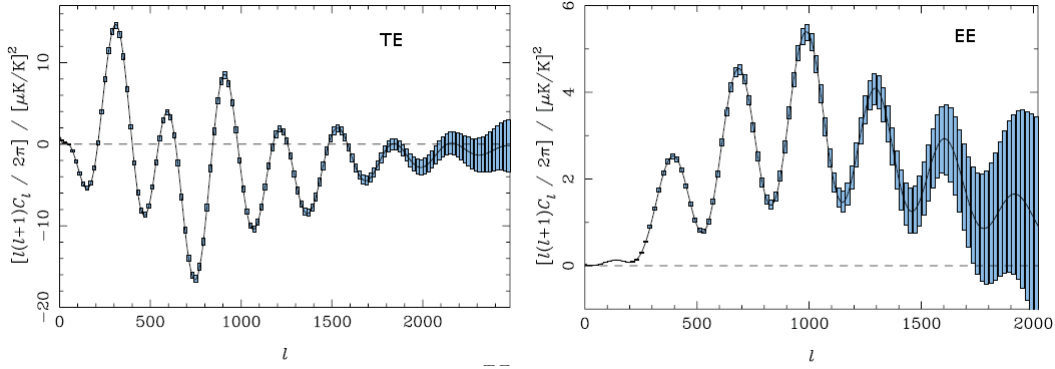


Figure 1.8: Expected results from the *Planck* polarization data. On the left TE, on the right EE. The bars show the expected uncertainties in the APS extraction [45].

pansion  $a_{E,\ell m}$  and  $a_{B,\ell m}$  have opposite behaviours under a P transformation:

$$\begin{aligned} a_{E,\ell m} &\rightarrow (-1)^\ell a_{E,\ell m} \\ a_{B,\ell m} &\rightarrow (-1)^{\ell+1} a_{B,\ell m} \quad . \end{aligned} \tag{1.19}$$

If P is conserved, the cross-correlations  $C_\ell^{EB}$  and  $C_\ell^{TB}$  should be zero. A Parity violation can be due to modification of electromagnetism [47] or of the standard picture of the Inflationary mechanism, where P is broken due to primordial (chiral) gravitational waves [48]. Chiral gravity produces such correlations at the CMB last scattering surface (impacting the lowest modes of the above cross-correlations), whereas general modification of the standard electromagnetism produces cross-correlations other than zero even at higher multipoles. The future *Planck* polarization data will allow to better constrain the parity (P) symmetry.

## 1.4 LFI Polarization Data acquiring methodology: the OrthoMode Transducer

To achieve the important objectives described above, it has been necessary to implement instrumentations of extreme precision. Among the various

components crucial for the instrument, it is unavoidable to assemble:

- Optics: the telescope size mainly determines the instrument resolution. *Planck* satellite has an off-axis telescope with a projected diameter of 1.5 m [49].
- Receivers: of various type according to the frequency, to measure temperature and polarization signals with the highest sensitivity as possible. *Planck* is equipped with 22 radiometers, that form the Low Frequency Instrument (LFI) working at 30 GHz (4), 44 GHz (6) and 70 GHz (12) [50], and with the High Frequency Instrument (HFI) composed by 20 spider-web bolometers working at 143 GHz (4), 217 GHz (4), 353 GHz (4), 545 GHz (4) and 857 GHz (4) and 32 polarization-sensitive bolometers working at 100 GHz (8), 143 GHz (8), 217 GHz (8) and 353 GHz (8) [51].
- Cryogenic systems: necessary to reach very low temperatures in order to enhance the sensitivity of the receivers and lower the noise. *Planck* uses a combination of passive radiative cooling and three active refrigerators. Passive system is composed by a baffle and three V-groove shields [49]. Active refrigerators are a closed-cycle hydrogen sorption cryocooler [52], that cools the LFI to 20 K and also provides 18 K pre-cooling to the HFI; a Joule-Thomson refrigerator driven by mechanical compressors [53], that cools the bolometers to 4 K; and an open-loop  $^3\text{He}^4\text{He}$  dilution refrigerator to 0.1 K for HFI [54].
- Polarization splitters: if the receivers are not directly sensible to the polarization signal, such as the LFI radiometers, it is necessary a device to separate the two polarized signals before the radiation reaches the receivers. This section is dedicated to this component of the *Planck* satellite.

The methodology for polarization measurement in *Planck* is the key of the high sensitivity and resolution polarization data. The *Planck* HFI instru-

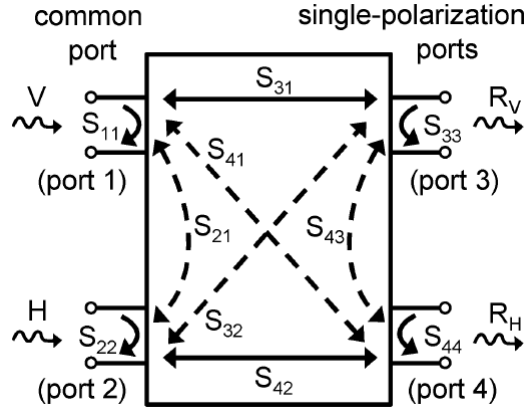


Figure 1.9: Representation of an OMT with relevant port-signals [56].

ment uses pairs of polarization-sensitive bolometers (PSBs) that consists of rectangular grids with metallization in one direction perpendicular to each other (see [51] for more details). Instead, the *Planck* LFI instrument uses the Orthmode Transducer (OMT) technology at the end of each feed [55]. I will focus on this second methodology.

The OMT is a diplexer that separates two orthogonal linearly polarized signals within the same frequency range. Usually, it consists of four electrical ports in which two of them are in common. The radiation enters the device from the common port (port 1 and 2) and the two split polarizations exit from the single-polarization ports (port 3 and 4) [56]. The general scheme of the device can be summarized in Fig. 1.9.

For a propagating waveguide mode we can define a generalized complex amplitude  $a$  so that  $P = a \cdot a^*$ . Calling  $a_i$  the generalized amplitude of the signal at frequency  $\nu$  entering the device from port  $i$ , and  $b_i$  that of the signal leaving the device from the same port, one can write the outputs as a function of the inputs with the matrix equation:

$$b = \mathbf{S} \cdot a \quad , \quad (1.20)$$

where  $\mathbf{S}$  is the Scattering Matrix. For the OMT the scattering matrix is a  $4 \times 4$  object:

$$\begin{pmatrix} b_1 \\ b_2 \\ b_3 \\ b_4 \end{pmatrix} = \begin{pmatrix} S_{11} & S_{12} & S_{13} & S_{14} \\ S_{21} & S_{22} & S_{23} & S_{24} \\ S_{31} & S_{32} & S_{33} & S_{34} \\ S_{41} & S_{42} & S_{43} & S_{44} \end{pmatrix} \cdot \begin{pmatrix} a_1 \\ a_2 \\ a_3 \\ a_4 \end{pmatrix} . \quad (1.21)$$

The elements of the matrix and also displayed in Fig. 1.9 have the following meanings:

- $S_{nn}$  are the reflection coefficient at port  $n$ , thus for example  $|S_{11}|^2$  is the fraction of power lost by impedance mismatch at port 1 and its reciprocal  $RL_{(1)} = |S_{11}|^{-2}$  is the return loss at port 1.
- $S_{31}$  (and  $S_{42}$ ) is the transmission coefficient, and  $|S_{31}|^2$  the fraction of power transmitted, including impedance mismatch, ohmic losses and mode conversions along the path from port 1 to 3, whereas its reciprocal  $IL_{31} = |S_{31}|^{-2}$  is the insertion loss for port 3.
- The quantity  $|S_{41}|^2$  (and  $|S_{32}|^2$ ) represents the fraction of power transmitted from port 1 to 4, and its reciprocal  $XP_{41} = |S_{41}|^{-2}$  is the cross-polarization at port 4.
- $|S_{34}|^2$  represents the fraction of power that can be transmitted across the output ports, and its reciprocal  $IS_{34} = |S_{34}|^{-2}$  is the output isolation.
- $|S_{12}|^2$  represents the cross-polarized reflection (i.e. the fraction of power converted in the wrong polarization at the input port and reflected towards the radiometer). Its reciprocal  $IS_{12} = |S_{12}|^{-2}$  is the input isolation.

Common electric requirements for the OMT design are: a very high transmission ( $S_{31}$  and  $S_{42}$ ) that is, in the dimensions usually considered for these kind of device ( $dB$ ), negative values as close as possible to  $0 dB$  and as lower as possible levels of cross-polar response ( $XP_{41}$  and  $XP_{32}$ ) and isolation ( $IS_{12}$  and  $IS_{34}$ ).

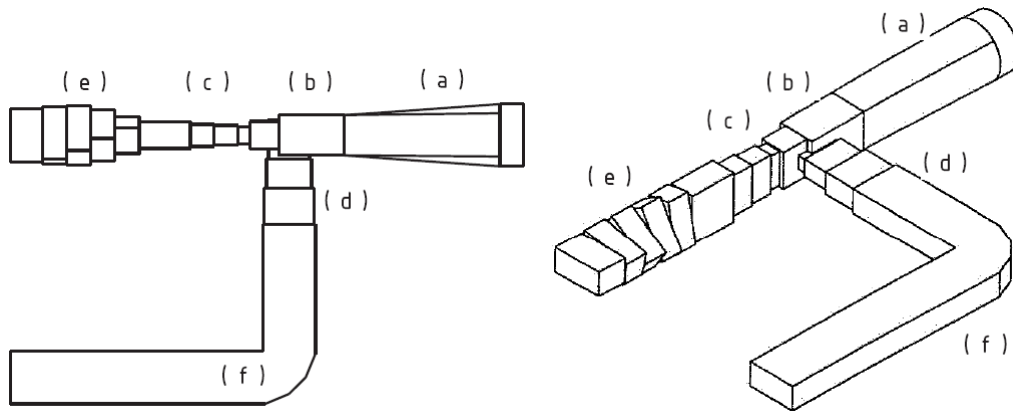


Figure 1.10: Sketch of the 44 GHz OMT used in the LFI *Planck* instrument [55].

The design of the OMT in the LFI *Planck* instrument is shown in Fig. 1.10. Six main sections can be identified in the design. Since a square waveguide is more useful in this kind of designs and the waveguide that recoils the output from the radiometer is circular, the first building block of the OMT is necessarily a circular-to-square waveguide transition (a). It transforms the two  $TE_{11}$  orthogonal circular waveguide modes (in the common port 1 and 2) into the two orthogonal modes  $TE_{10}$  and  $TE_{01}$  propagating in square waveguide. The square waveguide drives the radiation to the core of the OMT that is a directional coupler (b) where the two polarizations are separated. Referring to Fig. 1.9, the two orthogonal polarizations are coupled to port 3 (c) and 4 (d) respectively by means of polarization-coupling structures that select only one polarization and reflect the other one. In the end the two polarizations follow the waveguide along a bend (f) or they are rotated (e) in order to better interface with the Front End Unit Module where they will be collected.

Due to the faint level of the CMB polarized radiation, a high sensitivity of the correlation radiometers is mandatory. Consequently, the OMT should induce very low spurious contribution from the unpolarized radiation and separate the polarized signal in the two directions with high transmission and minimizing the power loss and the cross-polarization components. The

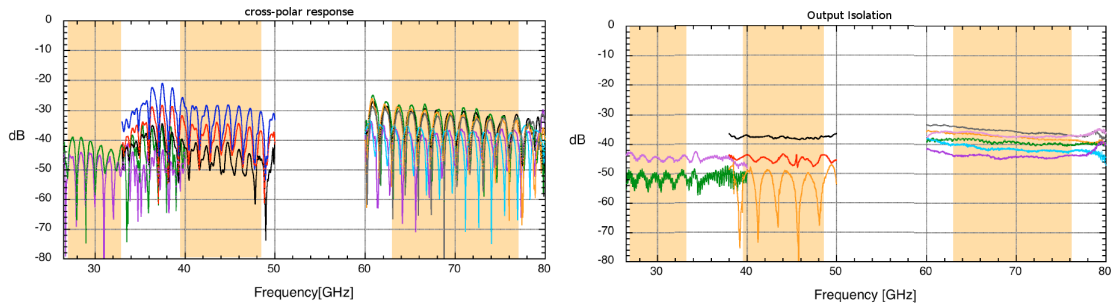


Figure 1.11: Side arm cross-polar response (left) and output isolation (right) for all the eleven OMT (amplitude). the LFI frequency bands are evidenced in the figure [55].

OMT design realized for the *Planck* LFI reaches the goals requested for a polarization detection. The 11 OMT mounted on the satellite are divided to work in three frequency bands: 26-40 GHz (2), 33-50 GHz (3), 60-80 GHz (6). All the devices achieve a very high transmission with values always higher than -0.4 dB and consequently very low power loss. Also the cross-polar response and the isolation are very good for all the frequency channels being both lower than -30 dB as shown in Fig. 1.11 [55].

## 1.5 Future expectation: CORE, PRISM and other projects

The excellent results of COBE opened the precision cosmology era. Subsequently, BOOMERanG, WMAP and *Planck* data confirmed the validity of the standard cosmological model in describing the evolution of the Universe. The "Inflationary" theory is the most accredited model to explain the early seconds of the Universe and solves some cosmological problems. However, there are still open questions: B modes must be detected in order to confirm the presence of a stochastic primordial field of gravitational waves, a strong prediction of the inflationary theory. A better measurement of the anisotropies will shed light on the real mechanism of the inflation among the large number of different theories formulated. Also better measurements will

lead to an analysis strictly connected to the particle physics because they will be useful in constraining the number of neutrinos, probing the existence or not of the sterile neutrino, and their total mass. Moreover they will help to understand which particle is the responsible for the Dark Matter effects that we see in the Universe and, most of all, the nature of the Dark Energy that accounts for about the 70% of the Universe density. These are only some of the most important open questions which scientists are trying to answer. For this reason a large number of projects are in development: EPIC [57], PIXIE [58], BICEP [59], ACBAR [60], EBEX [61], POLARBEAR [62], QUIET [63] and many others. I will focus here on four remarkable projects.

### ACT

The Atacama Cosmology Telescope (ACT) is an off-axis Gregorian telescope, with a six metre primary mirror and a two metre secondary mirror. Observations are made at resolutions of about one arcminute of three frequencies: 145 GHz, 215 GHz and 280 GHz. Each frequency is measured by a 3 cm x 3 cm, 1024 element array, for a total of 3072 detectors. The detectors are superconducting transition-edge sensors (TES), a new technology whose high sensitivity should allow measurements of the temperature of the CMB to within a few  $\mu K$  [64]. A system of cryogenic helium refrigerators keeps the detectors to about 0.3 K. ACT already released some interesting results [32], but the next surveys will be focused on CMB polarization observations for which the scientists are planning of increasing the number of detectors.

### SPT

The South Pole Telescope (SPT) is a 10 meter off-axis Gregorian telescope equipped with the so-called SPT-SZ camera. The name comes from the fact that it was designed to conduct a survey of galaxy clusters through their Sunyaev-Zel'dovich effect signature. It contains a 960-element bolometer array of superconducting TES. The focal plane for this camera was split into six pie-shaped wedges, each with 160 detectors. These wedges observed at three different frequencies: 95 GHz, 150 GHz, and 220 GHz. Since it is a ground-based experiment, SPT, like ACT, can observe only a small fraction

of the sky. In any case, thanks to its very high resolution (about 1 arcmin) its already published data [33] are very useful and complementary to WMAP and *Planck*. The next observational campaign is already planned and will be performed with a new detector called SPTpol camera, sensitive to polarization. The 780 polarization-sensitive pixels (each with two separate TES bolometers, each sensitive to one linear polarization) are divided between observing frequencies of 90 GHz and 150 GHz, and pixels at the two frequencies are designed with different detector architectures. The 150 GHz pixels are corrugated-feedhorn-coupled TES polarimeters fabricated in monolithic arrays while the 90 GHz pixels are individually packaged dual-polarization absorber-coupled polarimeters. Its very sensitive data will lead to a very precise observation of the E and B modes at very small scales ( $\ell > 2000$ ).

### COrE

The Cosmic Origins Explorer (COrE) is a mission proposed to the European Space Agency (ESA) as M-class (middle class) fourth generation satellite after COBE, WMAP and *Planck*. It will achieve full sky coverage at millimetre wavelengths up to arcminute resolution observing from the Sun-Earth Lagrangian point L2 in a quasi periodic Lissajous orbit [65]. The design is made up of approximately 6400 large array dual polarized detectors, a crucial number for achieving high sensitivity. The large focal plane is ensured by an off-axis reflective telescope, although the detector array is supplied by coupled feedhorns-OMTs which separate the polarization signal in two linear components towards bolometric detectors. The cryogenic system guarantees a temperature of about 100 mK for the feedhorns, OMTs and detectors at the centre of the focal plane which is enclosed by successive temperature stages up to 35 K.

COrE was proposed to map the CMB polarization pattern with unprecedented sensitivity in 15 frequency bands, from 45 GHz to 795 GHz. Thanks to its very high resolution and sensitivity it will be possible to detect the Tensor to Scalar ratio ( $r$ ) at a precision level of  $3\sigma$  up to  $r \sim 10^{-3}$ , two orders of magnitude better than *Planck*, close to the cosmic variance limit.

Thanks to its full sky coverage, COre will be able to disentangle between different reionization models, such as double peaked or very high reionization redshift histories, accurately measuring the Thomson optical depth to reionization. Moreover, full sky observations allow the satellite to improve our knowledge on primordial non Gaussianity given its high accuracy maps up to multipoles  $\ell \sim 2000$ . Finally, COre will provide an accurate detection of magnetic fields at sub nano-Gauss level unveiling their origin and evolution. This measurement will lead to understand if they have been generated by an inflationary mechanism or derived from a subsequent formation and amplification through astrophysical processes. Also COre will have a remarkable astrophysical legacy in both Galactic and extragalactic fields.

### PRISM

The Polarized Radiation and Spectroscopy Mission (PRISM) [66] has been proposed to ESA in May 2013 as L-class (large class) mission designed to carry out the ultimate survey of the microwave to far-infrared sky in both intensity and polarization as well as to measure its absolute emission spectrum. PRISM, with a 3.5 m usable diameter telescope cooled to below 10K, will consist of two instruments: a high angular resolution polarimetric imager and a low angular resolution spectrometer. The former will map the intensity and polarization of the complete sky in 32 broad frequency bands between 30 GHz ( $\sim 1\text{cm}$ ) and 6 THz ( $\sim 50\mu\text{m}$ ) with unprecedented sensitivity and with an angular resolution ranging from about 17 arcminutes to about 6 arcseconds. The latter will compare the sky frequency spectrum to a nearly perfect reference blackbody and measure the absolute sky emission over the same frequency range.

With its large frequency range and very high sensitivity and resolution PRISM will lead to: an unprecedented characterization of the B modes from primordial gravitational waves since it will be able to detect the Tensor to Scalar ratio ( $r$ ) at a precision level of  $3\sigma$  up to  $r \sim 10^{-4}$ ; a very deep search for primordial magnetic fields and non Gaussianity imprints in polarization; with a sensitivity at  $1\sigma$  of about  $\Delta I_\nu = 10^{-26}$  it will provide a search for

distortions from a perfect CMB blackbody spectrum or those generated by many astrophysical processes such as the Comptonization during the reionization epoch or Silk damping of small-scale perturbations of the photon fluid or decaying and annihilating particles at different cosmological times. Also, PRISM will detect about  $10^6$  galaxy clusters using the SZ effect and to study the properties and evolution of the faintest dusty galaxies, that produce the Cosmic Infrared Background (CIB) and in which the first stars were formed.

### 1.5.1 The research for new device

All the projects presented are the consequence of the continuous efforts to reach better measurements with higher sensitivity and resolution. The quality proposed for CORe and PRISM will be the result of the present and future research for new devices with characteristics better than those used in previous projects. But this research will not end with the next generation of missions. There will be always a challenge to find new technologies or to optimize the usual ones in order to continuously improve instruments for cosmology. The challenge of these days is to measure the polarization signal in the microwaves. One of the most important instrument components to extract this signal is the OMT described in Section 1.4 in the context of *Planck* satellite, designed to separate two orthogonal polarization signals.

In the context of developing more efficient devices, part of my PhD project is based on the properties of a technology called Photonic Crystals. As discussed in Chapter 6, this technology is candidate to substitute the OMT technology thanks to its precision in separating the two polarizations of the radiation. Although the project of a polarization splitter is still under validation and characterization tests, this device would perfectly suit between the optics and the receivers of ground-based telescopes dedicated to high precision polarization measurements of microwave signals, in particular at small scales. Future developments will achieve the integration of the receiver inside the polarization splitter in order to lower the power lost and improve the efficiency of the device.

## Chapter 2

# Microwave Foregrounds

Any cosmological observation campaign from the ground or from satellite must face the fact that there are a lot of processes that emit in the microwaves. For this reason the original maps produced by CMB experiments contain a mixture of cosmological and non-cosmological signal, the latter resulting in the sum of many contributions depending on the kind of observation carried out. For example satellite missions dedicated to full sky surveys collect the signal from all the diffuse and discrete emissions caused by astrophysical processes. Ground based telescopes and balloon borne experiments have an additional contribution coming from the atmosphere. Moreover, in the resulting maps it must be considered the presence of the instrumental noise and possible systematic effects that must be taken into account in the data analysis process and removed. All the astrophysical contributions generated between the LSS and the observer are known as *foregrounds*. They represent the most important contaminants for CMB dedicated projects, but at the same time they carry out crucial astrophysical and cosmological information about structure evolution.

Fig. 2.1 illustrates the position on the sky and the intensity of the astrophysical emissions showing the complexity of the total signal observed because they are also superimposed each others. In Fig. 2.1 are reproduced the foreground point sources on the left and the diffuse foreground emissions

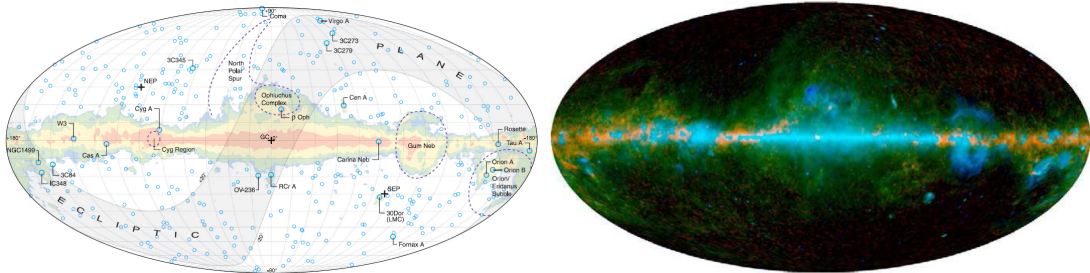


Figure 2.1: WMAP foreground emissions separated results. On the left blue circles represent the positions of the brightest point sources, on the right false colour image derived from a combination of WMAP band differences chosen to highlight differing spectral components. Red (W-V) highlights regions where thermal emission from dust is highest. Blue (Q-W) is dominated by free-free emission. Green ((KKa)-1.7(Q-W)) illustrates contributions from synchrotron and spinning dust [31].

on the right obtained from the analysis of WMAP data in 5 different frequency bands: 23 GHz (K band), 33 GHz (Ka band), 41 GHz (Q band), 61 GHz (V band) and 94 GHz (W band). Strong efforts have been made for understanding how to separate the different components contributing to the observed maps and several methods have been worked out, which operate either in the real or in the harmonic space.

The most powerful and therefore commonly adopted approach to the component separation issue is to use multifrequency data [67], since the CMB radiation and the foregrounds have very different spectral behaviours. In this approach, the observed map  $x_i$  at the frequency  $i$  is assumed as the result of different components  $s_j$ , mixed up by a matrix  $A_i^j$ , known as the mixing matrix, that considers the different frequency scalings of the components:

$$x_i = A_i^j s_j + n_i \quad (2.1)$$

where  $n_i$  is the instrumental noise and  $s_j$  takes into account all the possible contributions to the observed map, including the CMB.

A wide set of different methodology has been applied to recover the signal  $s_j$  in the microwave maps, but, generally, they can be divided in three different approaches. The first makes assumptions concerning the foregrounds

coming from an *a priori* knowledge of their emission processes and their frequency dependence. This has been implemented in methods as Linear Filtering [68] or Maximum Entropy Methods (MEM) [69]. A great limitation to the accuracy in the results of these methods comes from the few number of surveys in a limited number of frequencies available and from possible limitations in accuracy of the assumptions. The second approach is known as blind because the only assumption is the statistical independence of the CMB and the Galactic emissions to be separated. For example, some methods assume that the CMB is the only Gaussian contribution to the total signal. Examples of this approach are the Independent Component Analysis (ICA) [70], Multidetector Multicomponent Spectral Matching (MDSM) [71], Separation by Parameter Estimation [72], Wavelet based Fitting of Internal Templates (WI-FIT) [73] and Phase Analysis [74] based on the uncorrelation of the phases between the CMB and the foregrounds. Semi-blind approaches are in the middle between these two different methodologies. A remarkable example is the Correlated Component Analysis (CCA) [75] that build the mixing matrix through a parametrization of the different foregrounds with parameters estimated on patches of the sky. Once the mixing matrix have been recovered, component separation can be performed with traditional non-blind methods.

The most recent methods have been developed in the *Planck* Collaboration in order to obtain the true CMB signal after a removal of the foreground contributions. Among the huge number of methods proposed, four have been selected and used in the 2013 data release [76]: Needlet Internal Linear Combination (NILC), Spectral Estimation Via Expectation Maximization (SEVEM), Spectral Matching Independent Component Analysis (SMICA) and Commander-Ruler (C-R).

NILC [77] is a method to extract the CMB (or any component with known spectral behaviour) in needlet space. This is a particular framework in which the spherical harmonics, results of the map expansion, are filtered by suitably chosen functions. The method applies the ILC technique to multi-frequency

observations, that is, a linear combination of maps at different frequency with weights that are allowed to vary over the sky and over the full multipole range. The ability to linearly combine input maps varying over the sky and over multipoles is called localization. In the needlet space, harmonic localization is achieved using a set of bandpass filters defining a series of scales, and spatial localization is achieved at each scale by defining zones over the sky in order to determine the properties of the different contributions to the total map.

The original SEVEM algorithm [78] produces clean CMB maps at several frequencies through template fitting, followed by an estimation of the CMB APS from the clean maps using a method based on the Expectation Maximization algorithm [79]. In the harmonic space, the method treats the non-CMB emission as noise. Thus, using simulations of CMB plus noise obtains the bias and statistical error of the estimated power spectrum and construct an unbiased version of the CMB APS. This unbiased power spectrum is used to recover the CMB map through multifrequency Wiener-filtered method. In the recent *Planck* results, only the first step of the method has been considered. In addition, the clean maps have been optimally combined to produce a final CMB map.

Since CMB, foregrounds and noise are independent component of the total signal, SMICA [80] performs a decomposition of the spectral covariance matrix by fitting the parameters of the different components in the region of multipoles in which they are dominant. The covariance matrix contains the weights of the linear combination in harmonic space of the multi-frequency maps from which the CMB map is reconstructed. This map, among the four maps produced, has been chosen as the official CMB map released by *Planck*.

The Commander-Ruler [81] approach implements Bayesian component separation in pixel space, fitting a parametric model to the data by sampling the posterior distribution for the model parameters. For computational reasons, the fit is performed in a two-step procedure. First, both foreground amplitudes and spectral shape parameters are found at low-resolution us-

ing Markov Chain Monte Carlo (MCMC)/Gibbs sampling algorithms [82]. Second, the amplitudes are recalculated at high resolution by solving the generalized least squares system (GLSS) per pixel with the spectral shape parameters fixed to the values obtained from the low-resolution run.

Foreground knowledge is fundamental for all the three kinds of methodology. The most simple needs *a priori* knowledge of the foreground, but it is important even for blind methods in which the results from the fit of the cleaning procedures must be compatible with our knowledge of the properties of the astrophysical processes. For this reason it is necessary to continuously improve our knowledge of the foreground processes from the data coming from microwave surveys to obtain cleaned CMB maps. The following section will present the state of the art about all the astrophysical processes relevant in the microwaves on the light of the *Planck* most recent results.

## 2.1 The Foregrounds

All the foregrounds that can be found in microwave maps are divided in two wide categories: diffuse and discrete sources. Diffuse foreground emissions are generated by free electrons, nuclei "clouds" and dust grains located in our Galaxy (Galactic Synchrotron, Free free, thermal and spinning dust emission and the new emissions revealed by *Planck* the Haze and the CO emission) or in our Solar System (Zodiacal light, Kuiper Belt emission). This last contribution appears in the sky as structures of large angular size because of their relatively small distances. Discrete sources are generated by localized region in our Galaxy emitting in the sky and from extragalactic sources (galaxies and cluster of galaxies). All the extragalactic sources below the experiment detection threshold generate a background signal, discrete in origin, but appearing as diffuse cosmic background\*.

---

\*Note that, in principle, also undetected Galactic sources generate a background signal.

### 2.1.1 Diffuse foreground

#### Solar System

The diffuse foreground emitted in the Solar System, also known as Local Foreground, contains all the emissions coming from planets, comets, and asteroids present in the Main Belt (between Mars and Jupiter) and the Kuiper Belt (outside the orbit of Pluto). But the most important contribution to the Local foreground comes from the dust particles in the Solar system. The radiation emitted by the interplanetary dust inside the Solar System, principally located in the Main Belt, is called Zodiacal Light Emission (ZLE). At wavelengths shorter than  $12\mu m$  ZLE is mainly due to scattering of solar radiation, while at longer wavelengths thermal emission is the most important generation mechanism. In fact, these grains are in thermal equilibrium at around 240 K having a blackbody emission that mostly affects the higher CMB frequencies ( $\nu \gtrsim 200GHz$ ). Another source of foreground comes from the thermal emission of dust in the outer regions of the Solar System, principally in the Kuiper Belt region, that are responsible for the Kuiper Belt Objects Emission (KBOE). These grains are more distant from the Sun, though they emits approximatively as a blackbody with a temperature of  $30 - 60K$ . Their contribution is still largely unknown because of the faintness of the emission compared to the ZLE emission. However, it is not negligible for frequencies below 400 GHz. The dust grain are mainly located in clouds with a certain (angular) height scale on the ecliptic plane. These foregrounds affect also the high Galactic latitudes, usually not excluded by the common masks typically adopted to avoid, in CMB analysis, the most affected pixels close to the Galactic plane. Moreover, ZLE is characterized by an apparent variability of the brightness at the different pointing directions due to the change of the relative position of the observer with respect to the Sun and then with respect to the dust clouds [83]. Consequently, the emission can be appreciated in particular from the difference between two contiguous sky survey of the *Planck* satellite. In Fig. 2.2 we show the result of the difference between

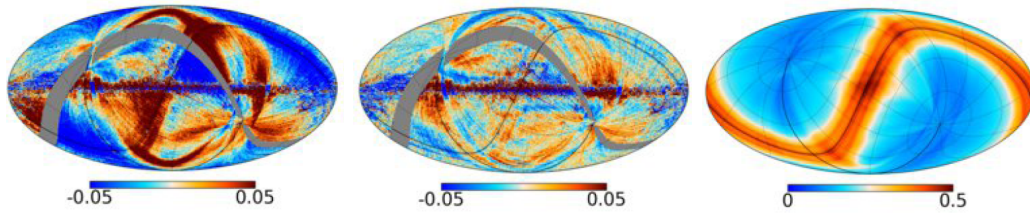


Figure 2.2: Survey 2 minus survey 1 difference maps at 857 GHz before (left) and after (center) Zodiacal emission removal, as well as the total (i.e., not differenced) Zodiacal emission removed from the nominal mission HFI maps (right). Units are in MJy/sr [84].

the survey 1 and 2 at 857 GHz with (left) and without (center) the Zodiacal light. On the right there is the emission subtracted [84]. Since the Kuiper Belt is in the outer regions of the Solar System, the KBOE is not affected by the periodic brightness variability as the Zodiacal Light and to separate its contribution it has to be taken into account inside the component separation techniques.

### Galactic diffuse foregrounds

Our Galaxy strongly contributes to the foreground radiation. I will focus this thesis on diffuse signals. The main diffuse components come from synchrotron, free-free (Bremsstrahlung) and thermal dust emissions as shown in Fig. 2.3. The first two are particularly important at frequencies ( $\nu$ ) lower than 100 GHz. Instead, the thermal dust emission is the dominant part for  $\nu \geq 70\text{GHz}$ . In addition, some subdominant emissions have been recently identified and must be taken also into account: the anomalous microwave emission (AME) due to spinning dust, providing an important contribution at lower frequencies, the Haze, and CO emission recently confirmed by *Planck* results.

- **Free-free**

Bremsstrahlung arises from the interaction of free electrons and ions in the interstellar medium. In our Galaxy ionized gas is principally generated by UV radiations emitted by hot O and B stars that are

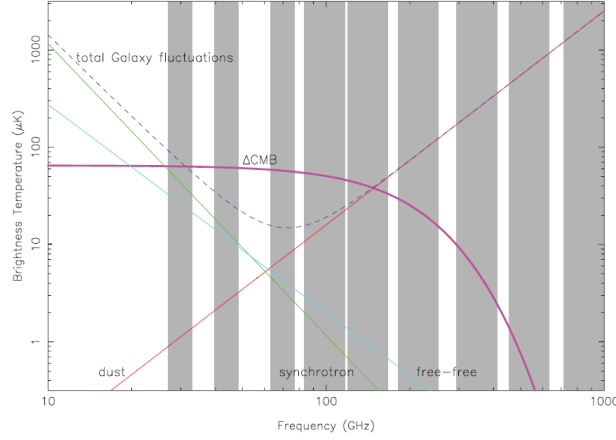


Figure 2.3: Spectra of the main diffuse Galactic foregrounds emissions in "brightness temperature" (in which a Rayleigh-Jeans  $\nu^2$  spectrum is flat), superimposed on the *Planck* frequency bands (grey regions). At higher latitudes CMB is clearly dominant in the range of frequency  $50 \leq \nu \leq 100$  [45].

generally located in a narrow width in latitude along the Galactic plane. The free-free intensity emission,  $I_{ff}(\nu, T)$ , integrated over the line of sight  $l$  is usually described by:

$$I_{ff} \propto \int n_e \sum_k Z_k^2 n_i^k T^{-1/2} dl \quad (2.2)$$

where  $n_e$  is the density distribution of free electrons,  $n_i$  is the density distribution of free ions with atomic number  $Z$  and is summed over the  $k$  different elements present in the gas of temperature  $T$ . Generally, the main contribution comes from ionized hydrogen. For a gas of pure hydrogen obviously  $n_e = n_i$ . The amount of free electrons and ions in a ionized gas is defined by the Saha equation and depends on the temperature of the gas,  $n_e(T)$ , and on the local intensity of the UV radiation flux that crosses the gas cloud. The same equation is valid to calculate the fraction of free ions,  $n_i(T)$ .

From the observational point of view, in the optically thin regime and in the Rayleigh-Jeans approximation, the measured free free emission

in antenna temperature can be described by a power law:

$$T_{ff} \sim I_{ff} \nu^{-2} \sim EM \nu^{-\beta_{ff}} \quad (2.3)$$

where the emission measure,  $EM \propto \int n_e \sum_k Z_k^2 n_i^k dl$ , is integrated over the line of sight  $l$  [85]. An approximate tracer of the Galactic free-free emission at intermediate and high latitudes is the Balmer line produced by the 3-2 transition in the atomic hydrogen, called  $H_\alpha$  [86]. On the Galactic plane the radio recombination lines (RRLs) are used because of the strong dust obscuration of the  $H_\alpha$  emission line. The maps of these tracers have been used as templates in component separation tools to remove the free-free emission from CMB maps. The brightness temperature spectral index,  $\beta_{ff}$ , is well determined at *Planck* frequencies with  $\beta_{ff} \sim 2.13$  at 30 GHz [76]. Since the free-free spectral index is lower than the synchrotron one, even if it constitutes a small fraction of the Galactic emission at low frequencies ( $\lesssim 10\%$  at 408 MHz), it becomes comparable to synchrotron emission around  $\nu \sim 20$  GHz. Free-free emission is not intrinsically polarized, although it could reach a small polarization degree ( $\ll 10\%$ ) via Thomson scattering at the edges of HII-regions [87], so its contribution is relevant only in Temperature maps.

- **Synchrotron**

Synchrotron emission is due to cosmic ray (CR) relativistic electrons spiralling around the lines of the Galactic magnetic field. Relativistic electrons are mainly produced by supernovae explosions. Such as the bremsstrahlung, synchrotron brightness temperature,  $T_{synch}$ , can be described by a power law:

$$T_{synch} \propto \nu^{-\beta_s} \quad (2.4)$$

where  $\beta_s$  is the synchrotron spectral index. The intensity of the synchrotron emission depends on the energy distribution function of the

electronic component of cosmic rays, on the intensity of the magnetic field and on the spatial distribution of the electrons. Typical values for  $\beta_s$  are around 2.7 [88] up to few GHz, but the spectrum steepens at higher frequencies with  $\beta_s$  closer to 3.0 [40]. However, the emission properties show a slight dependence with the position in the sky as it will be described in Chapter 5. Synchrotron emission is also strongly linearly polarized, with the polarization direction orthogonal to the magnetic field direction. Theoretically, the level of polarization can locally reach the 75%, but the observed average value for our Galaxy usually is in the range 10% - 50% changing with the latitude and the position in the sky.

At  $\nu \lesssim$  few GHz synchrotron emission is the dominant component outside the Galactic plane, so it is very useful to study this process with radio surveys. On the Galactic plane free-free (in temperature) and depolarization phenomena (in polarization) leads to a most uncertainty results. Nonetheless it is still the main source of foreground in CMB maps for  $\nu \leq 70$  GHz at large and intermediate latitudes and it affects the large and intermediate scales of the APS. A more detailed description of its properties will be presented in Section 2.2.

- **Thermal and Spinning Dust**

The thermal dust emission is due to the vibrational emission from dust heated by the interstellar radiation field. Dust is composed by grains of various sizes, from few nm up to several hundreds of nm and it is made of PAHs (Polycyclic Aromatic Hydrocarbon molecules), amorphous silicate (slightly colder) and carbonate compounds (slightly warmer). Assuming a grey body spectrum, in the Rayleigh-Jeans approximation, the thermal dust emission can be modelled as a power law [89, 90]:

$$I_{dust}(\nu, T_{dust}) = \nu^{\beta_d} B_{BB}(\nu, T_{dust}) \sim \nu^{\beta_d+2} \quad (2.5)$$

where  $T_{dust}$  is the temperature of the grains,  $B_{BB}$  is the black body

spectrum and  $\beta_d$  is the emissivity spectral index that is related to the shape, size, orientation and temperature of the grains. From Eq. 2.6, the antenna temperature,  $T_{dust}^{ant}$ , associated to the thermal dust emission, measured by the instrument in the Rayleigh-Jeans approximation is

$$T_{dust}^{ant} \sim I_{dust} \nu^{-2} \propto \nu^{\beta_d} \quad (2.6)$$

with a spectral index value of about  $\beta_d \sim 1.5 - 2$  [91] with a preference value of 1.7 [92]. Thermal dust emission is the dominant component in the sky for frequencies larger than 100 GHz along the Galactic plane, but also at intermediate latitudes. Infrared surveys are often used as component separation template. The 547 and 848 *Planck* maps are also very useful to remove dust emission from CMB maps. Thermal dust emission shows a small degree of linear polarization due to the grains that are oriented along the Galactic magnetic field. The level of polarization is usually small (3-4%) but reaches 10% towards particularly dense clouds [93, 94]. Nevertheless it is the strongest contaminant in polarization maps at frequencies higher than 100 GHz.

The cross-correlation of COBE-DMR maps with those of COBE-DIRBE showed the existence of an excess of power in the foreground microwave emission [95]. This excess, later confirmed also by WMAP [96], in the range of frequencies  $\nu \sim [10, 60]$ , is not correlated with free-free or synchrotron emission, but with the emissions in the maps at higher frequencies where dust is the dominant component. This effect, called Anomalous Microwave Emission (AME), has been associated to the electric dipole radiation due to the rotational excitation of small dust grains (spinning dust) [97]. The emission is supposed to be weakly polarized with a polarization degree, typically about  $\sim 7\%$  at 2 GHz. For the first time, *Planck* has been able to define the shape of the spectrum on the high frequency side of the emission peak in a number of dust/molecular/HII regions [98]. This work has provided a rich source

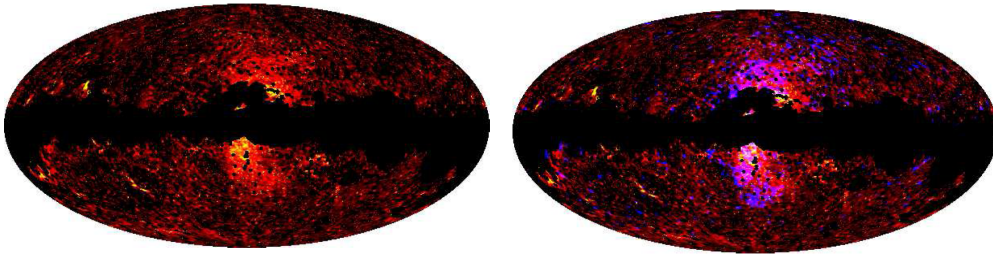


Figure 2.4: *Left.* The microwave haze as measured by *Planck* at 30GHz (red) and at 44GHz (yellow). *Right.* The same but including the Fermi 2-5 GeV haze/bubbles (blue). The very good spatial correspondence between the two suggests that this is a multi-wavelength view of the same underlying physical mechanism [100].

of data to explore the emission mechanism in detail.

- **Haze**

The WMAP observations evidenced the presence of an additional excess of diffuse microwave emission at low frequencies (23 and 33 GHz) around the Galactic center region (within 20 degrees), with an approximate radial symmetry [99]. This emission is not compatible with free-free or synchrotron mechanism and has been called *Haze*. Recent *Planck* temperature data allowed to better identify and characterize the emission [100]. It is a diffuse component coming from the regions around the Galactic center and extends to  $|b| \sim 35$  degree in Galactic latitude and  $|l| \sim 15$  degree in longitude. The derived spectrum is consistent with a power-law emission with spectral index  $\sim -2.55$ , harder than the typical synchrotron one. The Galactic Haze measured by *Planck* is shown in Fig. 2.4 (left). On the right, Haze morphology is compared with the Fermi gamma ray "bubbles", indicating a multi-wavelength view of the same distinct component of our Galaxy [101]. Several explanations have been proposed for this unusual behaviour, including enhanced supernova rates [102], galactic winds [103] and even annihilation of dark-matter particles [104]. Thus far, none of them have been confirmed and the issue remains open.

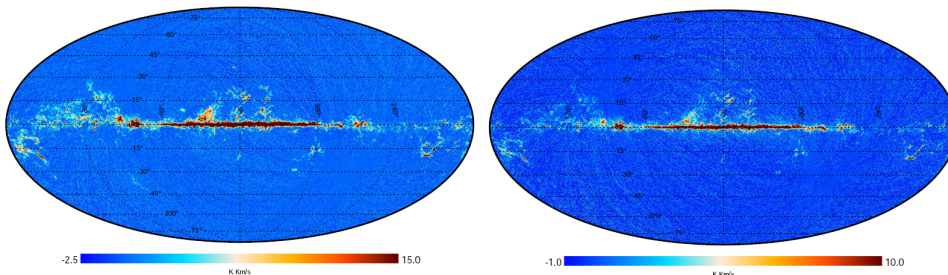


Figure 2.5: CO maps for the transitions  $J = 2 \rightarrow 1$  (left) and  $J = 3 \rightarrow 2$  (right) as measured by *Planck* [105].

- **CO line emission**

*Planck* HFI instrument produced for the first time a high sensitivity all-sky survey of the CO molecule [105]. In fact several rotational transition lines of this molecule, principally  $J = 1 \rightarrow 0$ ,  $J = 2 \rightarrow 1$  and  $J = 3 \rightarrow 2$ , falls at 115, 230 and 345 GHz and enter in the 100, 217 and 353 GHz HFI channels respectively. Fig. 2.5 shows the CO maps relative to transition  $J = 2 \rightarrow 1$  (left) and  $J = 3 \rightarrow 2$  (right) obtained with a component separation analysis of the *Planck* data. CO is known as a good tracer of gas molecular clouds mainly located in a narrow region along the Galactic plane [106]. Its detection is one of few methods to detect the molecular clouds that contain about the 50% of the entire Interstellar Medium, responsible for about 10-15% of the total mass of the Milky Way [107].

### 2.1.2 Extragalactic Discrete Foreground

In the millimetre domain different extragalactic foregrounds affect sky maps. The main contribution comes from the extragalactic point sources that are principally radio sources and infrared dusty galaxies that dominates respectively at low and high frequencies. Their contribution affects the smallest scales of the APS ( $\ell \gtrsim 500$ ) and must be detected and subtracted from the CMB maps to avoid biases in APS analysis and in the determination of the cosmological parameters. The capability of an instrument to detect point

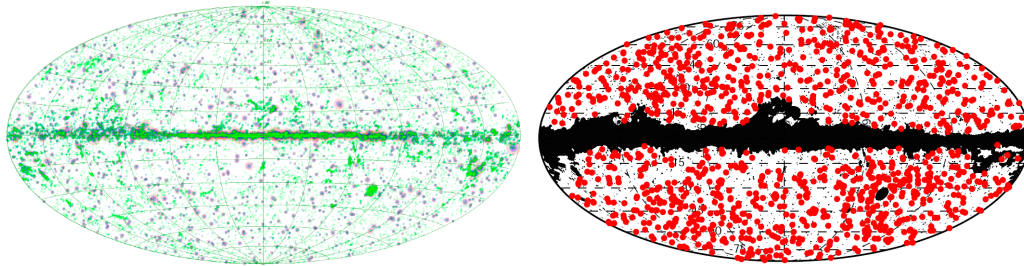


Figure 2.6: *Left.* Sky distribution of the PCCS sources at three different channels: 30 GHz (pink circles), 143 GHz (magenta circles), and 857 GHz (green circles). The dimension of the circles is related to the brightness of the sources and the beam size of each channel [108]. *Right.* Distribution of the 1227 *Planck* clusters and candidates across the sky (red thick dots). In black the masked pixels where the analysis could not be applied because of the presence of point-sources (black thin dots), the Magellanic clouds (large black areas) and the Galactic mask [109].

sources is quantified by the detection threshold flux. This is the flux limit below which a source is not distinguished from the background. It depends on the optical properties of the instrument (mainly the angular resolution), on the global fluctuation level of the sky at the considered frequency, and on the algorithm used to extract the sources from the maps. Typically, a confidence level equal or greater than  $5\sigma$  for the detection is assumed. Another important extragalactic foreground source is the SZ effect generated by the presence of galaxy clusters in our Universe. In 2013 the *Planck* Collaboration released the most complete full-sky catalogue of bright sub-millimeter extragalactic compact sources (PCCS) [108] and detected hundreds of clusters of galaxies through the thermal SZ effect [109].

- **Extragalactic point sources**

Radio sources relevant in the microwaves are principally BLlac and Flat Spectrum Radio Quasars (FSRQ), collectively called as "blazars". These are jet-dominated extragalactic objects characterized by a strongly variable and polarized emission of non-thermal radiation, from low radio energies up to high energy gamma rays [110]. The spectrum of extragalactic point sources is usually parametrized as a power law:

$$S_\nu \sim \nu^\alpha \quad (2.7)$$

Radio sources are characterized by a flat spectrum with  $\alpha \sim -0.39$  recently measured by ACT [111] and confirmed by SPT and *Planck*. The flat spectrum is generally believed as the result of synchrotron self-absorbed emission in the inner part of AGN relativistic jets [112].

Infrared galaxies are dominated by thermal dust emission at temperature of  $\sim 20\text{K}$  that presents a steeper spectrum with  $\alpha \sim 3.5$ . Recent observation of local dusty galaxies detected a new population of cool sub-mm galaxies, with presence of very cold dust ( $T = 10\text{-}13\text{ K}$ ) [113] suggesting that previous studies of dust in local galaxies have been biased away from such luminous cool objects.

In addition to this general classification, there are anomalous objects like Gigahertz Peaked Spectrum (GPS), Advection Dominated Accretion Flows/Adiabatic Inflow Outflow Solution (ADAF/ADIOS), star-forming galaxies and radio afterglows of Gamma Ray Burst (GRB) [114]. In particular, GHz Peaked Spectrum (GPS) objects present a convex spectrum which peaks around few GHz and are believed to be young and compact radio sources with a self absorbed synchrotron emission. Advection Dominated Accretion Flows (ADAF) and Adiabatic Inflow Outflow Solution (ADIOS) are objects, typically early type galaxies, in which the central engine emits in the late stages of evolution and the accretion efficiency of the central black hole is very low. This causes the emission to be mainly in the cm and mm ranges. Starforming galaxies are either late type or starburst galaxies at low redshift, dominated by synchrotron and free free emission, or high redshift protospheroid with active star formation. Radio afterglows of Gamma Ray Burst are rare, their synchrotron emission in radio has a flux which scales as  $S_\nu \propto \nu^{1/3}$  up to a peak frequency which decreases with time. Except for the starburst galaxies, that are numerous, all

these objects are almost rare and their contribution to CMB maps is practically negligible.

- **Galaxy clusters and the Sunyaev-Zeldovich effect**

The CMB study is very important for its possibility to indirectly detect the presence in the Universe of clusters of galaxy through the thermal Sunyaev-Zeldovich (SZ) effect [115]. This effect occurs when CMB photons travel through the hot gas of galaxy clusters and interact with the free electrons that transfer energy to the photons through the inverse Compton scattering. In the Rayleigh-Jeans region the net effect is a decrement of the CMB surface brightness,  $\Delta I_{th}$ , towards the cluster [116]. In the non relativistic approximation,

$$\Delta I_{th} = \frac{2h_P}{c^2} \left( \frac{k_B T_{CMB}}{h_P} \right)^3 g(x)y, \quad (2.8)$$

where  $h_P$  and  $k_B$  are the Planck and the Boltzmann constants, respectively,  $T_{CMB}$  is the temperature of the CMB photons and  $g(x) = x^4 e^x / (e^x - 1)^2 [x(e^x + 1) / (e^x - 1) - 4]$  is a function of the dimensionless photons frequency,  $x = h_P \nu / k_B T_{CMB}$ . The Comptonization parameter,  $y$ , contains all the cluster information and is defined as:

$$y = \int \left( \frac{k_B T_e}{m_e c^2} \right) n_e \sigma_T dl, \quad (2.9)$$

where  $T_e$  and  $n_e$  are the temperature and density of the free electrons in the hot gas,  $\sigma_T$  is the Thompson scattering and it is integrated over the cluster along the line of sight.

This formulation is valid in the non relativistic approximation. In the relativistic case the collision term of the Boltzmann equation, that describes the hot gas of the cluster, is numerically solved to obtain a correction term to the non relativistic case. The correction is of few percent in the amplitude of the effect and depends on the temperature of the hot gas of the cluster [117, 118].

The thermal SZ effect has a frequency dependence and causes a shift of the CMB blackbody spectrum to higher frequencies independently from the distance of the galaxy cluster. The net effect in the non relativistic case is that at low frequencies ( $\nu < 217$  GHz) the CMB behind the clusters appears slightly colder, at high frequencies ( $\nu > 217$  GHz), instead, it appears slightly hotter. This effect has been measured by ACT and SPT ground-based experiments on small patches of the sky [119, 120]. *Planck* satellite was equipped by frequency channels between 30 GHz and 353 GHz including the band around 217 GHz in which the SZ contribution is particularly low and hidden below the primary anisotropy signal, the instrumental noise and residual foregrounds. Thus, *Planck* could observe the SZ effect in the all-sky map detecting 1227 candidates with 178 new cluster detection, never observed before. In total it detected 861 confirmed clusters of which 683 already known and 366 are candidates to be confirmed by independent observations [109]. In fact, the same electrons in the hot gas of galaxy clusters emit X-ray through the bremsstrahlung process. The X-ray emission at high energies depends on the square of the electronic density and its measure can represent an important tool to estimate the expected SZ effect of the single cluster, but also to study in more detail the cluster gas properties.

If the cluster has a peculiar velocity,  $V_r$ , the associated Doppler effect causes an additional spectral distortion called the kinetic SZ effect. In the non relativistic limit the effect causes a decrement or an increment in the CMB brightness,  $\Delta I_k$ , depending on the direction of the cluster velocity with respect to the observer

$$\Delta I_k = -\frac{2h_P}{c^2} \left( \frac{k_B T_{CMB}}{h_P} \right)^3 \left( \frac{V_r}{c} \right) \tau_e h(x), \quad (2.10)$$

where  $\tau_e = \int n_e \sigma_T dl$  is the Thomson optical depth and the function  $h(x) = x^4 e^x / (e^x - 1)^2$  depends on the dimensionless photons frequency

$x$  [116,121]. The thermal and kinetic effects have a different frequency dependence that in principle allows their separation through multi-frequency observations. However, the kinetic SZ is a second order effect and it is an order of magnitude lower than the thermal SZ. Relativistic corrections to the kinetic SZ are due to the Lorentz boost to the electrons provided by the cluster velocity. The correction to the non relativistic term is of the order of few percent [122].

At a level of APS, the estimated global contribution of the ensemble of SZ effects, both thermal and kinetic, to the CMB APS is important at intermediate and small scales. In particular, their maximum contribution occurs at about  $\ell \sim 3000$  with the kinetic effect subdominant up to multipoles of the order of  $\ell \sim 10^4$  [115,123,124]. Recently the ACT and SPT experiments measured the global contribution of the thermal SZ effect to the APS [125,126].

### 2.1.3 The Cosmic Infrared Background

The Cosmic Infrared Background (CIB) is a background emission, at wavelengths larger than a few microns, of the formation and evolution of the galaxies of all types. Its constituents are high density, faint and distant galaxies, that is starburst galaxies, Luminous InfraRed Galaxies (LIRGs,  $10^{11}L_{\odot} < L_{IR} < 10^{12}L_{\odot}$ ) and Ultra Luminous InfraRed Galaxies (ULIRGs,  $L_{IR} > 10^{12}L_{\odot}$ ), plus a little contribution by AGN [127–129]. One of the greater complexity related to CIB is that infrared emission collects contributions from very different populations at different redshifts. In particular, the two main CIB contributions come from the LIRGs dominating at low and intermediate redshifts,  $0.5 < z < 1.5$ , and from the ULIRGs dominating at higher redshifts,  $2 < z < 3$  [130]. Overall, CIB accounts for roughly half of the total energy in the optical/infrared Extragalactic Background Light (EBL), and its SED peaks near  $150\mu m$ . Recent measurement by Spitzer resolved only 10% of the CIB at  $160\mu m$  [131], Herschel resolved the 10% of the CIB at  $350\mu m$  [132] and SCUBA-2 Cosmology Legacy Survey (S2CLS)

reached the 16% at  $450\mu\text{m}$  [133].

CIB anisotropies are expected to trace large-scale structures and probe the clustering properties of galaxies, which in turn are linked to the dark matter halos distribution. Since the clustering of dark matter is well understood, observations of anisotropies in the CIB constrain the relationship between dusty, star-forming galaxies at high redshift, i.e.  $z \geq 2$ , and the underlying dark matter distribution.

The APS of CIB anisotropies has two contributions, a white-noise component caused by shot noise and an additional component caused by spatial correlations between the sources of the CIB. Depending on the frequency, the angular resolution and size of the survey, recent measurements could probe two different clustering regimes. On small angular scales ( $\ell \geq 2000$ ), there is the signal coming from the clustering within a single dark matter halo and, accordingly, the physics governing how dusty, star-forming galaxies form within a halo. On large angular scales, i.e.  $200 \geq \ell \geq 2000$ , CIB anisotropies measure clustering between galaxies in different dark matter halos. An important parameter of the analysis of CIB is the bias that describes the relation between the infrared galaxies and the dark matter distribution underneath them. Although bias of optical and radio galaxies is well known thanks to a large amount of data, the infrared bias is relatively poorly understood and the present simulations of the CIB typically use a constant bias approximation.

Recent *Planck* data [134] were able to measure the clustering of dusty, star-forming galaxies at 217, 353, 545, and 857 GHz with unprecedented precision and to put strong constraint to the CIB APS and to the bias value, as shown in Fig. 2.7.

## 2.2 The Galactic Synchrotron Emission

Synchrotron radiation is emitted from charged particles, mainly electrons, accelerated by a magnetic field. The general properties of the synchrotron

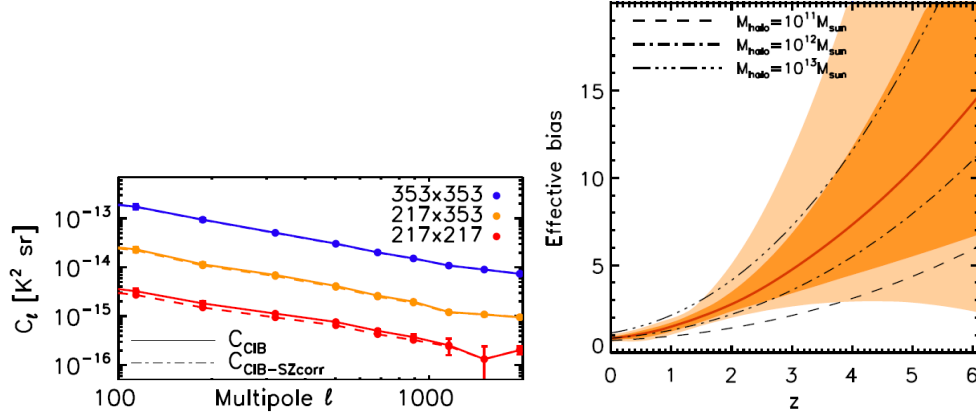


Figure 2.7: Recent *Planck* results about CIB. *Left*. The measured CIB auto and cross-spectra at 217 and 353 GHz. The dashed lines represent the measured power spectra corrected for the thermal SZ contamination. *Right*. Evolution of the effective bias as a function of redshift as constrained by the linear part of the power spectra. The median realization of the model is represented with a red line, the  $\pm 1\sigma$  confidence region with a dark orange area, and the  $\pm 2\sigma$  region with a light orange area. There are also plotted the evolution of the dark matter halo bias for different masses [134].

emission in temperature and polarization [135] are summarized in the following sections.

### 2.2.1 Temperature Synchrotron Emission

Let us consider a relativistic particle of mass  $m$  and charge  $q$  moving in an uniform magnetic field  $\mathbf{B}$ . We can derive the equation of its motion, starting from the Maxwell's equations:

$$\begin{aligned} \frac{d(\gamma m \mathbf{v})}{dt} &= \frac{q}{c} \mathbf{v} \times \mathbf{B} \\ \frac{d(\gamma m c^2)}{dt} &= q \mathbf{v} \cdot \mathbf{E} = 0 \end{aligned} \quad (2.11)$$

where  $\mathbf{v}$  is the particle velocity,  $c$  is the photon velocity,  $\gamma = (1 - \mathbf{v}^2/c^2)^{-1/2}$  is the gamma factor of the Lorentz transformations and  $\mathbf{E}$  and  $\mathbf{B}$  are respectively the electric field and the magnetic field. The second equation of 2.11 implies that  $\gamma = \text{constant}$ , that is  $|\mathbf{v}| = \text{constant}$ . Therefore it follows:

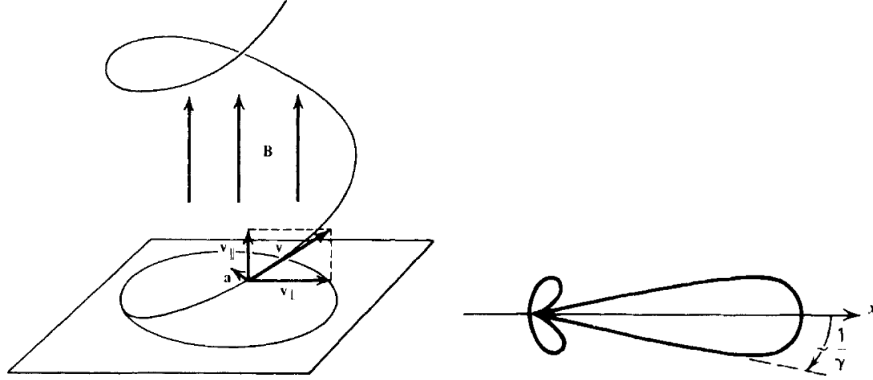


Figure 2.8: *Left.* The helical motion of a charged particle in an uniform magnetic field. *Right.* The angular distribution of the radiation emitted. The arrow is perpendicular to the acceleration and tangent to the circular motion [135].

$$m\gamma \frac{d\mathbf{v}}{dt} = \frac{q}{c} \mathbf{v} \times \mathbf{B} \quad (2.12)$$

Separating the velocity in its components  $\mathbf{v}_\perp$  and  $\mathbf{v}_\parallel$  respectively perpendicular and parallel to the magnetic field, we have:

$$\begin{aligned} \frac{d\mathbf{v}_\parallel}{dt} &= 0 \\ \frac{d\mathbf{v}_\perp}{dt} &= \frac{q}{\gamma mc} \mathbf{v}_\perp \times \mathbf{B} \end{aligned} \quad (2.13)$$

It follows that  $\mathbf{v}_\parallel = \text{constant}$  and since the total  $|\mathbf{v}| = \text{constant}$  also  $|\mathbf{v}_\perp| = \text{constant}$ . Equations 2.13 are describing a particle moving with constant velocity along the magnetic field and rotating with a circular motion on the plane perpendicular to  $\mathbf{B}$ , obtaining an helical motion of the particle as shown in Fig. 2.8 (left). The frequency of the rotation is:

$$\omega_B = \frac{qB}{\gamma mc}. \quad (2.14)$$

The particle feels an acceleration perpendicular to  $\mathbf{B}$  with a magnitude  $a_\perp = \omega_B v_\perp$  and consequently the power  $P$  of the total emitted radiation is:

$$P = \frac{2}{3} r_0^2 c \beta_\perp^2 \gamma^2 B^2, \quad (2.15)$$

where  $r_0$  is the radius of the circular motion and  $\beta_{\perp} = v_{\perp}/c$ . For an isotropic distribution of velocities, we can simply average the formula 2.15 over all the angles for a given speed  $\beta$ . Defining the *pitch angle*,  $\alpha$ , as the angle between the magnetic field and the velocity, we have:

$$\langle \beta_{\perp}^2 \rangle = \frac{\beta^2}{4\pi} \int \sin^2(\alpha) d\Omega = \frac{2\beta^2}{3} \quad (2.16)$$

and the total emitted radiation becomes:

$$P = \frac{4}{3} \sigma_T c \beta^2 \gamma^2 U_B, \quad (2.17)$$

where  $\sigma_T = 8\pi r_0^2/3$  is the Thomson cross-section and  $U_B = B^2/8\pi$  is the magnetic energy density.

The spectrum of the synchrotron radiation is related to the variation of the radiation field seen by the observer. The emission of the radiation is collimated in a beam along the relativistic velocity of the particle perpendicular to the acceleration and tangent to the circular motion as shown in Fig. 2.8 (right). For this effect the observer will see the pulse of the radiation for a period shorter than the gyration period and the spectrum will be spread over a much broader range of frequencies than one of the order  $\omega_B$ . It is demonstrated in [135] that the width in time of the observed pulse  $\Delta t$  is smaller than the gyration period by a factor  $\gamma^3$  and, consequently, the spectrum does not extend to about  $\omega_b$  before falling away, but up to something of the order of  $\omega_c$  that is defined as:

$$\omega_c = \frac{3}{2} \gamma^3 \omega_B \sin \alpha. \quad (2.18)$$

Another consequence of the beaming effect is that the electric field is a function of the polar angle about the direction of motion,  $\theta$ , only through the combination  $\gamma\theta$ . In a uniform circular motion the relationship between  $\theta$  and time  $t$  is:

$$\gamma\theta \approx 2\gamma(\gamma^2 \omega_B \sin \alpha)t \propto \omega_c t. \quad (2.19)$$

Therefore, the electrical field is proportional to  $\omega_c t$ .

The spectrum  $dW/d\omega d\Omega$  is proportional to the square of the Fourier transform of the electrical field. By integrating it over the solid angle and dividing by the orbital period, we obtain the power emitted per unit frequency  $P(\omega)$ , that is:

$$P(\omega) = \frac{dW}{dt d\omega} = \frac{\sqrt{3} q^3 B \sin\alpha}{2\pi mc^2} F\left(\frac{\omega}{\omega_c}\right). \quad (2.20)$$

From  $P(\omega)$  to  $P(\nu)$  we can use the simple relation  $P(\nu) = 2\pi P(\omega)$ .

Since the spectrum is a function of  $\omega/\omega_c$  (or  $\nu/\nu_c$  where  $\nu_c = 2\pi\omega_c$ ) alone, the 2.20 can be approximated by a constant power law with *spectral index*,  $s$ , defined as:

$$P(\nu) \propto \nu^{-s} \quad (2.21)$$

An analogous approach is used also to parametrize the distribution function of the particles responsible for the emission. In fact, in the case the number density of particles with energies between  $E$  and  $E + dE$  is described by a power law:

$$N(E)dE = CE^{-p}dE \quad E_1 < E < E_2 \quad (2.22)$$

with the quantity  $C$  that depends on the pitch angle, the total power per unit volume and frequency radiated by this distribution is obtained from the integral of  $N(E)dE$  the single particle radiation formula written in 2.20 over all the energies. It means:

$$P_{tot}(\nu) = C \int_{E_1}^{E_2} P(\nu) E^{-p} dE \propto \nu^{-\frac{p-1}{2}} \int_{x_1}^{x_2} F(x) x^{-\frac{p-3}{2}} dx. \quad (2.23)$$

where we changed the variables of integration to  $x = \nu/\nu_c$ . The limits of the integration depends on  $\nu_c$ , but if the energy limits are sufficiently wide, we can approximate  $x_1 \approx 0$  and  $x_2 \approx \infty$ , so that the integral is approximately constant. In this case we have:

$$P_{tot}(\nu) \propto \nu^{-\frac{p-1}{2}} \quad (2.24)$$

Finally, the Total Intensity,  $I$ , emitted by a region of the Galaxy with a power law distribution of the particles is defined as the power spectrum,  $P_{tot}$ , multiplied by the blackbody radiation,  $B_{BB}$ , in the Rayleigh-Jeans approximation at the temperature  $T$ :

$$I(\nu, T) \propto P_{tot}(\nu)B_{BB}(\nu, T) \propto \nu^{-\beta_s} \quad (2.25)$$

where  $\beta_s = s - 2$  is the same spectral index described in Eq. 2.4. From 2.24 and 2.25, a measurement of the synchrotron spectral index  $\beta_s$  reveals the properties of the particle distribution. In the case of a power law distribution as described in Eq. 2.22 the index  $p$  is related to the others by:

$$p = 2s + 1 = 2\beta_s + 3 \quad (2.26)$$

Previous analyses showed a typical value with  $\beta_s \sim 2.7$  [88] at few GHz and a steepening of the spectrum at higher frequencies with  $\beta_s$  closer to 3.0 [40, 76, 96, 136]. These values suggest a particle density distribution well described by a power law with  $p \sim 3$ , a value confirmed by independent observations [137–139].

A great complication in the analysis of synchrotron emission maps is due to the fact that the observed signal is the sum of all the contributions integrated along the line of sight through the Galaxy. Since the magnetic field and the particle density distribution are expected to change significantly in the Galaxy, their spectral energy index  $p$  will be different from region to region and the resulting power law approximation  $\beta_s$  of the observed signal will vary a lot depending on the direction of the sky.

In Chapter 5 radio surveys has been analysed to derive the spectral index  $\beta_s$  for different regions of the sky with the aim of increase our knowledge about the properties of the synchrotron emission and consequently of the Galactic magnetic field and electron density distribution.

Theoretical studies take great advantages from numerical tools that generate synthetic maps of synchrotron emission assuming Galactic magnetic fields and particle density distributions. Their output can be compared with the observations. Codes like GALPROP and HAMMURABI are the most used tools.

GALPROP [140] is a numerical code for calculating the propagation of relativistic charged particles and the diffuse emissions produced during their propagation. The code incorporates as much realistic astrophysical input as possible together with latest theoretical developments. GALPROP calculates the propagation of CR nuclei, antiprotons, electrons and positrons, and computes diffuse  $\gamma$ -rays and synchrotron emission in the same framework.

HAMMURABI [141] is a publicly available code for generating mock, total intensity and polarized observations of Galactic synchrotron emission based on model inputs for the Galactic magnetic field, the cosmic-ray density distribution, and the thermal electron density useful for comparison with observational data coming from telescopes such as LOFAR, SKA, *Planck*, and WMAP.

These tools are used reproduce the most important synchrotron features off the Galactic plane called "Galactic loops". These features are supposed to be the results of the emissions produced by the particles in supernovae remnants in the local region of our Galaxy.

### 2.2.2 Polarized Synchrotron Emission

As mentioned above, synchrotron emission appears linearly polarized. In fact, the radiation from a single charge is elliptically polarized. Considering a rotating particle around the Galactic magnetic field, at any rotation the beam emission will describe a region of the solid angle delimited by an angle  $1/\gamma$  of a cone of half-angle  $\alpha$  as shown in Fig. 2.9. The sense of the polarization (right or left handed) is determined by the position of the observer line of sight that can lie inside or outside the cone of radiation. However, for particles with a smoothly varying pitch angle distribution, the elliptical component cancels

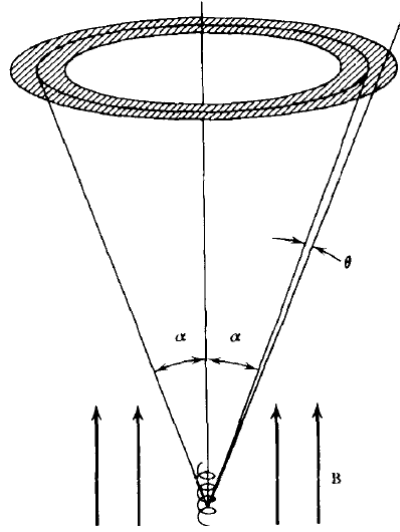


Figure 2.9: Synchrotron emission from a particle with pitch angle  $\alpha$ . Radiation is confined to the shaded solid angle [135].

out because the emission cones contribute equally from both sides of the line of sight. Consequently, the radiation will be linearly polarized.

The degree of synchrotron linear polarization,  $\Pi(\nu)$  depends on the intensity of the radiation along the direction parallel,  $P_{\parallel}(\nu)$ , and perpendicular,  $P_{\perp}(\nu)$ , to the projection of the magnetic field on the plane perpendicular to the line of sight:

$$\Pi(\nu) = \frac{P_{\perp}(\nu) - P_{\parallel}(\nu)}{P_{\perp}(\nu) + P_{\parallel}(\nu)} \quad (2.27)$$

For a great number of particles with a power law distribution of energies  $p$  as in 2.22, the degree of polarization is it demonstrated to be [135]:

$$\Pi = \frac{p + 1}{p + \frac{7}{3}}. \quad (2.28)$$

In general the polarization of the frequency integrated radiation is about 75% at maximum. However, it must be taken into account that the degree of polarization observed in real data ranges from zero to 75% depending on the particle property distribution processes that alter the polarization, such as

the Faraday depolarization and contaminations caused by radiation emitted by different processes.

### 2.2.3 The Synchrotron APS

Radio observations at  $\nu \lesssim 5$  GHz provide the clearest picture of the Galactic synchrotron morphology, since this non-thermal diffuse radiation dominates over the other components away from the Galactic plane regions. Part of this thesis is dedicated to the analysis of two full-sky surveys suitable for studying Galactic synchrotron emission in total intensity at relatively large angular scales ( $\theta \gtrsim 1$  deg): the 408 MHz survey [142] and the 1.4 GHz survey [143, 144]. In the past, these surveys have been exploited by several authors with essentially two purposes. On one hand, the 408 MHz all-sky map has been extensively used as template for the Galactic synchrotron emission in foreground separation activities (see, e.g., [76, 96, 145]). In this case, the 408 MHz map is usually extrapolated to the microwave range adopting a constant spectral index at high latitudes. Although in Chapter 5 we will show a slight variation of the spectral index across the sky, this approximation is good to have accurate component separation results. Along the Galactic plane a more detailed approach is necessary to take into account for the presence of free free emission. On the other hand, the radio surveys have been exploited to find an appropriate parametrization of the APS of the synchrotron emission to be extrapolated to the microwave range for an estimate of the contamination to the CMB at different angular scales [146] and used as prior in foreground separation applications [68, 145, 147]. The general outcome of these analyses is that the APS of the synchrotron emission, computed over the full sky, large areas and patches, can be modelled by a power law as:

$$\ell(\ell + 1)C_\ell^{TT} \propto k\ell^\alpha. \quad (2.29)$$

This approach has been theoretically justified by invoking the magneto-hydrodynamical (MHD) turbulence of the Galactic magnetic field interacting

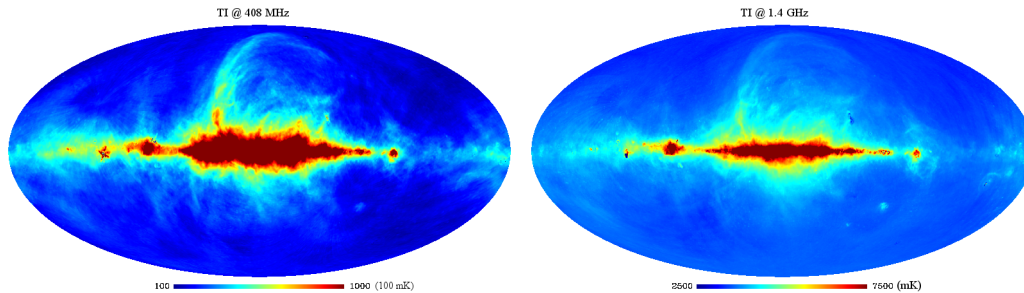


Figure 2.10: Synchrotron maps analysed in this thesis: the 408 MHz (*left*) and 1.4 GHz (*right*).

with the interstellar medium. It is demonstrated in a simple model that for turbulences of Kolmogorov-type spectrum the total synchrotron emission integrated over the line of sight can be well approximated by a power law such as defined in Eq. 2.29 (see [148, 149] and references therein). In the same paper, the expected values of the angular spectral index  $\alpha$  are derived to be in the range  $[-5/3; 1]$ , respectively obtained in the limit of large and small angles between two adjacent lines of sight. Although the method does not take into account possible inhomogeneities in the distribution of the emissivity, the power law approximation expectation has been largely confirmed by the observations, with a spectral index  $\alpha \sim [-1, -0.5]$  for  $\ell \lesssim 200$ , corresponding to angular scales  $\theta \gtrsim 1^\circ$  [68, 145, 146, 150–152]. However, a constant spectral index for the all-sky does not exhaustively describe the complexity of the synchrotron emission APS.

Chapter 5 is devoted to the analysis of the variations of the spectral index of the APS depending on the frequency and the region analysed.

### 2.2.4 The 408 MHz and 1.4 GHz surveys

The maps at 408 MHz and 1.4 GHz are shown in Fig. 2.10.

The 408 MHz map [142] was produced by merging different datasets obtained with large parabolic reflectors telescopes (namely the Jodrell Bank MkI and MkIA, the Effelsberg 100 meters and the Parkes 64 meters tele-

scopes) using a similar observing strategy and the same calibration procedure. The final map is characterized by an angular resolution of  $0.85^\circ$  and a pixel rms-noise of about 2 K. The map has been subsequently reprocessed by P. Reich and W. Reich, who found and corrected a calibration problem concerning the portion of the sky observed in the Jodrell Bank section [153].

The total intensity map at 1420 MHz has been obtained combining two surveys: one was performed in the Seventies with the Stockert 25m telescope and extending in declination in the range  $[-19^\circ, 90^\circ]$  [143, 144], the other was carried out with the Villa Elisa 30-m telescope in Argentina and covers  $\delta \in [-90^\circ, -10^\circ]$  [154]. Both have an angular resolution  $\theta_{HPBW} \sim 36'$  and overlap for latitudes in the range  $[-19^\circ, -10^\circ]$ . The resulting map has a typical pixel rms-noise of about 15 mK.

The original maps are provided to the scientific community in different projections, for example in the equidistant cylindrical. The maps used in the analysis described in this thesis have been previously elaborated by L. La Porta and collaborators by re-projecting them into HEALPix [155], the pixelization scheme adopted by the WMAP and *Planck* Consortia that will be widely described in Chapter 3 (Section 1.1). In this way, the maps are directly comparable with those produced by recent satellites observations can be analysed via fast Spherical Harmonic Transform decomposition and are suitable for component separation applications. For more details about the description of the projection method see [156]. Moreover, the most intense discrete sources (DS) have been already removed from the maps by L. La Porta and collaborators using the NOD software facility [157] that performs a 2-dimensional Gaussian fitting of the source and provides an estimate of the diffuse background as well. Namely, for  $|b| \geq 45$  deg all the sources with peak flux above  $\sim 0.8$  Jy (resp.  $\sim 6.4$  Jy) have been subtracted from the map at 1420 MHz (resp. 408 MHz), whereas for  $|b| \leq 45$  deg such lower limit is  $\sim 4.6$  Jy (resp.  $\sim 63.8$  Jy) [158, 159]. The subtracted DSs are mostly point sources, except for some rather extended objects: Galactic sources, such as HII regions, supernovae remnants, and extragalactic sources, such

as galaxy Centaurus A. Except for Centaurus A, such extended sources are concentrated close to the Galactic plane. Despite the DS subtraction, at high latitudes the global Galactic fluctuation field is superimposed to a significant contribution from DS that are below the detection threshold and form a diffuse background emission. Moreover, the maps have been produced with a relatively large beam that does not allow an analysis of the small scales. For these reasons the analysis has been limited to scales relative to  $\ell \lesssim 200$ .

Chapter 5 is dedicated to the analysis of the 408 MHz and 1.4 GHz maps taking into account regions (or patches) of the sky of particular interest because of their morphology correlations, such as the Galactic spurs and loops, or their physical implications, such as regions with a particular low synchrotron emission. The aim of this analysis is to better characterize the properties of the synchrotron emission.

# Chapter 3

## Data analysis

The data reduction process is an important step in any kind of observational campaign, from ground based, balloon telescopes or from satellite. The instrument scientific telemetry and the housekeeping data need to be transformed into frequency maps to be analysed in order to extract scientific results.

Generally, we can divide the data reduction process in three steps called Level 1 (L1), Level 2 (L2) and Level 3 (L3). In Level 1 the observational data are retrieved and all the auxiliary information necessary to understand and correct the data are accumulated. Examples of auxiliary data are the direction pointing, the temperature inside the cryogenic vessels where the receivers have been placed and the status of the atmosphere. In Level 2 the scientific knowledge of the instrument and the auxiliary information are used to calibrate and clean the data, to reconstruct the data knowing the scanning strategy adopted by the satellite or ground based or balloon telescopes and, from the ground, to correct for possible spurious signals due to the presence of the atmosphere. In the end, Level 3 collects L2 outputs to generate the products to be ingested in the scientific analyses.

For a more detailed example, Fig. 3 shows the data reduction pipeline used for the LFI of the *Planck* satellite [160]. In the L1 pipeline the satellite data are received by the Data Processing Center (DPC) as a stream of pack-

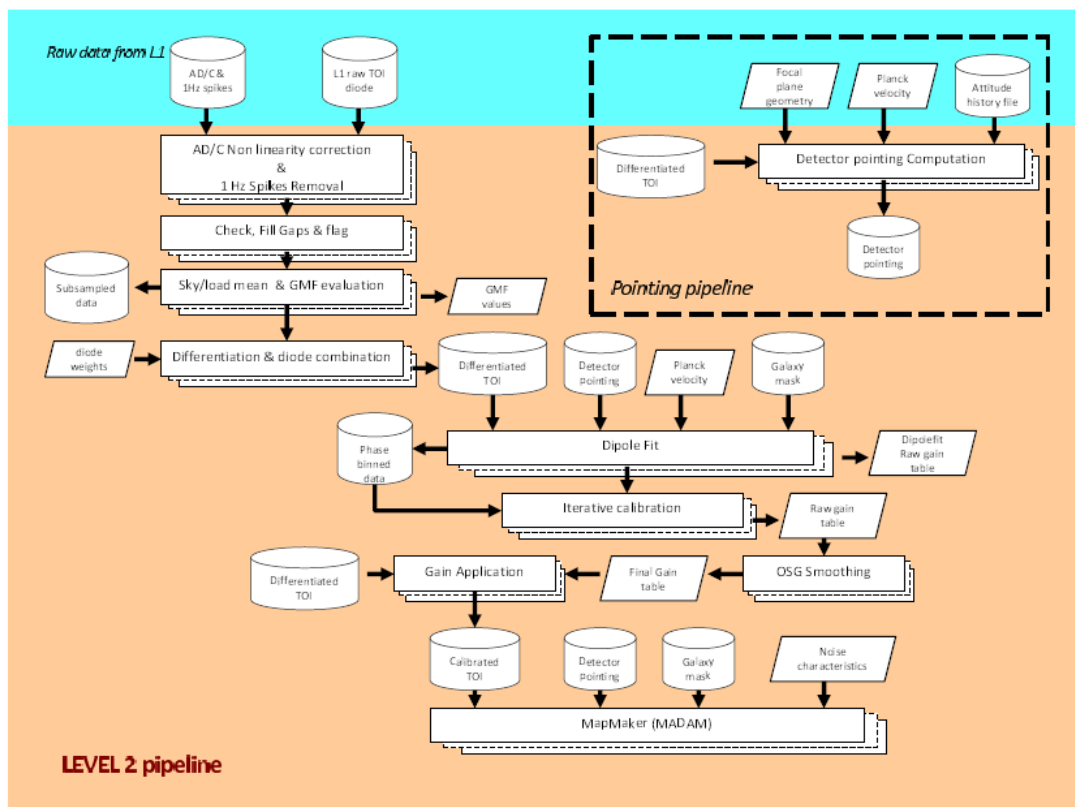


Figure 3.1: Schematic representation of L1, L2 and pointing pipeline of LFI DPC [160].

---

ets. In every packet there are the observational data and the telemetry data that collect all the auxiliary information about the status of the satellite. The L1 pipeline uncompresses the packets retrieving the Analog-to-Digital units (ADU) that are transformed into a voltage. At this stage, some data are flagged because associated to non-scientific events. They can be missing data when the arithmetic compression of the telemetry data has been incorrect, anomalous fluctuations or jumps in the data, or data acquired during the manoeuvres performed by the satellite according to the *Planck* scanning strategy. Finally, time information is associated to the stream of data in order to obtain scientific timelines.

The L2 pipeline queries the database where the L1 data has been stored and, using scientific and housekeeping information, performs the following steps:

- remove the electronic noise that affects the data such as the AD/C non linearity;
- compute and apply the gain modulation factor to minimize the  $1/f$  noise;
- build the LFI reduced instrument model (RIMO) that contains all the main characteristics of the instrument;
- compute the detector pointing for each sample, based on auxiliary data and beam information;
- calibrate the scientific timelines to physical units,  $K_{CMB}$ , using a 4K reference load signal and perform an estimation of the dipole convolved with the  $4\pi$  beam representation;
- remove, from the scientific calibrated timelines, the dipole convolved with the  $4\pi$  beam representation;

Finally, in the L2 pipeline the data are used as input for the map-making tools that add information from the detector pointing and noise characteristics and produce the full-sky temperature and polarization fluctuation maps

that are analysed in order to retrieve scientific results. LFI frequency maps were produced by the `Madam` map-making code [161]. The algorithm of the code is based on the destriping technique that, through a maximum-likelihood analysis, models the correlated noise component of the data. Also, `Madam` uses available information on the noise properties, in the form of a noise prior in order to increase the efficiency of the destriping method. The results of the code are the LFI maps at 30, 44 and 70 GHz discretized in pixels following the HEALPix pixelization scheme [155].

The L3 pipeline in *Planck* is dedicated to the component separation analysis, already described in Chapter 2. Various tools have been developed to clean the maps from the foregrounds making them useful for cosmological studies.

In this context, this chapter is dedicated to the analysis of some steps of data reduction processes: the change of coordinates of the maps inside the HEALPix pixelization scheme; the APS extraction from the maps using pixel-based or pseudo- $C_\ell$  methods; the aliasing problem in the degradation of the maps to lower resolutions. The first is very useful in the component separation analyses because it allows to compare maps or patches obtained from different missions or observational campaigns that are typically released in different coordinate frames. The second is at the basis of the CMB analysis both at small and large scales. The third is important in order to obtain maps at low resolution, useful for the large scales analyses, without any additional spurious signal due to the degradation process. We analyse the tools used to perform these data reduction steps and quantify their quality and performances to understand their effects on the scientific data.

### 3.1 The pixelization problem

The choice of the method for sky maps discretization is one of the most important issue for data analysis processes. Satellite missions such as WMAP and *Planck* produced multifrequency data sets suitable for the construction of

full-sky maps of the microwave sky at an angular resolution of few arcminutes. Such a massive full-sky data sets require the development of a mathematical structure which supports a suitable discretization of functions on a sphere at sufficiently high resolution and facilitates fast and accurate statistical and astrophysical analysis.

The standard operations of numerical analysis that one might wish to execute on the sphere include convolutions with local and global kernels, Fourier analysis with spherical harmonics and power spectrum estimation, wavelet decomposition, nearest neighbour searches, topological analyses including searches for extrema or zero crossings and the computation of Minkowski functionals and the extraction of patches. Some of these operations become prohibitively slow if the sampling of functions on the sphere and the related structure of the discrete data set are not designed carefully.

The requirements for a fast and accurate statistical analysis can be achieved if the mathematical structure of discrete full-sky maps follows these conditions [155]:

- 1) Hierarchical structure of the database. This is recognized as essential for very large databases as already described in the construction of the Quadrilateralized Spherical Cube (QuadCube) [162], which was used for the generation and analysis of COBE sky maps. This property guarantees that the data elements, that are nearby on the surface of a sphere, are also nearby in the tree structure of the database. This property facilitates various topological methods of analysis and allows for easy construction of wavelet transformations on triangular and quadrilateral grids through fast lookup of nearest neighbours.
- 2) Equal area of the discrete elements of the partition. This means that independently from the position on the sphere all pixels have the same identical area. This is particularly advantageous for the statistical analysis of the properties of both the signal and the noise present on the maps. For example, the Nyquist criterion states that the minimum

number of pixels necessary to accurately sample the data coming from a telescope is  $\text{FWHM} \simeq 3$  pixels, where FWHM is relative to the beam of the telescope. This criterion is simple to be addressed in the entire sky map when the pixels are everywhere identical.

- 3) Isolatitudes distribution for the discrete area elements on the sphere. This property is essential for computational speed in all operations involving evaluations of spherical harmonics. In fact, spherical harmonics calculation along the parallel of the sky (that is at fixed latitude) can be easily performed with an FFT [163]. Since the associated Legendre polynomials are evaluated via slow recursions, any sampling grid deviation from an isolatitude distribution implies huge computational resources, increasing with the growing of the number of sampling points.

In literature, various possible methods for sampling distributions on the sphere have been employed, but each of them fails at least in one of the above requirements.

In the QuadCube method [162], the celestial sphere is projected onto six faces of a cube in a tangent plane projection. The lines of latitude and longitude are then curved such that, when the cube face is divided into equally spaced rows and columns of pixels, the area of each pixel is equal to that of every other pixel. This method does not obey to the requirement number 3, since pixels have not an isolatitude distribution.

The Equidistant Cylindrical Projection (ECP), usually adopted for geophysics and climate modelling and implemented for CMB work in [163], is a simple map projection in which the distance between two points on the sphere is conserved on the projection plane. By construction this method does not satisfy the requirement number 2.

The hexagonal sampling grids with icosahedral symmetry [164] can be adjusted in order to have equal area [165], but can not satisfy the requirements number 1 and 3.

Igloo-type constructions [166] have pixels with an exact discrete azimuthal symmetry at each latitude, allowing fast and exact spherical harmonic trans-

forms (requirement 3), but it is not hierarchical (requirement 1). It can be made hierarchical but only causing pixel distortions and violating the requirement 2.

The Gauss–Legendre Sky Pixelization (GLESP) construction [167] is based on the Gauss–Legendre polynomial zeros, allowing to perform strict orthogonal spherical harmonic expansions (requirement 3). This scheme presents irregular variations in the pixel area and is not hierarchical.

All the requirements described above are satisfied by the HEALPix scheme.

### 3.1.1 The HEALPix package

HEALPix [155], an acronym for Hierarchical Equal Area isoLatitude Pixelization of a 2D-sphere, is a software package for maps projection, pixelization and analysis of a 2D-sphere. As suggested by the name, this pixelization satisfies the condition 2. Several possible equal-area isolatitude tessellations of the sphere are possible, based on two parameters:  $N_\theta$  is the number of base-resolution pixel layers between the north and south poles and  $N_\phi$  is the multiplicity of the meridional cuts, or the number of equatorial or circum-polar base-resolution pixels. The HEALPix implementation is described by  $N_\theta = 3$  and  $N_\phi = 4$  and shown in Fig. 3.2 (left). With this pixelization scheme, it can be introduced also the parameter  $\theta_*$  that defines the line of constant colatitude that separates the equatorial region from the northern polar region. This choice allows to minimize the number of pixels at the poles to be only 4 to avoid acute angles. Also the number of pixels on rings in the equatorial zone are minimized and presents a  $2^n$  multiplicity with respect to the resolution leading to perform fast harmonic transformations.

This preferred implementation, is a geometrically constructed, self-similar, refinable quadrilateral mesh on the sphere as shown in Fig. 3.2 (right). The base resolution comprises 12 pixels in three rings around the poles and equator. This property satisfy the requirement 1 of hierarchical structure of the pixels. The resolution of the grid is expressed by the parameter  $N_{side}$ , which defines the number of divisions along the side of a base-resolution pixel that is

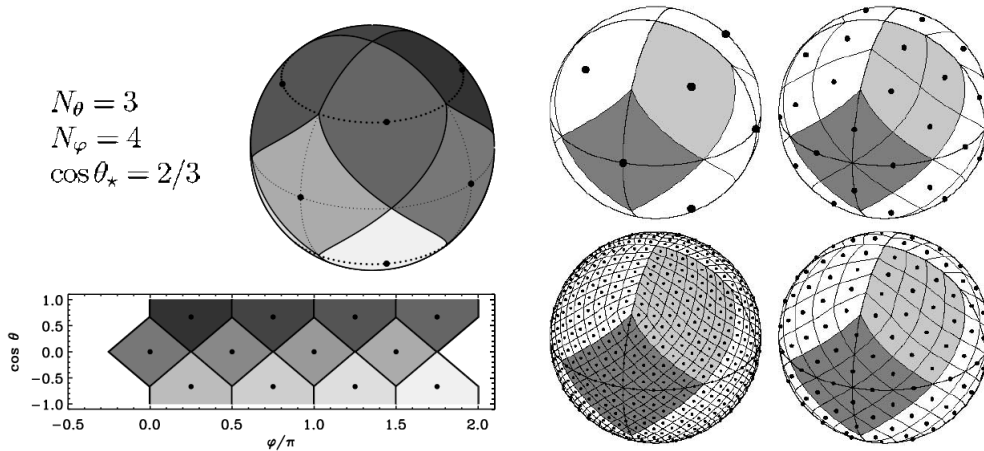


Figure 3.2: Orthographic (*top left*) and cylindrical (*Bottom left*) projection of the HEALPix basic tessellation scheme. The same pixels in the two projection schemes have the same colours. (*right*) Moving clockwise from the top left panel, the orthographic view of the HEALPix partition of the sphere in which the grid is hierarchically subdivided with increasing value of the grid resolution parameter [155].

needed to reach a desired high-resolution partition. The HEALPix pixelization supports two different numbering schemes for the pixels called "ring" and "nest" schemes. The ring scheme is obtained by simply counting the pixels moving down from the north to the south pole along each isolatitude ring. In this scheme Fourier transforms with spherical harmonics are easy to be implemented. The nest scheme is obtained by replicating the tree structure of pixels. In this scheme, moving from a given resolution to an higher one, the numbers of the pixels at high resolution are directly related to the number of the original pixel at low resolution that includes them. This tree structure allows to implement efficiently nearest-neighbor searches and fast wavelet transformations. All pixel centres are placed on rings of constant latitude, and are equidistant in azimuth (on each ring) satisfying the requirement 3. All isolatitude rings located between the upper and lower corners of the equatorial base-resolution pixels (i.e.,  $-\frac{2}{3} < \cos(\theta) < \frac{2}{3}$ ), or in the equatorial zone, are divided into the same number of pixels being  $N_{eq} = 4N_{side}$ . The remaining rings are located within the polar cap regions ( $|\cos(\theta)| > \frac{2}{3}$ ) and

contain a varying number of pixels, increasing from ring to ring, with increasing distance from the poles, by one pixel within each quadrant. Totally, an HEALPix map has  $N_{pix} = 12N_{side}^2$  pixels of the same area  $\Omega_{pix} = \pi/(3N_{side}^2)$ . In Fig. 3.2 (right) are shown different grid resolutions parametrized by the grid parameter  $N_{side} = 1, 2, 3$  and 4 and corresponding to a total number of pixels respectively of 12, 48, 192, 768.

Given the pixelization of the sphere, the HEALPix package equips the user of a large number of based mathematical tools, consisting of Fortran90 (F90) and IDL source codes. Among the tasks performed by the components of the HEALPix package the most important are: **synfast** that simulates the full sky CMB temperature and polarisation maps as realisations of random Gaussian fields starting from a prior CMB APS\*; **anafast** that analyses the full sky and masked sky CMB temperature and polarisation maps by extracting the angular power spectra and spherical harmonic coefficients; **smoothing** that performs a convolution of the map with a Gaussian beam with given FWHM; **udgrade** that is used for the degradation and upgrade of the resolution of the maps; **mollview** for the visualisation of the HEALPix formatted sky maps.

It is important to underline that the facilities **synfast** and **anafast** generate a link between the data in the pixel space and in harmonic space by expanding in discretized spherical harmonics the pixel data. The consequence of the HEALPix discretization of the spherical harmonics is that the linearly independent spherical harmonics that can be extracted are limited by the parameter  $\ell_{max}$  that is related to the resolution ( $N_{side}$ ) of a given map by:

$$\ell_{max} = 3N_{side} - 1. \quad (3.1)$$

Another procedure implemented in the HEALPix package allows to change the coordinate system of the maps that may differ also depending on the place where the maps have been collected. Maps obtained by satellites like WMAP

---

\*The HEALPix routine **alm2map**, instead, reproduces the maps directly from the  $a_{\ell m}$  coefficients of the spherical harmonics.

and *Planck* are in Galactic ('G') coordinates, while usual coordinates for the maps obtained by ground based telescopes are Ecliptical ('E') or Equatorial ('C' or 'Q'). The analyses of CMB and foreground maps can take advantages of ground based observations of different sources in the sky. Consequently a correct change of coordinates of these maps to the coordinates of the others and vice versa is really important. The following section is dedicated to the analysis of the performances of the HEALPix routines in changing the coordinates by quantitatively estimating the errors that affect the output map with respect to the input map. These errors are also compared with the WMAP and *Planck* sensitivities to check if they can be considered negligible in scientific analyses. This is certainly not the case for the future missions, like CORe and PRISM, for which the extreme sensitivity achieved will be much lower than the errors considered and will have to be taken into account. These results have been collected in [168].

## 3.2 The effect of the change of coordinates

In HEALPix it is possible to change the coordinates by rotating the map in pixel space, using the IDL facility `rotate_coord` or in harmonic space by the mean of the F90 subroutine `rotate_alm*`. In this section, some optimizations of the two methods are considered together with the analysis of their efficiencies in changing the coordinates of simulated pure CMB maps, foreground reduced maps and the W-band map of the WMAP 7 year results [169].

### 3.2.1 Change of coordinates in pixel space

The IDL facility `rotate_coord` provides a mean to rotate a set of 3D position vectors between astronomical coordinates systems by using Euler matrix. Every pixel of the map is determined by the 3D position vector of its center, so map rotation can be done easily by associating the same pixel value at the vector of the original pixel rotated to the new coordinates. By

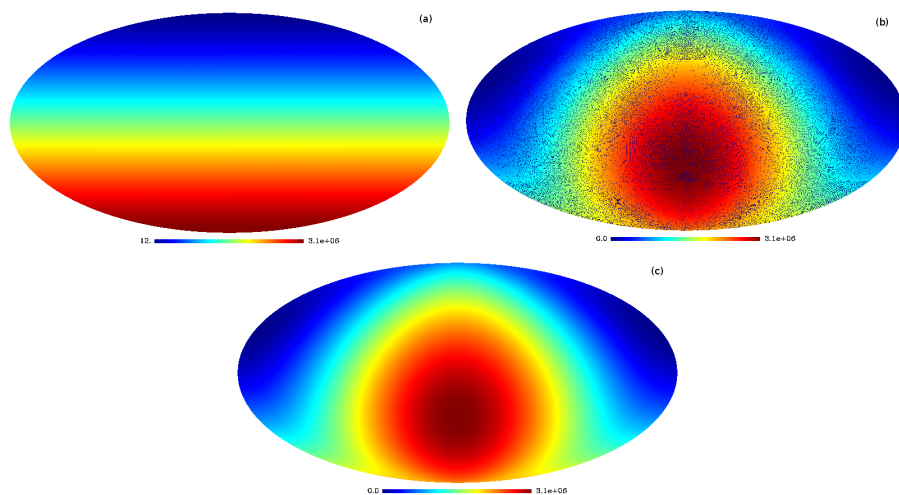


Figure 3.3: An example of what happens if the direct change of coordinates is used. (a) The initial map to be rotated in new coordinates. (b) The map in new coordinates. In this map there are pixels with zero value as consequence of errors in changing the coordinates. (c) Map in new coordinates obtained by rotating in the "opposite" direction. There are no void pixels.

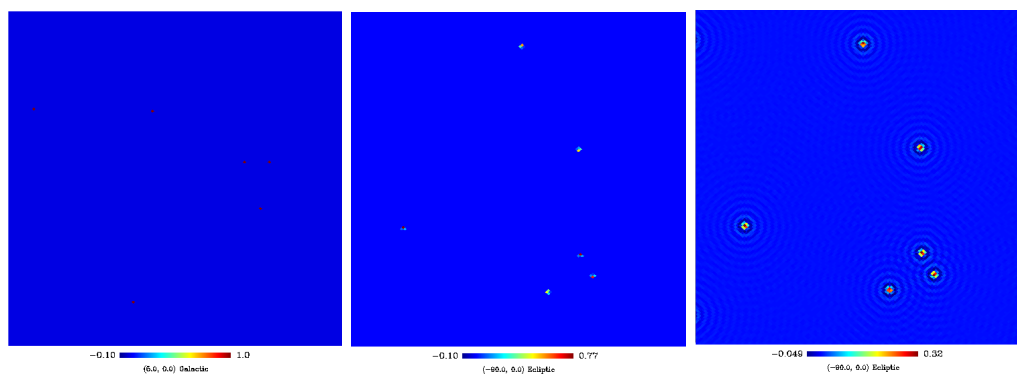


Figure 3.4: An example of what happens in rotating maps with strong point sources and very low background with the pixel and harmonic method. (a) The initial map to be rotated in new coordinates, and the map rotated (b) by pixel method and (c) by harmonic method. Respect to pixel method sources are smoothed on more pixel. However this error affects very weakly CMB temperature maps.

performing rotations in this way, some of the pixels in the new map will be without a value as shown in Fig. 3.3 (a-b). This is due to the fact that pixels in different coordinates are not perfectly superimposed.

To avoid pixels without a value, maps rotation must be performed in the "opposite" direction as applied by the procedure we wrote and called `rotation2.pro`. The new map obtained in this way has no null pixel as shown in Fig. 3.3 (c). In this case there are still errors due to a mismatch of pixels, but without new pixel artificially void.

### 3.2.2 Change of coordinates in harmonic space

Another way to rotate CMB maps is to work in Fourier space, by rotating directly the  $a_{lm}$  coefficients obtained by a spherical harmonics expansion of the map. In order to do this, we wrote new routines in F90 by using HEALPix subroutines. The F90 subroutine `rotate_alm*` transforms the scalar  $a_{lm}$  coefficients to emulate the effect of an arbitrary rotation of the underlying map. The general idea of the F90 program (called `harmonic_rotation.f90`) is to read a temperature CMB map and to analyse it in order to obtain coefficients  $a_{lm}$  from its expansion in spherical harmonics. Then it rotates these coefficients to the new coordinates, synthesizes a new rotated map with the new coefficients  $a_{lm}$  and writes it in a new `.fits` file. In this case the mismatched pixels are absent because we are not using pixels. However, there is another problem that remarkably emerged when we rotated a  $N_{side} = 512$  map with all the pixels equal to zero except for a few thousands that have value 1, as shown in Fig. 3.4 (a). In Fig. 3.4 (c) there is the map rotated with "harmonic method". As shown by the colour scale the effect of rotation is a strong smoothing of the non-zero pixels that lost two-third of their original signal and the appearance of alias pixels of the same intensity. The rotated original pixels are unrecognisable. For maps with strong point sources in a low background this routine is not useful, but for temperature CMB map in which there are not this kind of sources these errors are negligible.

There is another very interesting issue. The previous map has been also

rotated by using the "pixel method". For both the rotated maps we eliminated alias pixels by sorting pixels in intensity and choosing the ones with highest value. In Figure 3.5 (a) are shown positions and intensities of some of these pixels of the two maps. In addition to the lack of intensity, positions of pixel differ all at least of one pixel and not ever in the same direction. This is probably a bug of the software that causes a different rotation result when one uses pixel or harmonic method. For a more deep understand of this effect, we generated a map with null pixel value except for 91 Normalized Gaussian Point Spread Function (PSF) with FWHM of 10 arcmin, similar to WMAP and *Planck* satellites characteristics. PSF are placed randomly on the map by avoiding superpositions of their codes. PSF are better modelled by an harmonic expansion of the map compared to single pixel sources, so we expected to cut down the aliasing effects observed in the map rotated with harmonic method in the previous case. We rotated the new map both with the pixel and harmonic method. In Fig. 3.6 are shown the original map and the two rotated maps. In the table of Fig. 3.6 (b) we report the peak intensities of the PSF after rotation that result to be very close to 1 confirming that the aliasing effect in the map rotated with harmonic method is negligible, so we could move to a stronger comparison between the two methods. In the same table it is still evident the mismatch in pixel positions of the PSF peaks between the rotated map with the two different methods. When we rotate the same temperature CMB map (see the follow for details on the map) by using both the methods and compare the two rotated maps, the differences are of the order of CMB fluctuation (order of  $100 \mu\text{K}$  for a signal of at maximum  $400 \mu\text{K}$ ) as shown in Figure 3.5 (b). Probably the pixel mismatch is the cause of these errors and this is very problematic because we don't know what the exact rotation is and furthermore it is impossible to compare directly rotated maps with the two different methods.

Consequently in the following sections we analyse the errors that affect pixels of the rotated map by making comparisons between the twice rotated map with the same method and the original one separately and the compar-

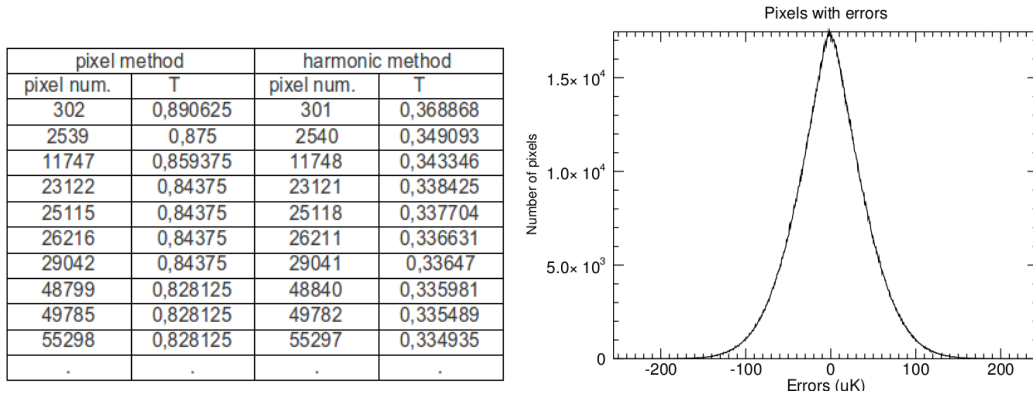


Figure 3.5: (*On the left:*) Table with some of pixel positions and temperature of non-zero pixels of rotated maps with pixel and harmonic methods. Notice that pixel positions differ for at least one pixel. (*On the right:*) Differences in temperature between the two rotated maps of an original synthetic only CMB map. Errors are taken by subtracting the two maps pixel per pixel and making an histogram of non-zero pixels. Differences are of the order of CMB fluctuation.

ison between the two methods will be done only after a statistical analysis of temperature errors that affect pixels and APS of the maps.

### 3.2.3 Results on pure CMB simulated maps

In this section we present results obtained by rotating synthetic maps of only CMB, without foreground. These maps are generated by the HEALPix F90 facility `synfast` with  $N_{side} = 512$  in Galactic coordinates. To generate a map, `synfast` needs only a file with the CMB APS. We used the APS released by WMAP 1st year best fit [170]. At the moment maps are generated without beam.

Before presenting the results we have to describe the method used to obtain them. Errors, that we are going to present, are obtained by changing the coordinates twice in order to return to a map in the initial coordinates. For example a CMB map in Galactic coordinates is rotated to Ecliptic coordinates and the new map is rotated again back to Galactic coordinates. In our IDL routine `medvarerror.pro` the two maps in Galactic coordinates are subtracted pixel per pixel. After subtraction, we histogram every pixel

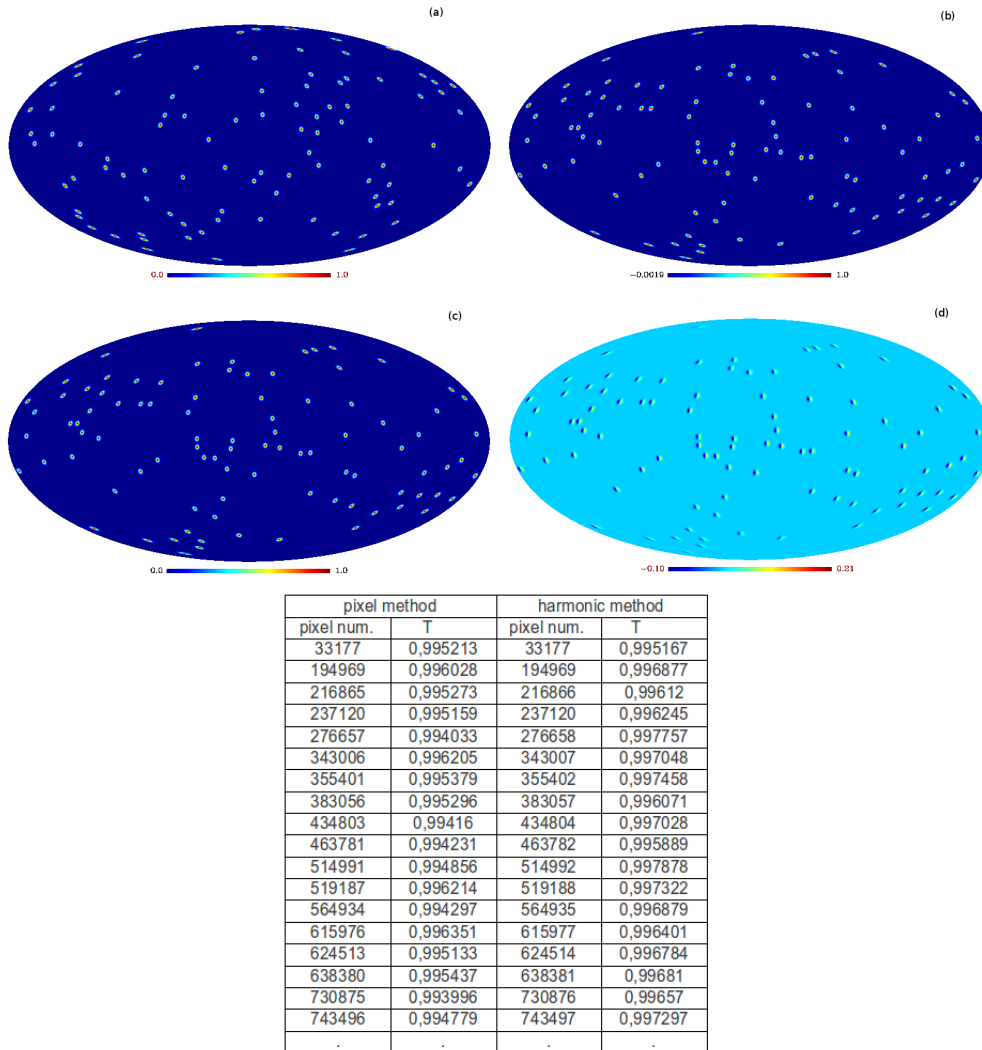


Figure 3.6: (a) Original map with null pixel except for 91 Normalized Gaussian Point Spread Function randomly placed. (b) The map rotated with harmonic method. (c) The map rotated with pixel method. (d) Map of the differences between the maps resulting from the rotation with the two methods. (e) Table with position and intensities of some of the PSF peaks. Note the pixel mismatch in peak position between the maps rotated with pixel and harmonic methods.

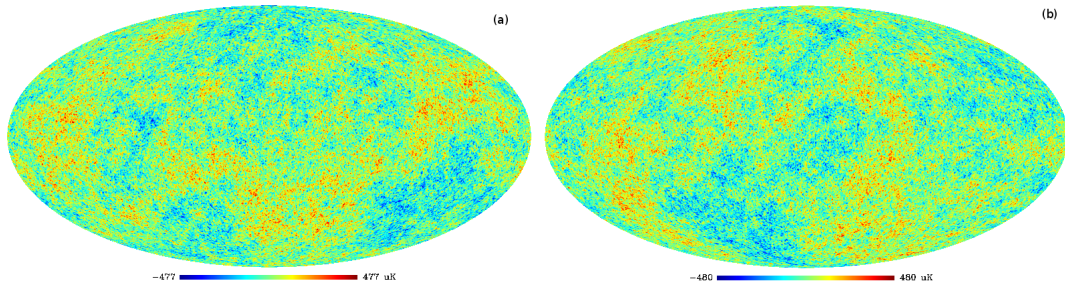


Figure 3.7: (a) Example of an only CMB map in Galactic coordinates and (b) the results after rotation in Ecliptic coordinates. Map looks very similar, but deep analysis revealed that the rotated map is affected by errors generated during rotation.

with a non-zero value and this is what we are going to report in the following figures.

A second analysis is done on the APS of the maps. By using the HEALPix F90 facility `anafast`, we obtained APS of the maps allowing us to compare the effect of rotation also in harmonic space by directly comparing the APS of the original map with the one of the rotated map in the new coordinates.

### ”Pixel” method: an improved approach

In Figure 3.7 we show the original synthetic map in Galactic coordinates and the map in Ecliptic coordinates rotated with the ”pixel” method. After twice rotations, errors that affect maps are of the order of  $100 \mu\text{K}$  as shown in Figure 3.8 (a). They are very high, in fact they are of the same order of CMB fluctuations.

In order to find a way to lower these errors, maps are modified by the mean of the HEALPix IDL facility `ud_grade` that, in general, resamples the map generating a new map with a different resolution. Since the change of coordinates is applied in the opposite direction, so that every pixel of the map in the new coordinates takes the value of the pixel of the map in the old ones, before the rotation the map in the new coordinates is upgraded to an higher resolution. In this process every pixel is substituted by a larger number of smaller pixels having the same value of the previous greater one. No errors

are generated in this procedure. Thus, during the rotation, some pixels of the previous great one fall in the correct great pixel in the old coordinates, others in the closest pixel because of the mismatch. Finally the expanded map in the new coordinates is downgraded to the original resolution of  $N_{side} = 512$ . In this step the `ud_grade` routine performs an average over all the pixels that fall in the new greater pixel of the downgraded map and, consequently, the possible mismatch effect is weighted between all the pixels of the high resolution and the errors showed by the rotated map are minimized.

The results confirm that although the number of pixels with errors increase in number (working at  $N_{side} = 512$  number of pixels that shows an error is 20%, while when the maps is upgraded to  $N_{side} = 4096$  this fraction increase to 98%), the errors committed are considerably lower. In Fig. 3.8 we compared the errors committed by changing the coordinates of a CMB map (a) without the expansion and (b) by expanding the map to  $N_{side} = 4096$ . The higher is the expansion, the lower are the final errors.

Comparing these errors with the sensitivity of WMAP satellite from which the map has been obtained, we notice that W-band WMAP sensitivity after 7 years observation [169] is of the order of  $56\mu\text{K}$  while errors committed by expanding maps to  $N_{side} = 4096$  are of the order of  $5\mu\text{K}$ . Errors are also lower than sensitivity of *Planck* satellite [171]. So changes of coordinates does not longer affect maps significantly.

As a further optimization, we tried to limit the computational time that computers need to change the coordinates. We created a routine (called `rotation_matrix.pro`) that generates a matrix that contains the links between old coordinates of the pixels and the new ones. In this routine the only parameters are the two coordinates (Galactic, Equatorial or Ecliptic) and the resolution ( $N_{side}$ ) of the expanded map that has to be changed. Links are still determined by the HEALPix IDL facility `rotate_coord`. Hence, we wrote a second routine (called `rotation3.pro`) that reads the matrix (saved as a `.fits` file) and performs the change of coordinates. Time that computer needs to generate the matrix is the same that it needs to change the

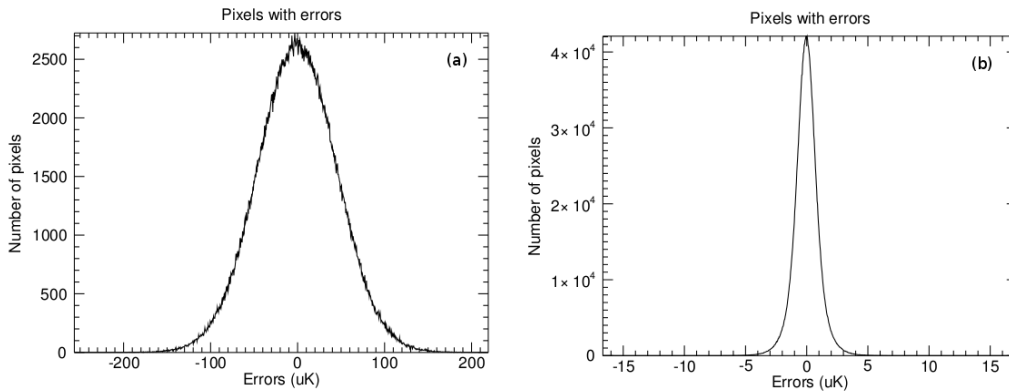


Figure 3.8: (a) Histogram of temperature errors of non-zero pixel after the subtraction between the original map and the one rotated twice. (b) The same of (a), but in this case map was upgraded to  $N_{side} = 4096$  before rotation and downgraded to the original  $N_{side} = 512$  after rotation.

coordinates with the old routine, but now the first routine has to be run only one time and then the matrix generated in this way can be used by the routine `rotation3.pro` every time is needed and for any map. Computers need a lower time to read a file than to calculate the change of coordinates, as shown in Figure 3.9 in which are displayed, for different resolutions, (a) the time that our computer needed to directly change the coordinates with `rotation2.pro` and (b) the one that it needed to run `rotation3.pro`. In order to obtain these time estimations we used one node of the CINECA PLX cluster that contains 2 Intel(R) Xeon(R) Westmere six-core E5645 processors, with a clock of 2.40GHz and 47 GB of allocatable memory. For all the map resolutions, the use of matrix leads to save almost 40% of computational time independently of the  $N_{side}$  of the map. This means that the higher the resolution of the map is, the higher is the computational time saved. The results obtained and the errors committed with these two routines are identical.

We showed that by upgrading and downgrading the map to higher resolution the errors that affect the rotated maps decrease. There are two important limits for this kind of analysis. The first one is the computational time. In Fig. 3.9 it is shown that the rotation can least only several seconds

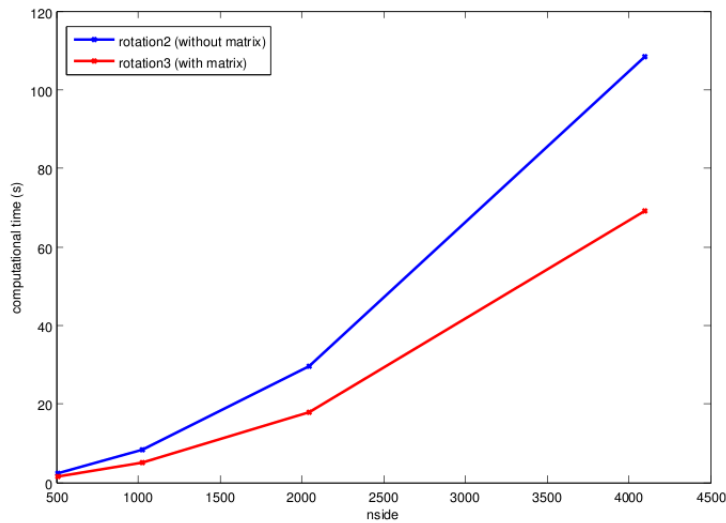


Figure 3.9: Computational time necessary at different resolutions (blue) to directly change the coordinates and (red) to read matrix previously generated and then change coordinates.

to be done, but we want to notice that CINECA PLX is one of the most powerful computers cluster in the world. It is ranked at the 54<sup>th</sup> position in the TOP500 list<sup>†</sup>. A more common computer can spend several hours to rotate the maps and the more the upgraded map resolution is, the more is the computational time needed. The second and most important limit is the RAM memory that computers need to allocate the maps. A map at  $N_{side} = 512$  in double precision needs about 25 MB of allocatable memory, but a map at  $N_{side} = 4096$  needs more than 1.6 GB. A program that allocates this huge memory for the original map and the same for the rotated map and by considering all the vectors used to calculate the rotation is impracticable for a common computer. The allocatable memory needed grows up with the square of the  $N_{side}$  of the map. For this two important reasons it is impossible to reach higher resolution than  $N_{side} = 4096$  without the use of computers cluster.

Before presenting results about our APS analysis of rotated maps, we

<sup>†</sup><http://www.top500.org/list/2011/06/100>

want to report an interesting consideration about the capability of the HEALPix F90 facilities `synfast` and `anafast` in creating maps from a given APS and extracting APS from maps respectively. By using `synfast` we generated a synthetic CMB map at  $N_{side} = 512$  without Galactic foreground and without beam. Then, by using `anafast`, we analysed the CMB map re-obtaining its APS. The facility `synfast` can synthesize a map from a given APS by generating random  $a_{\ell m}$  coefficients of spherical harmonics up to  $\ell_{max}$  defined in Eq. 3.1. At the same time, `anafast` can reproduce the initial APS inside the same range of multipoles maintaining low errors up to  $\ell_{max}$ . However, as shown in Fig. 3.10 the power losses are negligible at  $\ell = 512$  ( $N_{side}$ ) and  $\ell = 1024$  ( $2 \times N_{side}$ ) while at  $\ell = 1530$  ( $\ell_{max}$ ) the power loss is of the order of 10%. Consequently it is important to take into account the APS analysis results up to  $\ell = 2 \times N_{side}$  because at higher multipoles results show a little but not negligible power loss.

In the following analysis we compare the APS of maps in the new coordinates directly with the APS extracted by `anafast` from the original map in the old coordinates. We do not use the theoretical APS for the comparison because the map is only a single realization of the APS. According to the cosmic variance, the APS of both the generated map and the rotated one scatter around the theoretical APS such as in Fig. 3.10 (b). This would lead to difficulties in recovering the errors caused by the rotation. Moreover, this would not consider the effect of the power loss due to the use of `anafast` that affects exactly in the same way both the APS of the original map and of the rotated one.

Once we extracted the initial APS from the maps used in this section, we changed coordinates with routine `rotation3.pro` without expansion and with an expansion to  $N_{side} = 4096$ . We re-analysed APS of rotated maps and compared them with the initial APS. Results are shown in Fig. 3.11: (a) absolute APS and (b) normalized to the initial APS.

From this figure we can observe two important properties of HEALPix tools. Although at pixel intensity level, expansion to higher resolution causes

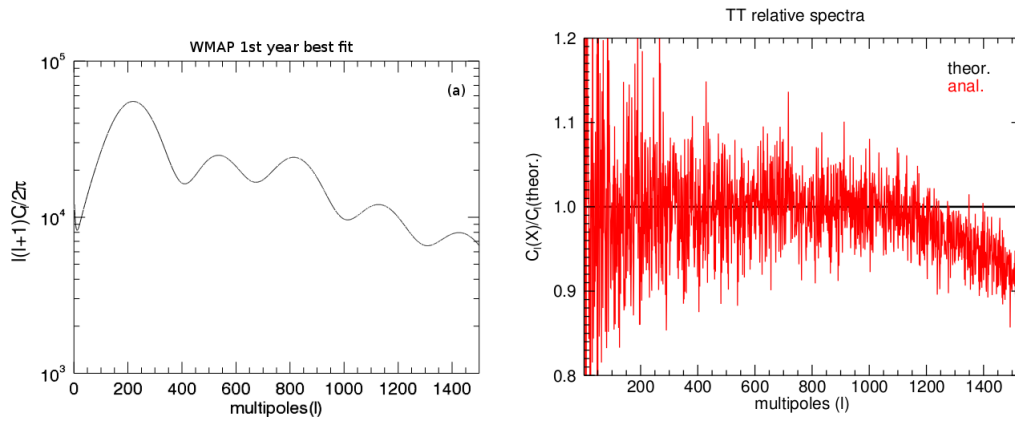


Figure 3.10: (a) WMAP 1st year best fit of the CMB APS. (b) Angular power losses by simulating CMB map with *synfast* and analyzing them with *anafast*. It is normalized to the WMAP 1st year best fit used to synthesize the map. APS are corrected for the window function due to the map pixelization.

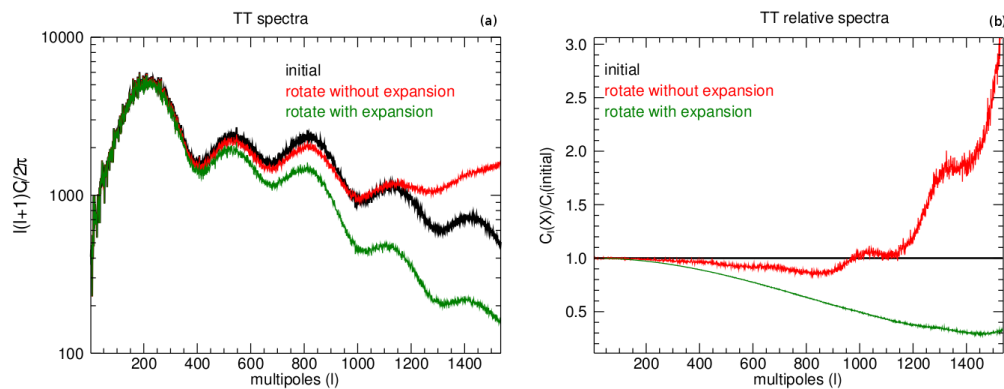


Figure 3.11: Comparison between APS of initial map and the rotated one. (a) absolute APS, (b) normalized to the initial APS. The angular power spectra are corrected for the window function due to the map pixelization.

lower errors in the rotated maps, in harmonic space APS of rotated maps with expansion to higher resolution shows larger power losses. In fact, the power losses for the not expanded map are of the order of 10% at about  $l = 800$  and for multipoles higher than 1024 there is an important increase in power due to the errors committed during rotation. In fact, pixel intensity errors change the correlation between pixel at small scales. On the other hand, for the map rotated with the expansion, a comparison between its APS and the initial one reveals that APS rotated after the map being expanded to higher resolution has power losses at  $l = 1024$  of the order of 50% yet. At  $l = 1535$  power losses for the expanded map is more than 65%. Part of this effect can be explained by considering that, when the code downgrades the map from higher resolution to the original ones, it performs the average of the pixels that fall in the same greater pixel of the downgraded map. This average calculation modifies the correlation among pixel and causes the power loss observed in the APS. However the pixel method is optimized to work at pixel level, so we will consider the method with the addition of the expansion to higher resolution as the best one because it affects pixel intensities lower than the method without the expansion of the map.

### **”Harmonic” method**

Rotation in harmonic space is executed by a code written in F90. In this language we can find and isolate all the routines that most contribute to the errors during the rotation. The following sections are dedicated to the analysis of every single step of the program, to quantify how it affects rotated maps, and finally to the comparison of these results with those obtained in the previous section in which we used the ”pixel method”.

#### **Fortran90 subroutines or facilities?**

Firstly we analyse the capability of the program to extract coefficients  $a_{\ell m}$  of a spherical harmonics expansion of the map and to resynthesize the map from the same coefficients. No rotations are involved for the moment. This

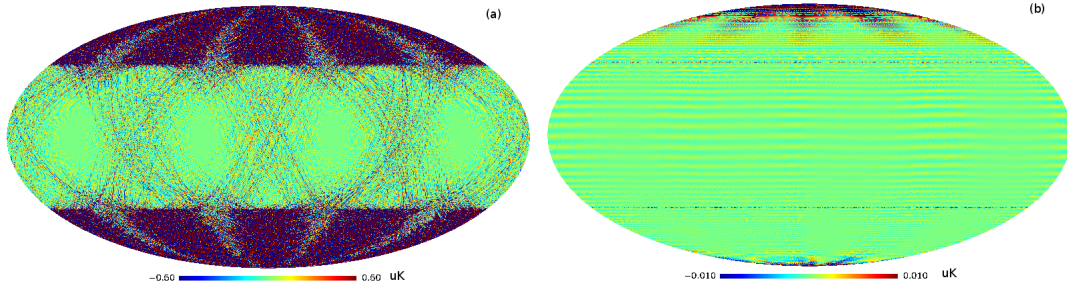


Figure 3.12: Distribution of the errors committed by the routines during the analysis of a CMB temperature map. A synthesized CMB map generated with `synfast` is analyzed by HEALPix F90 subroutine `map2alm` to extract  $a_{\ell m}$  coefficients and then we resynthesize the map with HEALPix F90 subroutine `alm2map`. We show the results from the subtraction of the resynthesized map and the original one. (a) Maps generated, read and wrote with a number of multipoles equal to three times the resolution of the map. (b) The same as (a), but with a number of multipoles only equal to two times the resolution of the map. Notice the different scales.

procedure is made by the HEALPix F90 subroutines `map2alm` and `alm2map`. Exactly as the HEALPix F90 facilities `anafast` and `synfast`, we can synthesize and analyse maps using the spherical harmonics inside a multipole range lower than  $\ell_{max}$  defined in Eq. 3.1. We generated two maps with resolution of  $N_{side} = 512$  but considering a number of multipole of 1535 and 1024, respectively equal to three and two times the value of  $N_{side}$ . We analysed the map with the HEALPix F90 subroutine `map2alm` to extract  $a_{\ell m}$  coefficients and then we resynthesized the map with HEALPix F90 subroutine `alm2map`.

In Fig. 3.12 are shown the errors that affect the resynthesized map respect to the original map. We point out the fact that this extreme analysis allows to reach a number of multipoles equal to three times the resolution of the maps but it affects the resynthesized map with important errors. However their values are really negligible compared to the sensitivity of current missions. In Fig. 3.12 it is shown that by using multipoles only up to twice the resolution of the map, errors fall down more than one order of magnitude in respect to the other case. Considering these results about "harmonic method" and the power loss in APS of rotated maps with "pixel method" in the following

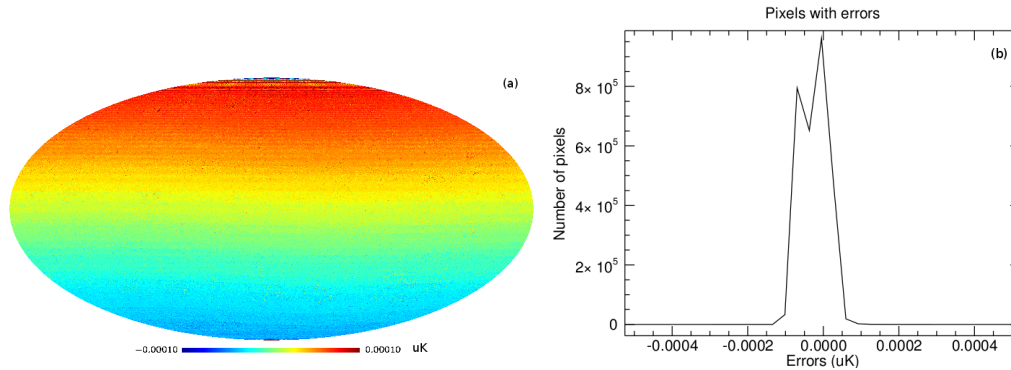


Figure 3.13: Errors committed by analysing CMB maps with HEALPix facilities `anafast` and `synfast`. (a) Errors distribution, (b) their histogram. Compare them with the histograms of the errors showed in the previous figures.

analysis we take into account multipoles up to 1024 equal to twice the map resolution with  $N_{side} = 512$ .

We made the same analysis with the HEALPix F90 facilities. By using `anafast` we analyzed the map until a number of multipoles equal to 1535 and by using `synfast` we resynthesized the map. In Fig. 3.13 we show the errors committed by the facilities.

Errors that affect the maps are more than two orders of magnitude lower than errors committed by HEALPix F90 subroutines used previously. Consequently, it should be more useful to analyse and synthesize maps with HEALPix facilities than with HEALPix subroutines. There are subroutines that can read  $a_{\ell m}$  coefficients directly, but the output of these subroutines are in a different format than the ones that rotation subroutine needs. Otherwise the errors committed by the subroutines are at least three orders of magnitude lower than the sensitivity of WMAP satellite and two orders of magnitude lower than the sensitivity of *Planck* satellite. For these reason we keep to use HEALPix F90 subroutines.

### Upgrading and downgrading: effects on maps

Such as in the pixel method, we considered the possible improvement of

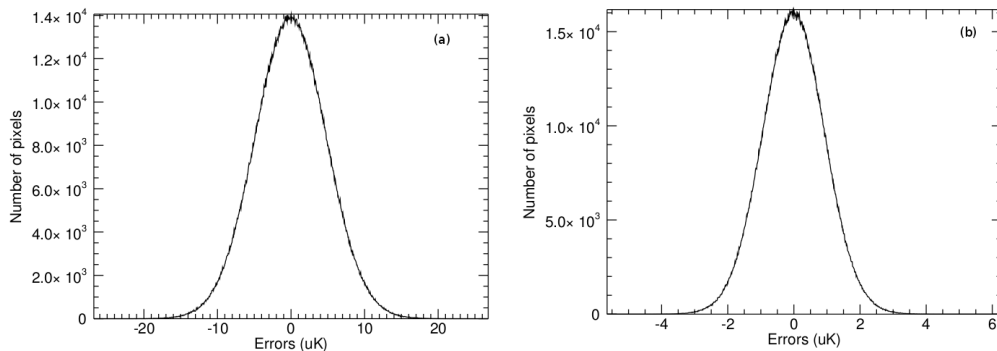


Figure 3.14: Histograms of the errors affecting the rotated maps. These maps are obtained by upgrading to (a)  $N_{side} = 1024$  and (b)  $N_{side} = 4096$  the original maps before analyzing them to recollect the  $a_{\ell m}$  coefficients.

increasing the resolution of the maps before change the coordinates. In this Section we test the effect of upgrading the maps before analysing them to obtain  $a_{\ell m}$  coefficients.

Fig. 3.14 shows that the subroutine that has to recollect  $a_{\ell m}$  coefficients from upgraded maps affects them with important errors. These errors effectively decrease as the resolution increase, but at  $N_{side} = 4096$  they are two orders of magnitude higher than errors committed without upgrading the maps as shown in Fig. 3.15 (a). This part of the program affects maps so much that all the others sources of error become negligible. In Fig. 3.14 are shown these errors for (a) a upgraded map to  $N_{side} = 1024$  and (b) a upgraded map to  $N_{side} = 4096$ .

Another disadvantage of upgrading and downgrading CMB maps is the computational time necessary to run the program because of the higher number of pixel from which subroutine has to obtain  $a_{\ell m}$  coefficients. As in pixel space, the computational time depends on the resolution of upgraded maps. The higher the resolution of upgraded maps is, the higher is the computational time. For this motivations, we will not expand the maps in the following cases when we change the coordinates with the harmonic method.

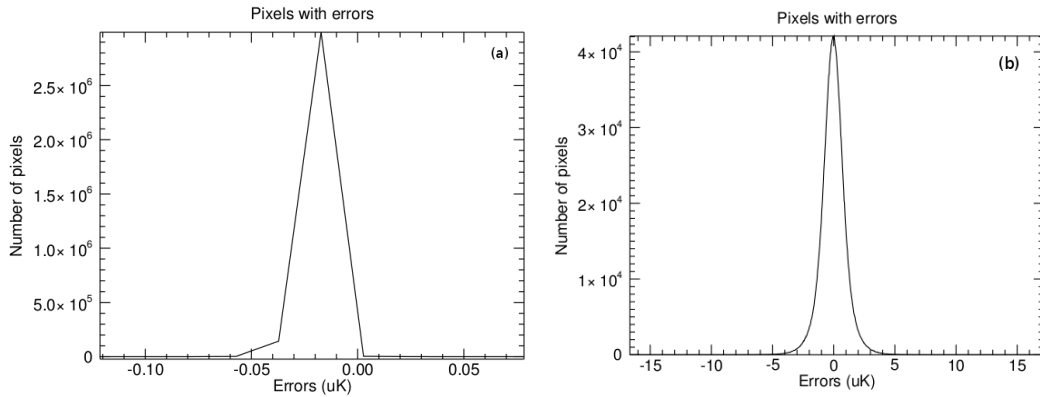


Figure 3.15: Histograms of the errors affecting the rotated maps. These maps are obtained by rotating them using (a) the harmonic method and (b) the pixel method. In this last method we upgraded map to  $N_{side} = 4096$ .

### Errors on pixelized maps and APS: comparisons between "pixel" and "harmonic" method

The best combination of steps for rotating CMB maps with the harmonic method is to read the map, recover  $a_{\ell m}$  coefficients, rotate them and at the end recreate the rotated map from the new  $a_{\ell m}$  coefficients.

Fig. 3.15 shows the histograms of the errors that affect maps rotated twice with both methods: (a) the harmonic and (b) the pixel one.

As shown in figure, harmonic method is very high-quality, affecting maps with errors of the order of  $0.05 \mu\text{K}$  when used on maps of only synthetic CMB, that is when the contribution of foreground signal is null. Pixel method doesn't reach similar results in this case. However both the methods affect map with errors very much lower than sensitivity of WMAP and *Planck* missions.

In Fig. 3.16 are shown APS of rotated maps by using both methods.

As in pixel space, harmonic method is the most powerful in rotating maps, affecting APS of rotated maps with very low errors. Instead, there is a considerably power loss in the APS of map rotated with pixel method. As already shown in Fig. 3.11 at  $\ell = 512$  it is about 15% but at  $\ell = 1024$

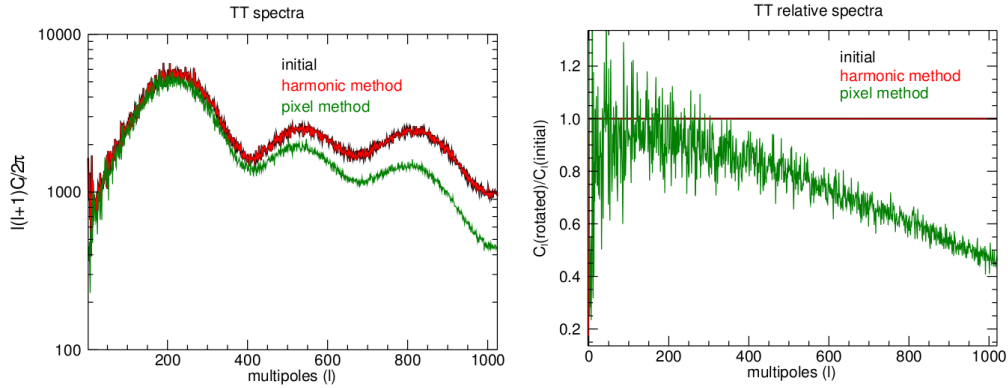


Figure 3.16: APS of rotated map by using both methods compared to the initial map: (a) absolute values, (b) relative to the initial APS. In the pixel method we upgraded map to  $N_{side} = 4096$ . APS are corrected for the window function due to the map pixelization.

it is higher than 50%. The power lost with harmonic method is everywhere negligible compared with the pixel method.

### 3.2.4 CMB maps with beam

In the previous section the change of coordinates has been performed over simulated maps without foregrounds obtained starting from the WMAP 1st year best fit model of CMB APS. These maps were generated without a beam smoothing, that is with a beam of 0 arcmin of FWHM. Missions like WMAP or *Planck* generate maps observing the sky with instruments that present a beam. Still using the HEALPix F90 facility `synfast` we generate maps with a FWHM similar to the *Planck* beam that, according to [172], for the *Planck* Low Frequency Instrument at 44GHz has a FWHM of about 28 arcmin. Our maps were generated with a beam with FWHM of 20 arcmin in Galactic coordinates. An example is shown in Figure 3.17 compared with a map generated without a beam (b).

We applied the same procedure of the previous section. The maps are rotated to Ecliptic coordinates with both the methods, the pixel and the harmonic one. We analyse the rotated maps with HEALPix F90 facility `anafast` obtaining their APS. Finally, we change again coordinates of the

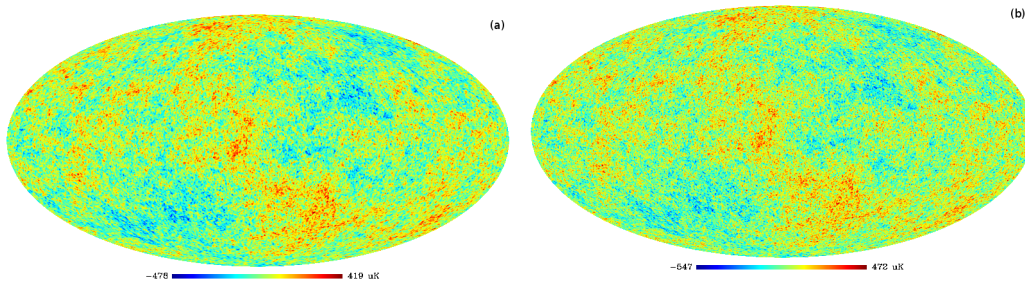


Figure 3.17: Examples of synthetic CMB maps generated by the HEALPix F90 facility `synfast`: (a) with a beam with FWHM of 20 arcmin, (b) without a beam.

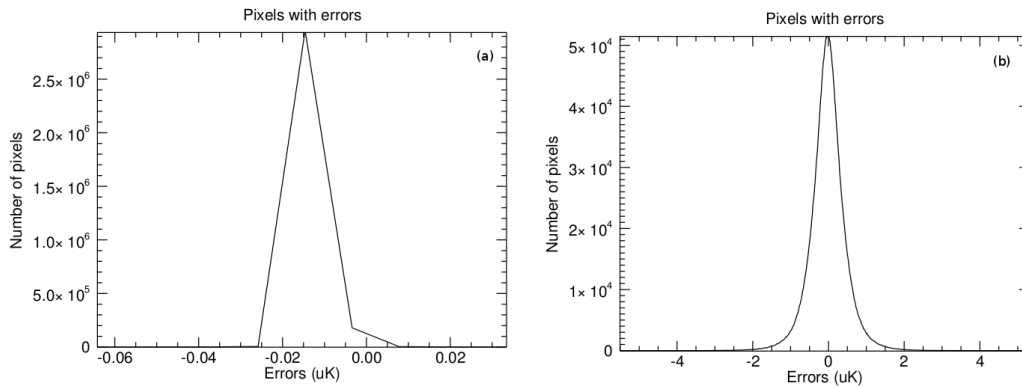


Figure 3.18: Histograms of the errors affecting the twice rotated maps in the presence of a non-zero beam (beam with FWHM of 20 degrees). These maps are obtained by rotation using (a) the harmonic method and (b) pixel method. In this last method we upgraded map to  $N_{side} = 4096$  before the change of coordinates.

map back to the Galactic ones and compare its pixel values with the ones of the original map. The results are reported in Figs. 3.18 and 3.19.

At pixel level, comparing Fig. 3.15 and 3.18, we observe an improvement in the accuracy for both the methods with errors decreased by more than a half. This is probably due to the presence of the beam that smooths CMB temperature peaks. In the harmonic method there are not strong point peaks that make great problems in recovering  $a_{\ell m}$  coefficients. Similarly to the case of no beam, harmonic method is still the most powerful in rotating and maintaining APS unchanged. In APS we observe a decrease in power loss for the pixel method while the harmonic method keeps its performances

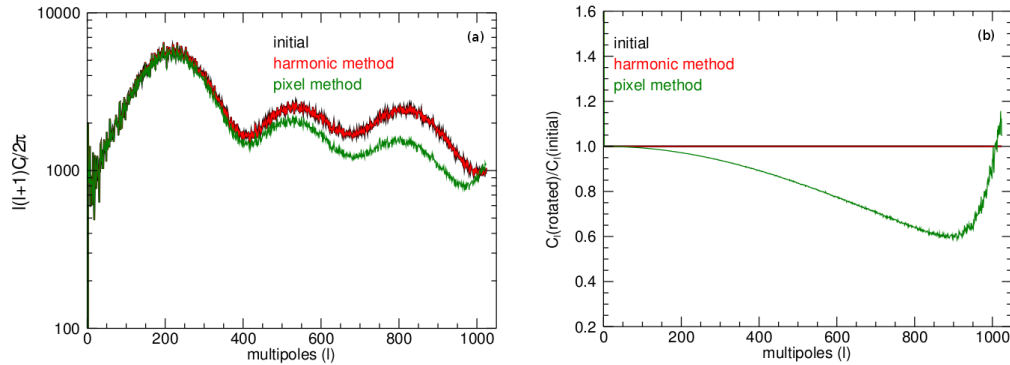


Figure 3.19: APS of rotated map by using both methods compared to the initial map: (a) absolute values, (b) relative to the initial APS. In the pixel method we upgraded the map to  $N_{side} = 4096$ . APS are corrected for the window function due to the map pixelization and to the beam.

unchanged. The presence of the beam that smooths pixel intensities and causes a lower change in pixel correlations is the reason of the lower power loss for pixel method.

### 3.2.5 Application to WMAP maps

When an instrument observes the sky at the microwaves, it collects all the signals coming from very different sources, not only the CMB, but also Galactic and extragalactic microwave emissions collected under the name "foregrounds". WMAP and *Planck* maps, generated by their instruments, have all these contributions. These are the real maps and probably the ones that it is useful to rotate in different coordinates. For this reason, we apply both the HEALPix methods to change coordinates and report their performances on WMAP maps. Fig. 3.20 shows patches of WMAP maps accessible from the LAMBDA website<sup>‡</sup>. There are two different kinds of maps: (a) the original map generated by the satellite and (b) the foreground reduced map in which a previous analysis has been done and most part of the non-CMB signal has been removed.

<sup>‡</sup><http://lambda.gsfc.nasa.gov/>

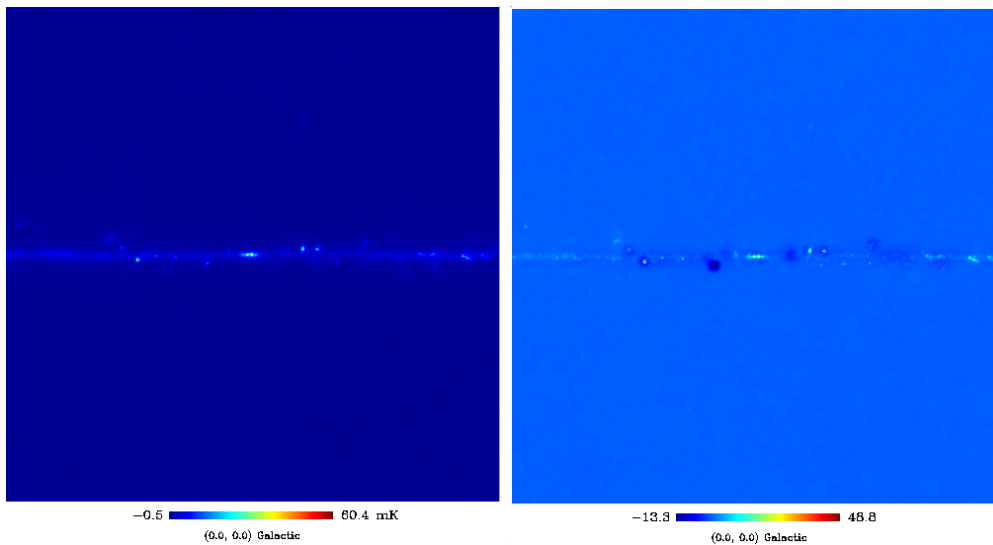


Figure 3.20: Examples of patches along the Galactic equator of sky maps generated by WMAP satellite. (a) Original map at 94 GHz, (b) the same of (a) but with mostly of the foreground removed.

We first concentrate on foreground reduced maps and then analyse HEALPix performances on original (not-cleaned) WMAP maps.

### Foreground reduced maps

As evident in Figure 3.20 (b), although part of the foreground has been removed, the presence of the Galaxy at low latitudes is still strong. For a correct analysis of the CMB is necessary the presence of a mask. The mask chosen for this map is a cut below 20 degrees of latitude, so about the 65% of the sky map is available for our analysis. We have two approaches available: first put a mask on the map in which the masked pixels have zero value and after rotate the map, otherwise first perform the change of coordinates and only then apply the mask on the rotated map. The mask in Ecliptic coordinates is obtained by rotating the mask in Galactic coordinates with the pixel method upgrading the map to  $N_{side} = 4096$ .

We explored both the two approaches and found that there are no differences between them but for a slightly lower loss of power in APS at high

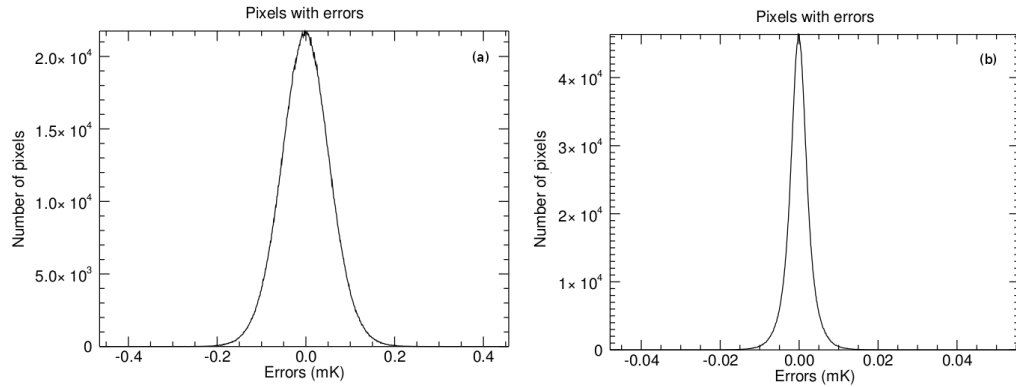


Figure 3.21: Histograms of the errors affecting the rotated foreground reduced maps. These maps are obtained by rotating using (a) the harmonic method and (b) pixel method. In this last method we upgraded map to  $N_{side} = 4096$ .

multipoles for the harmonic method when the mask is applied before the rotation. In Figs. 3.21, 3.22 and 3.23 we present results when the rotation of maps is done before the application of the mask. It is important to emphasize that the mask is applied only when we recover APS from the maps. When we extract the histograms of pixel errors no mask is used.

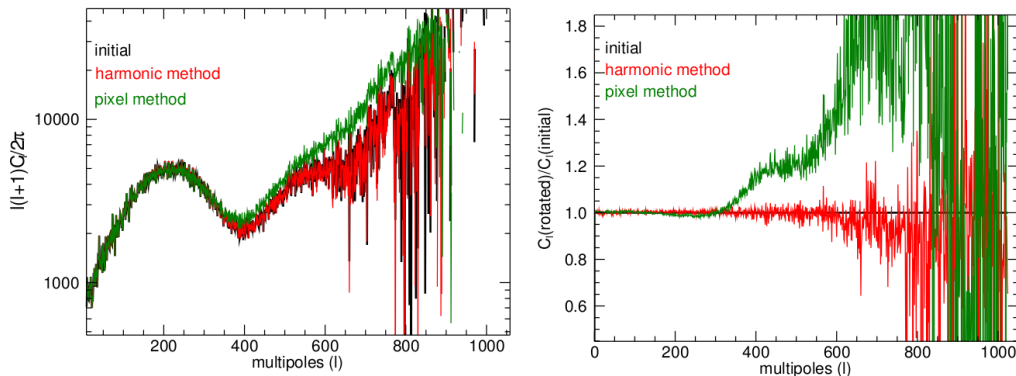


Figure 3.22: APS of rotated foreground reduced map by using both methods compared to the initial map: (a) absolute values, (b) relative to the initial APS. In the pixel method we upgraded map to  $N_{side} = 4096$ . APS are corrected for the window function due to the map pixelization and to the beam. The noise APS has been also removed.

In Fig. 3.21 we show an important change in the performances of the methods with respect to the previous cases. Now it is the pixel method that

less affects rotated maps. Its errors are an order of magnitude lower than the errors committed by the harmonic method. Our interpretation is that  $a_{\ell m}$  coefficients are more affected by the presence of the foreground especially in the presence of a strong Galactic emission, as close to the Galactic plane. On the other hand, pixel method is not sensible to higher fluctuations in pixel values. Errors increase of one order of magnitude respect to the only CMB case because of the higher pixel values at low latitudes. Errors that affect rotated maps in pixel method are lower than WMAP sensitivity, but similar to the *Planck* one.

Fig. 3.22 shows the APS of the maps after the masking process. As already mentioned, mask is a cut at 20 degrees of latitude so more than 65% of the sky is available to obtain the APS. In this way most part of the Galactic APS is cut away. We also performed a rough noise estimation by considering that it is a white-noise with a flat APS. At high multipoles noise is dominant so by calculating the mean of the  $C_\ell$  inside the range  $900 \leq \ell \leq 950$ , we estimated the flat noise APS and subtracted it from the  $C_\ell$  estimated by **anafast**. The mask and the noise estimation allow us to reach the first part of the second peak of CMB APS. In fact CMB is the most important contribution up to  $\ell = 600$ . At higher multipoles the presence of a residual noise completely covers CMB signal. Better available masks and noise estimates allow to reach higher multipoles, but it is beyond our aims. At the APS level, instead, harmonic method is still the most powerful to save the original APS of the map. Its errors at  $\ell \simeq 600$  is lower than 10%. The pixel method is able to accurately reproduce APS of the map only up to  $\ell \simeq 350$ . At higher multipoles the errors rapidly increase and reach more than  $\simeq 40\%$  at  $\ell \simeq 600$ .

### Original maps

In the previous section we analysed the performances of HEALPix tools to change coordinates over foreground reduced maps, but often the analysis of foreground is the topic of a scientific work and it is in these cases that the

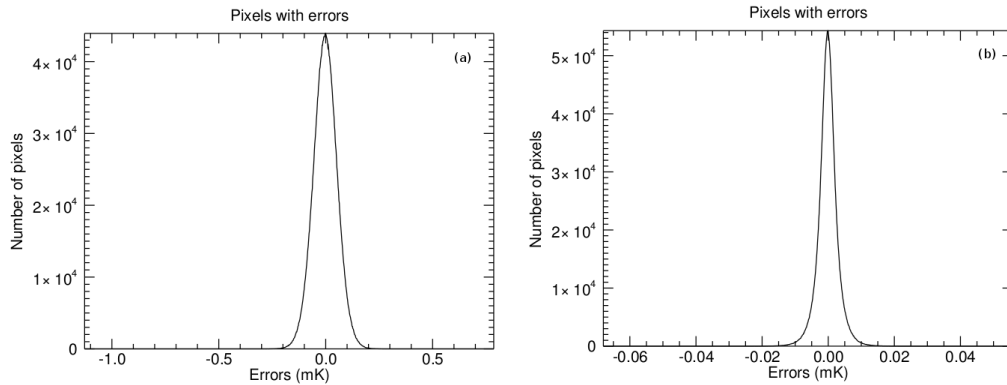


Figure 3.23: Histograms of the errors affecting the rotated WMAP maps. These maps are obtained by rotating using (a) the harmonic method and (b) pixel method. In this last method we upgraded map to  $N_{side} = 4096$ .

change of coordinates is particularly important. For this reason we applied the same procedure of the previous sections to WMAP maps without any pre-cleaning of the foreground. An example is shown in Figure 3.20 (a). It is a map of the microwave temperature sky at 94 GHz obtained by WMAP satellite [169]. The results about the errors in the pixel domain are shown in Fig. 3.23.

Similarly to the case of the foreground reduced maps, the pixel method less affects rotated maps. Its errors are lower than  $5 \mu\text{K}$ , only a little bit smaller than the *Planck* sensitivity. This source of errors will have to be taken into account in future analyses. Errors generated by the harmonic method show a little increase with respect to the foreground reduced case. As in the previous case the problem comes from the higher signal fluctuations close to the Galactic equator that cause higher errors.

In this last case the CMB APS extraction is highly contaminated by the presence of the foregrounds and the noise. At high multipoles (higher than 500) the presence of noise is the most important contribution to APS, while at low multipoles (lower than 500) the presence of Galactic emission and all the other sources completely cover the CMB APS. However, a preliminary analysis was done and it confirms that also in this case maps rotated with

the harmonic method have an APS closer to the initial one with respect to the performances of the pixel method.

The results obtained demonstrate that there is not a better method, but it depends on the type of map that one wants to rotate and what type of information of the map one wants to keep less affected: pixel intensities or APS. In fact, considering the case of only CMB fluctuation maps, harmonic method is the best one, keeping unaffected both the APS and pixel signals. The case of a change of coordinates of maps in which the signal is a superposition of CMB and foreground emissions is more complicated. In this case the pixel method less affects the pixel values of the maps, but the harmonic method works better to estimate the APS. In any case the errors committed changing the coordinates of CMB maps are lower than the WMAP and *Planck* sensitivity. In future CMB observations performed by ground based or balloon telescopes, like SPT, or satellite missions, like CORE or PRISM, that will have higher sensitivities, the errors that affect rotated maps can become relevant and thus will have to be taken into account in the future CMB analyses. For example, at 105 GHz, the expectations in sensitivity per arcminute respectively for CORE and PRISM are  $2.68 \mu K$  after 4 years of data and  $2.88 \mu K$  for a single survey. These values are of the same order of the values shown in Fig. 3.23.

### 3.3 Angular Power Spectrum estimators

The Temperature and Polarization APS of CMB maps carry out crucial "compressed" information about the early stages of the Universe. Huge efforts in the last years have been spent to develop codes in order to extract the APS working in harmonic space or in pixel space. Focusing at large scales, several strategies for measuring  $C_\ell$  have been developed and applied to CMB data with excellent results. These methods include different sampling techniques such as Gibbs [82, 173, 174], adaptive importance [175] and Hamiltonian [176]. At high multipoles ( $\ell > 30$  [177]) the so called pseudo- $C_\ell$

algorithms are usually preferred to others techniques. They implement the estimation of power spectral densities from periodograms [178]. Basically, they estimate the  $C_\ell$  through the inverse harmonical transform of a masked map that is then deconvolved with geometrical kernels and corrected with a noise bias term. These techniques, such as Master [179], Cross-Spectra [180–182], give unbiased estimates of the CMB power spectra and, moreover, it has been shown they work successfully when applied to real data at high multipoles [183–186]. These estimators are pretty quick and light from a computational point of view. However, it is well known that at low multipoles they are not optimal since they provide power spectra estimates with error bars larger than the minimum variance. This section is devoted to present two APS estimators used in this thesis: Cromaster that implements a pseudo- $C_\ell$  estimator and BolPol that instead uses a QML estimator. Section 3.4 is dedicated to the comparison of their performances and results in APS extraction focusing on the largest scales ( $\ell \leq 100$ ).

### 3.3.1 The Cromaster code

Cromaster is an implementation of the pseudo- $C_\ell$  method proposed by [179], extended to allow for both auto- and cross-power spectrum estimation in [181]. A given sky map  $\mathbf{x}$  can be decomposed in CMB signal and noise as  $\mathbf{x} = \mathbf{s} + \mathbf{n}$ , and, accordingly to Eq. 1.13, we define the masked sky pseudo-spectrum as:

$$\tilde{C}_\ell = \frac{1}{2\ell + 1} \sum_{m=-\ell}^{\ell} |a_{\ell m}|^2 = \tilde{C}_\ell^S + \tilde{N}_\ell, \quad (3.2)$$

where  $\tilde{C}_\ell^S$  is the pseudo-spectrum of the sky signal,  $\tilde{N}_\ell$  is the pseudo-spectrum of the noise present in the map. The pseudo- $a_{\ell m}$  coefficients are computed as:

$$\tilde{a}_{\ell m} = \int d\Omega x(\theta, \phi) w(\theta, \phi) Y_{\ell m}^*(\theta, \phi), \quad (3.3)$$

where  $w$  is the applied mask and  $Y_{\ell m}^*$  are the spherical harmonics of the expansion.

In order to recover the full sky power spectrum, Cromaster employs the following estimator:

$$\hat{C}_\ell = \sum_{\ell'} K_{\ell\ell'} (\tilde{C}_{\ell'} + \tilde{N}_{\ell'}), \quad (3.4)$$

where the mode-mode coupling kernel  $K_{\ell\ell'}$  is a geometrical correction that accounts for the loss of orthonormality of the spherical harmonic functions in the cut sky (see [179] for more details). In fact, for an isotropic sky signal that is a realization of a theoretical power spectrum  $C_\ell$ , one can write:

$$\langle \hat{C}_\ell \rangle = C_\ell. \quad (3.5)$$

Hence, Eq. 3.4 defines an unbiased estimator provided that the noise term  $\tilde{N}_\ell$  is properly removed, which is usually done through Monte Carlo simulations. However, for current generation high-sensitivity experiments, such as WMAP and *Planck*, the noise bias has to be known to better than 0.1% accuracy, and therefore the cross-spectrum approach is preferred (see, e.g. [31,187]). In the cross-spectrum approach, the pseudo- $C_\ell$  are computed by combining the spherical harmonic coefficients from two or more maps with uncorrelated noise so that the ensemble average of  $\tilde{N}_\ell$  is null, making the cross-spectrum estimator naturally unbiased.

The error bars for pseudo- $C_\ell$  methods can be roughly approximated accordingly to Eq. 1.15 for a masked sky as:

$$\Delta \hat{C}_\ell = \sqrt{\frac{2}{(2\ell + 1) f_{sky}^{eff}}} (C_\ell + N_\ell) \quad (3.6)$$

where  $f_{sky}^{eff}$  is the effective fraction of the sky used for the analysis which accounts for the weighting scheme of the pixels. For a given sky coverage, a uniform weighting scheme produces the largest sky fraction and is therefore the optimal choice in the signal dominated regime, which corresponds to large angular scales. On the other hand, an inverse noise weighting scheme reduces

$N_\ell$  and is the best choice in the noise dominated regime, i.e. at small angular scales. A trade off between the two weighting scheme should be applied in the intermediate regime, and an optimal pseudo- $C_\ell$  method should employ the best weighting scheme at a given multipole according to the S/N ratio at that multipole.

A more accurate approach to associate an error bar to the estimated APS, obtained with Eq. 3.4, is to build a covariance matrix, that in this case is an  $\ell_{max} \times \ell_{max}$  matrix, where  $\ell_{max}$  indicates the maximum multipole of the APS extraction. For practical applications, i.e. involving coloured noise properties and arbitrary masks incorporating possible non-uniform weighting of the data, there is no readily available exact analytical expression for the covariance matrix of this estimator. In these cases, the elements of the covariance matrix are defined as:

$$Cov \left\{ \hat{C}_\ell, \hat{C}_{\ell'} \right\} = \langle (\hat{C}_\ell - \langle \hat{C}_\ell \rangle) (\hat{C}_{\ell'} - \langle \hat{C}_{\ell'} \rangle) \rangle_{MC}, \quad (3.7)$$

where the  $C_\ell$  are the results of signal and noise MC simulations. This approach has been widely used (see e.g. [160,184,188]) and it is also the baseline procedure for Cromaster used for the analysis reported in Section 3.4. At the first order, the error bars associated to the APS can be approximated as the elements of the diagonal of the matrix, but the approximation is accurate only if the off-diagonal elements are order of magnitudes lower than diagonal elements. Estimating off-diagonal elements of the covariance matrix with high accuracy requires a huge number of simulations. In fact, assuming that the covariance estimate is Wishart distributed<sup>§</sup> [189], the uncertainty on the diagonal elements simply scales as  $\sqrt{(2/N_{sim})}$ , while for the off-diagonal elements it scales as  $\sqrt{1/N_{sim}} \times \sqrt{(Cov_{\ell\ell} * Cov_{\ell'\ell'})/Cov_{\ell\ell'}}$ , which is significantly worse in the presence of small correlations. In addition, Cromaster implements an approach for error estimation based on bootstrapping: for a given  $\ell$ , we generate a set of fake  $\tilde{a}_{\ell m}$  by resampling the observed  $a_{\ell m}$  with

---

<sup>§</sup>The Wishart distribution is a generalization to multiple dimensions of the chi-squared distribution

uniform probability, and these are used to compute a set of fake  $\tilde{C}_\ell$  to be fed into Eq. 3.7 to estimate the diagonal elements of the matrix. In order to account for the sky cut, only  $(2\ell + 1)f_{eff}^{sky}$  elements of the  $\tilde{a}_{\ell m}$  are averaged to compute the fake  $\tilde{C}_\ell$ . This is a very fast procedure based only on real data, and it is especially useful for testing purposes (i.e. when having a quick look to the data or checking for instrumental systematic effects). However, it is not accurate enough for cosmological analysis especially at low multipoles and when only a small fraction of the sky is considered.

In [190] an analytical approximation involving measured auto- and cross-power spectra has been proposed. The method is accurate only at high multipoles and for large sky fraction. *Planck* power spectrum covariance is also based on an analytical approximation [187], that apart from being rather more complex, involves a fiducial model  $C_\ell$  and assumes uncorrelated pixel noise.

In any case this method is really fast and can extract the APS from a map with a resolution of  $N_{side} = 512$  in few minutes on a common laptop.

### 3.3.2 The BolPol code

The BolPol code estimates the APS of a full sky or masked sky map directly in pixel space through an implementation of the Quadratic Maximum Likelihood (QML) estimator. This method has been derived for CMB Temperature analysis in [191] and successively extended to the polarization signal in [192]. We can define a CMB temperature and polarization map as a vector  $\mathbf{x}$  that has  $3 \times N_{pix}$  elements as the  $N_{pix}$  pixels of the map multiplied by 3 to take into account the T, Q and U Stokes parameters. Following the QML method defined in [191], we can start writing its covariance matrix  $\mathbf{C}$  as a sum of two contributions coming from the CMB itself and from instrumental noise:

$$\mathbf{C} = \langle \mathbf{x}\mathbf{x}^t \rangle = \mathbf{S}(C_\ell) + \mathbf{N} = \sum_{\ell} \mathbf{C}_\ell \mathbf{P}^\ell + \mathbf{N}, \quad (3.8)$$

where  $\mathbf{C}_\ell$  is an initial assumption for a fiducial APS and  $\mathbf{N}$  is our expected noise estimation. Coherently to the fact that the method is pixel based, in opposition to the pseudo- $C_\ell$  case described above, we note here that the covariance matrix  $\mathbf{C}$  is built in pixel space and thus has  $3N_{pix} \times 3N_{pix}$  elements. The  $\mathbf{P}^\ell$  are defined as:

$$\mathbf{P}_{ij}^\ell = \frac{2\ell + 1}{2\pi} P_\ell(\hat{r}_i \cdot \hat{r}_j) \quad (3.9)$$

where  $P_\ell$  denotes the Legendre polynomials, whereas  $\hat{r}_i$  and  $\hat{r}_j$  are the unit vectors pointing respectively in the direction of pixel  $i$  and  $j$  of the map to be analysed.

From the covariance matrix expressed by Eq. 3.8, we can build the QML estimator for  $\hat{C}_\ell^X$  as:

$$\hat{C}_\ell^X = \sum_{\ell', X'} (\mathbf{F}^{-1})_{\ell\ell'}^{XX'} \left[ \mathbf{x}^t \mathbf{E}_{\ell'}^{X'} \mathbf{x} - \text{tr}(\mathbf{N} \mathbf{E}_{\ell'}^{X'}) \right], \quad (3.10)$$

where  $X = TT, EE, BB, TE, TB, EB$  is one of the possible APS and  $\mathbf{F}_{\ell\ell'}^{XX'}$  is the Fisher matrix, defined as

$$\mathbf{F}_{\ell\ell'}^{XX'} = \frac{1}{2} \text{tr} \left[ \mathbf{C}^{-1} \frac{\partial \mathbf{C}}{\partial C_\ell^X} \mathbf{C}^{-1} \frac{\partial \mathbf{C}}{\partial C_{\ell'}^{X'}} \right], \quad (3.11)$$

and the  $\mathbf{E}_\ell^X$  matrix is given by

$$\mathbf{E}_\ell^X = \frac{1}{2} \mathbf{C}^{-1} \frac{\partial \mathbf{C}}{\partial C_\ell^X} \mathbf{C}^{-1}. \quad (3.12)$$

Although an initial assumption for a fiducial power spectrum  $C_\ell$  is needed in order to build the signal covariance matrix  $\mathbf{S}(C_\ell)$ , it has been proven that the QML method provides unbiased estimates of the power spectrum contained in the map regardless of the initial guess

$$\langle \hat{C}_\ell \rangle = \bar{C}_\ell, \quad (3.13)$$

where the average is taken over the  $C_\ell$  extracted from an ensemble of maps realizations with fiducial APS,  $\bar{C}_\ell$ , or, in a practical test, over MC realizations

extracted from an a priori APS.

According to the Fisher-Cramer-Rao inequality [193], the inverse of the Fisher matrix of a set of parameters which we want to estimate represents the best covariance matrix in the parameter space. Therefore, if the covariance matrix associated to an estimator is just the Fisher matrix as in the QML case

$$\langle \Delta \hat{C}_\ell \Delta \hat{C}_{\ell'} \rangle = (F^{-1})_{\ell\ell'}, \quad (3.14)$$

then that estimator provides the minimum variance, that is, it has the smallest error bars and we may call it *optimal*.

BolPol is a fully parallel implementation of the QML method written in Fortran90. Since the method works in pixel space the computational cost rapidly increases as one considers higher resolution maps of a given sky area. The code has been originally created to analyse both Temperature and Polarization CMB data and has been applied to WMAP maps with interesting results [194, 195]. With the aim of increasing the computational speed and the maximum resolution achievable, the code has been modified to work only on the temperature signal.

In both the cases, the inversion of the covariance matrix  $\mathbf{C}$  scales as the third power of the side of the matrix, i.e.  $O(N^3)$  being  $N$  the number of observed pixels. The number of operations is roughly driven, once the inversion of the total covariance matrix is done, by the matrix-matrix multiplications to build the operators  $\mathbf{E}_\ell^X$  in Eq. 3.12 and by calculating the Fisher matrix  $\mathbf{F}_{XX'}^{\ell\ell'}$  given in Eq. 3.11. The memory, RAM, required to build these matrices is of the order of  $O(\Delta\ell N^2)$  where  $\Delta\ell$  is the range in multipoles of  $\mathbf{C}^{-1}(\partial\mathbf{C}/\partial C_\ell^X)$  (for every X) that are built and kept in memory during the execution time. This implementation is memory demanding, but it has the benefit of speeding up the computations. For a temperature all-sky map of  $N_{side} = 64$ , the total amount of RAM needed by BolPol is 19 TB. When we run the code into massively parallel computer clusters such as FERMI, at CINECA, it takes around 3 hours using 16384 cores to perform a MC of

100 maps with 48% of the sky masked. Due to the high computational costs of the implementation presented, the QML method can be applied only to low resolution maps. Future developments and optimizations of the code will allow to apply the QML method in order to analyse high resolution patches of the sky by binning the Fisher matrix and even higher resolution full sky maps. These developments will be very useful for the analyses of the future observational campaigns that will obtain higher resolution and accurate maps of the CMB.

### 3.4 Comparison between pseudo- $C_\ell$ and QML estimators at large scales

From the observational point of view, the CMB anisotropies temperature map, as observed by WMAP after 9 years of data, is cosmic variance dominated, that is cosmic variance exceeds the instrumental noise, up to  $\ell = 946$  [31]. For *Planck* data this crossing happens at  $\ell \sim 1500$  [187]. Therefore at the largest scales, the effect of instrumental noise is almost negligible and, from the data analysis point of view, the only source of uncertainty, apart the unavoidable cosmic variance, is coming from the method used to extract the APS<sup>¶</sup>. As described in Chapter 4, one of the possible imprints generated by an inflationary mechanism are large scales CMB anomalies [38,196]. In order to detect these imprints we need APS estimators with the lowest error bars. In this section we compare the two aforementioned methods for APS extraction at the largest angular scales under realistic conditions. Our goal is to quantitatively find out to what extent it is worth to use an optimal but computational demanding QML method with respect to a quicker and lighter but non optimal pseudo- $C_\ell$  approach. Here we quantitatively address this problem through realistic Monte Carlo (MC) simulations. The following results are collected in [197].

---

<sup>¶</sup>For real CMB maps, the presence of residual foregrounds and possible systematic effects causes both a bias in the APS extracted and in its uncertainty.

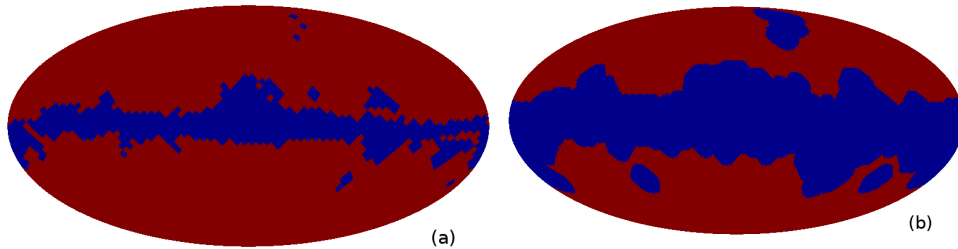


Figure 3.24: The masks used for the analyses in this section. (a) WMAP kq85 temperature mask. (b) WMAP kq85 mask extended by 8 degrees.

### 3.4.1 Details of the simulations

We consider several cases summarized in Table 3.1. The low resolution case, namely case 1, is parametrized by  $N_{side} = 64$  and corresponds to the maximum resolution that *BolPol* is currently capable to treat. The high resolution case, i.e. case 2, with  $N_{side} = 256$ , is analysed by Cromaster. Of course Cromaster can be run also at higher resolution but this does not impact the range of multipoles where we wish to compare the two codes which essentially is  $\ell \lesssim 90$ . The noise value of  $1 \mu\text{K}^2$  at  $N_{side} = 256$  corresponds to the typical variance for a *Planck*-like experiment [8]. The noise of  $1 \mu\text{K}^2$  is added to the maps both at  $N_{side} = 64$  and  $N_{side} = 256$ . This is done to regularize the numerics for this case. In practice, even if the noise is the same for different resolution maps, for both cases of Table 3.1 the noise contribution to the APS is negligible and does not impact the analysis.

Each of the cases of Table 3.1 is analysed with and without Galactic masks. For the former option, we used the WMAP kq85 temperature mask (Fig. 3.24a), publicly available at the LAMBDA website<sup>||</sup>, and an extended version of the kq85 that we call "kq85 + 8 deg" (Fig. 3.24b) where we have extended the edges of the mask by 8 degrees. The former mask excludes about 20% of the sky, the latter about 48%. In the full sky case and in a signal dominated regime, the two codes are algebraically equivalent. We

<sup>||</sup><http://lambda.gsfc.nasa.gov/>

Case	Res	Beam	Noise	$N_{sim_s}$	Code	Masks
	$N_{side}$	deg	$\mu K^2$			
1	64	0.916	1.0	1000	B,C	a,b
2	256	0.573	1.0	1000	C	a,b

Table 3.1: Details of the considered MC simulations. Two cases are taken into account, each of them consist of 1000 realizations from the best fit of *Planck* model (in fact the choice of the model is irrelevant for our purposes). First column "Case" is for type of simulations. Second column "Res" is for the resolution which is expressed in terms of the parameter  $N_{side}$ . Third column "Beam" is for the adopted FWHM. Fourth column is for the level of "White noise" which is given in  $rms^2$ . Fifth column " $N_{sim_s}$ " contains the number of considered simulations. Sixth column "Code" specifies which code is applied for each case, where B stands for BolPol and C for Cromaster. Seventh column "Masks" identify the masks that have been applied to the simulated maps to perform the analysis: the WMAP kq85 maks (a) and the kq85 enlarged by 8 degrees (b). See the text for more details.

have checked, for internal consistency, that this is indeed the case. The only differences arise because of the different resolutions, that is a different smoothing, i.e. FWHM. Since a Galactic masking is in practice unavoidable in CMB data analysis we do not report on this unrealistic case.

For case 1 and 2 we analyse 1000 "signal plus noise" MC simulations where the signal is randomly extracted through the `synfast` routine of the HEALPix package, from a  $\Lambda$ CDM *Planck* best fit model [187] and the noise from a Gaussian distribution with variance given by the value reported in Table 3.1.

The averages and variances of the APS of the two MC simulations are plotted in Fig. 3.25 where we considered the WMAP kq85 mask (*left*) and the kq85 mask enlarged by 8 degrees (*right*). These figures are considered as the validation of the performed extractions. In fact, Fig. 3.25 might be seen as a further validation of both codes and extractions at the same time (an extensive validation of the codes is already given in [194] and in [181]).

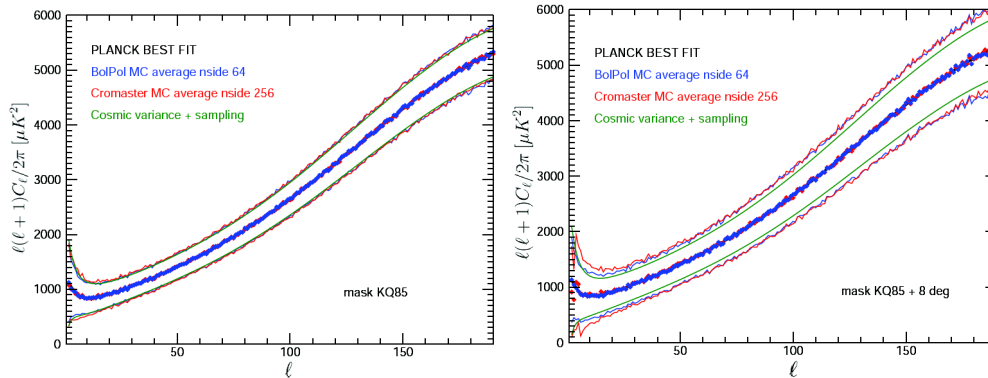


Figure 3.25: Average and variance of the APS of the MC simulations analyzed with BolPol (blue estimates) and Cromaster (red estimates) obtained masking the sky with the WMAP kq85 mask (*left*) and the kq85 enlarged by 8 degrees (*right*). See Table 3.1 for details.

### 3.4.2 Figure of Merit

In order to make a detailed comparison between the two methods, we have to define a suitable estimator. Our approach is very similar to that proposed in [177].

For each multipole and for each realization of MC simulations, we compute the APS and build plots as in Fig. 3.26. In such a figure each point  $P = (x, y)$  has the abscissa  $x$  given by the APS obtained with `anafast` run in the ideal case (i.e. full sky and no noise) and the ordinate  $y$  that is given by the APS estimated through the *BolPol* or *Cromaster* for the cases of Table 3.1.

Since the APS extracted by `anafast` from a full sky of pure CMB signal is the true APS of the map, if the two codes were "perfect" only the diagonal of these plots would be populated (see black solid line in Fig. 3.26). On the contrary, there are two clouds of points, one for BolPol estimates, shown in blue, and one for the Cromaster estimates, shown in red. The idea is to measure the dispersion of the two clouds around the solid black line. This defines our estimator aimed at the comparison of the two codes. The code that shows larger dispersion has an intrinsic larger variance in the determination

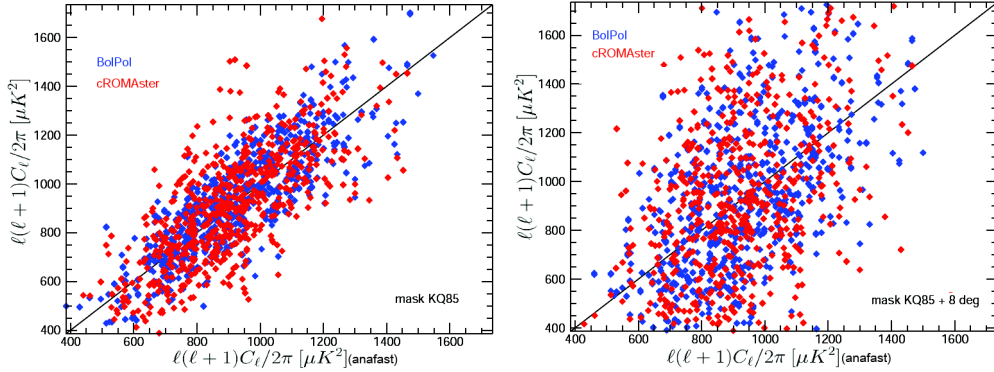


Figure 3.26: All the 1000 APS estimates at multipole  $\ell = 20$  for the masked case of Table 3.1 when we considered the WMAP kq85 mask (*left*) and the kq85 mask enlarged by 8 degrees (*right*). Blue estimates are for BolPol and red estimates for Cromaster.

of the APS. In practice, for each single multipole  $\ell$  we define the variance  $D_\ell^2$  as the mean of the squared distance  $d_\ell$  of each point  $P$  from the line  $y = x$ , which is the diagonal of the first quadrant of this Cartesian plane,

$$D_\ell^{2[B/C]} \equiv \langle d_\ell(P^{[B/C]}, diagonal)^2 \rangle, \quad (3.15)$$

where the labels  $B/C$  refer to BolPol and Cromaster and with  $\langle \dots \rangle$  standing for the "ensemble" average. We underline that, in this way, the estimator cancels the uncertainty due to the cosmic variance, that is the same for both the codes, and highlights their different intrinsic variances. Taking the square root of Eq. 3.15 we obtain

$$D_\ell^{[B/C]} = \frac{\ell(\ell+1)}{2\sqrt{2}\pi} \langle (C_\ell^{[B/C]} - C_\ell^A)^2 \rangle^{1/2}, \quad (3.16)$$

where  $C_\ell^A$  is the APS computed with `anafast` in the ideal case. From Eq. 3.16 it is clear that the physical unit of  $D_\ell^{[B/C]}$  is the same as the one used for the APS, that in our case is  $\mu\text{K}^2$ . Equation 3.16 is what we consider in the next section to perform the comparison.

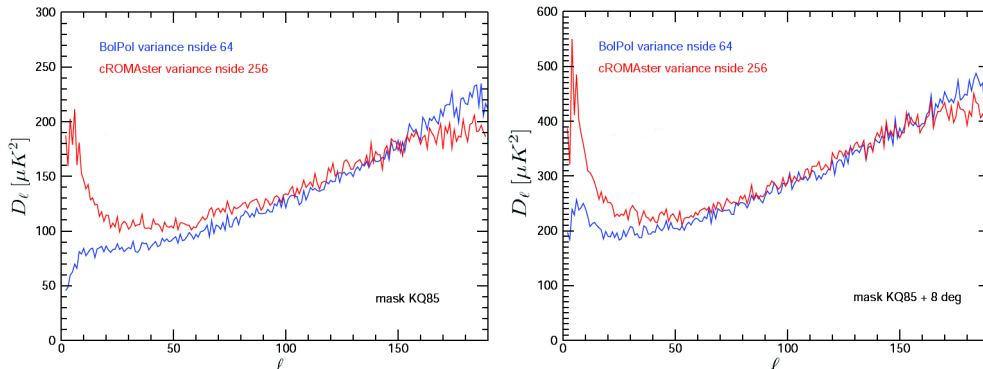


Figure 3.27:  $D_\ell$  vs multipole  $\ell$  for each of the cases described in Table 3.1, when we considered the WMAP kq85 mask (*left*) and the kq85 mask enlarged by 8 degrees (*right*).

### 3.4.3 Results

Fig. 3.27 shows the estimator  $D_\ell$ , defined in Eq. 3.16, as a function of the multipole  $\ell$  for each of the cases of Table 3.1. This plot demonstrates that the intrinsic variance of BolPol is lower than the intrinsic variance of Cromaster up to  $\ell \sim 100$ . The differences between the two estimators,  $(D_\ell^{[C]} - D_\ell^{[B]})$  versus  $\ell$  is shown in Fig. 3.28 (*left*). This makes clear that the difference in the accuracy of the two methods is higher at lowest multipoles and that it grows as the number of masked pixels increases. In particular, when we consider the WMAP kq85 mask (kq85 enlarged by 8 degrees), the intrinsic dispersion introduced by the pseudo- $C_\ell$  method is *at least* a factor of 3 (a factor of 2) greater than that of the QML estimates for  $\ell \leq 10$ . In the range  $20 \leq \ell \leq 60$  the QML is about 20% (15%) more accurate than the pseudo- $C_\ell$  method. We note here that although the ratios presented between the intrinsic dispersions of the two methods are smaller in the case where we used the more aggressive mask, this is only due to the fact that both the dispersions are increasing due to the mask. However, the differences of the two dispersions showed in Fig. 3.28 (*left*) demonstrates that as the effective sky fraction covered by the mask increases, the difference increases.

At higher multipoles, i.e.  $\ell > 100$ , the larger QML intrinsic variance displayed in Fig. 3.27 is entirely due to the lower resolution at which BolPol

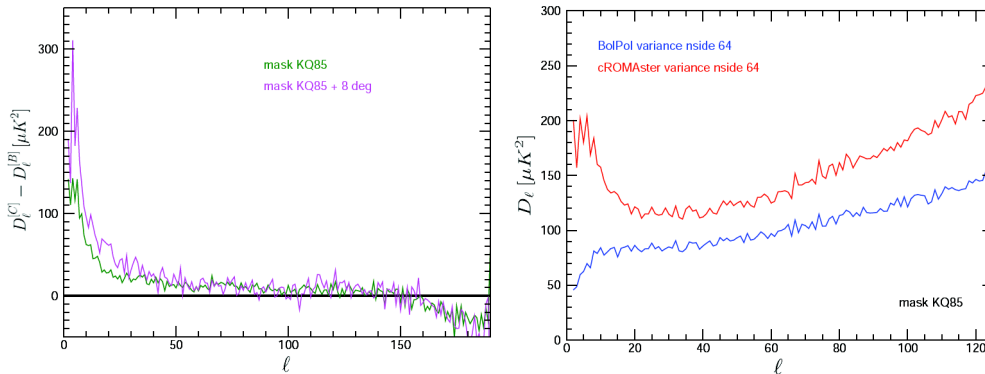


Figure 3.28: (*left*)  $D_\ell^{[C]} - D_\ell^{[B]}$  vs  $\ell$  when we considered the WMAP kq85 mask (*green*) and the kq85 mask enlarged by 8 degrees (*violet*). (*right*)  $D_\ell$  vs multipole  $\ell$  as in Fig. 3.27 (*left*), but with the codes run at the same resolution ( $N_{side} = 64$ ).

is run with respect to Cromaster. Note however that when the two codes are run at the same resolution, i.e.  $N_{side} = 64$ , the QML has always a smaller variance than Cromaster in the commonly valid multipole domain, as shown in Fig. 3.28 (*right*) when we used the WMAP kq85 mask. We obtained the same result when we considered the enlarged mask. These results show that the QML method applied to maps with resolution given by  $N_{side} = 64$  obtains an optimal APS extraction in the range of interest ( $\ell \lesssim 90$ ) compared to pseudo- $C_\ell$  estimates performed on maps at the best resolution allowed by the observations ( $N_{side} \geq 256$ ).

### 3.4.4 Applications

In this section we evaluate what is the benefit of considering an optimal APS estimation. In order to do that, we take into account two estimators of large scale anomalies that are used at large scales in CMB data analysis and will be better described in the following Chapter. We would like to illustrate the benefit of applying an optimal APS extractor. We consider the estimator  $R$ , introduced by [198] for the TT parity analysis, as

$$R = C_+^{TT} / C_-^{TT} \quad (3.17)$$

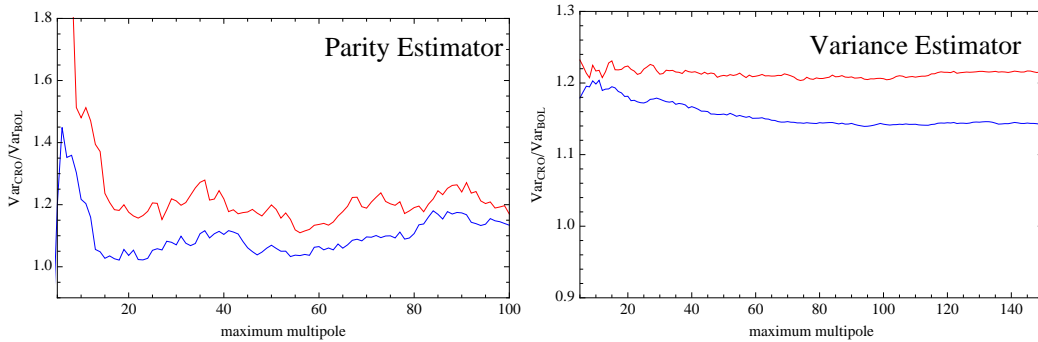


Figure 3.29: (*left*) Ratio of the variances (Cromaster over BolPol) for the TT Parity estimator as a function of the multipoles obtained from the BolPol and Cromaster APS extracted in the previous section when we considered the WMAP kq85 mask (*blue*) and the kq85 mask enlarged by 8 degrees (*red*). (*right*) The same as Fig. 4.4, but for the Variance estimator.

where  $C_{+/-}^{TT}$  is

$$C_{+/-}^{TT} \equiv \frac{1}{\ell_{tot}(+/-)} \sum_{\ell=2, \ell_{max}}^{+/-} \frac{\ell(\ell+1)}{2\pi} C_{\ell}^{TT}. \quad (3.18)$$

Here  $\ell_{tot}(+/-)$  is the total number of even (+) or odd (-) multipoles taken into account in the sum.

We also consider the Variance estimator  $\sigma^2$  (e.g. [196, 199, 200] and reference therein) defined as

$$\sigma^2 = \langle \delta T^2 \rangle = \sum_{\ell \geq 2}^{\ell_{max}} \left( \frac{2\ell+1}{4\pi} \right) C_{\ell}^{TT}. \quad (3.19)$$

The variances of these two estimators are affected by the uncertainties on the APS. In Fig. 3.29 (*left*) we show the ratio of the variances of  $R$  obtained through the APS extracted by Cromaster and BolPol for each  $\ell_{max}$ . Similarly in Fig. 3.29 (*right*) we show the ratio between the variances of  $\sigma^2$  obtained with Cromaster and BolPol.

From these figures it is clear that the lower uncertainty given by BolPol leads to a lower variance for both the two estimators in the range of interest ( $\ell \lesssim 90$ ). For the TT Parity estimator the average gain in efficiency of about

10% when we use the WMAP kq85 mask (20% for the kq85 mask enlarged by 8 degrees) with a peak at the lowest scales becoming higher than 40% for both the masks. In the case of Variance estimator, when we consider the WMAP kq85 mask, the variance obtained from BolPol APS is lower than the one obtained from the Cromaster APS by a factor of about 15% becoming even higher at very large scales ( $\ell \leq 40$ ). When we consider the kq85 mask enlarged by 8 degrees the gain in accuracy provided by the QML estimator is always about 22%. The use of BolPol for low resolution map analysis will bring to tighter constraints for these kinds of estimators. We also note that the ratios of Fig. 3.29 are always larger than 1, even for  $\ell > 90$  where the pseudo- $C_\ell$  method becomes more accurate due to the different resolutions of the maps analysed. This effect is due to the fact that both Variance and TT parity strongly depends on the very low multipoles where the QML method is more accurate than the pseudo- $C_\ell$  method.

The main results of this section are the Fig. 3.27 and 3.28 quantifying the differences between the intrinsic variance of the pseudo- $C_\ell$  and the QML methods. The results suggest to use the QML estimator and not the pseudo- $C_\ell$  method in order to perform accurate analyses based on the APS at large angular scales (at least  $\ell \leq 90$ ). This might be of particular interest for the analysis of the large scale anomalies in the temperature anisotropy pattern for which some estimators are based on the APS extracted. The large scale anomalies and their analysis are described in Chapter 4.

### 3.5 The aliasing effect in maps degradation

*Planck* produced maps with FWHM of  $\sim 5$  arcmin at frequencies of 217 GHz and above, and  $\leq 13$  arcmin from 70 to 143 GHz. In HEALPix resolution parameters, *Planck* produced maps at  $N_{side} = 2048$  at frequencies above 100 GHz and  $N_{side} = 1024$  at frequencies below 100 GHz.

The APS, extracted from these maps, are used to build the likelihood function that is a complete statistical description of the two-point corre-

lation function of the CMB temperature fluctuations that accounts for all known relevant uncertainties, both instrumental and astrophysical [34]. The likelihood is generated in order to estimate cosmological parameters also propagating the uncertainties of the power spectrum extracted.

The *Planck* maps have more than  $10^7$  pixels, so a likelihood described directly at pixel level would be too time consuming. The usual approach for likelihood generation is to separate the multipole range in two regions: the low- $\ell$  likelihood for  $\ell \leq 50$  and the high- $\ell$  likelihood for  $\ell > 50$ . For the high- $\ell$  part it is assumed a Gaussian form of the likelihood based on pseudo- $C_\ell$  power spectra that have been corrected to account for partial sky masking. At low multipoles ( $\ell \leq 50$ ), the distribution of the estimated  $C_\ell$  is not well approximated by a Gaussian due to the limited degrees of freedom per  $\ell$  [177]. In this case, the Temperature *Planck* likelihood has been generated through a Gibbs sampling approach [82, 173, 174], implemented by the Commander code [81]. This approach is a Monte Carlo sampling algorithm which allows both for physically motivated component separation and accurate likelihood estimation directly in pixel space. To avoid the method to be computational prohibitive its input maps are the high resolution maps downgraded from their native resolution to a lower resolution. Thus, an important step of this analysis is to generate low resolution maps without the introduction of spurious artefacts.

Low resolution maps are also very useful for the search of large scales anomalies (see Chapter 4) for which optimal APS estimators, that are pixel based such as the QML method, are strongly recommended [197]. For high resolution maps the use of these estimators on the whole sky is prohibitive because of the very large computational requirements or very long time needed for the analyses (even if there has been an attempt in the WMAP analysis, see [201]). At the same time, the largest scales of the temperature anisotropies map are of great interest because they directly probe the Early Universe and may show the imprints from the Inflationary Phase [24, 25, 202, 203]. Again, the production of low resolution maps without introducing spurious signals

is necessary.

The degradation of high resolution maps into low resolution maps is a not trivial procedure. There are three different methods that can be easily implemented using HEALPix tools [204].

- *Degradation*: it is the easiest way given by the average of the values of the smaller pixels of the higher resolution map that fall inside the larger pixel of the corresponding lower resolution map. This is performed by the F90 HEALPix facility `ud_grade`;
- *Noise weighting*: a more refined procedure that consists in performing a weighted average of the values in the smaller pixels taking into account the covariance matrix associated to the pixels;
- *Smoothing*: before the degradation procedure the pixels of the high resolution map are convolved with a Gaussian beam with FWHM whose typical value is few time the side of the pixel at low resolution. This is performed by the HEALPix facility `smoothing**`.

The average operation performed by the first two methods has the net effect of an under-sampling of the temperature fluctuations with larger pixels. In harmonic space, this process produces an aliasing signal. In fact, in analogy to the Nyquist theorem in the Fourier domain, the signal in the low resolution map is completely determined by the spherical harmonics up to  $\ell_{max}$  defined by Eq. 3.1. However, the original signal was determined by the spherical harmonics up to  $\ell'_{max}$  where the  $N_{side}$  is relative to the high resolution map. The aliasing effect is generated by all the spherical harmonics in the range  $\ell_{max} \leq \ell \leq \ell'_{max}$  that causes spurious correlation and thus an excess in the APS extracted by the low resolution map. The *smoothing* procedure is an easy way to alleviate this problem because it suppresses the

---

\*\*The smoothing procedure must take into account the FWHM of the original map. For example, to smooth a map from a beam with  $\sigma_1$  to  $\sigma_2$ , we must convolve the map with a Gaussian beam with  $\sigma_{appl}$  where  $\sigma_{appl} = \sqrt{\sigma_2^2 - \sigma_1^2}$

spherical harmonics with large  $\ell$  applying a beam window function,  $W_\ell$  for example defined in [205] as

$$W_\ell = e^{-\frac{1}{2}\ell(\ell+1)\sigma^2} \quad (3.20)$$

related to the FWHM of the Gaussian beam by  $\sigma = FWHM(rad)/(\sqrt{8 \ln 2})$ .

In this section we compare the three methods, described above, and take into account several smoothing convolutions with beams with different FWHM. The aim is to find the optimal approach to downgrade high resolution maps without generating artefacts.

### 3.5.1 Details of the simulation

All the considered cases comes from the degradation of a MonteCarlo of 1000 high resolution pure temperature CMB maps generated with the HEALPix facility `synfast` at  $N_{side}$  1024 and with a Gaussian beam with FWHM of 10 arc minutes. We used the WMAP 7 year Best Fit  $\Lambda$ CDM APS as input for the generation of the maps. The choice of the model is irrelevant since we are focusing only to compare the relative amount of aliasing effect generated by the methods used to downgrade the maps from the high resolution. Also, we added to these maps a realistic *Planck* noise generated as a random realization of the covariance matrix associated to the 70 GHz *nominal* mission (2 surveys).

These original maps have been downgraded to three different resolutions that is  $N_{side} = 8, 16$  and  $32$ , using 6 different methods summarized in Table 3.2. For each final resolution the maps have been:

- directly degraded using the HEALPix facility `ud_grade` (case 1 in the Table);
- degraded using a weighted average with the weight defined by the covariance matrix associated to the high resolution maps (case 2 in Table);

case	method	$N_{side} = 8$		$N_{side} = 16$		$N_{side} = 32$	
		beam	noise	beam	noise	beam	noise
		degree	$\mu K^2$	degree	$\mu K^2$	degree	$\mu K^2$
1	udgrade	-	0.25	-	1.0	-	4.0
2	noise weighted	-	0.25	-	1.0	-	4.0
3	smoothing10	7.33	0.25	3.66	1.0	1.83	4.0
4	smoothing15	10.99	0.25	5.50	1.0	2.75	4.0
5	smoothing20	14.66	0.25	7.33	1.0	3.66	4.0
6	smoothing25	18.32	0.25	9.16	1.0	4.58	4.0

Table 3.2: Details of the considered MC simulations. 1000 high resolution maps have been degraded with different methods into three low resolutions defined by the parameter  $N_{side}$ . First column "Case" is for type of simulations. Second column "method" is the name given to the different approaches to degrade the maps. Third column "beam" at  $N_{side} = 8$  is the FWHM in degree of the Gaussian beam for which the high resolution maps have been convolved before the degradation to low resolution. Fourth column "noise" at  $N_{side} = 8$  is the  $rms^2$  in  $\mu K^2$  of the white noise added to the maps after the degradation process. Fifth and sixth columns are the same of the third and fourth but at  $N_{side} = 16$ . Seventh and eighth columns are the same of the third and fourth but at  $N_{side} = 32$ .

- before the degradation they have been convolved with a Gaussian beam with FWHM respectively equal to 1.0 (case 3), 1.5 (case 4), 2.0 (case 5) and 2.5 (case 6) times the side of the pixel of the final resolution.

After this process, we added a white noise to regularize the numerics of BolPol, the APS estimator that we used in order to highlight the possible aliasing residual effect in the low resolution maps. The level of noise added depends on the resolution of the map (see Table 3.2), but it is important to underline that the sum of the added noise and the residual noise of the high resolution map is negligible in the range of multipoles taken into account in the low resolution analysis. In the end, the low resolution maps have been analysed in order to extract the APS using the optimal QML estimator [191] implemented in the BolPol code [194] described in the previous section. In this step the maps have been masked with the WMAP kq85 mask that covers

the 22% of the sky. For the aim of this study the use of a mask is irrelevant since we are analysing pure CMB maps with negligible noise. However, we decided to simulate the analysis of a realistic CMB map that could be affected by foregrounds residual along the Galactic plane, but we checked that full sky analyses give full compatible results.

### 3.5.2 Results

Fig. 3.30 shows the results of the average APS extracted from the MonteCarlo simulations at different resolution  $N_{side} = 8, 16$  and  $32$ . In Fig. 3.31 the average APS are subtracted by the WMAP 7 year best fit model that has been used to generate the high resolution maps. The less the difference between the model and the recovered APS is, the less the low resolution maps are affected by aliasing. For the degrading and noise weighting methods, the power excess is clearly visible at all the low resolutions already at  $\ell = 1.5 * N_{side}$ . At  $\ell = 2.5 * N_{side}$  the power excess is of the order of 50% for these cases compared to the real signal. Instead, in the smoothing cases, the aliasing effect is suppressed with the drawback of a larger uncertainty about the APS extracted due to the presence of a large beam, as highlighted by the larger error bars. Fig. 3.31 demonstrates that the case 5, in which the maps have been convolved with a beam of FWHM equal to twice the side of the pixel, shows the lower deviation at all the resolutions and also they decrease as the resolution increases. At  $N_{side} = 32$  the level of aliasing affecting the multipole around  $\ell = 2.6 * N_{side} = 85$  is less than 1%. Thus, we strongly recommend to apply the method described by the case 5 for a correct degradation of high resolution maps to lower resolutions.

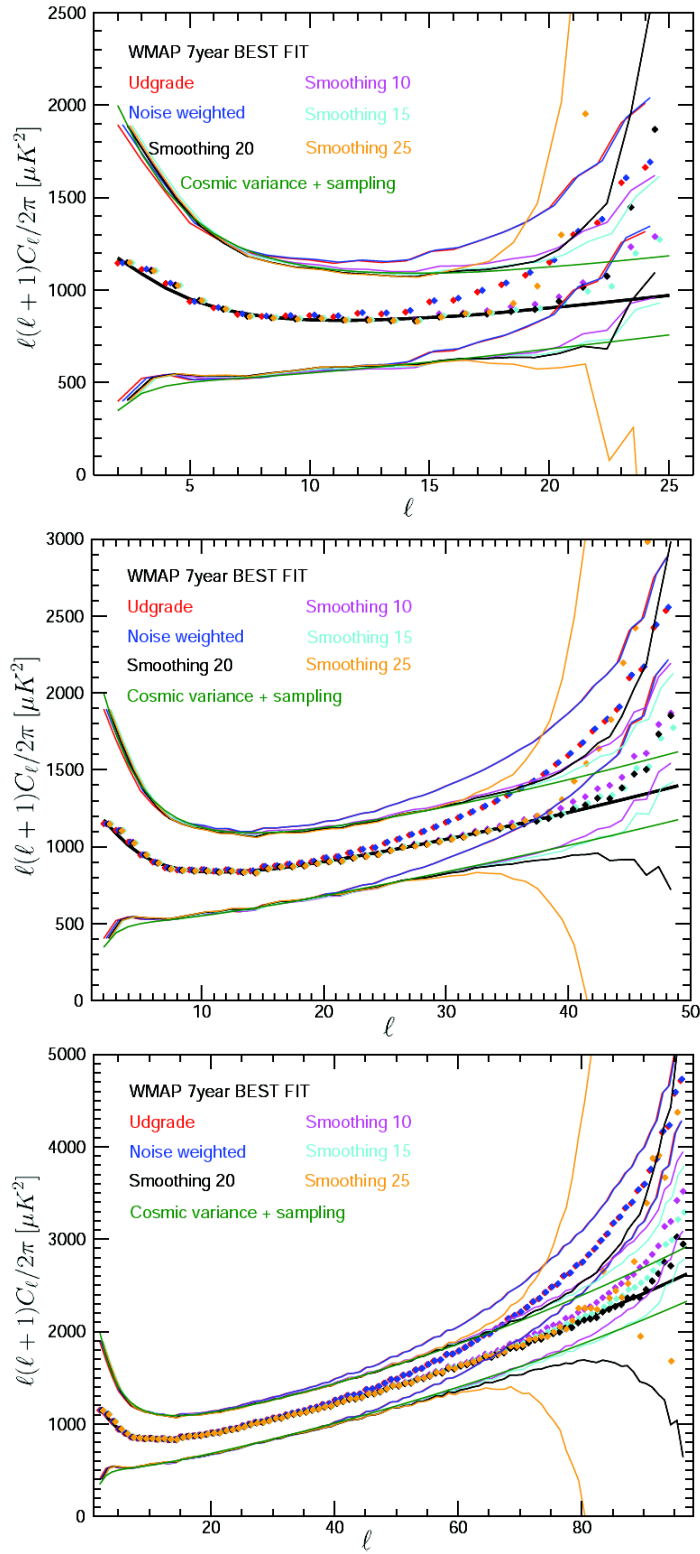


Figure 3.30: APS extracted by BolPol from the low resolution maps at  $N_{side} = 8$  (*upper panel*), 16 (*central panel*) and 32 (*lower panel*). Points have been slightly shifted in multipole in order to show all the results. See the text for comments.

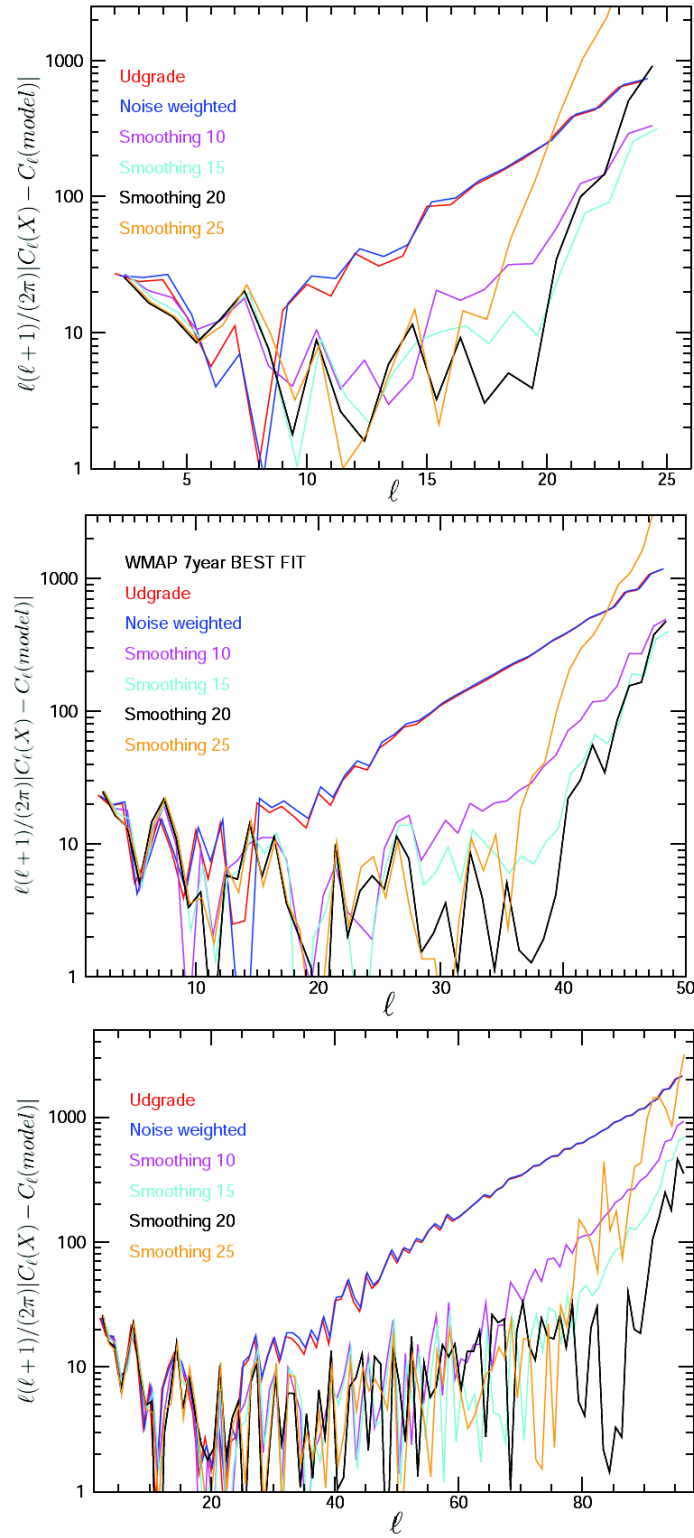


Figure 3.31: Differences between the WMAP 7 year best fit model used to generate the high resolution maps and the APS extracted by BolPol from the low resolution maps at  $N_{side} = 8$  (*upper panel*), 16 (*central panel*) and 32 (*lower panel*). See the text for comments.

# Chapter 4

## The CMB large scales analysis

The pattern of the cosmic microwave background (CMB) anisotropy field can be used to probe cosmology to high precision, as shown by the WMAP 9 years results [206] and by the very recent *Planck* cosmological results [8]. CMB data have given a significant contribution in setting up the ( $\Lambda$ CDM) cosmological concordance model. The latter establishes a set of basic quantities for which CMB observations and other cosmological and astrophysical data-sets (i.e. type Ia Supernovae and Galaxy clusters data) almost agree, as briefly described in Chapter 1 (Section 3).

In particular, the largest scales of the temperature anisotropy maps are of great interest because they directly probe the Early stages of the Universe and the most accredited models that assume an initial Inflationary Phase of its expansion [24, 25, 202, 203]. These scales correspond to angular sizes larger than the horizon at decoupling as observed today, i.e.  $\theta \gtrsim 2^\circ$  or, equivalently  $\ell \lesssim \ell_{dec} \sim 90$  (see for example [207]). They have remained largely primordial, having evolved only in amplitude since the end of the inflation. Thus, these scales are the most interesting for probing the standard cosmological model and the inflationary mechanism. In fact, many non-standard inflationary models predict observable effects on the largest scales due to their mechanisms that can cause also an either explicit or spontaneous violations of statistical isotropy [208–210].

The way in which Dark Energy affects the largest scales of the universe is directly related to its nature through the so-called integrated Sachs-Wolfe effect (ISW). Although the most straightforward explanation of the data is that Dark Energy is a cosmological constant, an alternative is dynamical Dark Energy [211–213]. This model is usually based on a scalar field that gives a contribution to the energy density of the Universe, particularly at  $z \leq 2$ , and slightly alters the CMB angular power spectrum at large scales.

The data shows that the CMB pattern is almost isotropic apart from a Doppler dipole dominated by our motion in the Universe. This result combined with the Copernican principle for which the Earth does not occupy a special place in the Universe contributed to the formulation of the so-called cosmological principle. It states that the distributions of matter and radiation in the Universe are homogeneous and isotropic at any epoch on sufficient large scales. This assumption allows to treat the CMB temperature fluctuations in different directions on the sky as multiple probes of a single statistical ensemble, leading to the precision determinations of cosmological parameters that we have today. However, although we have some observational evidence that homogeneity and isotropy are reasonably good approximations to reality, the data does not completely rule out cosmological models with non-trivial cosmic topology or anisotropic geometries. Statistical isotropy and homogeneity should be confirmed observationally, not only just assumed. These questions can only be answered observationally by looking at the large scales signal coming from the CMB. Testing these fundamental properties is crucial for the validation of the standard cosmological scenario, and has profound implications for our understanding of the physical nature of the Universe and the initial conditions of structure formation.

Recent remarkable results show that in WMAP and *Planck* CMB maps has been found a number of anomalies in the form of features of the observed sky that are not statistically consistent with the best-fit  $\Lambda$ CDM model [38, 196]. Each of these anomalies may represent different violations of the fundamental properties of isotropy and/or Gaussianity of the CMB data.

This Chapter is dedicated to describe the main results obtained from the analysis of the CMB large scales signal and few of its anomalies.

## 4.1 The origin of the large scales signal

At the LSS surface, the horizon that defines the maximum distance between regions causally connected each others corresponds to  $\ell \sim 90$ . Primordial perturbations on scales larger than the horizon evolves only because of the presence of a gravitational potential following Eq. 1.16 and, hence, they directly reflect the primordial spectrum of the perturbations. This effect is known as Sachs-Wolfe effect [28] and for a scale invariant power spectrum of the primordial density perturbations ( $n_s = 1$ ), it is demonstrated [214] that it gives:

$$\ell(\ell + 1)C_\ell = 2\pi A \quad (4.1)$$

where  $A$  is a constant and represents the amplitude of the primordial perturbations. It means that an exact scale invariance implies a flat angular power spectrum known as Sachs-Wolfe "plateau" for  $\ell \lesssim 90$ .

In the real CMB APS this plateau is only a good approximation of the signal expected at large scales. In fact, inflationary models predict a small departure from the scale invariance, which has been detected by *Planck* to be  $n_s = 0.959 \pm 0.007$  (68% Planck+WP+high- $\ell$ ) [34], that for the first time is far from unity for more than  $3 \sigma$ . This departure is responsible for a tilt in the plateau shown in Fig. 4.1\*.

Another interesting cause for a deviation from the flatness is the so-called integrated Sachs-Wolfe (ISW) effect [215–217], particularly important at very low  $\ell$ . It is a secondary anisotropy in the CMB, caused by the interaction of CMB photons with the time-evolving potentials from LSS. For cosmological models where the Universe is totally constituted by matter ( $\Omega_m = 1$ ), gravitational potentials remain constant during linear structure formation, and

---

\*<http://ned.ipac.caltech.edu/level5/March05/Scott/Scott4.html>

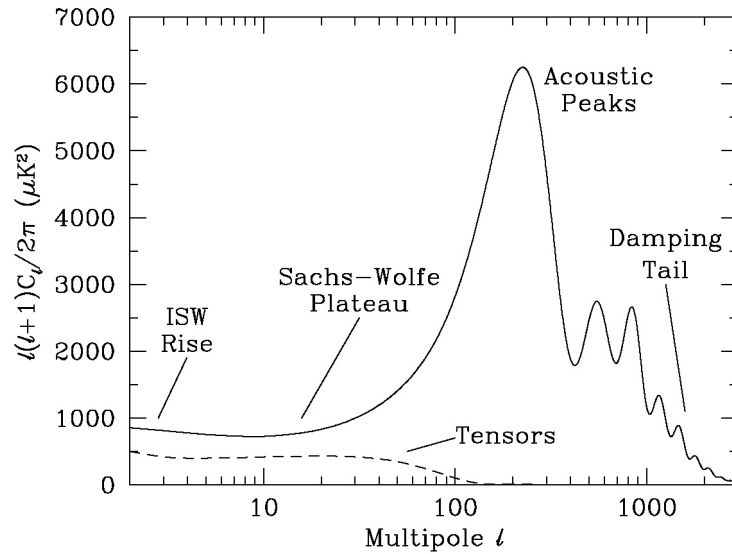


Figure 4.1: Example of a plot of the theoretical CMB anisotropy power spectrum obtained using the standard  $\Lambda$ CDM model. It can be recognised at the large scales the Sachs-Wolfe plateau and the peak due to the ISW effect.

the ISW signal to first order is negligible. In the presence of Dark Energy, decaying potentials due to the accelerated expansion rate result in a net ISW effect which is positive when the CMB photons cross overdense regions and negative when the CMB photons cross underdense regions. The dominance of the Dark Energy at low redshift makes the lowest  $\ell$  rise above the plateau as shown in Fig. 4.1. The level of increase given by the ISW effect is mainly related to the nature of the Dark Energy and to the possible presence of a non-zero curvature [218, 219]. Although different models predict different contributions at low  $\ell$ , the differences between them are buried inside the cosmic variance.

In principle, the mechanism that produces primordial perturbations would generate also tensor modes that, since they decay when entering the horizon, give a contribution mainly at large angular scales. However, this very small effect is impossible to be discriminated from other effects that might raise the level of the plateau, unless we obtain a direct measurement of the Tensor-to-Scalar ratio,  $r$ , from CMB polarization data.

## 4.2 Planck and WMAP9 results: the large scales APS

In order to test the cosmological principle assumptions and estimate the parameters of the standard cosmological model from the APS, the methodology is to build a so-called likelihood function that propagates also the uncertainties in the values of the *Planck* and WMAP maps. Since the probability distribution of the APS is not well approximated by a Gaussian at large scales as described in Chapter 3, the *Planck* analysis is based on the construction of a likelihood [177, 220] using a Gibbs sampling based approach at low multipoles (large scales) and a pseudo- $C_\ell$  technique at high multipoles (small scales) [179].

In particular, the large scales approach has been implemented by the Commander code [81] that allows both for physically motivated component separation and accurate likelihood estimation. A similar Gibbs sampling method was used to estimate the low- $\ell$  temperature likelihood for WMAP [44, 186], although not simultaneously accounting for component separation.

In this context, one of the main results of this thesis has been to assess the robustness of this method about the component separation results. This is performed through the comparisons of the APS extracted from the map cleaned with the Commander code with four alternative foreground-cleaned CMB maps. These are derived from *Planck* data with three methods (NILC, SEVEM, and SMICA [76] all presented in Chapter 3). The 9-year WMAP ILC temperature map [31] is also considered for an external test of consistency. We compute the APS from each map using Bolpol [194, 197], an implementation of the QML APS estimator presented in Chapter 3 (Section 3). Each map is smoothed to an effective resolution of  $329.81'$  FWHM, to suppress aliasing from high multipoles [204], and repixelized to  $N_{side} = 32$ . Gaussian white noise with a variance of  $4\mu K^2$  is added to each map to regularize the noise covariance matrix. Here we adopt the so-called U78 common mask, defined in [76], to exclude regions of high Galactic emission, leaving

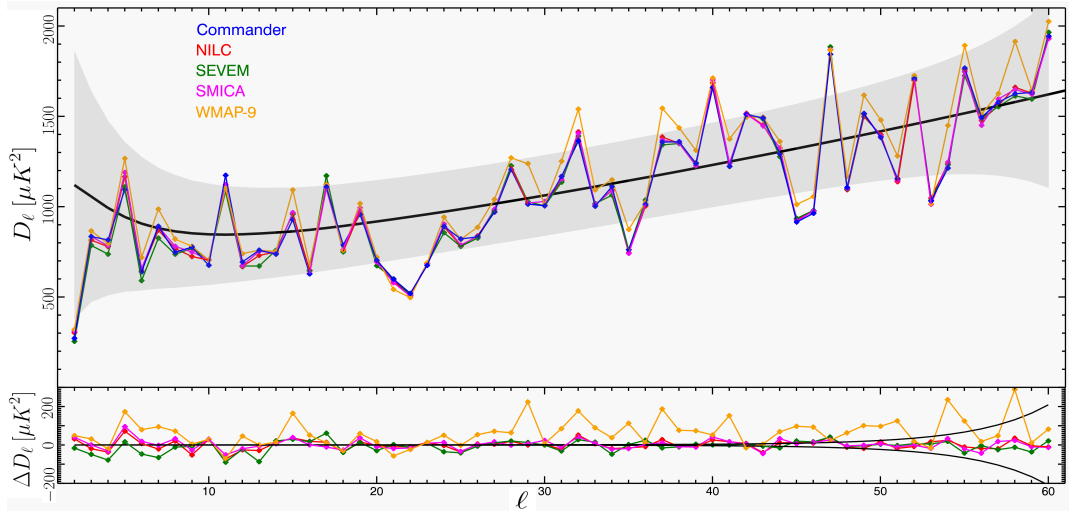


Figure 4.2: (*Top panel*) Temperature APS evaluated from downgraded *Planck* maps, with foregrounds cleaned by four different techniques (Commander, NILC, SEVEM and SMICA), and the 9-year WMAP ILC map. The APS has been estimated using the Bolpol code implementing a QML estimator. The grey shaded area indicates the  $1\sigma$  errors while the solid line shows the *Planck*  $\Lambda$ CDM best fit model. (*Bottom panel*) Differences between the APS from each algorithm and the Commander APS, computed from the spectra shown in the panel above. The black lines show the expected  $1\sigma$  uncertainty due to (regularization) noise.

78% of the sky for analysis. We remove the observed monopole and dipole in the mask.

The resulting APS up to  $\ell = 64$  are shown in the top panel of Fig. 4.2, while the bottom panel shows the power spectrum residuals for each map in comparison with the Commander map. Note that the same noise realization was added to each map, and the regularization noise therefore contributes little in this plot as shown by the black curves in the residuals plot. For the *Planck* component separated maps, the relative differences are typically  $\lesssim 50\mu K^2$  at  $\ell \geq 15$ . These results are very important because demonstrate the robustness of the foreground cleaning techniques and confirm the data internal consistency [187].

Moreover, the WMAP spectrum lies systematically above the *Planck* spectra and exhibits significantly larger residuals that are typically of the

order of  $100 \mu K^2$  at  $\ell \geq 30$ . We fit the APS with a two-parameter amplitude,  $q$ , and tilt,  $n$ , power spectrum model of the form  $C_\ell(q, n) = qC_\ell^{fid}(\ell/\ell_0)^n$  between  $\ell_{min} = 2$  and  $\ell_{max} = 30$  where the  $C_\ell^{fid}$  is the best-fit *Planck*  $\Lambda$ CDM spectrum, and  $\ell_0 = (\ell_{min} + \ell_{max})/2$ . The WMAP low- $\ell$  spectrum is 2.5-3% higher than the *Planck* spectrum and the effect is robust with respect to foreground removal and power spectrum evaluation algorithms, pointing out that this low multipoles effect is too large to be explained only by uncertainties in the *Planck* data. This effect, present even at higher multipoles, is still poorly understood and is under deep investigation in both WMAP and *Planck* data analysis teams [34, 187] and inside the cosmological community (see for example [221, 222]).

In Fig. 4.2 the black line corresponds to the *Planck* best-fit  $\Lambda$ CDM model built from the six parameters estimated using the full *Planck* likelihood (low- $\ell$  and high- $\ell$ ). Although the agreement between the observations and the best fit model is excellent at high multipoles (not shown in the figure), since the best-fit is almost exclusively determined by the small-scale spectrum, at low- $\ell$  it is clearly visible a systematic offset in the form of a slight power deficit, particularly evident in the range  $20 \leq \ell \leq 30$ . This effect has been observed also by WMAP team [38]. This apparently lack of power is only one of the so-called CMB anomalies that are discussed in the following Sections. Some of them will be examined in this chapter.

### 4.3 The large scales anomalies

While *Planck* and WMAP results probe the standard cosmological model, there are exceptions mainly located at large-angular scales, where *Planck* [196] data confirmed the presence of features consistent with various anomalies previously seen in the WMAP data [38] and even anticipated by COBE in some cases. In this Section, we briefly present several of the most important anomalies detected in the data, namely the quadrupole-octupole alignment, the low variance and the lack of large-scale power, hemispherical and dipole

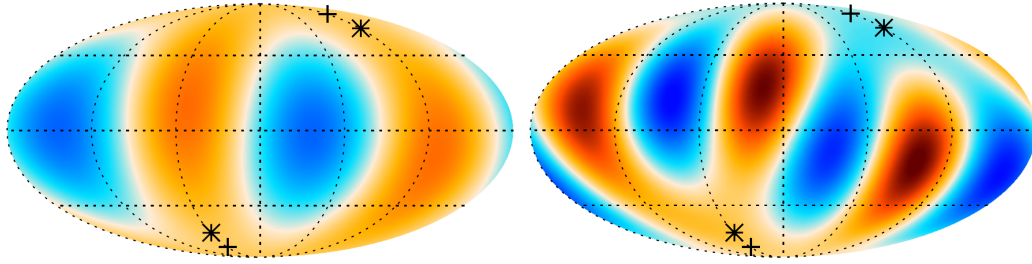


Figure 4.3: (*left*) The derived quadrupole and (*right*) the derived octupole (temperature range  $\pm 35\mu K$ ) temperature anisotropies of the *Planck* SMICA CMB map. Cross and star signs indicate axes of the quadrupole and octupole, respectively, around which the angular momentum dispersion is maximized [196].

asymmetry, parity asymmetry and the Cold Spot. Each of these anomalies may represent different violations of the fundamental properties of isotropy and/or Gaussianity of the CMB data. We will also focus on the low variance and the parity asymmetry, object of specific analyses carried out in this thesis. Finally, we discuss possible origins of these anomalies.

### Quadrupole-octupole alignment

The first indications of a significant alignment between the orientation of the quadrupole and the octupole appeared with the analysis of WMAP first year temperature data [223, 224]. The authors observed that the octupole is planar and the quadrupole and octupole planes are aligned. This alignment has been recently confirmed in the WMAP 9 year and *Planck* data. The anisotropies are shown in Fig. 4.3.

The way to study this effect goes through the analysis of the  $a_{\ell m}$  coefficients relative to the quadrupole ( $\ell = 2$  and  $-2 \leq m \leq 2$ ) and the octupole ( $\ell = 3$  and  $-3 \leq m \leq 3$ ) [38, 196] or by studying the multipole vectors that are an alternative representation of the data on a sphere [225, 226]. The results obtained from the two methods are in excellent agreement and show also that the quadrupole and octupole planes are orthogonal to the ecliptic and normal to the direction of the cosmological dipole. By analysing the four component separation maps delivered by *Planck*, it has been found that,

depending on the method, the quadrupole and octupole orientations are misaligned by an amount between  $\sim 9^\circ$  and  $13^\circ$  [196]. This is larger than the  $3^\circ$  reported recently about the 9 year WMAP ILC map [38]. However, by comparing the results with MonteCarlo simulations, the statistic probability of at least such an alignment to occur in an isotropic Universe is always below the 3%. This unlikely CMB alignment and its correlation to solar system features suggest the presence of a contamination by residual (solar system) foregrounds [227]. A possible candidate is the KBO emission [228], but the alignment can have other origins that must be investigated as will be described in Section 4.5.

### Lack of large-scale power and the low variance

In Fig. 4.2, we noticed that the APS of all the foreground cleaned maps tend to show values lower than the best-fit *Planck* APS model obtained by the estimation of the six parameters using the full *Planck* likelihood. This trend does not depend on the adopted component separation method nor in the considered *Planck* or WMAP map. This effect is known as low variance. We note that the largest contribution to this discrepancy comes from the quadrupole power that is particularly low. A lack of power at large scales has been already observed by looking at the 2-point correlation function,  $C(\theta)$ , in COBE [229] and then confirmed by WMAP [170, 199, 230] and *Planck* [196]. This lack of power is highlighted for  $\theta \geq 60^\circ$  where the measured curve lies very close to zero, away from the values expected by the  $\Lambda$ CDM model. Both the APS and the 2-point correlation function are driven by the low multipoles (mostly the quadrupole) that are particularly low with respect to the  $\Lambda$ CDM model. This apparent incompatibility between the best-fit and the low- $\ell$  APS obtained from the same data is due to the fact that the cosmological parameter fits are relatively insensitive to these low multipoles, and are instead largely dominated by scales corresponding to  $\ell > 50$ . Thus, the best-fit spectrum in the context of a 6-parameter  $\Lambda$ CDM model can have a mismatch with the data on these large scales, so that the corresponding

simulations will not adequately capture the dearth of power at low- $\ell$ . Since this region of the APS is dominated by the cosmic variance, it should be possible that the lack of power is simply an effect of the statistical realization of our single CMB map observed. By studying this effect with MonteCarlo simulations it has been demonstrated that this probability is very unlikely. To this aim, we deeply analysed the low variance anomaly as extensively discussed in the following Section.

### Hemispherical and dipole asymmetry

Since the delivery of the first year WMAP data, it was discovered that the angular power spectrum of the maps, when estimated locally at different positions on the sphere, appears not to be isotropic [231, 232]. Usually this asymmetry is distinguished between an “hemispherical” power asymmetry, in which the power spectrum is assumed to change discontinuously across a great circle on the sky, and a “dipole” power asymmetry or dipole modulation in which the CMB is assumed modulated by a smooth cosine function across the sky. Regarding the hemispherical asymmetry, the APS calculated for a hemisphere centered at  $(l, b) = (237^\circ; -20^\circ)$  (in Galactic longitude and latitude) is significantly higher than the APS calculated in the opposite hemisphere over the multipole range  $\ell = 2 - 40$ . Usually, the APS or the N-point correlation functions computed on the northern and southern hemispheres in ecliptic coordinates are compared to an ensemble of Monte Carlo simulations in a direct frequentist approach. Both in WMAP 7 year data and *Planck* data the presence of an hemispherical asymmetry is found. For WMAP [233], the statistical significance of a  $2 \leq \ell \leq 600$  hemispherical power asymmetry was quoted as 99.6%. The correlation functions for the four *Planck* maps are very consistent, and the observed behaviour is in agreement with that seen in the WMAP data [196]. For the dipole asymmetry, a simple test is usually performed. The power spectrum is computed on disks of  $22.5^\circ$  across the sky. The resulting APS is then divided into 6 independent blocks of 100 multipoles in the range  $\ell = 2 - 600$ . Finally each block is fitted for a dipolar

asymmetry in the power distribution. The resulting 6 multipole ranges considered showed evidence of a consistent dipole direction, while, from a set of thousands simulations, none showed a similarly strong asymmetry. A further extension of the analysis is to introduce a model selection procedure taking into account the statistical penalty for introducing an asymmetric model with additional parameters (direction of asymmetry, amplitude of asymmetry and asymmetric multipole ranges). Even in this case, the asymmetry was found to be highly significant for the whole range  $\ell = 2 - 600$  for both *Planck* and WMAP [38, 196].

### Parity asymmetry

The CMB sky map may be considered as the sum of even and odd parity functions, such as even and odd spherical harmonics. It is natural to assume a parity neutral Universe, and accordingly no particular parity preference in CMB sky. Thus, it has been suggested in [234, 235] that an estimator built upon the point parity symmetry might be used as a practical tool for detecting foregrounds. However, the authors claim that WMAP dataset never supports parity preference beyond the meagre 95% confidence level. Later, it has been found that the Parity symmetry in the temperature map of WMAP 3, 5 and 7 year data is highly anomalous at the level of about 0.4% up to  $\ell = 20$  [195, 198]. The asymmetry has been recently confirmed by the analysis carried out in this thesis (see also [196]). We consider the TT parity estimator,  $R(\ell_{max})$ , presented in [198] and previously introduced in Chapter 3 (Section 4):

$$R(\ell_{max}) = \frac{C_{+}^{TT}(\ell_{max})}{C_{-}^{TT}(\ell_{max})}, \quad (4.2)$$

where  $C_{+/-}^{TT}(\ell_{max})$  is

$$C_{+/-}^{TT}(\ell_{max}) \equiv \frac{1}{\ell_{tot}(+/-)} \sum_{\ell=2, \ell_{max}}^{+/-} \frac{\ell(\ell+1)}{2\pi} C_{\ell}^{TT}. \quad (4.3)$$

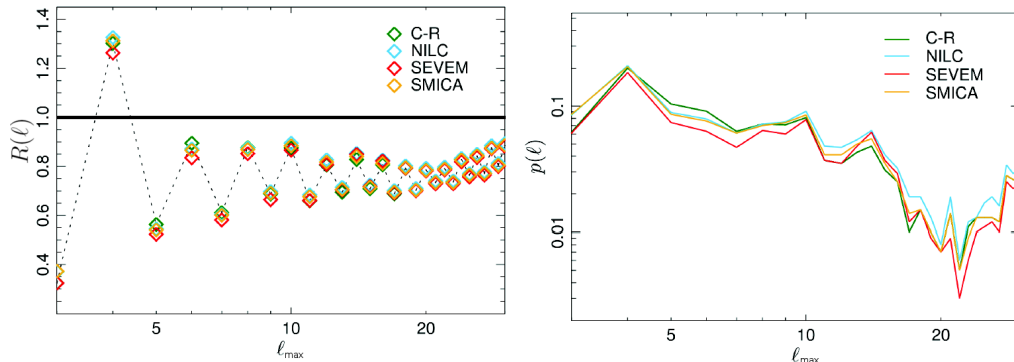


Figure 4.4: Parity estimator  $R$  (left panel) and probability  $p$  (right panel) versus  $\ell_{max}$  for the four component separated *Planck* maps: Commander-Ruler or C-R (black), NILC (red), SEVEM (blue) and SMICA (green). In the absence of parity asymmetry the points should oscillate around the value 1 in the left panel.

Here  $\ell_{tot}(+/-)$  is the total number of even (+) or odd (−) multipoles taken into account in the sum up to  $\ell_{max}$ . The ratio  $R(\ell_{max})$  is associated with the degree of parity asymmetry, where a value of  $R(\ell_{max}) < 1$  indicates odd-parity preference while  $R(\ell_{max}) > 1$  indicates even-parity preference.

Following the same approach on the WMAP data [198], we discuss the range of multipoles  $2 \leq \ell_{max} \leq 30$ , which belongs to the Sachs-Wolfe plateau of the TT power spectrum (see Eq. 4.1). Similarly to the analyses of the other anomalies, in order to make a rigorous assessment of the statistical significance of parity asymmetry at low multipoles, we compare  $R(\ell_{max})$  for the *Planck* power spectra with  $10^3$  simulated CMB maps based on the best-fit *Planck*  $\Lambda$ CDM cosmological model. We extract the APS applying a QML-estimator [194, 197] to *Planck* component separated maps at a resolution of  $N_{side} = 32$  and masked with the U73 mask presented in [76]. In Fig. 4.4 we show the parameter  $R(\ell_{max})$  for the *Planck* power spectra and the corresponding  $p$ -values. The  $p$ -value denotes the fraction of simulations in which the obtained value of  $R(\ell_{max})$  is as low as that observed in the data. Note that the results from the different *Planck* CMB maps yield consistent shapes for  $R(\ell_{max})$  and  $p(\ell_{max})$ . The parity asymmetry at  $\ell_{max} = 22$  is most anomalous, with a corresponding  $p$ -value falling in the range [0.002, 0.004].

Finally, the statistical significance of the parity asymmetry (i.e., low  $p$ -value) increases almost monotonously with  $\ell_{max}$  up to  $\ell_{max} = 22 - 25$ . Therefore, the odd parity preference cannot be simply attributed to the low quadrupole power. It is plausible that the low quadrupole power is not an isolated anomaly, but that it shares an origin with the odd parity preference (for details see [195, 198, 236]).

### Cold spot

Visual inspections of the WMAP first year ILC map revealed four elongated valleys of temperature cooler than the average. An analysis of them with the spherical Mexican hat wavelet (SMHW) on the WMAP data claimed a detection of a non-Gaussian signal on a scale of a few degrees, independent of the WMAP observing frequency [237]. The signal is a positive kurtosis (a measure of the peakedness of the distribution of a random variable and the heaviness of its tail) in the wavelet coefficients attributed to a larger than expected number of  $3^\circ$  to  $5^\circ$  cold spots in the southern Galactic hemisphere. Subsequently, the origin was attributed to a single cold spot in the sky map at Galactic coordinates ( $l = 209^\circ$ ,  $b = -57^\circ$ ) [238]. Using the data gathered by WMAP over 3 years, the statistical significance of such a large, cool region was estimated. The probability of finding a deviation at least as high in Gaussian simulations was found to be 1.85% [239], that is a  $2.35\sigma$  effect [240]. The same anomaly has been checked on the kurtosis of the coefficients corresponding to the four *Planck* CMB component separated maps. It is found that it is larger than the expected value obtained from simulations, with a modified upper tail probability of  $\simeq 0.01$  and compatible with the value obtained from WMAP [196]. In theory, cold spots in the CMB can be produced by the ISW effect as CMB photons traverse cosmic voids along the line of sight. If this Cold Spot is due to a cosmic void, it would have profound implications because  $\Lambda$ CDM does not produce voids of sufficient magnitude to explain it [241]. Other proposed explanations suggest that the cold spot could be the signature of a topological defect in the form of a cosmic tex-

ture rather than an adiabatic fluctuation [242]. Other positions are indeed more skeptical, considering that there is no sufficient statistical support to conclude that the cold spot is a CMB anomaly relative to  $\Lambda$ CDM. *Planck* polarization data will likely add the information necessary to determine the nature and the origin of this anomaly [243].

## 4.4 Low variance at large scales of WMAP 9 year data

In this section we focus on the low variance anomaly that claims an anomalous lower amplitude of the first multipoles compared to the  $\Lambda$ CDM model. We compare here the variance estimator extracted from the WMAP 9 year map with realistic MonteCarlo simulations in order to measure the statistic significance of the anomaly. The results have been recently presented in [200].

### 4.4.1 Data sets and estimators used

We use an optimal estimator (BolPol) to extract the APS from WMAP 9 yr ILC map smoothed at 9.1285 degrees and reconstructed at HEALPix resolution  $N_{side} = 16$ . In order to regularize the numerics, we added to the temperature map a random noise realization with variance of  $1\mu K^2$  as suggested in [186]. Consistently, the noise covariance matrix for TT is taken to be diagonal with variance equal to  $1\mu K^2$ . We checked also the stability of the results versus Galactic masking considering the masks shown in Fig. 4.5. More specifically, we consider the kq85 temperature mask and the extend versions of it in which the edges of the mask have been extended by 4, 8, 12, 16, 20 and 24 degrees. In table 4.1 we provide the sky fraction for each considered case and for reference we rename with the letters "a", "b", "c", "d", "e", "f" and "g" the seven cases taken into account.

In order to measure such a deviation from WMAP 9 fiducial model, we

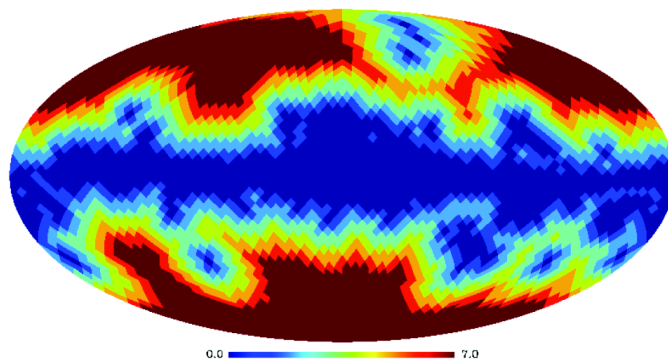


Figure 4.5: All the Galactic masks adopted for the Temperature analysis highlighted by different values on the map. Case "a" is masked where the value is 0. Case "b" is masked where the values are 1 and 0. Case "c" is masked where the values are 2, 1 and 0. Case "d" is masked where the values are 3, 2, 1 and 0. Case "e" is masked where the values are 4, 3, 2, 1 and 0. Case "f" is masked where the values are 5, 4, 3, 2, 1 and 0. Case "g" is masked where the values are 6, 5, 4, 3, 2, 1 and 0. See also table 4.1.

Case	Extension wrt kq85	Observed sky fraction
<i>a</i>	+0	0.78
<i>b</i>	+4	0.68
<i>c</i>	+8	0.56
<i>d</i>	+12	0.46
<i>e</i>	+16	0.36
<i>f</i>	+20	0.28
<i>g</i>	+24	0.22

Table 4.1: The masks used in the considered cases and their observed sky fraction. Second column describe the extension in degree of the edges of the kq85 mask (case *a*). See also figure 4.5.

consider the following expression for the Variance of the CMB fluctuations in pixel space:

$$\langle \delta T^2 \rangle = \sum_{\ell=2}^{\ell_{max}} \left( \frac{2\ell + 1}{4\pi} \right) C_{\ell}^{TT}, \quad (4.4)$$

where  $\delta T$  is the fluctuation of the temperature map. The variance estimator is applied to the APS extracted from the WMAP 9 year ILC map and compared to the results coming from 10000 "CMB plus noise" Monte-Carlo (MC) simulations, where the CMB is randomly extracted from a  $\Lambda$ CDM model and the noise is obtained through a Cholesky decomposition [244] of the noise covariance matrix. Consistently with WMAP data, also the temperature simulated maps have been smoothed at that scale, i.e. 9.1285 degrees.

#### 4.4.2 Results

In Fig. 4.6 we show the variance  $\langle \delta T^2 \rangle$  with  $\ell_{max} = 32$  for all the cases of Table 4.1. Each panel of Fig. 4.6 shows the histogram obtained with MC simulations and the vertical bar corresponds to the WMAP data. The results show that increasing the Galactic mask, the WMAP TT variance is more and more anomalous. The probabilities to obtain a value smaller than that of WMAP from random simulations are 9.87%, 2.2%, 0.4%, 0.01%,  $< 0.01\%$ <sup>†</sup>, 0.03% and 0.06% for the case "a", "b", "c", "d", "e", "f" and "g", respectively. These percentages are plotted versus the number of masked pixels in the bottom right panel of Fig. 4.6.

In Fig. 4.7 (*left panel*) we plot such a percentage for the cases "a", "c", "e" and "g" of Table 4.1 as a function of  $\ell_{max}$ . This figure makes clear that the behaviour found in Fig. 4.6 for  $\ell_{max} = 32$  is general, since it holds for every choice of  $\ell_{max}$  from 2 to 32. In particular, for the extension of 16 degrees, i.e. case "e", the temperature variance is not consistent with  $\Lambda$ CDM

---

<sup>†</sup>This value is an upper limit due to the number of MC simulations considered. No one of the 10000 simulated maps in this case showed a smaller value than that of WMAP.

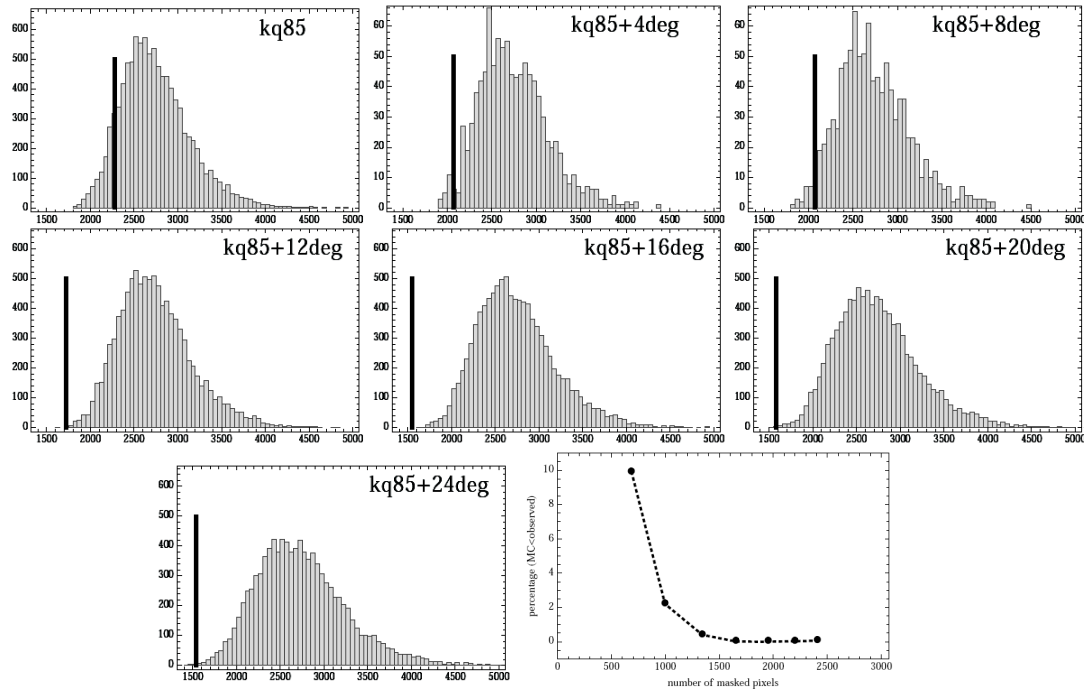


Figure 4.6: TT Variance computed with Eq. 4.4 with  $\ell_{max} = 32$  for the cases "a", "b", "c", "d", "e", "f" and "g" from top to bottom and left to right respectively. See also Table 4.1. Each panel shows counts versus  $\langle \delta T^2 \rangle$ . The vertical bars correspond to WMAP 9 year data. Histograms for "b" and "c" cases are built with  $10^3$  random extractions whereas all the other cases are built with  $10^4$  random extractions. (*bottom right panel*) Percentage of anomaly (i.e. lower tail probability) versus number of masked pixels.

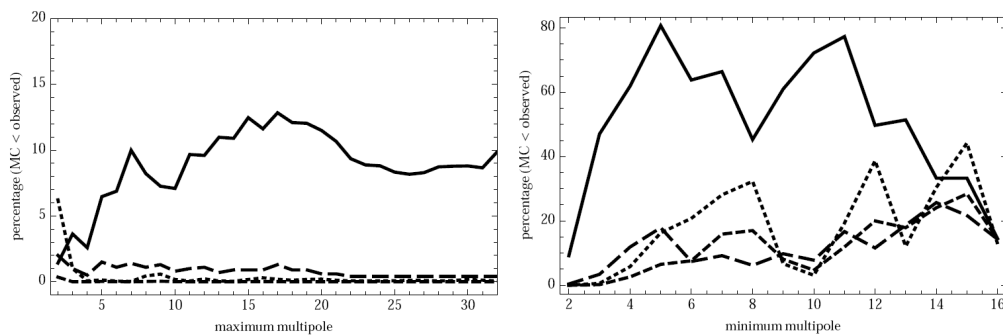


Figure 4.7: The probability for TT variance to obtain a smaller value than the WMAP one for the cases "a" (solid line), "c" (long dashed line), "e" (dashed line) and "g" (dotted line) of Table 4.1 as a function of  $\ell_{max}$  with  $\ell_{min} = 2$  (*left panel*) and as a function of  $\ell_{min}$  with  $\ell_{max} = 32$  (*right panel*).

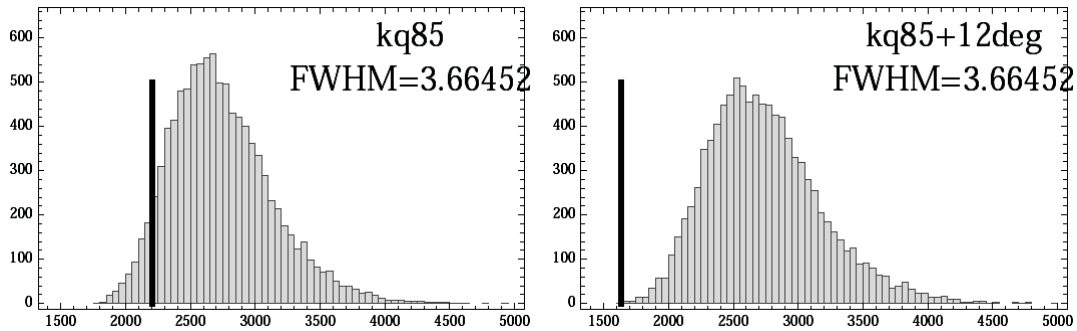


Figure 4.8: TT Variance computed with Eq. 4.4 with  $\ell_{max} = 32$  for the cases "a" and "d" from left to right respectively. Each panel shows counts versus  $\langle \delta T^2 \rangle$ . The vertical bars correspond to WMAP 9 year data of the ILC map pixellized at  $N_{side} = 16$  with smoothed to  $\text{FWHM} = 3.66453^\circ$ . The histograms are built with  $10^4$  random extractions.

model at more than 99.99% C.L. in the  $\ell_{max}$  range [25, 35].

The low amplitude of the TT variance measured for the WMAP 9 year data is dominated by the contributions from lowest multipoles. In order to show this, we plot in Fig. 4.7 (*right panel*) the probability for the TT variance to obtain a value smaller than the WMAP one for the cases "a" (solid line), "c" (long dashed line), "e" (dashed line) and "g" (dotted line) of Table 4.1 as a function of  $\ell_{min}$  with  $\ell_{max} = 32$ . Figure 4.7 (*right panel*) shows that excluding the quadrupole and the octupole the anomaly tends to disappear.

### 4.4.3 Impact of the smoothing procedure in the temperature analysis

We check here the stability of our findings against the degradation procedure of the Temperature map, needed to perform the analysis at low resolution. Specifically, we have degraded the WMAP 9 year ILC map to  $N_{side} = 16$  performing a smoothing with  $\text{FWHM} = 3.66453^\circ$  which corresponds to the angular scale of a pixel at  $N_{side} = 16$ . Thanks to  $10^4$  MC simulations we have re-computed Eq. 4.4 for cases "a" and "d" with  $\ell_{max} = 32$  (see Fig. 4.8). The probability to obtain from the random simulations a value smaller than that found for WMAP, therefore, is 5.96% and 0.01%, for the case "a"

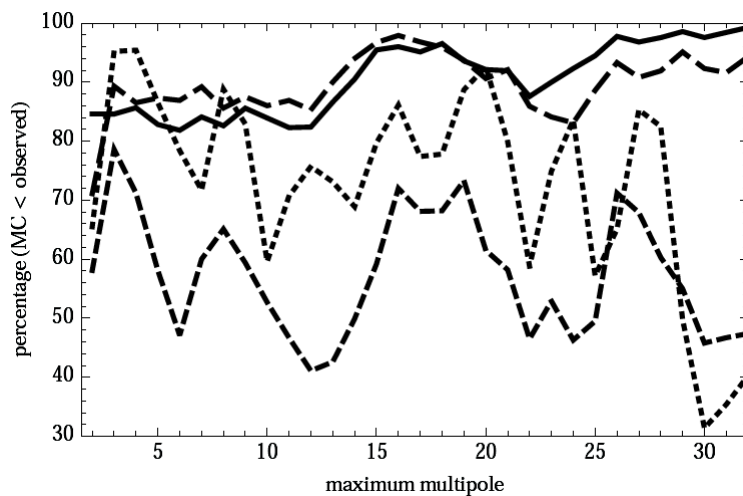


Figure 4.9: The probability for  $\langle Q^2 \rangle$  to obtain a smaller value than the WMAP one for the cases "a" (solid line), "c" (long dashed line), "e" (dashed line) and "g" (dotted line) as a function of  $\ell_{max}$ . There is no evidence for the presence of an anomaly.

and "d", respectively. Our results are proven to be stable with respect to the level of smoothing of the map.

#### 4.4.4 Polarization analysis

Similarly to the Temperature case, we can look for the presence of low variance anomaly in the CMB Polarization anisotropy. The data used are the foreground cleaned low resolution maps and the noise covariance matrix in  $(Q, U)$  publicly available at the LAMBDA website<sup>‡</sup> for the frequency channels Ka, Q and V, as considered in [31, 44] for the low  $\ell$  analysis. The maps of these frequency channels have been co-added as follows:

$$m_{tot} = C_{tot}(C_{Ka}^{-1}m_{Ka} + C_Q^{-1}m_Q + C_V^{-1}m_V), \quad (4.5)$$

where  $m_i$ ,  $C_i$  are the polarization maps and covariances (for  $i = Ka, Q$  and  $V$ ) and

<sup>‡</sup><http://lambda.gsfc.nasa.gov/>

$$C_{tot}^{-1} = C_{Ka}^{-1} + C_Q^{-1} + C_V^{-1}. \quad (4.6)$$

The masks considered are the P06 mask and its extended versions with the same cases of the Temperature. In Polarization the Variance estimator becomes:

$$\langle Q^2 \rangle = \sum_{\ell \geq 2}^{\ell_{max}} \left( \frac{2\ell + 1}{8\pi} \right) (C_\ell^{EE} + C_\ell^{BB}) \quad (4.7)$$

where  $Q$  and  $U$  are the Stokes parameters maps and also it is expected that  $\langle U^2 \rangle = \langle Q^2 \rangle$ . We have repeated for Polarization the same analysis we have performed for Temperature, finding no evident anomaly. We summarized the result in Fig. 4.9, the analogous plot for Polarization, already given in Fig. 4.7 for Temperature. Although in a regime that is noise dominated already at  $\ell \geq 10$ , it is interesting to notice that increasing the polarization mask, the percentages move towards less anomalous values in a roughly monotonic way with respect to the sky fraction.

#### 4.4.5 Discussion

By using realistic MC simulations we have found that the power of the lowest multipoles of the TT spectrum decreases as the Galactic mask increases. This indicates that the temperature anisotropies around the Galactic mask behave statistically differently from the anisotropies at high Galactic latitude. Recently *Planck* analysis of the variance for the Temperature CMB anisotropies has appeared [196]. We aim at analysing these data as well along the same lines as given here for the Temperature case since the pattern of TT APS at large angular scales is close to the WMAP 9 year data when the same mask is adopted [187]. If this anomaly has a primordial origin, the low variance would constitute a challenge to the standard  $\Lambda$ CDM cosmology emerging from a conventional inflationary expansion. Among the many possible alternatives to explain a low Sachs-Wolfe plateau, an inflationary stage short enough to solve the big bang puzzles and also disclose the preceding

stage is an interesting possibility [208, 209, 245–247]. Other possibilities are given by compact topology of the Universe: these models lead to similar effect in the Temperature maps but they also predict the existence of specific patterns like ”circles-in-the-sky” that have not been detected (see e.g. [248]).

## 4.5 Quest for an explanation to the anomalies

Understanding the origin of the CMB anomalies is clearly important. All the main anomalies presented here and others analysed in *Planck* and WMAP data are consistent with predictions of standard cosmological model only at few percent level or even less. They can be considered as statistical flukes, still compatible with the  $\Lambda$ CDM model, or as features in the sky which origin can be ascribed to four possible sources: artefacts of faulty data analysis, instrumental systematics, astrophysical foregrounds, cosmological origin [227].

The presence of foregrounds of different origins forced the analysis tools to cut the sky to avoid the presence of non CMB signals that can affect the data. The choice of the masks has been done in a conservative approach, and many different masks has been considered in the analyses. However, the large scales are recovered by considering the  $2\ell + 1$  independent modes available for each  $\ell$ . The presence of a cut sky and the use of non optimal estimators can lead to larger errors and the resulting uncertainty in the conclusions can be consistent with the presence of anomalies, but caused by artefacts in the data analysis. In this Chapter we showed that the anomalies persisted even by using optimal APS estimators (BolPol) at large scales. Moreover, we showed that by increasing the Galactic mask, the WMAP TT variance becomes more and more anomalous.

The presence of instrumental systematics could be the cause of few of the anomalies. Particular scanning strategies, or an imperfect instrument couples with dominant signal from the sky can create anomaly features. For example, the case of a non-linear instrumental response to the sky signal can lead to

a modulation of the true temperature [249]. However, both WMAP and *Planck* detectors are known to be linear to much better than 1%. Moreover, the fact that the results coming from two different missions (and, in the case of *Planck* from two different technologies) are compatible with the presence of large scale anomalies tends to exclude instrumental systematics, and their reduction through data analysis, as the source of these anomalies.

The microwave sky is manifestly non-Gaussian and anisotropic, with known contributions from Galactic astrophysical foregrounds, lensing of CMB anisotropies by the intervening matter distribution, and the ISW. However, the excellent quality of the component separation algorithms, used in *Planck* and WMAP in rejecting Galactic diffuse foregrounds, argues strongly against known Galactic emission as the source of the anomalies. On the other hand, the presence of unknown astrophysical emissions cannot be easily taken into account by the component separation tools and may affect the data. The alignment of some anomalies with the Ecliptic plane is particularly statistical unlikely. The main source of foregrounds is the Milky Way, thus one would expect that the anomalies would be aligned with Galactic foregrounds not Ecliptic ones [250]. Many authors have attempted to explain the observed quadrupole-octupole alignment in terms of a new foreground, for example the Rees-Sciama effect [251], interstellar dust [252], local voids [253], SZ effect [254], but the proposal can explain the anomalies only with severe fine tuning. Considering the Ecliptic alignment, an interesting source can be a Solar System foreground. Although *Planck* data ruled out the ZLE as possible candidate [84], the very symmetric Kuiper Belt emission in the outer solar system is still under investigation. There have been proposed simple models that suggest how the KBO emission can explain the lack of power at large scales and thus alleviate the anomalous alignment [228]. In fact, although in general at high multipoles (small scales) the presence of foregrounds statistically causes an enhancement of power in the APS due to the additional power averaged over a large number of  $a_{\ell m}$  coefficients, this statement does not hold at large scales where the number of  $a_{\ell m}$  coefficients is small. In

this range of multipoles the presence of an anticorrelation between the CMB intrinsic quadrupole and the KBO foreground emission is probable reaching the 30% of the possible events considered [228]. The anticorrelation effect can be the cause of the lack of power at very large scales, but these results depend on the emission level of the KBO foreground that is still unknown. More complex models consider also the presence of a dipole modulation in the WMAP 7 year ILC map and KBO foreground [255].

Another possibility is that the anomalies have their origin in the local Universe. The removal of the ISW signal originating within the volume at  $z < 0.3$  from WMAP data reduces the significance of the apparent alignment between the CMB quadrupole and octupole and the Cold Spot [256]. A similar correction yields an increase in the structure of the two-point correlation function for angular separations less than  $60^\circ$ , that had been noted as apparently anomalous since the first WMAP data release [257]. A future possibility is that full *Planck* data will lead to reconstruct the ISW signal and test its impact on issues related to isotropy and non-Gaussianity [258].

The most exciting possibility is that the observed anomalies have a primordial origin and potentially inform us about the conditions in the early Universe. There are many possibilities for how the absence of statistical isotropy might arise. For example, considering models with simply or multi-connected topology. In the *Planck* analysis a subset of such models and the signatures of their specific correlation structures on the sky have been considered, but no detection was found [248]. Alternately, in the early Universe, anisotropies in the distribution of the Dark Energy, such as the stress-energy tensor of Dark Energy [259], or a long-wavelength Dark Energy density mode [249] with a gradient in the desired direction could imprint the observed alignment in the ISW. However, this effect could be dominant only if the Sachs-Wolfe contribution is low or partially cancelled by the ISW. A commonly used mechanism to explain such anomalies are inflationary models that contain implicit breaking of isotropy. Models that consider a fast rolling stage in the evolution of the inflaton field [208] or various classes of

Bianchi models [260] are only two examples of a large class of possibilities. In particular, the Bianchi  $VII_h$  model shows statistical correlation with the WMAP data [261] and when the CMB sky is corrected for such a template, many of the large-scale anomalies are no longer present at a statistically significant level [196]. However, this template does not correct for the low variance anomaly. Furthermore, there are other possible explanations about the nature of the Cold Spot not only of cosmological origin but even related to possible foreground effects, for example the late evolution of the large-scale structure [253], the Sunyaev-Zeldovich effect [262], residual foregrounds [239], gravitational lensing [263], or a cosmic texture [242]. To conclude, outside of explaining the anomalies, the motivation for these anisotropic models did not convince the scientific community and are still matter of debates. The new polarization data coming from *Planck* will add new information that will help to better understand these anomalies.

# Chapter 5

## The Galactic Synchrotron emission

### 5.1 Introduction

Galactic synchrotron emission is due to cosmic ray (possibly relativistic) electrons spiralling around the lines of the Galactic magnetic field. Relativistic electrons are mainly produced by supernovae explosions. The synchrotron emission is one of the main sources of diffuse foregrounds for CMB surveys and it is the dominant one at intermediate and large angular scales ( $\theta \geq 1^\circ$ ) far from the Galactic plane at  $\nu \leq 50$  GHz. The possibility to accurately study the primordial phases of our Universe through the analysis of the CMB anisotropy field relies on our capability to precisely extract the cosmological signal from the observations [264]. The extraction goes also through an accurate removal of all the foreground signals, like the synchrotron one, for which a deep knowledge of these emissions is needed. For example, we showed in Chapter 4 that a possible solution to the presence of the anomalies in CMB maps relies in residuals of foreground emissions.

Radio surveys like the 408 MHz all-sky map have been extensively used as a template for the Galactic synchrotron emission in foreground separation models, but their analyses are also very useful to better model the

synchrotron emission and to reveal the properties of the electron density distribution and of the Galactic magnetic field. Recent detections of the Haze emission [99] and of giant magnetized outflows from the center of the Milky Way [101] pointed out the necessity of a complete exploitation of the full sky radio surveys for a better understanding of physical processes active in our Galaxy.

Radio frequencies observations at  $\nu \leq 5$  GHz provide the clearest picture of the Galactic synchrotron morphology, since the non-thermal diffuse radiation dominates there over the other components away from the Galactic plane regions. The released data suitable for studying the Galactic synchrotron in total intensity at relatively large angular scales ( $\theta \geq 1^\circ$ ) are the 408 MHz [142] and the 1.42 GHz all-sky surveys [143, 144]. These maps, already presented in Chapter 2 (Section 2), have been exploited in the past by several authors with essentially two purposes. On one hand, the 408 MHz all-sky map has been extensively used as template for the Galactic synchrotron emission in foreground separation activities [7, 145] usually extrapolated to the microwave range adopting a constant spectral index over the sky (see Eq. 2.25). On the other hand, these surveys have been exploited to find an appropriate parametrization of the synchrotron emission APS [68, 145, 146] that can be modelled by a power law over large portion of the sky (see Eq. 2.29).

In this context, this Chapter is dedicated to present some results of a new analysis of the 408 MHz and 1.42 GHz all-sky surveys, focusing on selected regions (or patches) of the sky of particular interest because of their morphology correlations, such as the Galactic spurs and loops, or their physical implications, such as regions with a particular low synchrotron emission. These regions are important in order to derive the electron density distribution and the properties of the Galactic magnetic field with the aim of adding information to generate 3D maps of the Galaxy. Moreover, CMB analyses are performed in regions where the foreground emissions are particularly low. A detailed knowledge of the properties of the foregrounds in these regions will

allow to better clean the CMB maps and to obtain more accurate results. The aim of this analysis is to better characterize the properties of the synchrotron emission and to extract information useful to a better characterization of the Galactic magnetic field and the electron density distribution.

## 5.2 The patch determination

In order to show the importance of analysing different regions of the sky separately, here, we report the results of an illustrative exercise. We estimated the temperature spectral index  $\beta_s$  of Eq. 2.25 comparing pixel by pixel the intensity of the two maps at 408 MHz and 1.42 GHz. In Chapter 2, we described the maps, their properties and the reprocessing processes applied to them in order to remove the most intense discrete sources. From these maps we could extract the frequency spectral index:

$$\beta_s = \frac{\log(T_1/T_2)}{\log(\nu_1/\nu_2)}, \quad (5.1)$$

where  $T_1$  is the temperature at the frequency  $\nu_1 = 1.42$  GHz and  $T_2$  is the temperature at  $\nu_2 = 408$  MHz. We previously smoothed the two maps to a common beam with FWHM =  $2^\circ$ . Since an accurate characterization of the noise was not possible, it is very difficult to check for the presence of possible biases in the maps of the order of the noise rms of the map. Therefore, we opted to subtract to the maps the minimum intensity emission calculated in regions where no strong local features superpose the general Galactic background. Although this exercise is not rigorous, the results shown in Fig. 5.1 are compatible with those obtained by more accurate analyses [88, 153, 265]. This simple exercise demonstrates the high spatial variability of the spectral index across the sky, showing features both in the north and in the south hemisphere even far from the Galactic plane.

In Fig. 5.1 the colours are related to the value of  $\beta_s$ , red for 3.0 and blue for  $\beta_s = 2.0$ . There is a large red feature extending from the loop 3 region (see text below) to the North Galactic pole. This is an artefact due

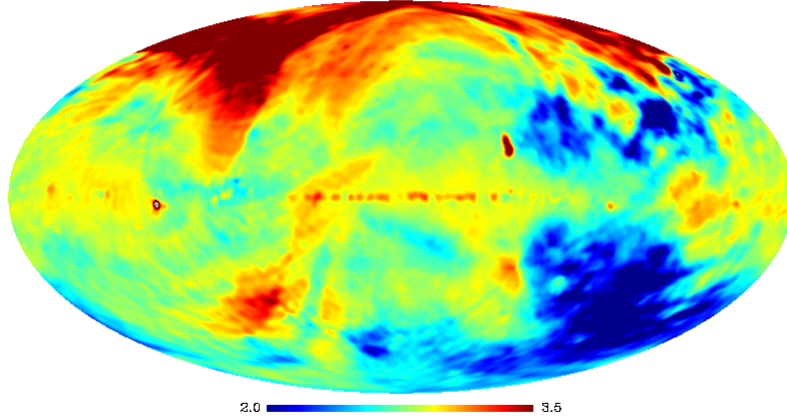


Figure 5.1: Spectral index( $\beta_s$ , see Eq. 2.25) map of the synchrotron emission estimated from the radio surveys at 408 MHz and 1.42 GHz. The large red feature with  $\beta_s > 3.5$  that extends from the loop 3 region (see text below) to the north Galactic pole, is an artefact due to the scanning strategy and beam convolution of the two surveys. We note here that the spectral index is highly variable across the sky.

to the scanning strategy and the final beam convolution used to merge the observations obtained by various telescopes into complete radio surveys. In the following analyses, in all the considered selected patches this region has been excluded. A flattening of the spectrum is observed along the Galactic plane due to the presence of free free emission, both diffuse and from HII regions that give a significant contribution to the total signal [153].

In the following, we will analyse the different regions of the sky by extracting the APS. Differently from the previous exercise, the presence of possible offsets in the data affect only the monopole, that is removed before APS estimation. Thus, this APS analysis avoids the problem of data reprocessing. As a first result, we estimated the APS from the 408 MHz map considering various Galactic masks (see Fig. 5.2 (*left panel*)). The masks are obtained by covering pixels above a certain intensity. The resulting observed sky fraction considered in the analyses are 96%, 88%, 81%, 64%, 48% 24%, respectively from the smallest to the most aggressive mask.

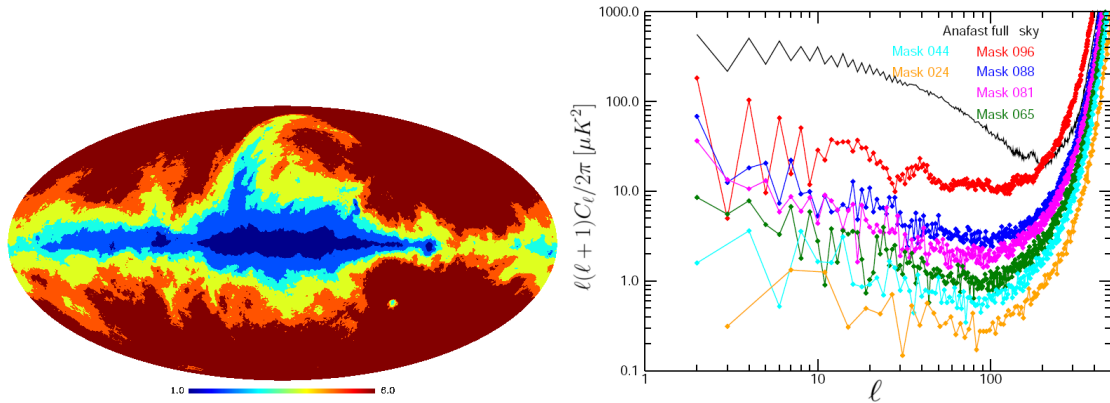


Figure 5.2: (*Left panel*) Galactic masks highlighted by different values on the map. "Mask 096" covers all the pixels associated to the reference mask values  $< 1.0$ . "Mask 088" covers all the pixels associated to values  $< 2.0$ . "Mask 081" covers all the pixels associated to values  $< 3.0$ . "Mask 065" covers all the pixels associated to values  $< 4.0$ . "Mask 044" covers all the pixels associated to values  $< 5.0$ . "Mask 024" covers all the pixels associated to values  $< 6.0$ . (*Right panel*) The APS extracted with Cromaster from the 408 MHz survey for the different masks. In black the full sky APS obtained with `anafast`.

The maps have a good signal to noise ratio, but an accurate noise characterization cannot be provided. In this case the use of an optimal but computational demanding APS extractor such as BolPol is not useful, thus, we adopted the fast and light pseudo- $C_\ell$  estimator called Cromaster described in Chapter 3 (Section 3). The APS extracted are shown in Fig. 5.2 (*right panel*) corrected for the beam, the pixel window function and the sky fraction. No noise subtraction has been applied in this analysis, since the absence of a sufficiently detailed noise determination from which extract the noise APS. However, the noise contribution is negligible for  $\ell \lesssim 150$ . For  $\ell > 200$  the combination of beam and noise causes the raising of the APS estimation that, thus, is completely unreliable. In any case, the first 150 multipoles have interesting properties. Although the APS is corrected for the sky fraction, as the masked pixels increase the APS decreases at all the multipoles. In particular, it is sufficient to cover only the 12% of the sky (the case where we used the "mask 088") to have a suppression of the APS amplitude by

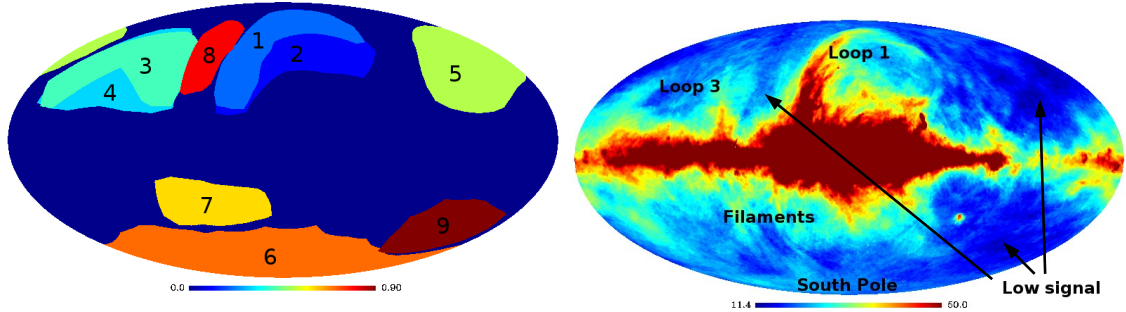


Figure 5.3: (*Left panel*) Patches selected for the analysis are numbered and highlighted with different colours. See table 5.1 for details. The patches relative to Loop 1 and Loop 3 consider only the portion of the loops that show the most important contribution to the total signal. (*Right panel*) The 408 MHz radio survey with the most intense discrete sources subtracted that has been analysed in this thesis.

about one order of magnitude. The "mask 088" covers mainly portion of the Galactic plane. Nonetheless, Fig. 5.2 (*right panel*) demonstrates that a non negligible contribution to the signal comes also from regions far from Galactic plane. The CMB anisotropy spectrum is usually estimated in these sky regions. Thus, an accurate foreground cleaning far from the Galactic plane is fundamental to derive accurate cosmological results.

In this thesis we focused the analysis to some regions (or patches) of the radio sky shown with different colours in Fig. 5.3 (*left panel*). The right panel displays the 408 MHz map, for a visual comparison of the features selected for this analysis. The various patches are also described in Table 5.1.

The large-scale loops dominate the synchrotron emission at high latitude, in particular Loop 1 of which the North Polar Spur forms the most prominent part. The origin of the loops was considered as synchrotron emission from the relativistic electrons present in supernovae remnants located close to us. Beneath the Loop 1 there is a large number of quasi-parallel ridges that has been interpreted as superimposed smaller loops. By the analysis of the polarization south sky survey at 2.3 GHz some of these structures were recently interpreted as structure in the Haze emission. Thus, even

Number (see Fig. 5.3)	Name	Region considered	Observed sky fraction
1	Loop 1 narrow	Loop 1	5.5%
2	Loop 1 broad	Loop 1	7.4%
3	Loop 3 narrow	Loop 3	5.3%
4	Loop 3 broad	Loop 3	7.6%
5	North region	Low signal	4.7%
6	South Pole	South Pole	7.6%
7	South region	Filaments	5.3%
8	Void North	Extreme low signal	1.5%
9	Void South	Extreme low signal	4.1%

Table 5.1: Names of the patches considered in the analysis, regions analysed and observed sky fraction of each patch. The patches relative to Loop 1 and Loop 3 consider only the portion of the loops that shows the most important contribution to the total signal. The numbers in the first column are related to Fig. 5.3.

the distance of Loop 1 has been put under discussion. The analysis carried out in this Chapter is part of a larger project with the aim at studying these as coherent features, looking for evidence of spectral differences (in APS as well as in spectral index) between the loops and the surrounding diffuse synchrotron emission (what we called Void North patch) in order to understand their origins. Similar to the Loop 1 there is a Loop 3 centred on the Galactic plane and at longitude  $l \sim 125^\circ$ . For these motivations, we chose a small patch (narrow) and a larger one (broad) that select the portion of the loops that show the most important contribution to the total signal looking for differences between them. As a matter of comparison we considered also what we called Void North patch as a sample of the diffuse Galactic background emission. In order to perform a comparison between regions with features of strong Galactic emission and regions where there are no particular features, we chose the patches called North Region, South pole and Void South where the signal is particular low. Moreover, we considered a region called South Region where the synchrotron emission seems to come from filaments clearly visible in Fig. 5.3 (*right panel*).

### 5.3 The Total Intensity results

The patches have been generated by considering masks that covers the whole sky apart from the selected feature. The borders of the masks have been determined by following the contours of the features on the sky. The resulting patches are shown in Fig. 5.3 (*left panel*).

Since there is not a net contour of these features, we perturbed the boundaries of each patch obtaining 5 similar patches for each region considered in the analysis. In order to assess the stability of the patch contour selection method, we compared the APS results of the similar patches of the same region. We extracted the APS of every single patch using Cromaster and by binning the multipole regime in order to regularize the kernel inversion (see Chapter 3 Section 3). The first bin of each APS takes into account also multipoles relative to angular dimensions larger than the patch itself and for this reason it has not been taken into account for the following analyses. The results are shown in Figs. 5.4 and 5.5.

In each panel there are five coloured APS corresponding to the five different realizations of the same patch. The APS are very similar confirming that the results are stable with respect to the perturbation in the construction of the patches. For multipoles  $\ell \gtrsim 200$  the steep rise of the APS is given by a combined effect of the large beam and residual noise and for this reason this part of the APS cannot be considered for astrophysical studies. We note also a flattening in the APS in the range  $100 \lesssim \ell \lesssim 200$  particularly evident in the patches relative to the loop features. This effect is due to the presence of unresolved point sources [114, 266]. The different level of point source contribution to the APS between the regions considered is well explained by the small portions of the sky considered by each patch. In fact, the possible presence or not of bright sources, just below the detection threshold, can result in different contribution levels between the different patches. Moreover, we must take into account that a bright background due to the presence of strong large scale features in the sky, such as spurs and loops, makes the point source detection more difficult. For these reasons the point source con-

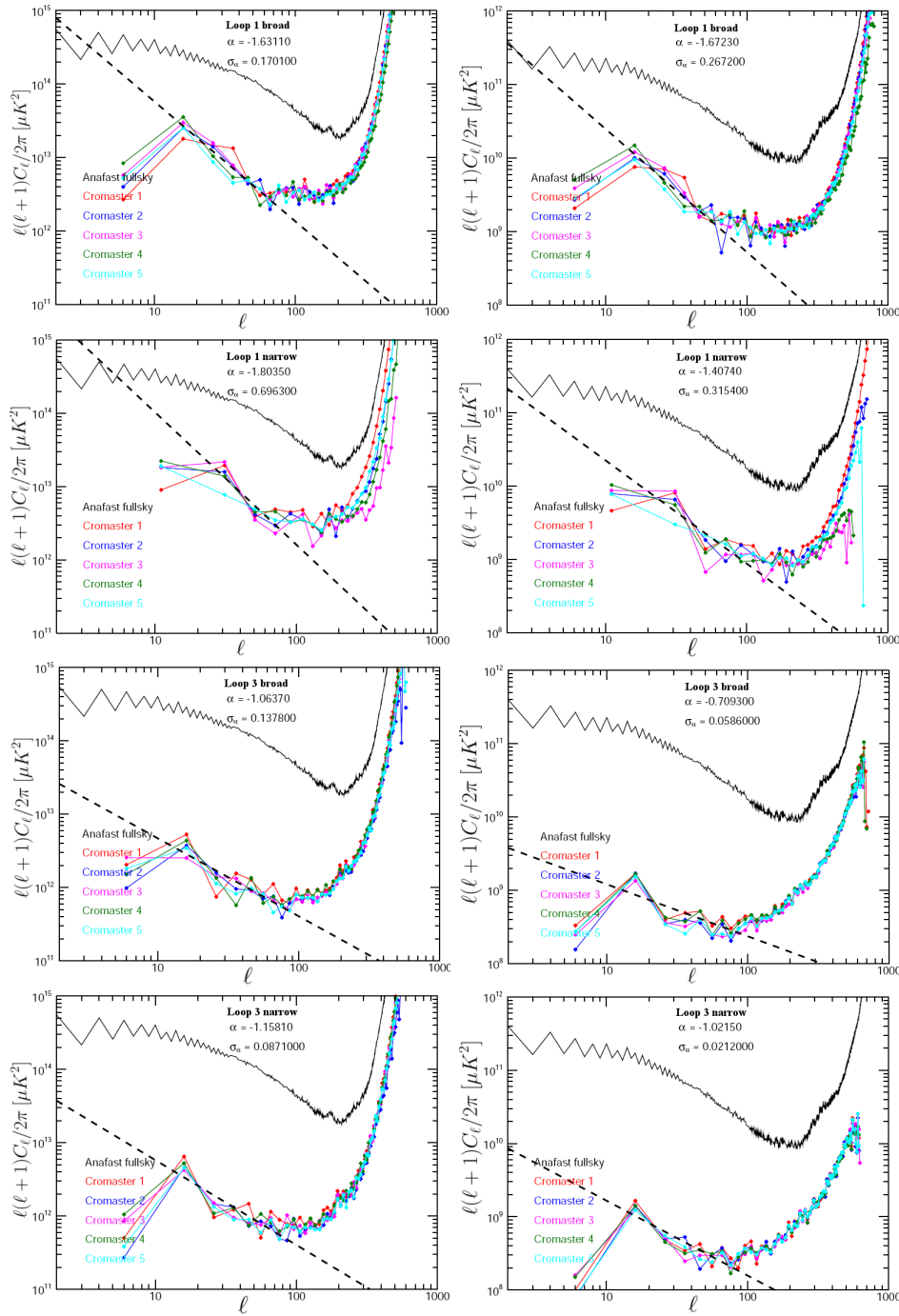


Figure 5.4: APS extracted from patches of 408 MHz (*left panels*) and 1.42 GHz (*right panels*). From top to bottom the "Loop 1 broad", "Loop 1 narrow", "Loop 3 broad" and "Loop 3 narrow" patches results. See Table 5.1 for details. For each feature analysed, we repeated the method to build the patch five times. These are represented by the five colours in each diagram. In black the full sky APS obtained using `anafast`. The dashed lines show the result of power law fit of the data.

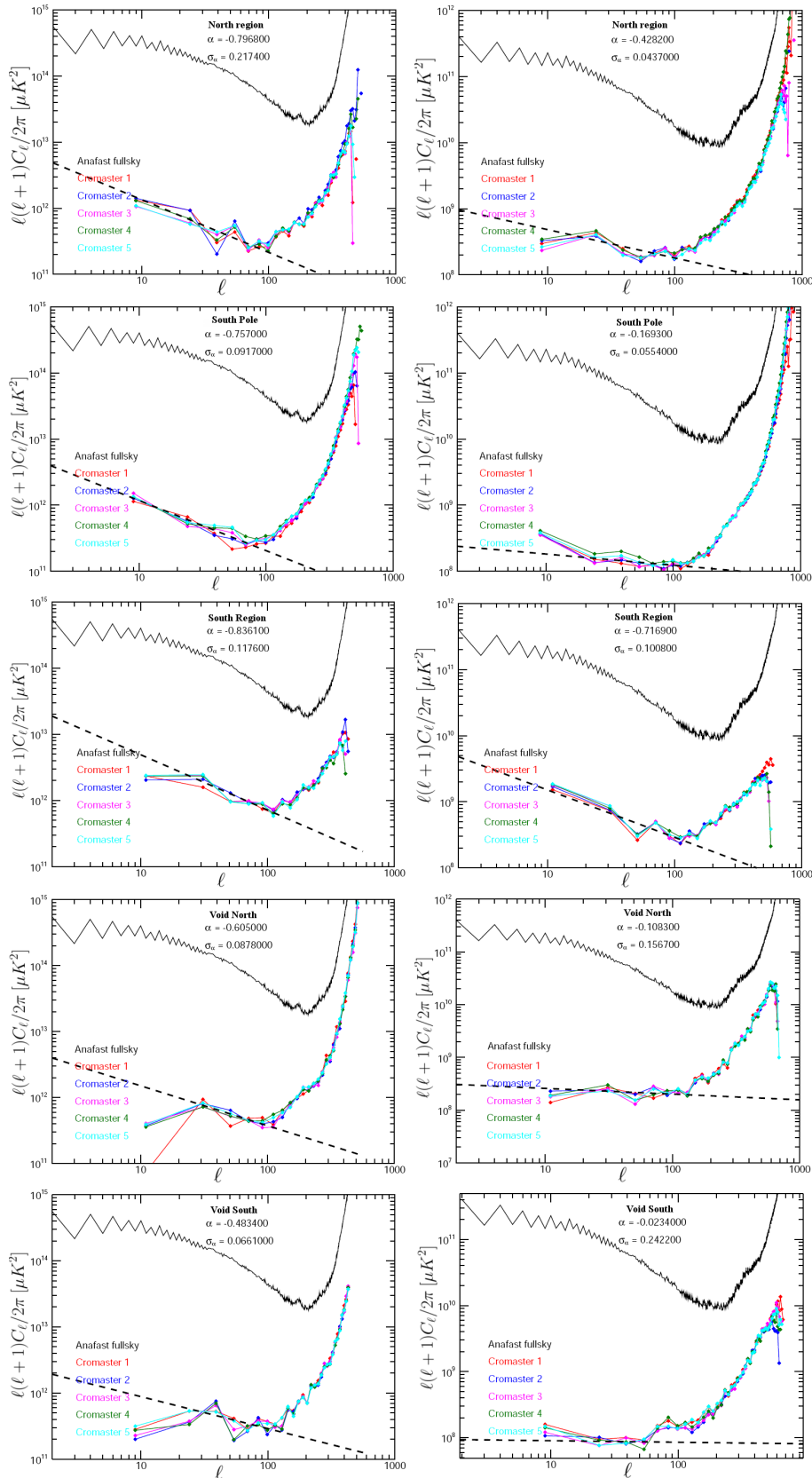


Figure 5.5: The same of Fig. 5.4, but for the "North region", "South Pole", "South region", "Void North" and "Void South" patches results from top to bottom.

tribution appears higher in the Loop 1 and 3 compared to the other regions (where the synchrotron emission is lower).

The APS for each patch at multipoles  $\ell \lesssim 100$  shows a power law behaviour. As described in Chapter 2 (Section 2), this can be explained by invoking a turbulent Galactic magnetic field following a Kolmogorov-type spectrum. Following the parametrization given by Eq. 2.29, we determined the APS spectral index  $\alpha$  and amplitude  $K$ . In Table 5.2 we quote the spectral indices  $\alpha$ , the error in their determination  $\sigma_\alpha$  and the APS amplitudes  $K_{100}$  calculated at  $\ell = 100$ , corresponding to angular scales of  $\sim 2^\circ$ . This analysis shows the great variability between the various patches of the same map and also between the same patch of the two maps. Inside the same map, the patches that select the most important synchrotron emission features (the loops) show the higher steepness. The slope flattens in the other regions where the synchrotron emission is lower. We note, also, that the different power law behaviour between the same patch of the two maps is always lower than  $2\sigma$ , except for the patches that show the lower synchrotron emission (South Pole, Void North and Void South) where the differences are larger than  $3\sigma$ . In all the cases, the deviations can be due to the differences in the noise level and in the contribution of unresolved point sources between the two maps. In fact, both these emission sources tend to flatten the synchrotron APS and this effect is relatively more important in those regions where the synchrotron emission is lower. This can explain the more than  $3\sigma$  differences. We need new maps with higher resolution and sensitivity and with a more treatable noise to significantly reduce these sources of uncertainty.

In the previous section, as an illustrative exercise, we used the pixel intensities of the maps to recover pixel by pixel the frequency spectral index of the synchrotron emission. Here, we perform a more rigorous analysis using the APS extracted from the patches and compare the frequency spectral index multipole by multipole for different regions of the sky. Following the Eqs. 2.25 and 5.1, we can derive the same relation using the APS:

Patch	408 MHz			1.42 GHz		
	$\alpha$	$\sigma_\alpha$	$K_{100}(K^2)$	$\alpha$	$\sigma_\alpha$	$K_{100}(mK^2)$
Loop 1 broad	-1.6311	0.1701	1.3503	-1.6723	0.2672	526.670
Loop 1 narrow	-1.8035	0.6963	1.6170	-1.4074	0.3154	873.915
Loop 3 broad	-1.0637	0.1378	0.4056	-0.7093	0.0586	236.241
Loop 3 narrow	-1.1581	0.0871	0.4031	-1.0215	0.0212	157.972
North region	-0.7968	0.2174	0.2143	-0.4282	0.0437	180.020
South Pole	-0.7570	0.0917	0.2051	-0.1693	0.0554	123.537
South region	-0.8361	0.1176	0.7168	-0.7169	0.1008	290.573
Void North	-0.6050	0.0878	0.3740	-0.1083	0.1567	184.473
Void South	-0.4834	0.0661	0.2900	-0.0234	0.2422	85.5447

Table 5.2: Results from the power law fit of the APS for each patch at the two considered frequencies. Following Eq. 2.29, for each patch of the two maps we report the spectral index  $\alpha$ , the error in its determination  $\sigma_\alpha$  and the amplitude  $K_{100}$  calculated at  $\ell = 100$ .

$$\beta_s = \frac{\log(C_\ell(1)/C_\ell(2))}{\log((\nu_1/\nu_2)^2)}, \quad (5.2)$$

where  $C_\ell(1)$  and  $C_\ell(2)$  are the APS respectively for the 1.42 GHz and 408 MHz maps. The frequencies are squared because we are considering the APS in which the physical dimensions are the squared pixel intensity (or temperature). We applied this process to the APS extracted from all the patches. The results are shown in Fig. 5.6. In the figure, the different patches have different colours. The shaded region determines  $1\sigma$  uncertainty on the APS extracted. In order to avoid confusion but still give an idea of the error bars of the results, we displayed the  $1\sigma$  level to the theoretical value of  $\beta_s \sim 3.0$  represented by the black line. Figure 5.6 shows a good agreement with the previous results at the multipoles  $\ell \lesssim 100$  [40, 76, 96, 136]. However, the results seem to prefer a slightly higher spectral index, around 3.2. Moreover, a slight scatter is shown between the APS of different regions and even inside the same APS along the multipole range.

This result, combined with the APS analysis and the frequency spectral

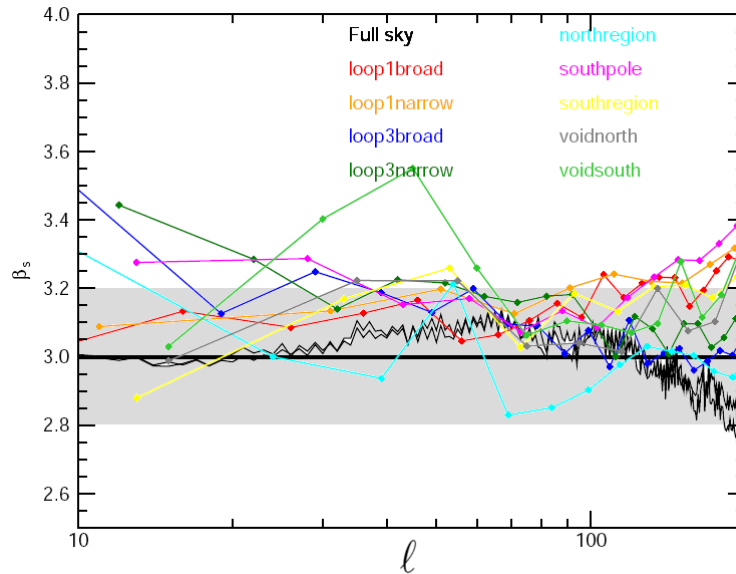


Figure 5.6: Frequency spectral index ( $\beta_s$ ) of the synchrotron emission APS as function of the multipole. Different colours are related to the different patches analysed. Thick black line represent the value of  $\beta_s = 3.0$ . Thin black lines represent the full sky analysis. Shaded region represent  $1 \sigma$  level of uncertainty in the recovery of the APS.

index obtained from the pixels intensities, advice against the use of a unique spectral index for the whole radio map when we use it as a synchrotron template in the component separation tools dedicated to the CMB analysis. These results are useful in order to have more accurate and detailed component separation tools and to better clean the foregrounds of the microwave maps obtained by *Planck* and WMAP.

At the same time the APS results and their (power law) behaviours give new information about the properties of the synchrotron emission features such as the loops and the spurs. However, these data are not sufficient to have a precise analysis of these features for which we need higher resolution and sensitivity maps and with a more treatable noise.

Future steps of this analysis will exploit theoretical results from tools like Hammurabi and Galprop, described in Chapter 2 (Section 2). These tools generate radio maps starting from the electron density and the Galactic magnetic field distribution. The synthetic radio maps obtained will be compared

with the observations both in pixel intensity (temperature and polarization) and in the APS behaviour for the single features and the whole sky. This analysis will give us a better knowledge of the possible distribution of the electron density and of the direction and intensity of the Galactic magnetic field on large and small scales [267–269] and will allow to understand the nature of the synchrotron emission process and determine its properties. One remarkable example is the solution of the debate about the Galactic position of the electron distributions that produce the loops, discriminating if they are inside supernovae remnants relatively close to us or in spurs emitted by the Galactic center.

## Chapter 6

# Future observation: the development of new devices

*Planck* polarization data will be published in 2014 and will achieve great results in cosmology and astrophysics [171]. Its temperature data already confirmed that the Universe is well described by the standard cosmological model with an Inflationary phase at the beginning of its existence [34]. Polarization data are necessary to directly measure the amplitude  $A_S$  and the scalar spectral index,  $n_S$ , of the primordial scalar perturbations and to detect the B-modes that will reveal the exact value of the Tensor-to-Scalar ratio,  $r$  that is directly related to the energetic scale of the Inflation. Also Inflation should have generated a bath of primordial gravitational waves (tensor perturbations of the spacetime), which can be characterized by an amplitude,  $A_T$ , and the tensor spectral index  $n_T$  in analogy to the scalar spectral index. These measurements will directly probe the physics of the early Universe and shed a light on the mechanism of the Inflation.

Thanks to the *Planck* data, cosmologists will test many different inflation models, but even a forecast *Planck* limit  $r < 0.05$  [45] would leave many interesting models unprobed. Given that the stochastic background of gravity waves is the smoking gun of Inflation, it is crucial to map as accurately as possible the CMB polarization and in particular characterize the BB angular

power spectrum. With this aim a large number of projects are in development (see Section 1.5 for more details) that are looking for new devices that can collect, manipulate and absorb the CMB polarized photons with unprecedented precisions. In this context, this Chapter is dedicated to present a new device for the polarization splitter based on the technology of the Photonic Crystals [270] that can be used for cosmological and astrophysical observations in future experiments and satellite missions.

In the last decades great efforts of the research activities have been focused on photonic devices with the ability of confine, manipulate and carry the electromagnetic field on scales comparable to the dimensions of the electrical devices, that for optical frequencies are of the order of nanometers. The aim of this research was to substitute the electrons with the photons as carriers of information obtaining higher velocity in the data transport and consequently achieving higher computational power of computers [271,272]. Moreover, this technology would be useful for the development of new receivers smaller and more precise for a new generation of scientific instruments.

In these research activities there have been developed various devices working by exploiting different properties of the photons: metallic waveguides, metallic cavities, dielectric mirrors and photonic crystals. Metallic waveguides [273,274] and cavities make use of the TIR effect [275] for which the incident light is reflected by a separation surface between two different media (usually the air or others dielectric media inside a metallic tube). This effect is used to generate electromagnetic waveguides. A great limitation of these devices is the high absorption. Instead, dielectric mirrors [276,277] are made of glass dishes covered by a thin layer of dielectric material that allows almost perfect reflection of certain frequencies. These instruments do not completely resolve the absorption problem and they have a limitation given by the narrow band of frequencies, that are not the same for the two polarizations of the signal. Moreover they work only in one dimension.

Photonic crystals (PC) [278–280] are a possible solution to these problems. In fact, by solving the Maxwell's equations it has been shown that

they can generate complete photonic band gaps even in 3 dimensions, an important ingredient to minimize the absorptions and to manipulate the electromagnetic field.

## 6.1 Photonic Crystals

An ideal crystal can be seen as a regular repetition of a basic building block, filling all the space covered by the crystal. This block is called *unit cell* and can be repeated in one, two or three dimensions to generate one, two or three dimensional PCs. We can define an grid in which any point is associated to the unit cell. This grid is called *space lattice*. Each point of the lattice is defined by three translation vectors  $\mathbf{a}_1$ ,  $\mathbf{a}_2$  and  $\mathbf{a}_3$ . The periodicity of the crystal is guaranteed if the lattice is identical when it is seen from a point  $\mathbf{r}$  and from a point  $\mathbf{r}'$  given by:

$$\mathbf{r}' = \mathbf{r} + m_1\mathbf{a}_1 + m_2\mathbf{a}_2 + m_3\mathbf{a}_3 = \mathbf{r} + \mathbf{R}, \quad (6.1)$$

where  $m_1$ ,  $m_2$  and  $m_3$  are arbitrary integer numbers. All the translation vectors  $\mathbf{R}$  that relate two general points  $\mathbf{r}$  and  $\mathbf{r}'$  of the lattice are called *lattice vectors*. This property implies that any arbitrary point in the crystal structure can be considered identical to a corresponding point within a chosen unit cell, differing only by a lattice vector. In a PC the dielectric permittivity  $\varepsilon$  is a periodic property and this periodicity alters the motion of an electromagnetic wave inside the crystal. This means that in order to understand the properties of this motion it will be sufficient to study it only in the points inside the unit cell.

Inside a crystal it can be found a large number of fundamental translation vectors, but only few of them can be called *primitive translation vectors*. Any set of translation vectors  $\mathbf{a}_1, \mathbf{a}_2, \mathbf{a}_3$  is said to be primitive if any two lattice points  $\mathbf{r}$  and  $\mathbf{r}'$  can be connected by a suitable choice of integers  $m_1, m_2, m_3$  as shown in Eq. 6.1. The three primitive translation vectors define the volume of the smallest unit cell that can be found in the crystal. Its volume results



Figure 6.1: (*left*) Example of a 2D triangular lattice. (*right*) Examples of unit cells and primitive translation vectors that can be identified inside this lattice.

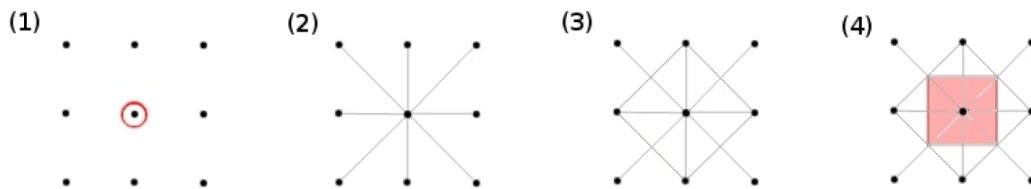


Figure 6.2: Explanatory process to determine a Wigner-Seitz cell starting from the points of a square lattice. Once shape and dimensions are determined, it can be translated and centered on any point of the lattice.

to be:

$$V = |\mathbf{a}_1 \cdot \mathbf{a}_2 \times \mathbf{a}_3|. \quad (6.2)$$

At the same time, the unit cell is not unique, even if it is built starting from the same primitive translation vectors. An example is shown in Fig. 6.1 in which for the same triangular lattice there can be found two different sets of primitive vectors and unit cells.

There is a systematic method to determine a primitive cell for a given lattice. The steps are graphically described in Fig. 6.2.

- 1 A lattice point is chosen to be the origin point and will be the center of the unit cell;
- 2 Connect the origin point to the nearest lattice points by straight lines;

- 3 Perpendicular lines are drawn passing through the midpoints of the previous straight lines;
- 4 The region delimited by the intersecting perpendiculars is the Wigner-Seitz cell.

The Wigner-Seitz cell encloses all the points inside the unit cell and also identify the symmetries of the lattice that are at the basis of the PC analysis. These primitive cells are called Wigner-Seitz cells. The most used basic 2D lattice structures are:

- *Square lattice* in which the two primitive vectors have the same length ( $|\mathbf{a}_1| = |\mathbf{a}_2|$ ) and are perpendicular each other ( $\mathbf{a}_1 \perp \mathbf{a}_2$ );
- *Rectangular lattice* similar to the quadratic one, but with the vectors of different length ( $|\mathbf{a}_1| \neq |\mathbf{a}_2|$ );
- *Triangular lattice* when the primitive vectors have same length and are divided by an angle multiple of 60 degrees ( $\angle \mathbf{a}_1, \mathbf{a}_2 = (3n \pm 1)\pi/3$ );
- *Oblique lattice* when there are not symmetries.

### 6.1.1 The reciprocal lattice and the Brillouin zone

As the periodicity of the lattice has been defined in real space, we can proceed in the same way in the Fourier space and define a reciprocal lattice related to the periodic lattice of the real space. The reciprocal lattice is also periodic and in analogy to Eq. 6.1, it must satisfy:

$$\mathbf{r}' = \mathbf{r} + n_1 \mathbf{g}_1 + n_2 \mathbf{g}_2 + n_3 \mathbf{g}_3 = \mathbf{r} + \mathbf{G}, \quad (6.3)$$

in which we defined the fundamental vectors of the reciprocal lattice ( $\mathbf{g}_1, \mathbf{g}_2, \mathbf{g}_3$ ) and the lattice vector  $\mathbf{G}$ . This vector can be directly related to the lattice vector  $\mathbf{R}$  of the real lattice simply considering the Fourier decomposition of the periodic dielectric permittivity  $\varepsilon$  of the lattice:

$$\varepsilon(\mathbf{r}) = \sum_{\mathbf{G}} \varepsilon(\mathbf{G}) e^{i\mathbf{G}\cdot\mathbf{r}}. \quad (6.4)$$

Since the expansion must preserve the periodicity of the crystal, we must constrain the  $\mathbf{G}$  vector imposing that

$$\varepsilon(\mathbf{r} + \mathbf{R}) = \sum_{\mathbf{G}} \varepsilon(\mathbf{G}) e^{i\mathbf{G}\cdot\mathbf{r}} e^{i\mathbf{G}\cdot\mathbf{R}} = \varepsilon(\mathbf{r}). \quad (6.5)$$

This condition is verified only if  $e^{i\mathbf{G}\cdot\mathbf{R}} = 1$  from which it follows that  $\mathbf{G} \cdot \mathbf{R} = 2\pi m$  where  $m$  is an integer. Once that the vector  $\mathbf{R}$  has been defined, the vector  $\mathbf{G}$  is determined following the condition:

$$\mathbf{g}_i \cdot \mathbf{a}_j = 2\pi\delta_{ij} \quad (6.6)$$

where  $\mathbf{g}_1$ ,  $\mathbf{g}_2$  and  $\mathbf{g}_3$  are the translation vectors of the reciprocal lattice. In fact, any lattice in the real space, with volume  $V$ , has its equivalent reciprocal lattice in the Fourier space with volume  $(2\pi)^3/V$ . As in the real lattice, we can define a Wigner-Seitz cell of the reciprocal lattice. This unit cell is known as first Brillouin zone, after Leon Brillouin who developed the concept [281]. The center of the zone is usually indicated by the letter  $\Gamma$  while the corner of important symmetry points are labeled with capital alphabetic letters according to a precise convention. Following the symmetric properties of the Brillouin zone (translation, rotation and spatial inversion) occurring when we consider waves propagating inside the periodic lattice of a crystal, inside the zone can be determined a so-called irreducible Brillouin zone, at the basis of the behaviour description of the motion of these waves. In fact, for the properties of periodicity and symmetry of the lattice, it is sufficient to solve the Maxwell's equations only inside the points enclosed by the irreducible Brillouin zone in order to characterize the behaviour of the electromagnetic waves inside the entire lattice because any point outside the irreducible Brillouin zone can be linked to a precise point inside it.

### 6.1.2 Waves in a periodic medium

In order to describe an electromagnetic wave propagating inside a lattice with a frequency  $\omega$ , we need to solve the Maxwell's equations. With the reasonable assumption that inside the PCs there are not free charges or electric currents the Maxwell's equations for the electric  $\mathbf{E}$  and magnetic  $\mathbf{H}$  field can be written as:

$$\begin{aligned}\nabla \times \mathbf{H}(\mathbf{r}) &= j\omega\varepsilon(\mathbf{r})\mathbf{E}(\mathbf{r}) \\ \nabla \times \mathbf{E}(\mathbf{r}) &= -j\omega\mu_0\mathbf{H}(\mathbf{r}) \\ \nabla \cdot \mathbf{H}(\mathbf{r}) &= 0 \\ \nabla \cdot [\varepsilon(\mathbf{r}) \cdot \mathbf{E}(\mathbf{r})] &= 0\end{aligned}\tag{6.7}$$

where we consider the periodicity of the electric permittivity  $\varepsilon(\mathbf{r}) = \varepsilon(\mathbf{r} + \mathbf{R})$  and that PCs are usually non-magnetic materials for which the magnetic permeability is constant  $\mu(\mathbf{r}) = \mu_0$ . The first two equations of 6.7 are invariant for translations, that is for the replacement of  $\mathbf{r}$  with  $(\mathbf{r} + \mathbf{R})$ . Moreover, by taking the curl of the second equation of 6.7 and using the first equation for eliminate the magnetic field we obtain:

$$\nabla \times [\nabla \times \mathbf{E}(\mathbf{r})] = \omega^2\mu_0\varepsilon(\mathbf{r})\mathbf{E}(\mathbf{r}).\tag{6.8}$$

In the same way we can eliminate the electric field from the first equation fo 6.7 obtaining:

$$\nabla \times \left[ \frac{1}{\varepsilon(\mathbf{r})} \nabla \times \mathbf{H}(\mathbf{r}) \right] = \omega^2\mu_0\mathbf{H}(\mathbf{r}).\tag{6.9}$$

Eq. 6.8 and 6.9 describe the properties of the electric and magnetic field inside the PC whose properties are considered in the dielectric permittivity  $\varepsilon(\mathbf{r})$ . These are eigenvalue equations and it can be demonstrated that the solutions are described by eigenvectors that are plane waves:

$$\begin{aligned}\tilde{\mathbf{E}} &= \mathbf{E}_k(\mathbf{r})e^{-i\mathbf{k}\cdot\mathbf{r}} \\ \tilde{\mathbf{H}} &= \mathbf{H}_k(\mathbf{r})e^{-i\mathbf{k}\cdot\mathbf{r}}\end{aligned}\tag{6.10}$$

with the amplitudes  $\mathbf{E}_k(\mathbf{r})$  and  $\mathbf{H}_k(\mathbf{r})$  periodic with the periodicity of the PC:

$$\begin{aligned}\mathbf{E}_k(\mathbf{r}) &= \mathbf{E}_k(\mathbf{r} + \mathbf{R}) \\ \mathbf{H}_k(\mathbf{r}) &= \mathbf{H}_k(\mathbf{r} + \mathbf{R})\end{aligned}\tag{6.11}$$

where  $k$  is known as the Bloch wave vector and it can assume the values described by the boundaries of the irreducible Brillouin zone. The corresponding eigenvalues  $\omega_k$  describe the frequency of the solutions. This result is known as Bloch theorem [282] and this kind of solutions are called Bloch waves. Thus, in a periodic media, an arbitrary solution to the Maxwell's equations can be expressed as superposition of Bloch waves independent on each other. Also, the velocity group,  $\mathbf{v}_g$ , that describes the propagation of the total electromagnetic field is demonstrated to be

$$\mathbf{v}_g(\mathbf{k}_0) = \nabla_k \omega|_{\mathbf{k}=\mathbf{k}_0}\tag{6.12}$$

where  $k_0$  is the wave vector of the Bloch wave.

For any given  $k$  we have a discrete set of eigenvalues  $\omega_k$ . Usually the eigenvalues are sorted following an order of increasing frequency. The enumerated frequencies are labelled by a counting index  $n$ . and are denoted by  $\omega_{nk}$ . All the solutions with a common counting index  $n$  are collectively called *photonic band*. We can build a graph with all the possible solutions up to a certain value of  $n$ . This graph with  $\omega$  versus  $k$  is called dispersion diagram or *band diagram*. An example of band diagram is shown in Fig. 6.3 for an 1D PC composed by two layers of dielectrics media, alternatively air ( $\varepsilon = 1$ ) and silicon ( $\varepsilon = 12$ ).

In the 1D case the x-axis is described by the unique direction of periodicity of the PC. In 2D there are more important directions described by the points in the irreducible Brillouin zone. In that case the x-axis will be divided in as many subdivisions as the number of points in the Brillouin zone. In Fig. 6.3 blue lines define the photonic bands, solutions of the Maxwell's

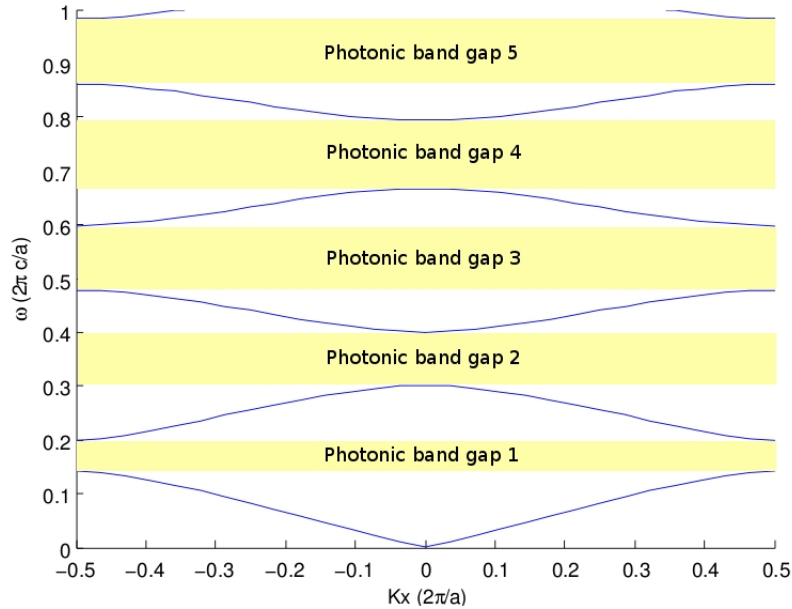


Figure 6.3: Band diagram for a 1D PC in which the unit cell is composed by two layers alternatively of air ( $\varepsilon = 1$ ) and silicon ( $\varepsilon = 12$ ). There are 5 different photonic band gaps.

equations. In this thesis we used the code MIT Photonic-Bands (MPB)\* that solves the Maxwell's equations in periodic dielectric structures for arbitrary wavevectors, using fully-vectorial and three-dimensional methods. The program, given a lattice and the dielectric media computes the band diagram of the PC.

The slope of any band represents the dispersion velocity of the associated Bloch waves. Thus, at the maximum and minimum points, since the slope is null, the Bloch modes are describing a stationary mode. For certain combinations of type of lattice and dielectric indices there are frequencies for which there are not solutions to the Maxwell's equations. In the band diagram these frequencies are determined by the absence of intersection points between the photonic bands and an horizontal line of a certain frequency value. These ranges are called photonic band gaps and are fundamental for the property of PCs of manipulating the electromagnetic field. In fact, electromagnetic

\*[http://ab-initio.mit.edu/wiki/index.php/MIT\\_Photonic\\_Bands](http://ab-initio.mit.edu/wiki/index.php/MIT_Photonic_Bands)

waves with a frequency inside the photonic band gap cannot propagate inside the crystal. It is important to underline that the bandwidth of the photonic band gap depends also on the difference between the dielectric indices of the two material used to generate the periodic lattice. The higher the difference is, the larger will be the bandwidth. This property allows a large number of applications as described in the following section and is used in this thesis to develop a high efficiency polarization splitter design.

### 6.1.3 2D photonic crystals: TE and TM modes

Before introducing the effect of defects inside PC lattices, we present an interesting property of the 2D PCs that will be very useful for the polarization splitter device. We consider an electromagnetic wave propagating inside a lattice in the absence of free charges and electric currents. In 2D PCs the structure is periodic along only 2 dimensions (say x and z directions) while the dielectric permittivity is constant along the third dimension (say y direction). In this case Eq. 6.7 can be transformed by expanding the curl and scalar operators. By isolating the time derivative we obtain:

$$\begin{aligned} \frac{\delta H_x}{\delta t} &= \frac{1}{\mu_0} \frac{\delta E_y}{\delta z} & \frac{\delta E_x}{\delta t} &= -\frac{1}{\varepsilon} \frac{\delta H_y}{\delta z} \\ \frac{\delta E_y}{\delta t} &= \frac{1}{\varepsilon} \left( \frac{\delta H_x}{\delta z} - \frac{\delta H_z}{\delta x} \right) & \frac{\delta H_y}{\delta t} &= \frac{1}{\mu_0} \left( \frac{\delta E_z}{\delta x} - \frac{\delta E_x}{\delta z} \right) \\ \frac{\delta H_z}{\delta t} &= -\frac{1}{\mu_0} \frac{\delta E_y}{\delta x} & \frac{\delta E_z}{\delta t} &= \frac{1}{\varepsilon} \frac{\delta H_y}{\delta z} \end{aligned} \quad (6.13)$$

in which we can recognise that there are two separated set of components of the electromagnetic field that are not interacting. These are  $(H_x, E_y, H_z)$  called Transverse Magnetic (TM) polarized field or TM modes and  $(E_x, H_y, E_z)$  called Transverse Electric (TE) polarized field or TE modes. This property demonstrates that TE and TM modes are decoupled inside a PC and propagate with different behaviours, that is with different Bloch waves and velocities. Note that in the TE modes there is the  $E_x$  field and in the TM modes the  $E_y$  field. They are the components from which we define the Stokes parameters Q and U from which we characterize the polarization signal. A

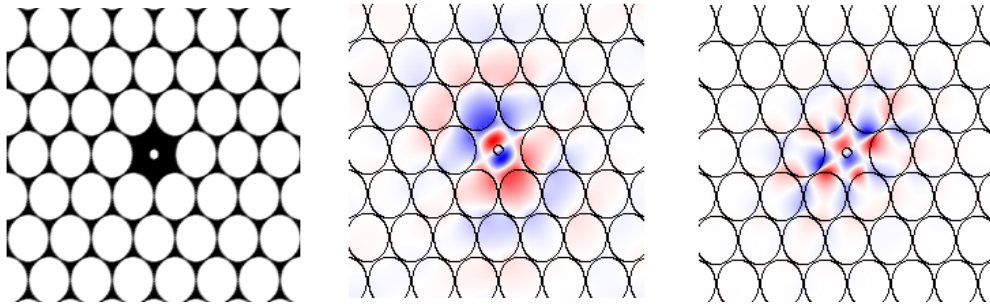


Figure 6.4: (*left*) Example of a point defect inside a PC lattice. Here it exhibits as a modification of the radius of a single column that composes the lattice. Electric (*centre*) and magnetic (*right*) fields inside the defect. Colours represents the intensity of the field that is localized inside the defect.

different propagation of TE and TM modes means a different behaviour of the two polarizations of the field. This concept is at the basis of the working principle of the polarization splitter that separates TE and TM modes, and thus, separates the two polarizations of a signal.

#### 6.1.4 Photonic cavities and waveguides

A PC is characterized by a periodicity of the dielectric properties in its lattice. However, there is the possibility to insert defects inside the lattice. These defects can be deformations of the elements that compose the unit cell, or the absence of an entire unit cell inside the lattice. For example we can modify the radius of a single column inside a 2D PC as shown in Fig. 6.4(left) in which there is a triangular lattice composed by holes inside a dielectric medium ( $\varepsilon = 13$ ). All the columns have a radius  $r = 0.48a$ , where  $a$  defines the scale dimensions of the crystal, except for one single column that has a radius  $r = 0.1a$ .

This is a point defect that will behave as an electromagnetic cavity. This happens because an electromagnetic field can excite a localized mode inside it. Certain frequencies, that are not allowed inside the PC because they belong to the photonic band gap, can be excited inside the defect. When an incident electromagnetic wave with a frequency of the photonic band gap

hits the crystal the field inside the crystal exponentially decays. Thus, in any case, the field penetrates a bit inside the crystal. If there is a defect, this field can excite modes that are localized because they cannot propagate in the rest of the crystal.

This effect can be observed in the band diagram as well. Inside the original photonic band gap appears horizontal lines relative to frequencies that couple with the cavity. Fig. 6.5 shows the band diagram for the lattice of Fig. 6.4. Yellow regions encloses the Bloch modes that can propagate inside the crystal. Inside the white region that delimits the photonic band gap there are two horizontal lines: one for the TM mode (red) the other for the TE mode (blue). Following Eq. 6.12 the propagation velocity of these Bloch waves is null, that is they are localized. Moreover, we note that the two polarized fields couple with the cavity in different ways and with a different frequency confirming that they behave differently inside the PC. Once the incident field does not supply the energy in the cavity, the mode will radiate slowly all its energy.

A natural expansion of this concept is to place multiple defects generating a linear defect. Inside the linear defect frequencies of the photonic band gap will propagate without losing their energy into the PC because they simply cannot propagate inside it. In this sense, we have generated a waveguide for the electromagnetic field. An example is shown in Fig. 6.6 where a linear defect has been created by eliminating a line of holes in the lattice. The lattice is composed by holes of radius  $r = 0.45$  in a dielectric medium ( $\varepsilon = 9$ ). The presence of a waveguide can be seen also in the band diagram. In fact, inside the photonic band gap there are curved lines describing the frequencies that can propagate inside the waveguide but not in the crystal. The lines are curved because the wave is not stationary, but it is propagating.

The possibility of building cavities and waveguides gave a strong impulse in the development of PCs because they allow to canalize a well known range of frequencies, to guide them inside the lattice without losses and to modify them through modifications to the lattice. This research activity

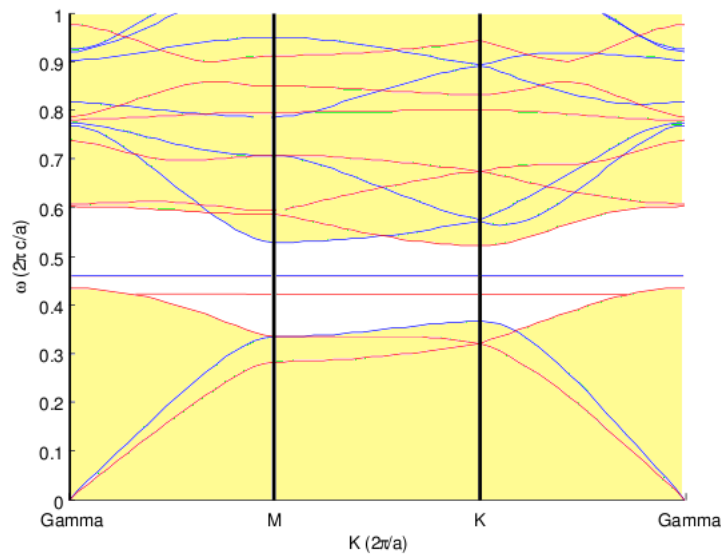


Figure 6.5: Band diagram of a triangular lattice with a point defect shown in Fig. 6.4. White regions represent the band gap, that is the frequencies that cannot propagate inside the crystal. The two horizontal lines describe the TM mode (red) and TE mode (TE) that can be excited in a localized field inside the cavity.

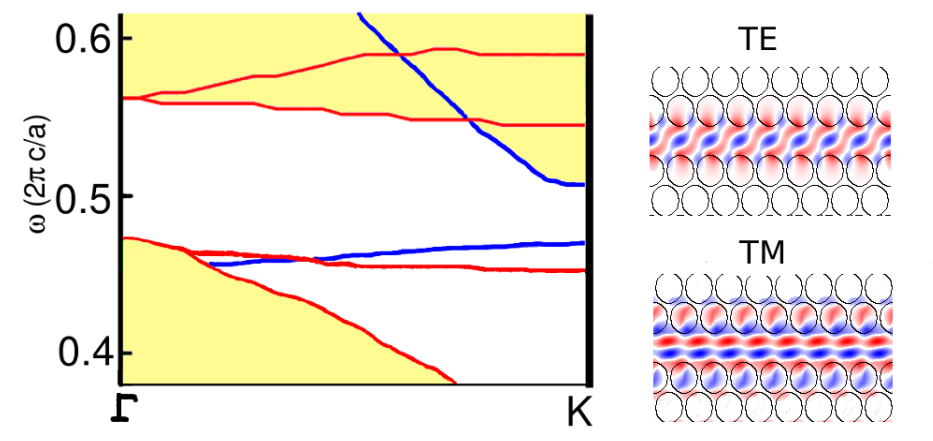


Figure 6.6: (*left*) Band diagram of a triangular lattice with a linear defect. White region that indicates the frequencies that cannot propagate in the crystal. The red and blue lines inside the white region describe respectively the TE and TM modes propagating inside the waveguide. (*right*) TE modes (*top*) and TM modes (*bottom*) propagating inside the waveguide built in a triangular lattice.

brought to the study of waveguide bends [283,284], narrow band beam splitter [285], channel-drop filters [286], optical spectrometers [287], nanocavity lasers [288,289] and many more. In this Chapter, waveguides and cavities are used in order to build a polarization splitter device working at the microwaves. This device can be used in observational campaigns, from the ground or by satellite, focused on the polarization signal measurement.

## 6.2 Ab-initio numerical simulations: the FDTD method

Waveguides and cavities are the basis of the power of PCs of manipulating electromagnetic fields. In this Chapter we used this concept to build a device dedicated to the separation of the polarization signals. When the PC and its defects become complicated, a band diagram cannot fully describe the behaviour of the electromagnetic wave inside it. There is the necessity to solve the Maxwell's equations in time in order to directly simulate a wave propagating inside the crystal. This is achieved by the Finite-Difference Time-Domain (FDTD) method [290]. The development of this method could enormously increase the study of PCs. However, a drawback in the use of this method is the high computational cost of its implementation. In fact, instead of finding the eigenvalues in the point of the irreducible Brillouin zone, it solves the Maxwell's equations in a spatial and time grid as large as the entire PC that can be composed by thousands of unit cells.

In order to understand the method, we start solving the equations for a one-dimensional scalar wave:

$$\frac{\delta^2 u}{\delta t^2} = c^2 \frac{\delta^2 u}{\delta x^2} \quad (6.14)$$

where  $u = u(x, t)$  is a generic field. We define a time and spatial grid with constant time step  $\Delta t$  and space step  $\Delta x$  and consider the Taylor series expansion of the field  $u(x, t_n)$  around the space point  $x_i$  to the space point  $x_i + \Delta x$  keeping the time  $t_n$  fixed:

$$u(x_i + \Delta x)|_{t_n} = u|_{x_i, t_n} + \Delta x \frac{\delta u}{\delta x}|_{x_i, t_n} + \frac{\Delta x^2}{2} \frac{\delta^2 u}{\delta x^2}|_{x_i, t_n} + \frac{\Delta x^3}{6} \frac{\delta^3 u}{\delta x^3}|_{x_i, t_n} + \frac{\Delta x^4}{24} \frac{\delta^4 u}{\delta x^4}|_{\xi_1, t_n} \quad (6.15)$$

The last term encloses the error due to the expansion in which the term  $\xi_1$  is an unknown point in the range  $(x_i, x_i + \Delta x)$ . We can also expand the field  $u$  to the point  $x_i - \Delta x$  still keeping the time  $t_n$  fixed:

$$u(x_i - \Delta x)|_{t_n} = u|_{x_i, t_n} - \Delta x \frac{\delta u}{\delta x}|_{x_i, t_n} + \frac{\Delta x^2}{2} \frac{\delta^2 u}{\delta x^2}|_{x_i, t_n} - \frac{\Delta x^3}{6} \frac{\delta^3 u}{\delta x^3}|_{x_i, t_n} + \frac{\Delta x^4}{24} \frac{\delta^4 u}{\delta x^4}|_{\xi_2, t_n} \quad (6.16)$$

Again we consider the error due to the expansion by calculating the last term in the unknown space point  $\xi_2$  in the range  $(x_i, x_i - \Delta x)$ . By summing Eq. 6.15 and 6.16 and rearranging it in order to isolate the second derivative, we obtain:

$$\frac{\delta^2 u}{\delta x^2}|_{x_i, t_n} = \left[ \frac{u(x_i + \Delta x) - 2u(x_i) + u(x_i - \Delta x)}{(\Delta x)^2} \right]_{t_n} + O[(\Delta x)^2] \quad (6.17)$$

where the term  $O[(\Delta x)^2]$  takes into account the errors due to the expansions. Eq. 6.17 is commonly referred as second order accurate, central-difference approximation to the second partial space derivative of  $u$ . In the following equations we adopt the index  $i$  for the space position and the index  $n$  for the time observational point. With this convention we can compact Eq. 6.17:

$$\frac{\delta^2 u}{\delta x^2}|_{x_i, t_n} = \frac{u_{i+1}^n - 2u_i^n + u_{i-1}^n}{(\Delta x)^2} + O[(\Delta x)^2] \quad (6.18)$$

where  $u_i^n$  denotes the field quantity calculated at the space position  $x_i = i\Delta x$  and at the time point  $t_n = n\Delta t$ . We can do the same steps for the second partial time derivative and by keeping fixed  $x_i$  expand the field  $u$  in forward and backward Taylor's series in time. We obtain:

$$\frac{\delta^2 u}{\delta t^2}|_{x_i, t_n} = \frac{u_i^{n+1} - 2u_i^n + u_i^{n-1}}{(\Delta t)^2} + O[(\Delta t)^2] \quad (6.19)$$

substituting the two central-difference expressions of Eq. 6.18 and 6.19 into Eq. 6.14 and arranging it in order to isolate the term  $u_i^{n+1}$ , we have

$$u_i^{n+1} = (c\Delta t)^2 \left[ \frac{u_{i+1}^n - 2u_i^n + u_{i-1}^n}{(\Delta x)^2} \right] + 2u_i^n - u_i^{n-1} + O[(\Delta t)^2] + O[(\Delta x)^2] \quad (6.20)$$

This is a fully explicit second order accurate expression for  $u_i^{n+1}$  in which all the quantities on the right-hand side are known because they were obtained during the previous time steps  $n$  and  $n - 1$ . Once we have calculated the values of the field in all the space points of the grid at the time  $n + 1$  we can start again and calculate the field at the time  $n + 2$ .

Of particular interest is the case in which  $c\Delta t/\Delta x = 1$ . This is called *magic time step* because it can be demonstrated that in this case we obtain a numerical finite-difference equation that is an exact solution to the original differential wave equation 6.14. It is:

$$u_i^{n-1} = u_{i+1}^n + u_{i-1}^n - u_i^{n-1} \quad (6.21)$$

in which there is not an error term.

### 6.2.1 The Yee algorithm

In this section we apply the central-difference method introduced above to numerically solve the Maxwell's equations. In the case of an electromagnetic wave propagating in a 2D PC with constant dielectric permittivity along the  $y$ -axis, Maxwell's equations are in the form of 6.13. The equations have been already introduced in Section 6.1.3 to introduce the two TE and TM polarized field. This case presents a difference with respect to the one dimensional field, because now we have two fields  $E$  and  $H$  interacting with each other.

In order to solve this problem we introduce the Yee algorithm (see [290] for more details). The discretization of the space in a spatial grid is done so that the components of the  $E$  field are always surrounded by 4 circulating components of the  $H$  field (and vice versa). This trick in general allows to

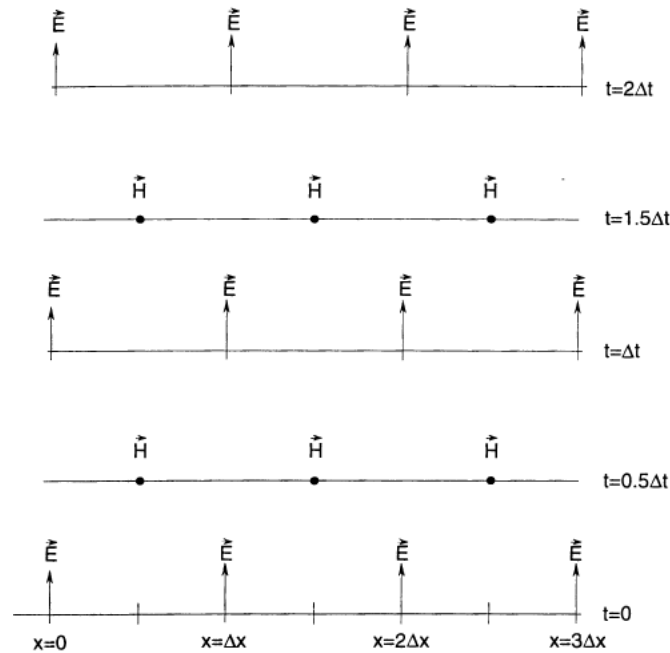


Figure 6.7: Space-time grid of the Yee algorithm for a one-dimensional case. This grid definition allows the use of central differences for the space derivatives and leapfrog for the time derivatives.

numerically solve the macroscopic integrals and the pointwise derivatives of the Maxwell's equations and to easily define the boundary conditions and the singularities. The finite differences inside the equations are fully explicit central-differences and second order accurate so we can easily apply the FDTD method. For the time increment the Yee algorithm uses the leapfrog method in the sense that the  $E$  field values are obtained from the  $H$  field values already obtained at the previous time step (and vice versa). Moreover, by using the magic time step we obtain non-dissipative results, that is a numerical wave mode propagating in a lattice does not spuriously decay due to non-physical artifacts of the time-stepping algorithm.

Before applying the method to Eq. 6.13, we describe here in detail the spatial and temporal grid of the Yee algorithm. We consider the one-dimensional case. By defining  $\Delta x$  and  $\Delta t$  as the space and time steps of the grid, Maxwell's equations will be solved by obtaining the values for the

fields  $E$  and  $H$  at a distance of one step with respect to the previous values. In the Yee algorithm the trick is to shift the grids in which the two fields are calculated by half a step in space and time as shown in Fig. 6.7 for the propagation along a one-dimensional axis. In this way the values of one field can be obtained using the fully explicit central differences equations. This concept is easily expanded to the 2D and 3D cases. By inserting the Yee algorithm into Eq. 6.13 we have for the TE modes:

$$\begin{aligned}
 E_x|_{i,j,k}^{n+1} &= E_x|_{i,j,k}^n - \frac{\Delta t}{\varepsilon_{i,j,k}} \left( \frac{H_y|_{i,j,k+\frac{1}{2}}^{n+\frac{1}{2}} - H_y|_{i,j,k-\frac{1}{2}}^{n+\frac{1}{2}}}{\Delta z} \right) \\
 H_y|_{i,j,k}^{n+\frac{1}{2}} &= H_y|_{i,j,k}^{n-\frac{1}{2}} - \frac{\Delta t}{\mu_{i,j,k}} \left( \frac{E_x|_{i,j,k+\frac{1}{2}}^n - E_x|_{i,j,k-\frac{1}{2}}^n}{\Delta z} - \frac{E_z|_{i+\frac{1}{2},j,k}^n - E_z|_{i-\frac{1}{2},j,k}^n}{\Delta x} \right) \\
 E_z|_{i,j,k}^{n+1} &= E_z|_{i,j,k}^n + \frac{\Delta t}{\varepsilon_{i,j,k}} \left( \frac{H_y|_{i+\frac{1}{2},j,k}^{n+\frac{1}{2}} - H_y|_{i-\frac{1}{2},j,k}^{n+\frac{1}{2}}}{\Delta x} \right)
 \end{aligned} \tag{6.22}$$

and for the TM modes:

$$\begin{aligned}
 H_x|_{i,j,k}^{n+\frac{1}{2}} &= H_x|_{i,j,k}^{n-\frac{1}{2}} - \frac{\Delta t}{\mu_{i,j,k}} \left( \frac{E_y|_{i,j,k+\frac{1}{2}}^n - E_y|_{i,j,k-\frac{1}{2}}^n}{\Delta z} \right) \\
 E_y|_{i,j,k}^{n+1} &= E_y|_{i,j,k}^n - \frac{\Delta t}{\varepsilon_{i,j,k}} \left( \frac{H_x|_{i,j,k+\frac{1}{2}}^{n+\frac{1}{2}} - H_x|_{i,j,k-\frac{1}{2}}^{n+\frac{1}{2}}}{\Delta z} - \frac{H_z|_{i+\frac{1}{2},j,k}^{n+\frac{1}{2}} - H_z|_{i-\frac{1}{2},j,k}^{n+\frac{1}{2}}}{\Delta x} \right) \\
 H_z|_{i,j,k}^{n+\frac{1}{2}} &= H_z|_{i,j,k}^{n-\frac{1}{2}} - \frac{\Delta t}{\mu_{i,j,k}} \left( \frac{E_y|_{i+\frac{1}{2},j,k}^n - E_y|_{i-\frac{1}{2},j,k}^n}{\Delta x} \right)
 \end{aligned} \tag{6.23}$$

Once we have solved the equations for the fields respectively in their own grids, we can calculate the value of the field in a point of the grid relative to the other field with a semi-implicit approximation. For example,

the component  $H_x$  at the time step  $n$  in which, with the Yee algorithm we calculate the field  $E$ , is obtained as:

$$H_x|_{i,j,k}^n = \frac{H_x|_{i,j,k}^{n+\frac{1}{2}} - H_x|_{i,j,k}^{n-\frac{1}{2}}}{2} \quad (6.24)$$

that is the average between the values of the field  $H_x$  at the time step  $n + 1/2$  and  $n - 1/2$ .

These concepts are at the basis of the code called NANOCPP<sup>†</sup> written by Prof. A. Fratolocchi that numerically solves the Maxwell's equations in time using the FDTD method and thus describing the electromagnetic waves moving inside 1D, 2D or 3D PCs. This code has been used in this thesis in order to simulate and optimize the polarization splitter.

### 6.2.2 Numerical stability

As in any kind of numerical code, the Yee algorithm used in the NANOCPP code must satisfy numerical stability conditions. This is done to avoid the explosion of the errors due to the approximations made in the algorithm. If the errors become too large, the results of the simulation will be unrealistic and unreliable. The approximations of the Yee algorithm are due to the discretization of the space and to the definition of the semi-implicit Eq. 6.24 due to the time discretization.

Considering the spatial discretization, we observe that Eq. 6.22 and 6.23 can be rewritten as eigenvalue problems. For example by setting the coefficients  $\varepsilon$ ,  $\mu$  and  $c$  to 1, the TM modes of the 6.23, at a fixed time step, become:

---

<sup>†</sup><http://primalight.org/category/primalight-research/ab-initio/>

$$\begin{aligned}
\left( \frac{E_y|_{i,j,k+\frac{1}{2}} - E_y|_{i,j,k-\frac{1}{2}}}{\Delta z} \right) &= \Lambda H_x|_{i,j,k} \\
\left( \frac{H_x|_{i,j,k+\frac{1}{2}} - H_x|_{i,j,k-\frac{1}{2}}}{\Delta z} - \frac{H_z|_{i+\frac{1}{2},j,k} - H_z|_{i-\frac{1}{2},j,k}}{\Delta x} \right) &= \Lambda E_y|_{i,j,k} \\
\left( \frac{E_y|_{i+\frac{1}{2},j,k} - E_y|_{i-\frac{1}{2},j,k}}{\Delta x} \right) &= \Lambda H_z|_{i,j,k}
\end{aligned} \tag{6.25}$$

The eigenvalue problem is solved by finding the eigenvalues that will depend on the spatial steps. It can be demonstrated [290] that the eigenvalues will follow these conditions:

$$\begin{aligned}
\operatorname{Re}(\Lambda) &= 0 \\
-2\sqrt{\frac{1}{(\Delta x)^2} + \frac{1}{(\Delta y)^2} + \frac{1}{(\Delta z)^2}} &\leq \operatorname{Im}(\Lambda) \leq 2\sqrt{\frac{1}{(\Delta x)^2} + \frac{1}{(\Delta y)^2} + \frac{1}{(\Delta z)^2}}
\end{aligned} \tag{6.26}$$

At the same time, considering the time approximation, we can rewrite the average of Eq. 6.24, again as an eigenvalue problem:

$$\frac{V|_{i,j,k}^{n+\frac{1}{2}} - V|_{i,j,k}^{n-\frac{1}{2}}}{\Delta t} = \Lambda V|_{i,j,k}^n \tag{6.27}$$

where  $V$  identifies the electric or magnetic field. It is demonstrated that the eigenvalues fall inside the range:

$$-\frac{2}{\Delta t} \leq \operatorname{Im}(\Lambda) \leq \frac{2}{\Delta t} \tag{6.28}$$

Following these conditions, to guarantee the numerical stability of the code for arbitrary spatial modes, the range of eigenvalues for the spatial modes set by 6.27 must be contained completely within the stable range of time-stepping eigenvalues set by Eq. 6.28. In the case of spatial steps equal in any direction  $\Delta x = \Delta y = \Delta z = \Delta$ , the code is numerically stable if:

$$\Delta t \leq \frac{\Delta}{3} \tag{6.29}$$

In the NANOCPP code this condition is satisfied, but the time step must also guarantee reasonable computational costs of the code, so for the NANOCPP code we used:

$$\Delta t \leq \frac{\Delta}{6} \quad (6.30)$$

### 6.2.3 Electromagnetic sources in the FDTD code

The FDTD method gives also the possibility to simulate sources of any kind, shape and intensity because the algorithm directly solves Maxwell's equations. In order to test any component of the polarization splitter we used three different kinds of sources: Gaussian sources, single pulses that cover a large range of frequencies and monochromatic sources at a single frequency. There are two ways to simulate sources inside a PC: the Hard source and the Total-Field/Scattered-Field.

#### The Hard source

The Hard source is a point source in which there is a numerical wave originating from only one or two points in the grid. The source can be placed in any grid point and generates waves in any direction, that is with any  $k$  of the band diagram. The Hard source is set up by simply assigning a desired time function to specific electric or magnetic field components. With this approach we can simulate sine waves of frequency  $f_0$  in the point  $i_s$  switched on at time  $n = n_0$ :

$$E_z|_{i_s}^n = E_0 \sin(2\pi f_0(n - n_0)\Delta t) \quad (6.31)$$

or Gaussian sources centered at time step  $n_0$  and with a  $1/e$  characteristic decay after  $n_{decay}$  time steps:

$$E_z|_{i_s}^n = E_0 e^{-\left(\frac{n-n_0}{n_{decay}}\right)^2} \quad (6.32)$$

or bandpass Gaussian pulse with Fourier spectrum symmetrical about  $f_0$ :

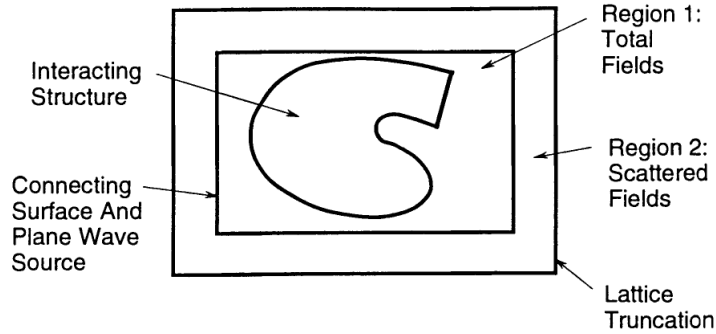


Figure 6.8: Subdivision of the computational region. The total field is present in region 1, while only the scattered field can propagate in region 2. On the connecting surface the algorithm is modified to keep the consistency of the equations.

$$E_z|_{i_s}^n = E_0 e^{-\left(\frac{n-n_0}{n_{decay}}\right)^2} \sin(2\pi f_0(n-n_0)\Delta t) \quad (6.33)$$

In the first case the field becomes different from zero exactly at time  $n = n_0$ . In the other two cases the source is not null at time  $n_0$ , thus, they are added inside the crystal with a smooth transition usually with duration of  $3n_{decay}$  that does not alter the shape of the source.

### The Total-Field/Scattered-Field formulation

This approach is based on the linearity of Maxwell's equations. In fact, we can decompose the total electric and magnetic field in incident ( $\mathbf{E}_{inc}$  and  $\mathbf{H}_{inc}$ ) and scattered ( $\mathbf{E}_{scat}$  and  $\mathbf{H}_{scat}$ ) wave fields. The incident fields are the values of the incident field in any point of the crystal. Instead, the scattered fields are the results of the interaction between the incident field and the lattice. The Yee algorithm can be applied to both the incident and the scattered field. This approach needs a subdivision of the computational region in two parts separated by a virtual connecting surface as shown in Fig. 6.8.

The internal region is called total-field region. Here the Yee algorithm works on the total field. The PC is always completely inside this region. The

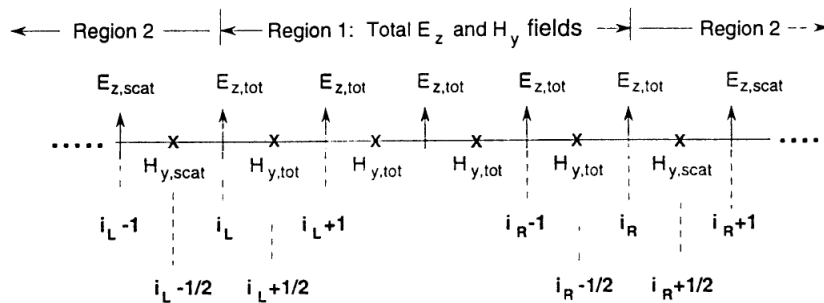


Figure 6.9: One dimensional example of the spatial disposition of the points and of the electric and magnetic fields. The two regions are described at the top. It is evident the inconsistency of the fields along the connecting surface.

external region is called scattered-field region. Here the incident field is null and the Yee algorithm works only on the scattered field. The TF/SF formulation is much more flexible compared to the Hard source. It can simulate any kind of arbitrary sources with selected wave shape, duration, incident angle, propagation direction and polarization. It is easier because the division between incident and scattered field is done only along the connecting surface. Moreover the external region allows the introduction of boundary conditions that simulate an infinite extension of the grid and suppress spurious reflection of the field that can arise when the field reaches the boundaries of the computational region. However, this approach needs the introduction of boundary conditions along the connecting surface to avoid inconsistency in the equations as shown in Fig. 6.9.

In fact, if we consider the Yee algorithm for a point on the connecting surface, the field in this point will be calculated starting from the values of the other component field in the points around the surface. In this case some points will be in the internal region, others in the external one. The inconsistency problem is solved in these cases by adding the value of the incident field calculated in the points of the external region needed by the Yee algorithm. In the case of the example of Fig. 6.9 it is:

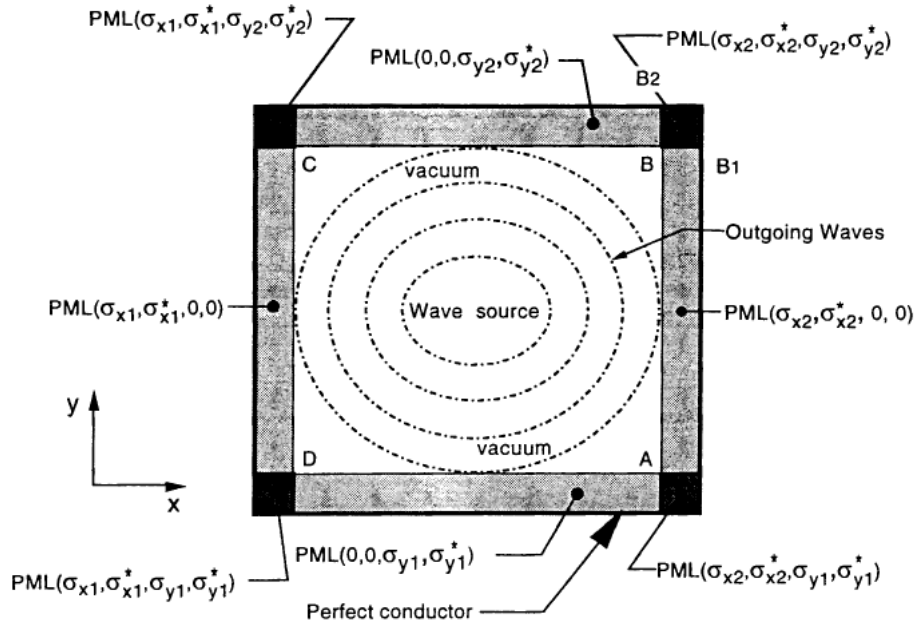


Figure 6.10: Structure of a two-dimensional FDTD grid with at the boundaries the PML absorbing conditions.

$$\begin{aligned}
 E_{z,tot}|_{i_L}^{n+1} &= E_{z,tot}|_{i_L}^n + \frac{\Delta t}{\varepsilon_0 \Delta x} (H_{y,tot}|_{i_L+\frac{1}{2}}^{n+\frac{1}{2}} - H_{y,scat}|_{i_L-\frac{1}{2}}^{n+\frac{1}{2}}) - \frac{\Delta t}{\varepsilon_0 \Delta x} H_{y,inc}|_{i_L-\frac{1}{2}}^{n+\frac{1}{2}} \\
 H_{y,scat}|_{i_L-\frac{1}{2}}^{n+\frac{1}{2}} &= H_{y,scat}|_{i_L-\frac{1}{2}}^{n-\frac{1}{2}} + \frac{\Delta t}{\mu_0 \Delta x} (E_{z,tot}|_{i_L}^n - E_{z,scat}|_{i_L-1}^n) - \frac{\Delta t}{\mu_0 \Delta x} E_{z,inc}|_{i_L}^n
 \end{aligned}
 \tag{6.34}$$

The same approach is extended to all the components of the electromagnetic field along the entire connecting surface between the internal region and the external region. The incident wave is calculated, at the space points and time in which the Yee algorithm calls the scattered wave, considering the internal region as the propagation region of the field without the PC so that it is not perturbed in its evolution.

### 6.2.4 Absorbing boundary conditions

The TF/SF formulation allows to introduce absorbing conditions in the scattered region.. The boundaries of the computational regions are a source

of problems for the Yee algorithm. In fact, at the boundary there is a strong variation in the dielectric permittivity that outside the computational region becomes zero. This strong variation can cause the total reflection of the field and alter the results of the simulation. The code NANOCPP uses the approach called Perfect Matched Layer (PML) conceived by Jean-Pierre Berenger [291]. The method consists in inserting a non-physical medium in the external part of the region of the scattered field. The medium has the properties of being highly absorbing and with an impedance independent on the incident angle or frequency of the wave and equal to the rest of the region.

Inside this region Maxwell's equations change and, for example for the TE modes, become:

$$\begin{aligned}\varepsilon_0 \frac{\delta E_x}{\delta t} + \sigma E_x &= \frac{\delta H_y}{\delta z} \\ \mu_0 \frac{\delta H_y}{\delta z} + \sigma^* H_y &= \frac{\delta E_x}{\delta z} - \frac{\delta E_y}{\delta z} \\ \varepsilon_0 \frac{\delta E_z}{\delta t} + \sigma E_z &= \frac{\delta H_y}{\delta x}\end{aligned}\quad (6.35)$$

where  $\varepsilon_0$  and  $\mu_0$  are the permeability and permittivity of the medium, while  $\sigma$  and  $\sigma^*$  are respectively the electric conductivity and the magnetic losses that cause the rapid drop off of the electromagnetic field. If the constants in these Maxwell's equations follow the condition:

$$\frac{\sigma}{\varepsilon_0} = \frac{\sigma^*}{\mu_0} \quad (6.36)$$

the impedance of this absorbing region is the same as in the external region. The electromagnetic wave enters the region without being reflected by the connecting surface and is completely absorbed by the medium.

## 6.3 Multimode interference

The Bloch waves are the solution to the Maxwell's equations describing an electromagnetic wave that propagates inside a PCs. In the case of a two-

dimensional lattice, these solutions are naturally separated in two sets of components related to the two polarizations of the signal: TE and TM modes. Also, by solving the equations we find that the two polarizations behave differently inside PCs. This particular property of the periodic dielectric lattices has been used to separate the two polarizations of the signal. In the literature, many different devices has been presented. The most used techniques are the coupling between waveguides, alterations into the lattice and the multimode interference.

The coupling effect between two waveguides is based on a mechanism similar to the tunnel effect for electrons [292]. When two waveguides are identical and very close each other, an electromagnetic field can "jump" from one waveguide to the other. The distance from the starting point of the coupling, at which the field is found in the other waveguide depends on the propagation velocity of the modes that form the wave. Since TE and TM modes have different velocity dispersions there will be a distance where a polarization is in the first waveguide and the other one is still in the original waveguide [293–295]. A drawback of this method is that these devices must be very long (a great number of wavelengths) to have a high level of separation.

By altering the radius of the columns of a two-dimensional PC, or their dielectric index, or the disposition of the columns in the lattice, the photonic band gap can be modified. Thus, in a well defined position in the lattice, the band gap of only one of the two polarizations can be closed and that polarization will be completely reflected, while the other one can go through the barrier [296]. In other cases the new lattice causes a dispersion angle that is different for the two polarizations [297–299]. However, these methods can cause the reflection of the incident waves due to the presence of a connecting surface between the original lattice and the altered one. This reflection results in a low efficiency in the separation of the two polarizations.

Multimode interference, indeed, allows to develop compact polarization splitters with high efficiency [300,301]. The mechanism of this effect is based

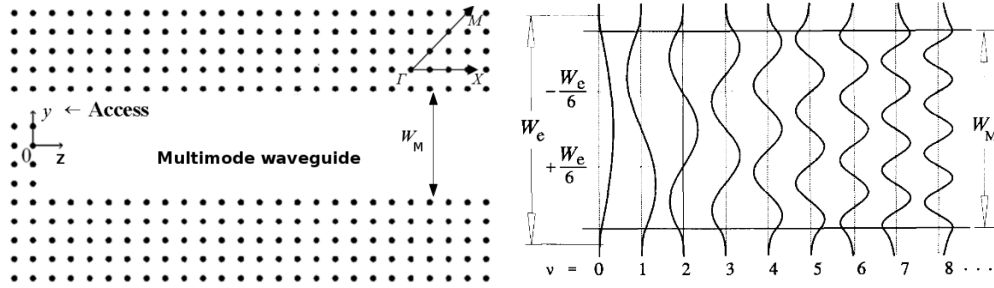


Figure 6.11: (*left*) Example of a multimode waveguide inside a square lattice. The width of the waveguide,  $W_M$ , is larger than a single period of the lattice. (*right*) The first modes coupled with the waveguide. The interference between the modes is at the basis of the self-imaging principle. The width of the fundamental mode,  $W_e$ , takes into account the penetration of the wave inside the PC at the borders of the waveguide. The number of the mode is defined by the parameter  $\nu$  [300].

on the self-imaging principle stating that inside a waveguide an input field profile is reproduced in single or multiple images at periodic intervals along the propagation axis. This effect is due to the constructive and destructive interference between many modes of the same electromagnetic wave that have been excited inside the waveguide.

In order to excite a great number of modes, the waveguide is obtained by eliminating multiple lines of the lattice of the PC as shown in Fig. 6.11(left). If  $W_M$  is the width of the waveguide, an incident electromagnetic wave with wavelength,  $\lambda_0$ , will excite multiple modes, that can be enumerated by the parameter  $\nu$ . The fundamental mode ( $\nu = 0$ ) has a width  $W_e$  that is larger than the width of the waveguide because of the penetration of the field in the PC at the borders of the waveguide.

The self-imaging effect is due to the different propagation velocities of the different modes,  $\beta_\nu$ . It can be demonstrated that it depends on the square of the number of the mode  $\nu$ :

$$\beta_\nu \simeq k_0 n_r - \frac{(\nu + 1)^2 \pi \lambda_0}{4 n_r W_e^2} \quad (6.37)$$

where  $k_0$  is the wave number and  $n_r$  is the refractive index. If the propa-

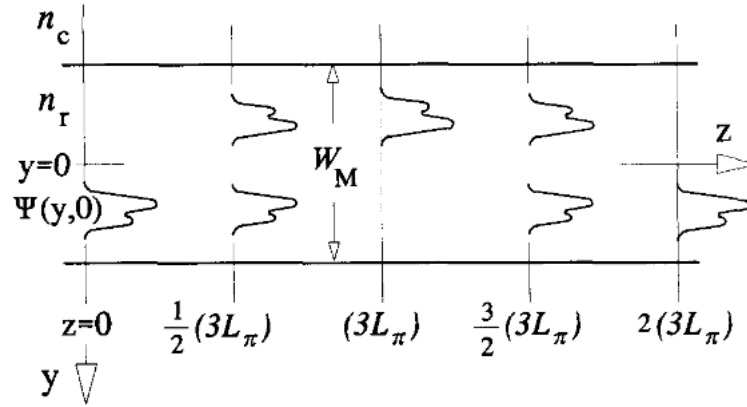


Figure 6.12: Schematic illustration of multimode waveguide showing the input field profile and a mirrored single image at  $(3L_\pi)$ , a direct single image at  $2(3L_\pi)$ , and two-fold images at  $\frac{1}{2}(3L_\pi)$  and  $\frac{3}{2}(3L_\pi)$  [300].

gation velocities are different, the intensity of the electromagnetic wave will depend on the number of the modes in constructive interference and in destructive interference in any point of the waveguide. The wave function of the electromagnetic field,  $\Psi(y, z)$ , at distance  $L$  from the beginning of the waveguide is:

$$\Psi(y, L) = \sum_{\nu=0}^{m-1} c_\nu \psi_\nu(y) e^{j \frac{\nu(\nu+2)\pi}{3L_\pi} L} \quad (6.38)$$

where  $m$  is the total number of mode excited inside the waveguide,  $c_\nu$  and  $\psi_\nu$  describe the input profile of the wave along the  $y$  direction and  $L_\pi$  is a characteristic length depending on the propagation velocities of the two lowest modes  $L_\pi = \pi/(\beta_0 - \beta_1)$ .

The constructive interference between the modes is totally depending on the phase of Eq. 6.38. In fact, for precise values of the phase related to the distance from the beginning of the waveguide,  $L$ , the wave profile  $\Psi(y, L)$  will be identical to the input profile  $\Psi(y, 0)$  (self-imaging). In particular the distances in which we have an exact reproduction of the input profile (direct image) are:

$$L = p(3L_\pi) \quad p = 0, 2, 4, \dots \quad (6.39)$$

But there are other interesting point. In facts, if

$$L = p(3L_\pi) \quad p = 1, 2, 5, \dots \quad (6.40)$$

the field profile will be the exact replica of the input profile, but will be mirrored (mirror image) with respect to the axis parallel to the waveguide that divides it in two equal parts ( $y = 0$  in Fig. 6.12). In addition to the single images at distances given by Eq. 6.39 and 6.40, multiple images can be found as well for half-integer values of  $3L_\pi$  at which are produced two-fold images with amplitudes reduced by a factor  $1/\sqrt{2}$ . Direct, mirror and two-fold images are illustrated in Fig. 6.12.

The multimode interference is at the basis of the polarization splitter device studied in this thesis. In fact, since TE and TM modes propagate with different velocities, also the single modes that they excite inside the waveguide will have different velocities and consequently their direct and mirror images will occur in different positions. With the idea of successfully separating the two polarization signals in a device as compact as possible, we studied cavity resonators that are defect regions inside the lattice of many periods in all the PC dimensions. In these objects the electromagnetic field excites multiple modes as well as the long waveguides but in a more compact region. Looking for possible optimizations we studied the shape of the resonator cavity keeping constant the area in order to find the shape in which an incident electromagnetic wave excites the largest number of modes. This study revealed that using chaotic resonators we can store six times more energy than in its classical counterpart of the same volume. These results have been published in [302].

## 6.4 Chaotic resonator to enhance the energy harvesting

The enhanced interaction between light and matter in optical cavity resonators is an interdisciplinary subject of great interest as it affects many areas of condensed matter physics, including cavity electrodynamics [303], quantum and nonlinear optics, but also more practical aspects such as optical signal processing [304–306] and resonantly enhanced optical absorption [307]. All these applications are enabled by highly optimized optical resonators that can efficiently trap electromagnetic energy in narrow frequency bands. In conventional cavities, there is a simple tradeoff between bandwidth and the enhancement of trapped energy: the higher the enhancement, the narrower the bandwidth. A great challenge in the field is therefore to develop a new generation of cavities that are able to break this fixed relationship and store more energy in a given bandwidth window than conventional cavities would allow. These are expected to provide new breakthroughs in the field, thus accessing a novel series of applications ranging from sensing to lasers, to energy harvesting and cavity quantum electrodynamics.

The maximum power that can be transferred into a conventional resonator depends on the coupling coefficient and loss of each given mode, and tends to vary across the mode spectrum, especially when broadband operation ( $\Delta\lambda$  on the scale of hundreds of nanometres) is considered. In addition, classical two- and three-dimensional geometries tend to accommodate modes with very different lifetimes in the same spectral region [308]. Therefore, the use of classical resonators for broadband energy storage is limited. Here, we overcome this intrinsic limitation by exploiting specific shape deformations that support chaotic trajectories for light rays. Surprisingly, we note that in a chaotic cavity, regardless of any regime of coupling, the lifetimes of all modes tend towards a common value, thus significantly improving the transfer of energy into the cavity and increasing its energy-storage capability. Such chaotic resonators [309] have been well exploited in the field of laser devices

[310–317]. We also note that the mode spectrum of deformed microsphere resonators has been studied recently, with remarkable changes in Q-factors being observed [318]. However, despite this large body of literature, nothing is known about the capacity of such resonators to store and collect light energy over a broad spectral range.

The increased energy storage capacity of a chaotic resonator when compared to a classical one can be explained intuitively by adopting a geometrical optics approach and considering that a suitable shape deformation is accompanied by the breaking of symmetry in the structure. As a consequence, the deformed resonator cannot support any cyclic motion of light, so the trajectory of light rays changes from regular to chaotic, that is highly sensitive to the initial conditions. This property statistically leads to a larger lifetime of the photons in the cavity [309]. To clarify this result, we start our analysis from a symmetric (classical) resonator and observe its capacity to trap energy as it is deformed. We define a deformation parameter  $\alpha$  describing the level of deformation of the resonator, where a  $\alpha = 0$  indicates the original, undeformed structure and  $\alpha > 0$  indicates a proportionally deformed geometry. For example, a circle would be described by a  $\alpha = 0$ , and a deformed circle by  $\alpha > 0$ . This parameter is generic and can be used to describe the deformation of any type of resonator, for example, square or disk in two dimensions or cube or sphere in three dimensions. In general, the larger  $\alpha$  is, the larger is the degree of chaos, until a saturation value is reached.

We perform our analysis with a single ab-initio numerical experiment. Such an analytic treatment allows us to study the lifetimes of the electromagnetic modes excited in the cavity and to examine the coherent buildup of energy inside the system. The theory is more easily developed in two dimensions, starting from a circular resonator. Our set-up consists of a silicon dielectric resonator with air holes, the shape of which is defined by the following function in polar coordinates  $(\rho_c, \theta_c)$ :

$$\rho_c = \sqrt{\frac{A}{\pi} - \frac{\alpha^2}{2}} + \alpha \cos(\theta_c) \quad (6.41)$$

where  $A$  is the resonator area and  $\alpha \geq 0$  is the single parameter that controls the resonator shape. Eq. 6.41 belongs to the family of analytic curves investigated by Robnik: for  $\alpha \geq 0$ , Eq. 6.41 supports chaos in the trajectory of light rays, which randomly bounce inside the resonator [319]. From a physical perspective, the shape defined by Eq. 6.41 is equivalent to an asymmetric deformation of a disk, and can be realized experimentally with conventional nanofabrication tools.

In our simulations, we fixed the resonator area to  $A = 30\mu m^2$  and numerically calculated the electromagnetic energy  $E$  stored inside the resonator for varying values of  $\alpha$ . Although the value of  $\alpha$  in Eq. 6.41 is not bound to an upper value, we note that the system reaches saturation for a maximum degree of chaos described by  $\alpha = 1.5$ . The saturation level is determined by the phase space complexity that is the result of the integration over the phase space of the Lyapunov exponent, that characterizes the rate of separation of infinitesimally close trajectories (see for details [320]). We therefore restrict our numerical analysis to  $\alpha \in [0, 1.5]$ . The calculation of the electromagnetic energy  $E(t) = \int_D H d\mathbf{r}$  is performed by a numerical integration of the energy density  $H(\rho, t) = 1/2(\mathbf{E} \cdot \mathbf{D} + \mathbf{H} \cdot \mathbf{B})$  in the volume  $D$  encompassed by the resonator and defined by  $\rho \leq \rho_c$  and  $0 \leq \theta \leq 2\pi$ . We simulated the input from a supercontinuum source centred at  $z = 0$  and propagating along  $z$  for wavelengths between  $\lambda = 300nm$  and  $\lambda = 1300nm$ , which simulates a broadband source such as sunlight. Figure 6.13(a,b) shows a time snapshot of the spatial distribution of  $H$  after  $t = 45fs$ . The geometries of the two resonators are delimited by dashed lines.

Figure 6.13 shows that even a small deformation in shape (at a constant volume) yields a radically different behaviour in the distribution of light energy inside the resonator. Figure 6.14, conversely, displays the time-averaged energy  $\langle E \rangle = 1/t \int_0^t dt' E(t')$  evolution with increasing parameter  $\alpha$ . Remarkably, the introduction of chaos into the motion of light is accompanied by a dramatic change in the energy stored inside the resonator; indeed, the steady-state regime (when the insertion of energy balances radiation losses)

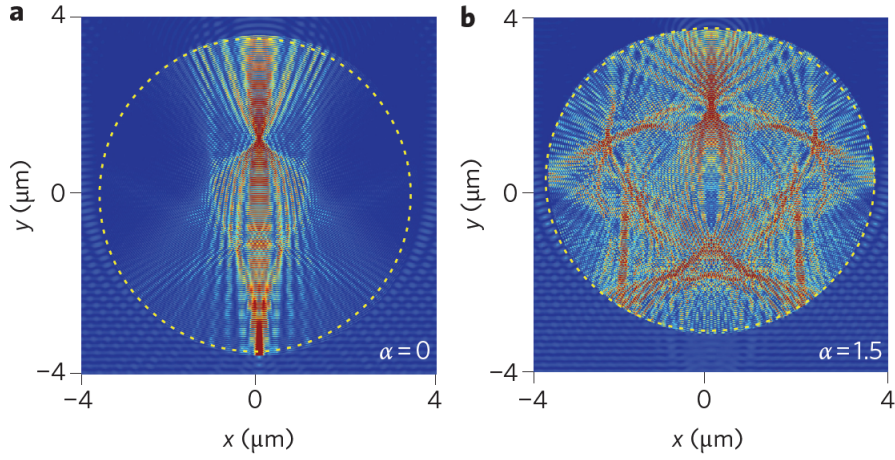


Figure 6.13: Ab-initio simulation results: snapshot of the electromagnetic energy density  $H$  distribution after  $t = 45$  fs in a resonator (dashed line) with  $V = 30\mu\text{m}^2$  for  $\alpha = 0$  (a) and  $\alpha = 1.5$  (b).

shows an approximately sixfold increase even for  $\alpha = 1.5$  (Fig. 6.13b). This energy accumulation grows with the deformation, and rises monotonically as  $\alpha$  increases from 0 to 1.5.

We use time-dependent coupled mode theory (TDCMT) [321] to develop a simple and reliable model for the light-resonator interaction. The system can be modelled as a side-coupled resonator, the dynamical equations of which can be easily solved to obtain energy  $E_k$  and power  $P_k$  stored in the the  $k$  mode:

$$\begin{aligned}
 E_k &= \frac{\tau_k^2}{\tau_e} (1 - e^{-\frac{t}{\tau_k}})^2 \\
 P_k &= \frac{2\frac{\tau_e}{\tau_{k0}}}{(1 + \frac{\tau_e}{\tau_{k0}})^2} |S|^2
 \end{aligned} \tag{6.42}$$

where  $|S|$  is the input source power and  $(1/\tau_k) = (1/\tau_{k0}) + (1/\tau_e)$  is the mode decay rate ( $1/\tau_{k0}$  is the intrinsic cavity decay rate of the  $k$ th mode and  $1/\tau_e$  is the escape rate due to coupling with the environment). The power  $P_k$  strongly depends on the ratio between the radiation and the coupling loss through the parameter  $\tau_{k0}/\tau_e$ , achieving the maximum value of  $P_k = 0.5|S|^2$

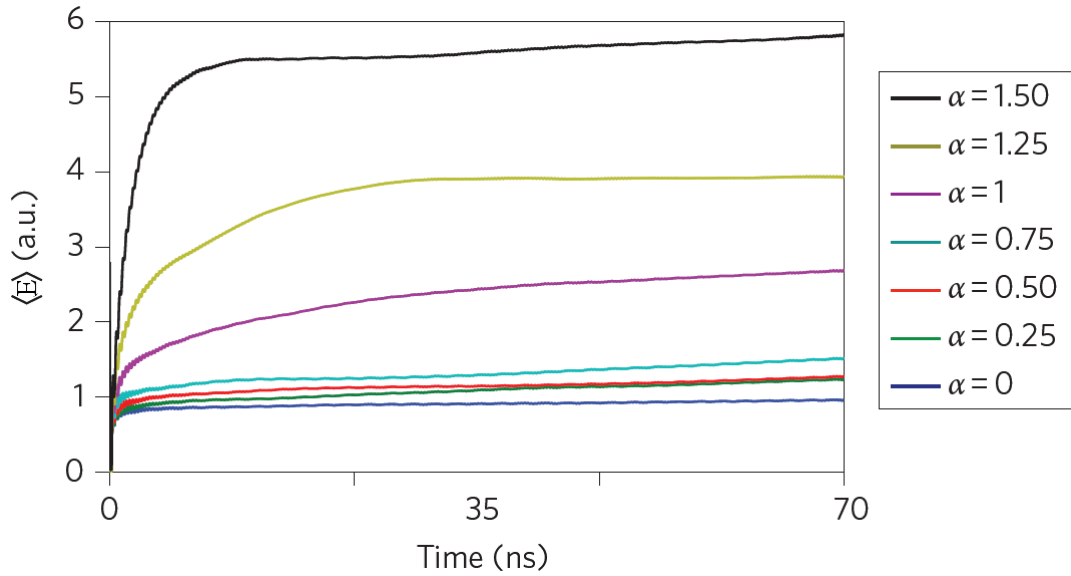


Figure 6.14: Time evolution of the average electromagnetic energy  $\langle E \rangle$  inside cavity resonators for different values of  $\alpha$ .

when  $\tau_e = \tau_{k_0}$ . Outside this matching condition, the power coupled into the structure decreases very quickly. To study how the dynamics of the decay rates can be affected by chaos, we began by calculating the evolution of the decay rates  $\tau_{k_0}$  for different  $\alpha$  in the resonator defined by Eq. 6.41. In a series of finite-difference time domain (FDTD) simulations, we first excited the resonator with a source and then monitored the energy evolution  $E(t)$  when the source was switched off. The decay constants  $\tau_{k_0}$  are extracted from the time energy evolution  $E(t) = \sum_k |A_k|^2 e^{-2t/\tau_{k_0}}$  by applying the Prony method [322].

Figure 6.15(a) shows two typical examples of numerical simulations (markers) and a fit (continuous line) for two different values of  $\alpha$ . In general, modes of different frequency exhibit different decay rates  $1/\tau_{k_0}$ . However, when strong chaos is generated in the structure, the distribution of  $\tau_{k_0}$  converges towards a frequency-independent delta function. In fact, calculations that start from initial conditions already belonging to the chaotic region of phase space will always be distributed according to the same probability distribution, which defines the so-called "natural invariant measures" of

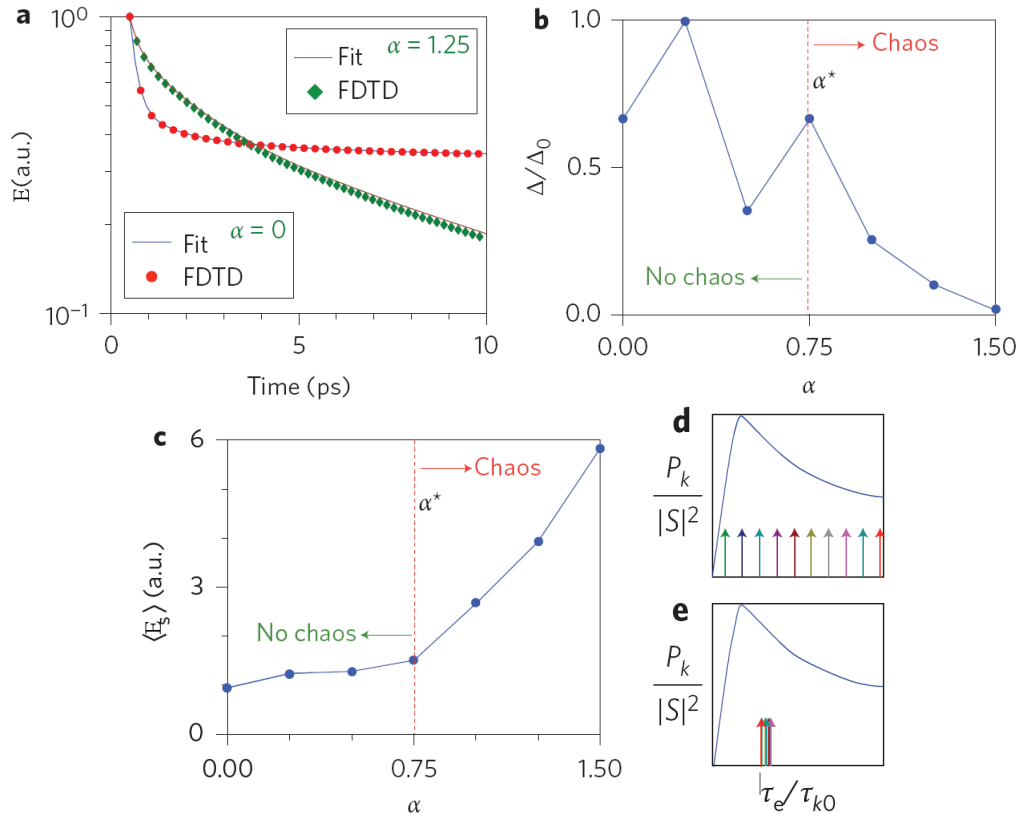


Figure 6.15: (a) Log-plot of the energy  $E$  relaxation dynamics for  $\alpha = 0$  and  $\alpha = 1.25$ , showing FDTD results (symbols) and Prony exponential fits (solid lines). (b) Normalized distribution of the difference between the maximum and minimum decay constants  $\Delta(\alpha)/\Delta(0) \equiv \Delta/\Delta_0$  versus  $\alpha$ . (c) Steady-state energy distribution  $\langle E_s \rangle = \langle E \rangle$  ( $t = 45$  fs) for varying values of  $\alpha$ . (d,e) Effects of convergence of the decay constants  $\tau_k$  on the power  $P_k$  transferred into the structure. This behaviour is plotted versus  $\tau_e/\tau_{k0}$  as a solid line. In the non-chaotic situation (d) the distribution of  $\tau_e/\tau_{k0}$  (coloured arrows) is broad and only a few frequencies efficiently transfer power. In the strongly chaotic case (e), conversely, a condensed distribution of  $\tau_e/\tau_{k0}$  yields the same contribution for all wavelengths and a much larger number of frequencies contribute to store energy.

the system [323]. As a result, when the entire phase space is dominated by chaos, we observe the same evolution of the decay rates, for all possible initial conditions, towards a frequency-independent decay rate  $\tau_{k_0} = \tau_0$ . A convenient way of highlighting this dynamics is to plot the difference between the maximum and the minimum decay constant,  $\Delta = \max(\tau_{k_0}) - \min(\tau_{k_0})$ , for different values of  $\alpha$  (Fig. 6.15b). We clearly observe a transition scenario. Below the chaos threshold,  $\alpha \leq \alpha^*$ , the dynamics simply shows an oscillation of  $\Delta$  around the same average value, while above it ( $\alpha \geq \alpha^*$ ), a clear convergence of  $\Delta \rightarrow 0$  is observed. The value  $\alpha^*$  depends on the specific geometry of the chaotic resonator, and can be assessed by calculating the relative area of the system phase space that encompasses chaos. The effect of this convergence towards a single lifetime of all the modes on the energy collected by the resonator can be readily evaluated from Eq. 6.42. The total power transferred into the structure, in particular, then becomes frequency-independent ( $P_k = P_0 = 2|S|^2(1 + \tau_e/\tau_0)^{-2}\tau_e/\tau_0$ ), and every mode contributes to the same extent to storing energy inside the resonator. When many modes are present in the resonator, their large number results in a coherent buildup process that leads to a significant accumulation of energy (Fig. 6.14, 6.15c). In the non-chaotic case, conversely, much fewer modes are able to efficiently transfer energy into the resonator due to the mismatch between  $\tau_{k_0}$  and  $\tau_e$  (Fig. 6.15d,e) and the system can store relatively less energy.

The chaos-assisted energy buildup process observed when  $\alpha \geq \alpha^*$  originates from the fundamental thermodynamic principle of equipartition, which can be highlighted using Eq. 6.42. By substituting  $\tau_{k_0} = \tau_0$  into the left-hand side of Eq. 6.42, and assuming a dense distribution of modes, with wavelength separation  $\lambda_{k+1} - \lambda_k = \delta\lambda = \lambda$ , we obtain

$$\frac{\delta E}{\delta \lambda} = \text{const} = E_0 \quad (6.43)$$

which can be regarded as an equipartition theorem, with the energy equally distributed among all degrees of freedom (that is, the spectral wavelengths)

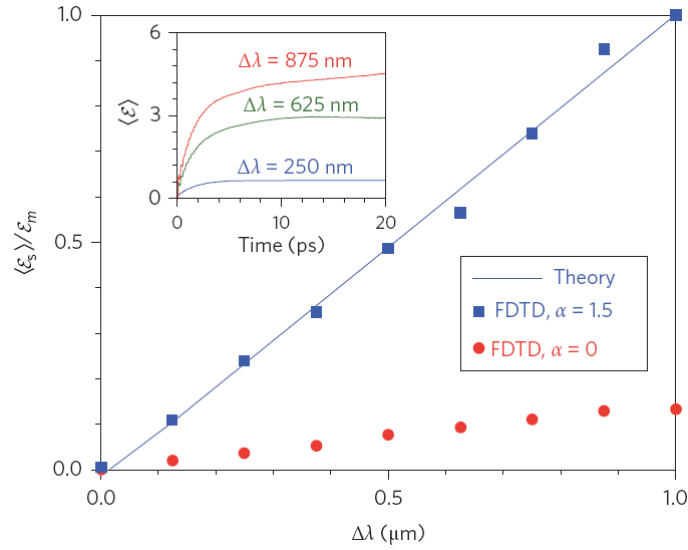


Figure 6.16: Simulation results for a variable-bandwidth source. FDTD computed steady-state average energy  $\langle E_s \rangle$  versus bandwidth  $\Delta\lambda$  for  $\alpha = 0$  (circle markers) and  $\alpha = 1.5$  (square markers). The solid line indicates the behaviour predicted by Eq. 6.43. The energy  $\langle E_s \rangle$  is normalized to the maximum value  $E_m$  attained for  $\alpha = 1.5$  and  $\Delta\lambda = 1\mu\text{m}$ . (Inset) FDTD calculated average energy  $\langle E \rangle$  versus time for  $\alpha = 1.5$  and different normalized bandwidth  $\Delta\lambda$  symmetrically centred at 800 nm.

due to the strongly chaotic nature of the system. Equipartition is at the foundation of classical statistical mechanics, and forms the basis for thermodynamic ensembles and the observation of different phases of matter [324]. Applied to photonics, we have the remarkable opportunity of exploiting this principle for enhancing the energy confinement properties of photonic structures. As already discussed above, this opportunity was confirmed by calculating the energy stored for a broadband source in the two limiting conditions of a fully chaotic geometry (Fig. 6.16, squares) and a non-chaotic geometry (Fig. 6.16, circles), finding a sixfold enhancement in the chaotic case.

Energy equipartition and chaotic energy harvesting occur because of the convergence of the modal lifetimes towards a single value  $\tau_{k_0}$ . This phenomenon has been investigated in real structures with controllable chaoticity, such as planar two-dimensional stadium-shaped resonators in planar PCs fabricated in silicon on insulator (SOI) where the chaoticity of the structure

has been tuned to reach full chaos. The results are in perfect agreement with the theoretical predictions and ab-initio simulations [302]. Similar compatible results occurred also when fine-tuning of chaos is not provided such as in three-dimensional PCs composed by a low-density monolayer of polystyrene microspheres that are being deformed by mechanical compression in order to obtain an asymmetric shape, thus providing chaotic light motion [302].

These very important results, with wide possible real-world practical implications, has been exploited to develop a compact polarization splitter.

## 6.5 The polarization splitter device

This section is dedicated to describe all the steps for the development and optimization of the PC polarization splitter device and to present the results obtained by simulations. The aim of developing this design was direct to its exploitation in astrophysical and cosmological observations in the microwaves dedicated to polarization measurement with very high sensitivity. In this context we developed the device in order to work at 100 GHz ( $\lambda \simeq 3mm$ ). Moreover in the context of a possible use on balloon-borne experiments or satellite missions we took into account that the device must be compact and robust to pass safely through the launch process.

The first step of the development is the selection of the materials. Considering the two media used to form the periodic lattice with different dielectric permittivity, in Section 6.1.2 we demonstrated that the higher the difference between the two dielectric indexes is, the larger is the photonic band gap. However, there are limitations to the possible materials given by their availability and the access to the instruments able to build the device that can result in an unfeasible costs for its realization. For these reasons, in our simulations the periodic lattice is formed by silicon, that is very common (thus, has a relatively low cost) and at around 100 GHz has a dielectric index of  $\varepsilon \simeq 12$  [325,326]. In order to maximize the difference of the dielectric indexes of the two materials, the second one is air that has  $\varepsilon = 1$ .

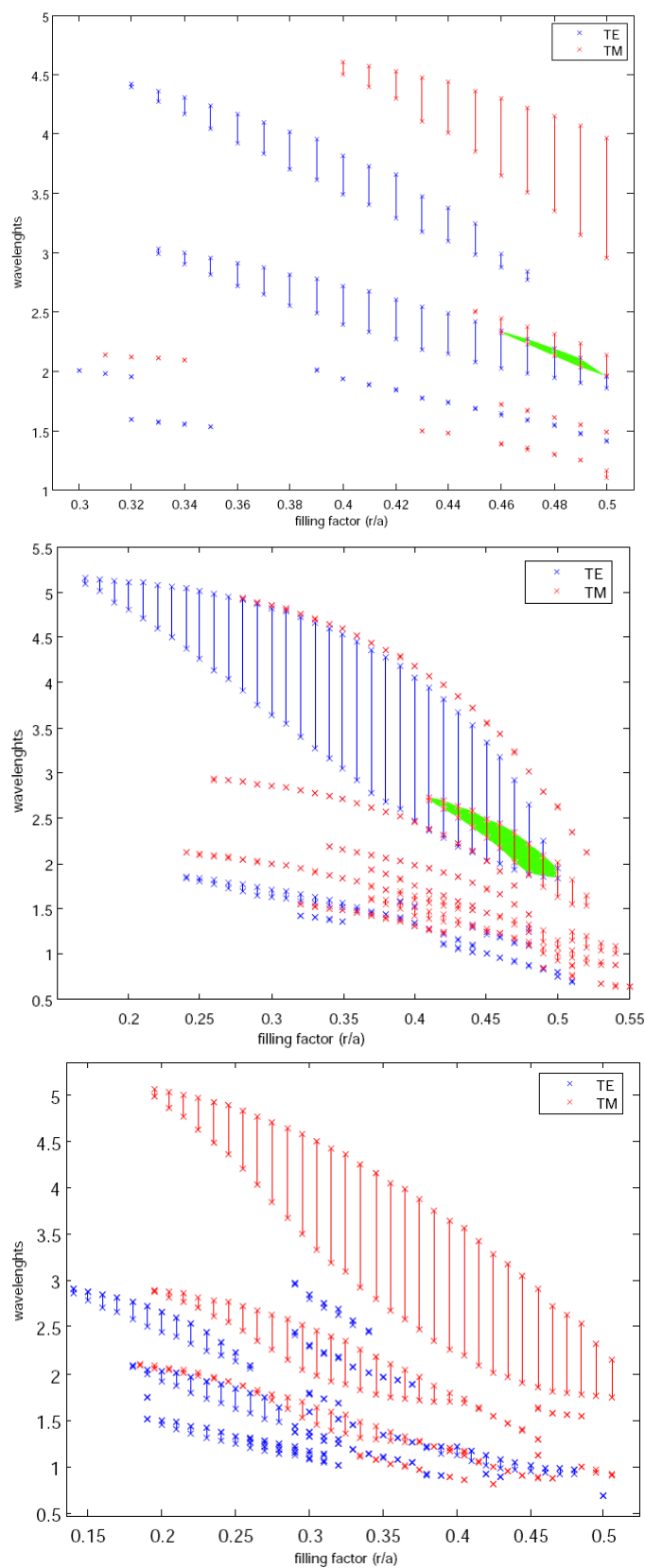


Figure 6.17: The extensions of the photonic band gaps for TE and TM modes (respectively blue and red lines) versus the filling factor ( $r/a$ ) for different lattices: square (*top panel*), triangular (*center panel*) and honeycomb (*bottom panel*). For all the cases the PC are constituted of holes of radius  $r$  inside a slab of silicon ( $\epsilon \simeq 12$ ).

Once we had chosen the materials, we explored the band diagrams of different kind of lattices. For our aims we opted for a two-dimensional PC because of a large number of possible lattices and their easier production compared to three-dimensional ones. On its third dimension, the dielectric index is constant and as long as the wavelengths manipulated in order to excite the fundamental mode inside the waveguides and the cavity. With the necessity of a robust device, we discarded the possibility of displacing silicon columns in air for obvious reasons. Thus, we considered holes (that is column of air) inside a slab of silicon. With this configuration the most used holes dispositions are: square, triangular and honeycomb lattice. Using the MPB program we obtained the band diagrams for each lattice and for different filling factors that is the ratio between the radius,  $r$ , of the columns (or holes) and the scale factor  $a$  that identify the period inside the lattice. We explored the range  $r/a = [0.1, 0.6]$  and selected the width of the opened photonic band gaps. In Fig. 6.17 we show the width of the photonic band gaps of the TE and TM modes versus the filling factor. The green regions contains the complete band gap in which both TE and TM modes have a band gap.

In order to have waveguides and cavities in which both TE and TM modes are guided without losses, we needed to choose the lattice and the radius of the columns among the ones that present a complete band gap. As shown in Fig. 6.17, the maximum extension of the complete band gap is exhibited by the triangular lattice. In order to guarantee also the robustness of the device we opted for the lattice with holes of radius  $r = 0.46a$  that avoids the superposition of the holes and also keeps a sufficient quantity of silicon between them. The corresponding complete band gap falls in the range of wavelengths  $\lambda = [2.17, 2.44]a$ .

These results have been confirmed by the NANOCPP code in which we generated a Gaussian source with a broad bandwidth inside the lattice. The wavelengths that do not present excited Bloch waves belong to the photonic band gap. In Fig. 6.18 there are the band diagrams of this lattice obtained

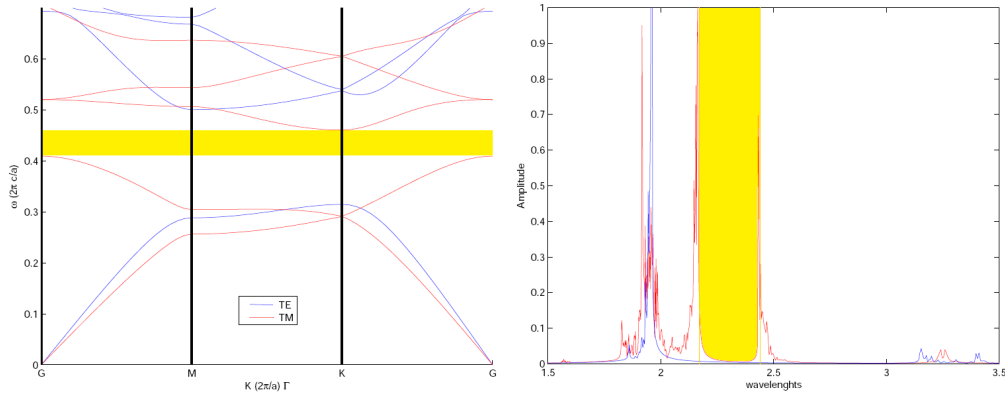


Figure 6.18: Band diagram of the triangular lattice constituted by silicon ( $\varepsilon = 12$ ) with air columns of radius  $r = 0.46a$  obtained with different programs: MPB (*left*) and NANOCPP (*right*). Results are in good agreement showing a complete band gap in the range  $\lambda = [2.17, 2.44]a$ .

with the two codes showing a very good agreement in the width of the complete band gap.

Once the parameters of the lattice and the materials have been chosen, we inserted waveguides and cavities inside the PC, in order to obtain the separation of the polarizations of an incident signal. We used the NANOCPP code, that implements the FDTD method described in Section 6.2, to perform 2D simulations of the device. The results of the code describe in time electromagnetic waves flowing into the device from which we could quantify and optimize its properties in the polarizations splitting. The resulting device is shown in Fig. 6.19.

The electromagnetic field with both the polarizations enters the device from the waveguide A and flows into the resonator cavity at the center of the device. Few periods of the PC at the borders of the cavity are sufficient to trap all the electromagnetic field inside the cavity without losses. The shape of the cavity is a quarter of billiard that as demonstrated in Section 6.4 has the property to enclose six times the energy compared to a classical shape of the same area and also an higher number of modes can be excited. Inside the cavity, accordingly to the multimode interference described in Section 6.3, the

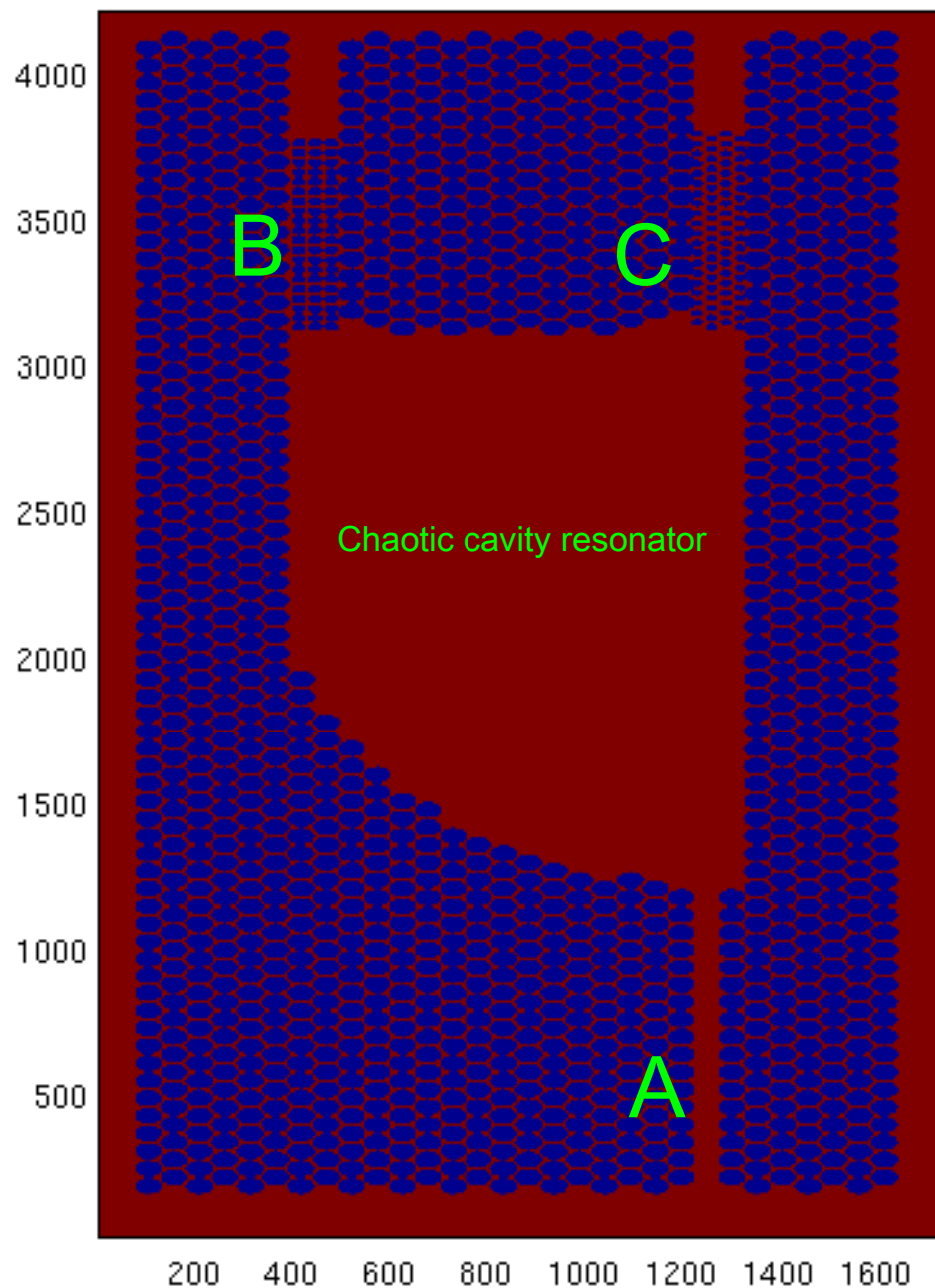


Figure 6.19: The dielectric distribution of the polarization splitter device seen from the edge with index  $\epsilon = 1$  (blue regions) and  $\epsilon = 12$  (red regions). Through the waveguide A the electromagnetic field enters the chaotic resonator that is a quarter of billiard. Inside the cavity the polarizations are separated and the TE modes flow through the waveguide B, while TM modes through the waveguide C. The PC inside the two waveguides B and C have the function of filters that further suppress the presence of the wrong polarization in the output waveguides and enhance the separation properties of the device.

modes excited generate regions of constructive and destructive interference. Since TE and TM modes are described by different Bloch waves that excite modes with different properties, there are regions in which one polarization has a maximum in the field while the other is close to a minimum. In correspondence to these regions we placed the two output waveguides that collect only one polarization with a very low spurious signal coming from the residual field of the other polarization. Thus, the two polarizations are easily divided and the TE modes flow out of the device from the waveguide B, while the TM modes from the waveguide C.

In addition to this mechanism, in order to increase the level of separation, we placed two filters in correspondence to the output waveguides. These filters are PC constituted by different lattices that present a photonic band gap only for the spurious polarization that flows inside the "wrong" output waveguide. Thus, for example, while the TE modes go through the filter inside the waveguide B with a good level of efficiency, TM modes are reflected by the same filter decreasing their presence inside the waveguide B by many orders of magnitude. In waveguide B we placed a square lattice of columns of air in the silicon with  $r = 0.244a$ . In waveguide C there is a triangular lattice of columns of air in silicon with  $r = 0.198a$ . The radii of the lattices are chosen in order to have the maximum efficiency for the correct polarization to go through the filter.

In Fig. 6.20(*top panels*) we show a snapshot of the electromagnetic energy density after  $t = 0.5$  ns. At  $t = 0$  we placed a monochromatic ( $\nu = 100$  GHz) plane wave source at the beginning of the waveguide A. The source is TE (Fig. 6.20 *top left panel*) or TM (Fig. 6.20 *top right panel*) polarized. The snapshots show that the field enters the cavity without losses and flows through only one of the two output waveguides depending on the polarization direction.

In order to quantify the properties of the polarization splitter we considered two measurable quantities in our 2D simulations: the efficiency and the crosstalk. The efficiency is calculated as the ratio between the energy that

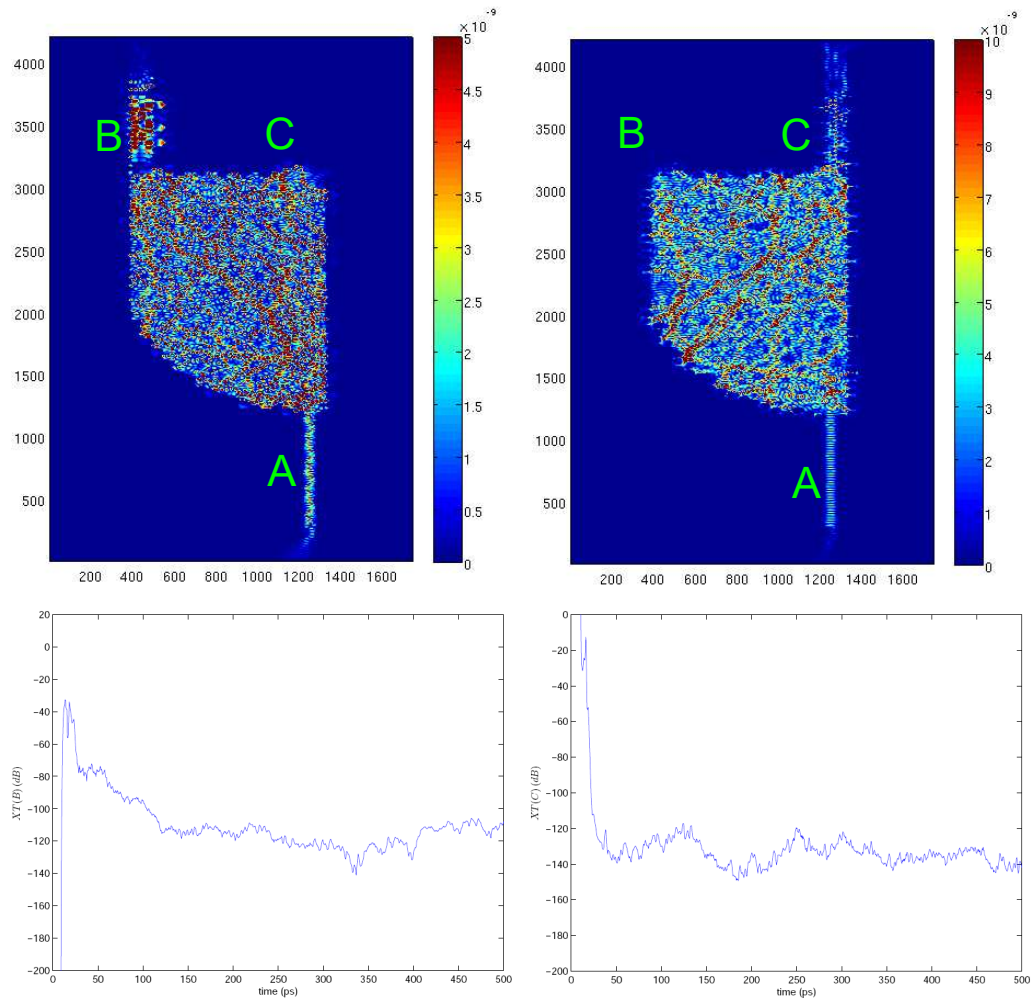


Figure 6.20: (*Top panels*) Snapshot of the electromagnetic energy density after  $t = 0.5$  ns. We simulated a monochromatic ( $\nu = 100$  GHz) plane wave source TE (*top left panel*) or TM polarized (*top right panel*) at the beginning of waveguide A. Letters B and C show the position of the output waveguide. Colours are related to the intensity of the field. (*Bottom panels*) Plot of the crosstalk versus time in waveguide B (*Bottom left panel*) and waveguide C (*Bottom right panel*) for the same monochromatic electromagnetic wave. Crosstalk is measured in dB.

flows through the output waveguide (B for TE modes, C for TM modes) and the energy of the polarized field (TE or TM) that enters the cavity from the waveguide A. Considering almost negligible the spurious signal in the second output waveguide, the efficiency after 0.5 ns is 72% for TE modes in waveguide B and 83% for TM modes in waveguide C. The crosstalk,  $XT$ , instead defines the level of separation by measuring the ratio between the spurious signal of the undesired polarization in one output waveguide and the signal of the correct polarization in the same waveguide. In our device, it is:

$$XT(B) = 10 \log_{10} \left( \frac{TM(B)}{TE(B)} \right) \quad XT(C) = 10 \log_{10} \left( \frac{TE(C)}{TM(C)} \right) \quad (6.44)$$

where B and C identify the waveguides.

Fig. 6.20(*bottom panels*) shows the crosstalk versus time for the two output waveguides B and C. After a brief time in which the cavity needs to be charged, the level of crosstalk reaches almost stable values around  $-111 \text{ dB}$  for the waveguide B and  $-139 \text{ dB}$  for waveguide C. When we consider an electromagnetic wave with a bandwidth as large as the complete photonic band gap  $\lambda = [2.17, 2.44]a$ , crosstalk results to be about  $-60 \text{ dB}$  for the waveguide B and  $-100 \text{ dB}$  for the waveguide C. This last case shows a little bit worse results because of the lower efficiency of the filters for such a broad bandwidth. However, these numbers are very competitive compared to the characteristics, for example, of the OMT of the *Planck* LFI instrument as described in Section 1.4 for which crosstalk is always higher than  $-40 \text{ dB}$ . Also, the planar orthomode transducers used in the ACTpol camera for the polarization measurements shows a crosstalk of about  $-50 \text{ dB}$  [327], while the feedhorn and detector arrays of the SPTpol camera exhibit a crosstalk higher than  $\sim -25 \text{ dB}$  [328]. The scientific interest in the detection of (large scale) primordial B modes shows the importance to achieve high level of separation of the two polarizations, that means very low values of crosstalk. In fact, the contaminations in the polarization separation causes the presence of a spurious signal in the BB APS proportional to the amplitude of the EE angular spectrum, since the BB spectrum is at least one order of magnitude

lower than the EE spectrum. Consequently, the accuracy in the polarization splitting contributes to the total sensitivity in the BB extraction. Passing from  $-40$  dB to  $-100$  dB manages to reduce of about 6 order of magnitudes the level of contamination and consequently to have a great improvement in the polarization sensitivity of the instrument.

With the encouraging simulation results we developed a real project by setting the scale factor  $a$  in order to have the 100 GHz frequency exactly at the center of the band gap. This design is the stamp for the production of a prototype to be tested in labs. For this real case, the bandwidth of the complete photonic band gap is enclosed in the range  $\nu \in [94.3, 106.1]$  GHz. The device dimensions are  $8.7 \times 3.4 \times 0.3$  cm with the radius of the air columns  $r = 0.6$  mm. At the moment we are working to perform lab tests in order to verify the results obtained with the simulations and proceed with other optimizations. Although, the device is quite bigger than the OMT developed for the ACT and SPT ground-based experiments, the very competitive crosstalk results exhibited in the simulations are encouraging for its implementation between the optics and the receivers of ground-based telescopes dedicated to high precision polarization measurements of microwave signals. Moreover, future developments will achieve the integration of the receiver inside the polarization splitter in order to lower the power lost and improve the efficiency of the device.

# Conclusions

The CMB anisotropies are a fundamental tool to investigate the standard cosmological model and to probe the early stages of the Universe. In the epoch of precision cosmology, the accuracy of the results are strongly dependent on the data analysis tools that scientists apply to the maps obtained by the instruments. Recent WMAP and *Planck* results confirmed the standard cosmological model and put tighter constraints to its parameters. Also, in order to investigate the still open questions, huge efforts are dedicated to improve the instrumental performances to acquire more accurate data, with higher resolution and sensitivity and suppression of potential systematic effects.

In this context, this PhD thesis is dedicated to the optimization of some tools and aspects of the data analysis, to their application to the WMAP and *Planck* data, contributing to the most recent *Planck* results published [8] (Chapter 3 - 5). In addition, in this thesis we investigated the possibility of exploiting a technology called Photonic Crystals in order to produce a polarization splitter with high performances suitable for future observations (Chapter 6).

Chapter 3 is divided into three parts. In the first part, the routines of the HEALPix pixelization package that allow to change the coordinates of the maps are discussed and their performances analysed. The change of coordinates is useful in order to compare data obtained by different instruments from the ground, on balloons or from satellite missions and eventually to combine them achieving better results. We described two different meth-

ods to perform the change of coordinates that work respectively in pixel space (pixel method) or in harmonic space (harmonic method). In the pixel method, the change of coordinates is performed by rotating the vector, that indicates the pixel, from the new coordinates to the old ones and taking the value of the pixel indicated by the rotated vector. The main source of error comes from the mismatch between the initial and the final pixel. We optimized the method showing that by increasing the resolution of the map in the new coordinates, the mismatch effect is mitigated and the errors that affect the rotated map are consistently minimized. In the harmonic method the main source of error comes from the extraction of the  $a_{\ell m}$  coefficients from the maps and the reconstruction of the map at the end of the change of coordinates. We applied these methods to a synthetic CMB map and to either foreground cleaned or not cleaned WMAP 7 year maps both quantifying the errors in the pixel intensities and in the extracted APS. For pure CMB map the harmonic method is very accurate and works better affecting pixels with errors of the order of  $0.05\mu K$  and affecting the APS of the rotated map with almost negligible errors. However, in the WMAP maps, the pixel method shows lower errors in pixel intensities of about  $5\mu K$ , but the harmonic method is still the most powerful to keep unchanged the original APS of the map showing errors at  $\ell = 600$  lower than 10%. Therefore, the choice of the method depends on the properties of the maps are going to be analysed. We also demonstrated that, for both the optimized methods, the errors that affect the rotated maps are well below the sensitivity of *Planck* data, but they can be not negligible for data from future missions.

An important aspect of CMB data analysis is the estimation of the APS at large angular scales ( $\ell < 100$ ). At these scales, the likelihood codes that explore the parameters of the standard cosmological model work directly using the maps data. Moreover, low resolution maps and their APS analysis are very useful to test for the presence of large scales anomalies in the CMB maps. These can be imprints of deviations from the standard cosmological model or from the standard inflationary mechanisms, or imprints of spurious

signals due to systematics, data analysis artefacts or residual foregrounds. An accurate extraction of the APS at large angular scales is crucial for testing the likelihood results and to determine the nature of the CMB anomalies.

Therefore, in the second part of Chapter 3, we considered two APS estimators: the optimal Quadratic Maximum Likelihood (QML) estimator implemented in the code called BolPol and working in pixel space, and the pseudo- $C_\ell$  estimator implemented in the code called Cromaster and working in the harmonic space. The QML method is optimal in the sense that it provides the lowest error bars to the APS extracted, but it is computationally demanding and needs to be run on clusters even to analyse low resolution all sky maps up to  $\ell \simeq 190$  or, in principle, limited sky patches at high resolution. The pseudo- $C_\ell$  method is fast and light and can be run with a common laptop to extract the APS to higher range of multipoles ( $\ell > 3000$ ). Focusing on the large angular scales ( $\ell < 190$ ), we compared the two methods and quantitatively determined the differences in their accuracies in extracting the APS. By exploiting 1000 realistic Monte Carlo (MC) simulations using two different masks that exclude the 20% and the 48% of the sky, respectively, we found that the QML approach is always markedly better in the range  $2 \leq \ell \leq 100$  and the differences in accuracy increase as the number of excluded pixels increases. We have also analysed how the accuracies of the two APS methods impact on some typical large angular scales anomaly estimators like the TT Parity estimator and Variance estimator, demonstrating that the use of BolPol for low resolution map analyses will bring to tighter constraints for these kinds of estimators.

In the third part of Chapter 3, we further considered various methods for downgrading high resolution maps to low resolution. During this process the resulting maps can be affected by errors due to aliasing. Through MC simulations we compared the different methods looking for the one that affects the maps the less. Our results suggest to convolve the map with a beam with FWHM equal to twice the side of the pixel of the low resolution map before downgrading it.

In Chapter 4 we described the results obtained by applying the APS estimator BolPol to the low resolution maps provided by the four component separation *Planck* tools (SMICA, NILC, Commander-ruler, SEVEM) and the WMAP ILC. We compared their APS demonstrating the good agreement of the *Planck* component separation methods that show relative differences of typically  $\lesssim 50\mu K^2$  at  $\ell \geq 15$ . We displayed the small differences between the *Planck* and the WMAP APS, where the last shows residuals typically of the order of  $100\mu K^2$  at  $\ell \geq 30$ . The WMAP low- $\ell$  spectrum is 2.5-3% higher than the *Planck* spectrum and the effect is robust with respect to foreground removal and power spectrum evaluation algorithms. In addition, we noted the anomalous low APS of all the maps when they are compared with the *Planck*  $\Lambda$ CDM best fit model especially for the lowest multipoles ( $\ell = 2 - 3$ ). In order to investigate the anomalies in the APS of the low resolution CMB maps, we applied two particular large angular scale anomaly estimators (the TT parity and the TT Variance) to the WMAP 9 year ILC map. Our results show that at large scales the WMAP data are highly anomalous. For the parity asymmetry, the statistical significance for the presence of an anomaly for  $\ell_{max} = 22$  is  $> 99.9\%$  and increases including the range of multipoles up to  $\ell_{max} = 25$  suggesting that the odd parity preference cannot be simply attributed to the low quadrupole power. The low amplitude of the TT variance measured for the WMAP 9 year data is dominated by the contributions from lowest multipoles ( $\ell = 2 - 3$ ). The results show that increasing the Galactic mask, the WMAP TT variance is more and more anomalous and, in particular, for one of the most aggressive masks, that covers the 64% of the sky, the temperature variance is not consistent with  $\Lambda$ CDM model at more than 99.99% C.L. in the  $\ell_{max}$  range [25, 35].

The possibility to accurately study the primordial phases of our Universe through the analysis of the CMB anisotropy field relies on our capability to precisely extract the cosmological signal from the observations by applying component separation tools to accurately remove the foregrounds from the maps. The Galactic synchrotron emission is one of the main sources of diffuse

foregrounds for CMB surveys and it is the dominant one at intermediate and large angular scales ( $\theta \geq 1^\circ$ ) far from the Galactic plane at  $\nu \leq 50$  GHz. The study of the diffuse synchrotron emission will also contribute to build 3D Galactic maps of the free electron distribution and of the Galactic magnetic field both responsible for this emission. In Chapter 5 we applied Cromaster to the 408 MHz and 1.42 GHz surveys focusing on the extraction of the APS of selected regions of particular interest for their morphology or for their emission intensity, such as the loops and the spurs. We observed a power law behaviour of the APS of all the considered regions probably related to a turbulent regime of the Galactic magnetic field. For each region considered, we determined the slope  $\alpha$  and the amplitude  $K$  of the APS. The results show a significant variation across the sky of the slope that for example at 408 MHz varies from  $\alpha = -1.63$  of the Loop 1 region to  $\alpha = -0.48$  of the Void South region. Moreover, using the APS extracted at the two different frequencies we estimated the frequency spectral index of the synchrotron emission of the same selected regions. The results show a good agreement with the previous results at the multipoles  $\ell \leq 100$ . However, the results prefer a slightly higher spectral index, around 3.2 and a slight scatter is shown between the APS of different regions and even inside the same APS along the multipole range. These results give new information about the properties of the synchrotron emission features and advise against the use of a unique spectral index for the whole radio map when we use it as a synchrotron template in the component separation tools dedicated to the CMB analysis.

The analysis of CMB polarization is fundamental to investigate still opened questions including the inflationary mechanism, the nature of the Dark Energy and the origins of the observed anomalies. Moreover, new accurate microwave polarization measurements will produce important data suitable for the astrophysical studies of the foreground emissions. In Chapter 6 we described the technology of the Photonic Crystals, that are periodic dielectric media in 1, 2 or 3 dimensions. For certain periodic dispositions of two different dielectric media, photons of a determined range of frequency can-

not propagate through them. This property has been used in this thesis to develop a polarization splitter device with very high efficiency and very low crosstalk. We firstly demonstrated that using chaotic Photonic Crystal resonators, we can store six times the electromagnetic energy in the same area compared to regular cavities. Then, we presented the polarization splitter device that exploits the multimode interference and a chaotic resonator to separate the polarizations of an incoming electromagnetic field. We showed also some optimizations in order to achieve the best performances at 100 GHz. Using ab-initio simulations, implemented in the code called NANOCPP, we tested the performances of the device, finding an efficiency higher than 70% and a crosstalk lower than  $-110$  dB for a monochromatic radiation at 100 GHz and lower than  $-60$  dB for a larger range of frequencies  $\nu \in [94.3, 106.1]$  GHz. In the second case the performances are lower because of the efficiency of the filters used inside the polarization splitter. However, these values of crosstalk are very competitive with the actual polarization splitter devices used by a satellite as *Planck* and ground based telescopes such as ACT and SPT. Although the project of a polarization splitter is still under validation and characterization tests in laboratory, this device would perfectly suit between the optics and the receivers of future ground-based telescopes dedicated to high precision polarization measurements of microwave signals, in particular at small scales.

In 2014 *Planck* will publish its results about the CMB anisotropies in polarization. The methods described in this thesis will be extended to the analysis of *Planck* polarization data. Future developments of the polarization splitter will be dedicated to reduce its dimensions and achieve the integration of the receiver inside the polarization splitter in order to lower the power lost and improve the efficiency of the device for possible future implementations.

# Acknowledgements

The results described in this thesis have been possible only through the *Planck* mission and its data. So, my first acknowledgements go to the *Planck* Collaboration, the LFI Consortium and Core Team, and the LFI Principal Investigator Nazzareno Mandolesi. This work was supported by the Bologna University and also by the Marco Polo program, allowing my research activity at the University of Manchester's School of Physics and Astronomy. I gratefully thank the Jodrell Bank Centre for Astrophysics for the logistic support at Manchester and Dr. Paddy Leahy for his supervision of my research activity there. This work was supported by ASI through ASI/INAF Agreement I/072/09/0 for the Planck LFI Activity of Phase E2 and by MIUR through PRIN 2009 (grant n. 2009XZ54H2). I acknowledge the use of computing facilities at IASF, CINECA (Italy), NERSC (USA) and KAUST (Saudi Arabia). I acknowledge the use of the HEALPix software [155] and analysis package for deriving the results in this thesis. I acknowledge the use of the Legacy Archive for Microwave Background Data Analysis (LAMBDA), part of the High Energy Astrophysics Science Archive Center (HEASARC). HEASARC/LAMBDA is a service of the Astrophysics Science Division at the NASA Goddard Space Flight Center. Radio maps was obtained by courtesy of P. Platania, L. La Porta, P. Reich and their collaborators that I gratefully thank. I especially thank A. Gruppuso and A. De Rosa for their important training in the use of BolPol and P. Natoli and G. Polenta for the use of Cromaster. I acknowledge the use of the CAMB code for cosmic microwave background anisotropies (<http://camb.info>).

My first thanks go to my supervisor Carlo Burigana that supported me step by step in my research activity through these three years with great patience. I gratefully thank Andrea Fratolocchi for its fundamental support in my Photonic Crystal's research. I especially thank Paolo de Bernardis and Silvia Masi for having believed in me and for giving me the occasion to arrive here. My thanks go also to Daniele Dallacasa for supporting me at the Bologna University.

I would like to thank the IASF for its logistic support and Alessandro Gruppuso, Fabio Finelli, Luca Valenziano and all the other IASF people who encouraged and stimulated me in the course of these last three years. A special thank goes to Mario, Daniela, Tiziana, Caterina, Adriano, Andrea and (yes, I have to admit) also to Enrico for having been more than colleagues, but real friends. With you everyday at IASF has been a nice surprise.

I special thank my parents, my grandparents and my brother for their everyday support and their love. I hope to make you proud now and in the future. A great thank goes to my wonderful girlfriend supporting me unflinching and bearing my scattering mood especially in these last months.

I thank also my piano teacher, Alfio Biuso, that not only taught me how to play the piano, but also to love the good music that followed and supported me through all these years.

I would like to thank my flatmates and friends Fabio and Veronica that have been my friendly teachers of the flatmate world. Also I thank all the new friends I found in Bologna especially Ghisa, Gaspe, Dave, Toro, Bastian, Save, Giulia, Eda and the others for the nights spent watching trash movies, playing cards, D&D, laser game or simply laughing together. A special thank goes to my old and new friends in Rome Manuel, Luca, Niccolò, Simone, Valeria, Maria Rita, Maria Chiara, Valeria, Laura, Leonardo, Giulia, Nico, Francesca, Erlind, Veronica, Mirko (I hope I named all of you...ops, and obviously Emilia...) that, although I moved to Bologna, are still my special friends with whom every week end has been special distracting and helping me to recharge the batteries and be ready for another week.

# Bibliography

- [1] A. A. Penzias and R. W. Wilson, “A Measurement of excess antenna temperature at 4080-Mc/s,” *Astrophys.J.*, vol. 142, pp. 419–421, 1965.
- [2] R. Dicke, P. Peebles, P. Roll, and D. Wilkinson, “Cosmic Black-Body Radiation,” *Astrophys.J.*, vol. 142, pp. 414–419, 1965.
- [3] R. Alpher, H. Bethe, and G. Gamow, “The origin of chemical elements,” *Phys.Rev.*, vol. 73, pp. 803–804, 1948.
- [4] J. C. Mather, E. Cheng, R. Shafer, C. Bennett, N. Boggess, *et al.*, “A Preliminary measurement of the Cosmic Microwave Background spectrum by the Cosmic Background Explorer (COBE) satellite,” *Astrophys.J.*, vol. 354, pp. L37–L40, 1990.
- [5] G. F. Smoot, C. Bennett, A. Kogut, E. Wright, J. Aymon, *et al.*, “Structure in the COBE differential microwave radiometer first year maps,” *Astrophys.J.*, vol. 396, pp. L1–L5, 1992.
- [6] P. de Bernardis, P. Ade, J. Bock, J. Bond, J. Borrill, *et al.*, “Multiple peaks in the angular power spectrum of the cosmic microwave background: Significance and consequences for cosmology,” *Astrophys.J.*, vol. 564, pp. 559–566, 2002.
- [7] C. Bennett *et al.*, “First year Wilkinson Microwave Anisotropy Probe (WMAP) observations: Preliminary maps and basic results,” *Astrophys.J.Suppl.*, vol. 148, p. 1, 2003.

- 
- [8] Planck Collaboration, “Planck 2013 results. I. Overview of products and scientific results,” *ArXiv 1303.5062*, 2013.
- [9] G. Sironi and G. Bonelli, “The temperature of the diffuse background radiation at 12 centimeter wavelength,” *Astrophys.J.*, vol. 311, pp. 418–424, 1986.
- [10] S. Levin, C. Witebsky, M. Bensadoun, M. Bersanelli, G. De Amici, *et al.*, “A measurement of the Cosmic Microwave Background radiation temperature at 21 cm,” *Astrophys. J.*, 1987.
- [11] G. de Amici, G. Smoot, J. Aymon, M. Bersanelli, A. Kogut, S. Levin, and C. Witebsky, “Measurement of the intensity of the cosmic background radiation at 3.7 GHz,” *Astrophys. J.*, vol. 329, pp. 556–566, 1988.
- [12] A. Kogut, M. Bersanelli, G. de Amici, S. Friedman, M. Griffith, B. Grossan, S. Levin, G. Smoot, and C. Witebsky, “The temperature of the cosmic microwave background radiation at a frequency of 10 GHz,” *Astrophys. J.*, vol. 325, pp. 1–15, 1988.
- [13] G. F. Smoot, G. De Amici, S. D. Friedman, C. Witebsky, G. Sironi, *et al.*, “Low Frequency Measurements of the Cosmic Background Radiation Spectrum,” *Astrophys.J.*, vol. 291, pp. L23–L27, 1985.
- [14] P. Lubin, T. Villela, G. Epstein, and G. Smoot, “A map of the cosmic background radiation at 3 millimeters,” *Astrophys.J.Letters*, vol. 298, pp. L1–L5, 1985.
- [15] D. Fixsen, E. Cheng, and D. Wilkinson, “Large-Scale Anisotropy in the 2.7-K Radiation with a Balloon-Borne Maser Radiometer at 24.5 GHz,” *Physical Review Letters*, vol. 50, pp. 620–622, 1983.
- [16] N. Mandolesi, P. Calzolari, S. Cortiglioni, F. Delpino, and G. Sironi, “Large-scale homogeneity of the universe measured by the microwave background,” *Nature*, vol. 319, pp. 751–753, 1986.

- [17] I. Strukov, A. Brukhanov, D. Skulachev, and M. Sazhin, “The Relikt-1 experiment - New results,” *MNRAS*, vol. 258, pp. 37P–40P, 1992.
- [18] G. Lemaitre, “The Expanding Universe,” *MNRAS*, vol. 91, pp. 490–501, 1931.
- [19] A. Friedmann, “Über die Krümmung des Raumes,” *Zeitschrift für Physik*, vol. 10, pp. 377–386, 1922.
- [20] V. M. Slipher, “Nebulae,” *Proc.Am.Phil.Soc.*, vol. 56, pp. 403–409, 1917.
- [21] E. Hubble, “A relation between distance and radial velocity among extra-galactic nebulae,” *Proc.Nat.Acad.Sci.*, vol. 15, pp. 168–173, 1929.
- [22] S. Perlmutter, S. Gabi, G. Goldhaber, A. Goobar, D. E. Groom, I. M. Hook, Kim, *et al.*, “Measurements of the Cosmological Parameters Omega and Lambda from the First Seven Supernovae at  $Z \geq 0.35$ ,” *Astrophys.J.*, vol. 483, p. 565, 1997.
- [23] A. G. Riess, A. V. Filippenko, P. Challis, A. Clocchiatti, A. Diercks, P. M. Garnavich, Gilliland, *et al.*, “Observational Evidence from Supernovae for an Accelerating Universe and a Cosmological Constant,” *The Astronomical Journal*, vol. 116, pp. 1009–1038, 1998.
- [24] A. H. Guth, “The Inflationary Universe: A Possible Solution to the Horizon and Flatness Problems,” *Phys.Rev.*, vol. D23, pp. 347–356, 1981.
- [25] A. A. Starobinsky, “A New Type of Isotropic Cosmological Models Without Singularity,” *Phys.Lett.*, vol. B91, pp. 99–102, 1980.
- [26] D. Langlois, “Lectures on inflation and cosmological perturbations,” *Lect.Notes Phys.*, vol. 800, pp. 1–57, 2010.
- [27] J. D. Jackson, *Classical electrodynamics*. Wiley, 3rd ed., 1999.

- [28] R. Sachs and A. Wolfe, “Perturbations of a cosmological model and angular variations of the microwave background,” *Astrophys.J.*, vol. 147, pp. 73–90, 1967.
- [29] J. Silk, “Cosmic black body radiation and galaxy formation,” *Astrophys.J.*, vol. 151, pp. 459–471, 1968.
- [30] G. Hinshaw *et al.*, “Three-year Wilkinson Microwave Anisotropy Probe (WMAP) observations: temperature analysis,” *Astrophys.J.Suppl.*, vol. 170, p. 288, 2007.
- [31] C. Bennett *et al.*, “Nine-Year Wilkinson Microwave Anisotropy Probe (WMAP) Observations: Final Maps and Results,” *Astrophys.J.Suppl.*, vol. 208, p. 20, 2013.
- [32] J. L. Sievers, R. A. Hlozek, M. R. Nolta, V. Acquaviva, G. E. Addison, P. A. R. Ade, P. Aguirre, *et al.*, “The Atacama Cosmology Telescope: Cosmological parameters from three seasons of data,” *ArXiv 1301.0824*, 2013.
- [33] K. Story, C. Reichardt, Z. Hou, R. Keisler, K. Aird, *et al.*, “A Measurement of the Cosmic Microwave Background Damping Tail from the 2500-square-degree SPT-SZ survey,” *ArXiv 1210.7231*, 2012.
- [34] Planck Collaboration, “Planck 2013 results. XVI. Cosmological parameters,” *ArXiv 1303.5076*, 2013.
- [35] M. Archidiacono, E. Giusarma, A. Melchiorri, and O. Mena, “Neutrino and Dark Radiation properties in light of latest CMB observations,” *Phys.Rev.*, vol. D87, p. 103519, 2013.
- [36] Planck Collaboration, “Planck 2013 results. XVII. Gravitational lensing by large-scale structure,” *ArXiv 1303.5077*, 2013.
- [37] Planck Collaboration, “Planck 2013 Results. XXIV. Constraints on primordial non-Gaussianity,” *ArXiv 1303.5084*, 2013.

- [38] C. Bennett, R. Hill, G. Hinshaw, D. Larson, K. Smith, *et al.*, “Seven-Year Wilkinson Microwave Anisotropy Probe (WMAP) Observations: Are There Cosmic Microwave Background Anomalies?,” *Astrophys.J.Suppl.*, vol. 192, p. 17, 2011.
- [39] Planck Collaboration, “Planck 2013 results. XIII. Galactic CO emission,” *ArXiv 1303.5073*, 2013.
- [40] B. Gold, N. Odegard, J. Weiland, R. Hill, A. Kogut, *et al.*, “Seven-Year Wilkinson Microwave Anisotropy Probe (WMAP) Observations: Galactic Foreground Emission,” *Astrophys.J.Suppl.*, vol. 192, p. 15, 2011.
- [41] Planck Collaboration, “Planck Intermediate Results. IX. Detection of the Galactic haze with Planck,” *ArXiv 1208.5483*, 2012.
- [42] G. Hinshaw *et al.*, “First year Wilkinson Microwave Anisotropy Probe (WMAP) observations: The Angular power spectrum,” *Astrophys.J.Suppl.*, vol. 148, p. 135, 2003.
- [43] D. Hanson *et al.*, “Detection of B-mode Polarization in the Cosmic Microwave Background with Data from the South Pole Telescope,” *ArXiv 1307.5830*, 2013.
- [44] D. Larson, J. Dunkley, G. Hinshaw, E. Komatsu, M. Nolta, *et al.*, “Seven-Year Wilkinson Microwave Anisotropy Probe (WMAP) Observations: Power Spectra and WMAP-Derived Parameters,” *Astrophys.J.Suppl.*, vol. 192, p. 16, 2011.
- [45] Planck Collaboration, “Planck (bluebook): The scientific programme,” *ESA-SCI*, 2005.
- [46] Burigana, C. and Popa, L.A. and Finelli, F. and Salvaterra, R. and De Zotti, G. and others, “Cosmological reionization after WMAP: Perspectives from PLANCK and future CMB missions,” *arXiv 0411415*, 2004.

- [47] S. M. Carroll, “Quintessence and the rest of the world,” *Phys.Rev.Lett.*, vol. 81, pp. 3067–3070, 1998.
- [48] L. Sorbo, “Parity violation in the Cosmic Microwave Background from a pseudoscalar inflaton,” *JCAP*, vol. 1106, p. 003, 2011.
- [49] J. Tauber, H. Norgaard-Nielsen, and P. e. a. Ade, “Planck pre-launch status: The optical system,” *Astron.Astrophys.*, vol. 520, p. 22, 2010.
- [50] M. Bersanelli, N. Mandolesi, and R. e. a. Butler, “Planck pre-launch status: Design and description of the Low Frequency Instrument,” *Astron.Astrophys.*, vol. 520, p. 21, 2010.
- [51] J.-M. Lamarre, J.-L. Puget, and P. e. a. Ade, “Planck pre-launch status: The HFI instrument, from specification to actual performance,” *Astron.Astrophys.*, vol. 520, p. 20, 2010.
- [52] G. Morgante, D. Pearson, and F. e. a. Melot, “Cryogenic characterization of the Planck sorption cooler system flight model,” *Journal of Instrumentation*, vol. 4, p. 2016, 2009.
- [53] T. Bradshaw and A. Orłowska, “Technology developments on the 4 K cooling system for ‘Planck’ and FIRST,” in *Sixth European Symposium on Space Environmental Control Systems* (T.-D. Guyenne, ed.), vol. 400 of *ESA Special Publication*, p. 465, 1997.
- [54] A. Benoît, A. Sirbi, and T. e. a. Bradshaw, “Development of a 0.1 K cryocooler for space applications,” in *Sixth European Symposium on Space Environmental Control Systems* (T.-D. Guyenne, ed.), vol. 400 of *ESA Special Publication*, p. 497, 1997.
- [55] O. D’Arcangelo, A. Simonetto, L. Figini, E. Pagana, F. Villa, *et al.*, “The PLANCK LFI flight model ortho-mode transducers,” *JINST*, vol. 4, p. T12005, 2009.

- [56] O. A. Peverini, R. Tascone, G. Virone, A. Olivieri, and R. Orta, “Ortho-mode transducer for Millim.-wave correlation receivers,” *IEEE Trans. Microw. Theory Tech.*, vol. 54, pp. 2042–2048, 2006.
- [57] J. Bock *et al.*, “Study of the Experimental Probe of Inflationary Cosmology (EPIC)-Intermediate Mission for NASA’s Einstein Inflation Probe,” *ArXiv 0906.1188*, 2009.
- [58] A. Kogut, D. Fixsen, D. Chuss, J. Dotson, E. Dwek, *et al.*, “The Primordial Inflation Explorer (PIXIE): A Nulling Polarimeter for Cosmic Microwave Background Observations,” *JCAP*, vol. 1107, p. 025, 2011.
- [59] K. W. Yoon, P. Ade, D. Barkats, J. Battle, E. Bierman, *et al.*, “The Robinson Gravitational Wave Background Telescope (BICEP): A bolometric large angular scale CMB polarimeter,” *ArXiv 0606278*, 2006.
- [60] M. Runyan, P. Ade, R. Bhatia, J. Bock, M. Daub, *et al.*, “The Arcminute Cosmology Bolometer Array Receiver,” *Astrophys.J.Suppl.*, vol. 149, p. 265, 2003.
- [61] B. Reichborn-Kjennerud, A. Aboobaker, P. Ade, F. Aubin, C. Baccigalupi, *et al.*, “EBEX: A balloon-borne CMB polarization experiment,” *ArXiv 1007.3672*, 2010.
- [62] Z. Kermish, P. Ade, A. Anthony, K. Arnold, K. Arnold, *et al.*, “The POLARBEAR Experiment,” *ArXiv 1210.7768*, 2012.
- [63] C. Bischoff *et al.*, “The QUIET Instrument,” *ArXiv 1207.5562*, 2012.
- [64] J. M. Fowler, M. Niemack, S. Dicker, A. Aboobaker, P. Ade, *et al.*, “Optical Design of the Atacama Cosmology Telescope and the Millimeter Bolometric Array Camera,” *Appl.Opt.*, vol. 46, pp. 3444–3454, 2007.
- [65] C. Collaboration, “COre (Cosmic Origins Explorer) A White Paper,” *ArXiv 1102.2181*, 2011.

- [66] P. Collaboration, “The Polarized Radiation Imaging and Spectroscopy Mission,” *ArXiv 1310.1554*, 2013.
- [67] W. Brandt, C. Lawrence, A. Readhead, J. Pakianathan, and T. Fiola, “Separation of foreground radiation from cosmic microwave background anisotropy using multifrequency measurements,” *Astrophys.J.*, vol. 424, pp. 1–21, 1994.
- [68] M. Tegmark and G. Efstathiou, “A method for subtracting foregrounds from multifrequency CMB sky maps,” *MNRAS*, vol. 281, pp. 1297–1314, 1996.
- [69] A. Jones, M. Hobson, and A. Lasenby, “Separation of foregrounds from cosmic microwave background observations with the map satellite,” *ArXiv 9810236*, 1998.
- [70] C. Baccigalupi, L. Bedini, C. Burigana, G. De Zotti, A. Farusi, *et al.*, “Neural networks and separation of cosmic microwave background and astrophysical signals in sky maps,” *MNRAS*, vol. 318, p. 769, 2000.
- [71] J. Delabrouille, J.-F. Cardoso, and G. Patanchon, “Multi-detector multi-component spectral matching and applications for CMB data analysis,” *MNRAS*, vol. 346, p. 1089, 2003.
- [72] H. Eriksen, C. Dickinson, C. Lawrence, C. Baccigalupi, A. Banday, *et al.*, “CMB component separation by parameter estimation,” *Astrophys.J.*, vol. 641, pp. 665–682, 2006.
- [73] F. Hansen, A. Banday, H. Eriksen, K. Gorski, and P. Lilje, “Foreground subtraction of cosmic microwave background maps using wi-fit (wavelet based high resolution fitting of internal templates),” *Astrophys.J.*, vol. 648, pp. 784–796, 2006.
- [74] P. Naselsky, O. Verkhodanov, L. Chiang, and I. Novikov, “Phase analysis of the 1 - year WMAP data and its application for the CMB foreground separation,” *Astrophys.J.*, 2003.

- [75] A. Bonaldi, L. Bedini, E. Salerno, C. Baccigalupi, and G. De Zotti, “Estimating the spectral indices of correlated astrophysical foregrounds by a second-order statistical approach,” *MNRAS*, vol. 373, pp. 263–270, 2006.
- [76] Planck Collaboration, “Planck 2013 results. XII. Component separation,” *ArXiv 1303.5072*, 2013.
- [77] J. Delabrouille, J. Cardoso, M. Le Jeune, *et al.*, “A full sky, low foreground, high resolution CMB map from WMAP,” *Astron. Astrophys.*, vol. 493, pp. 835–857, 2009.
- [78] R. Fernandez-Cobos, P. Vielva, R. Barreiro, and E. Martinez-Gonzalez, “Multi-resolution internal template cleaning: An application to the Wilkinson Microwave Anisotropy Probe 7-yr polarization data,” *MNRAS*, vol. 3, pp. 2162–2169, 2012.
- [79] E. Martinez-Gonzalez, J. Diego, P. Vielva, and J. Silk, “CMB power spectrum estimation and map reconstruction with the expectation - Maximization algorithm,” *MNRAS*, vol. 345, p. 1101, 2003.
- [80] J. Cardoso, M. Martin, J. Delabrouille, M. Betoule, and G. Patanchon, “Component separation with flexible models. Application to the separation of astrophysical emissions,” *ArXiv 0803.1814*, 2008.
- [81] H. Eriksen, J. Jewell, C. Dickinson, A. Banday, K. Gorski, *et al.*, “Joint Bayesian component separation and CMB power spectrum estimation,” *Astrophys. J.*, vol. 676, pp. 10–32, 2008.
- [82] J. Jewell, S. Levin, and C. Anderson, “Application of Monte Carlo algorithms to the Bayesian analysis of the cosmic microwave background,” *Astrophys. J.*, vol. 609, pp. 1–14, 2004.
- [83] M. Maris, C. Burigana, and S. Fogliani, “Zodiacal light emission in the PLANCK mission,” *Astron. Astrophys.*, vol. 452, pp. 685–700, 2006.

- 
- [84] Planck Collaboration, “Planck 2013 results. XIV. Zodiacal emission,” *ArXiv 1303.5074*, 2013.
- [85] C. Dickinson, R. Davies, and R. Davis, “Towards a free-free template for CMB foregrounds,” *MNRAS*, vol. 341, p. 369, 2003.
- [86] D. Finkbeiner, “A Full - sky H-alpha template for microwave foreground prediction,” *Astrophys.J.Suppl.*, vol. 146, p. 407, 2003.
- [87] B. Keating, P. Timbie, A. Polnarev, and J. Steinberger, “Large angular scale polarization of the cosmic microwave background and the feasibility of its detection,” *Astrophys.J.*, vol. 495, p. 580, 1998.
- [88] A. Broadbent, J. Osborne, and C. Haslam, “A technique for separating the galactic thermal radio emission from the non-thermal component by means of the associated infrared emission,” *MNRAS*, vol. 237, pp. 381–410, 1989.
- [89] E. Wright, J. Mather, C. Bennett, E. Cheng, R. Shafer, *et al.*, “Preliminary spectral observations of the Galaxy with a 7 deg beam by the Cosmic Background Explorer (COBE),” *Astrophys.J.*, vol. 381, pp. 200–209, 1991.
- [90] D. Finkbeiner, M. Davis, and D. Schlegel, “Extrapolation of galactic dust emission at 100 microns to CMBR frequencies using FIRAS,” *Astrophys.J.*, vol. 524, pp. 867–886, 1999.
- [91] L. Dunne and S. Eales, “The SCUBA Local Universe Galaxy Survey. 2. 450 micron data - Evidence for cold dust in bright IRAS galaxies,” *MNRAS.*, vol. 327, p. 697, 2001.
- [92] Planck Collaboration, “Planck Early Results XIX: All sky temperature and dust optical depth from Planck and IRAS: Constraints on the dark gas in our galaxy,” *ArXiv 1101.2029*, 2011.

- [93] S. Sethi, S. Prunet, and F. Bouchet, “Galactic dust polarized emission at high latitudes and CMB polarization,” *ArXiv 9803158*, 1998.
- [94] A. Benoit, P. Ade, A. Amblard, R. Ansari, E. Aubourg, *et al.*, “First detection of polarization of the submillimetre diffuse galactic dust emission by archeops,” *Astron.Astrophys.*, vol. 424, pp. 571–582, 2004.
- [95] A. Kogut, A. Banday, C. Bennett, *et al.*, “High-Latitude Galactic Emission in the COBE Differential Microwave Radiometer 2 Year Sky Maps,” *Astrophys.J.*, vol. 460, p. 1, 1996.
- [96] C. Bennett *et al.*, “First year Wilkinson Microwave Anisotropy Probe (WMAP) observations: Foreground emission,” *Astrophys.J.Suppl.*, vol. 148, p. 97, 2003.
- [97] B. Draine and A. Lazarian, “Electric dipole radiation from spinning dust grains,” *Astrophys.J.*, vol. 508, pp. 157–179, 1998.
- [98] Planck Collaboration, “Planck Early Results XX: New Light on Anomalous Microwave Emission from Spinning Dust Grains,” *Astron.Astrophys.*, vol. 536, p. A20, 2011.
- [99] B. Gold *et al.*, “Five-Year Wilkinson Microwave Anisotropy Probe (WMAP) Observations: Galactic Foreground Emission,” *Astrophys.J.Suppl.*, vol. 180, pp. 265–282, 2009.
- [100] Planck Collaboration, “Planck Intermediate Results. IX. Detection of the Galactic haze with Planck,” *Astron.Astrophys.*, vol. 554, 2012.
- [101] E. Carretti, R. Crocker, L. Staveley-Smith, M. Haverkorn, C. Purcell, *et al.*, “Giant Magnetized Outflows from the Centre of the Milky Way,” *Nature*, vol. 493, p. 66, 2013.
- [102] P. L. Biermann, J. K. Becker, G. Caceres, *et al.*, “The WMAP haze from the Galactic Center region due to massive star explosions and a reduced cosmic ray scale height,” *Astrophys.J.*, vol. 710, p. L53, 2010.

- [103] R. M. Crocker and F. Aharonian, “The Fermi Bubbles: Giant, Multi-Billion-Year-Old Reservoirs of Galactic Center Cosmic Rays,” *Phys.Rev.Lett.*, vol. 106, p. 101102, 2011.
- [104] M. M. Forbes and A. R. Zhitnitsky, “WMAP Haze: Directly Observing Dark Matter?,” *Phys.Rev.*, vol. D78, 2008.
- [105] Planck Collaboration, “Planck 2013 results. XIII. Galactic CO emission,” *ArXiv 1303.5073*, 2013.
- [106] T. M. Dame and P. Thaddeus, “A Large extension of the CfA Galactic CO survey,” *ASP Conf.Ser.*, 2003.
- [107] K. M. Ferriere, “The interstellar environment of our galaxy,” *Rev.Mod.Phys.*, vol. 73, pp. 1031–1066, 2001.
- [108] Planck Collaboration, “Planck 2013 results. XXVIII. The Planck Catalogue of Compact Sources,” *ArXiv 1303.5088*, 2013.
- [109] Planck Collaboration, “Planck 2013 results. XXIX. Planck catalogue of Sunyaev-Zeldovich sources,” *ArXiv 1303.5089*, 2013.
- [110] C. M. Urry and P. Padovani, “Unified schemes for radio-loud active galactic nuclei,” *Publ.Astron.Soc.Pac.*, vol. 107, p. 803, 1995.
- [111] T. Marriage, J. Juin, Y.-T. Lin, D. Marsden, M. Nolta, *et al.*, “The Atacama Cosmology Telescope: Extragalactic Sources at 148 GHz in the 2008 Survey,” *Astrophys.J.*, vol. 731, p. 100, 2011.
- [112] K. Kellermann and I. Pauliny-Toth, “The Spectra of Opaque Radio Sources,” *Astrophys.J.Letters*, vol. 155, p. L71, 1969.
- [113] Planck Collaboration, “Planck Early Results XVI. The Planck View of Nearby Galaxies,” *Astron.Astrophys.*, vol. 536, p. A16, 2011.
- [114] G. De Zotti, R. Ricci, D. Mesa, L. Silva, P. Mazzotta, *et al.*, “Predictions for high-frequency radio surveys of extragalactic sources,” *ArXiv 0410709*, 2004.

- [115] R. Sunyaev and Y. Zeldovich, “The Observations of relic radiation as a test of the nature of X-Ray radiation from the clusters of galaxies,” *Comments Astrophys.Space Phys.*, vol. 4, pp. 173–178, 1972.
- [116] C. Burigana, G. De Zotti, and L. Feretti, “Sunyaev-Zeldovich effects, free-free emission, and imprints on the cosmic microwave background,” *New Astron.Rev.*, vol. 48, pp. 1107–1117, 2004.
- [117] Y. Rephaeli, S. Sadeh, and M. Shimon, “The sunyaev-zeldovich effect,” *Riv.Nuovo Cim.*, vol. 29N12, pp. 1–18, 2006.
- [118] N. Itoh, Y. Kohyama, and S. Nozawa, “Relativistic Corrections to the Sunyaev-Zel’dovich Effect for Clusters of Galaxies,” *Astrophys.J.*, vol. 502, pp. 7–15, 1998.
- [119] M. Hasselfield, M. Hilton, T. Marriage, G. Addison, L. Barrientos, *et al.*, “The Atacama Cosmology Telescope: Sunyaev-Zel’dovich selected galaxyclusters at 148 GHz from three seasons of data,” *JCAP*, vol. 1307, p. 008, 2013.
- [120] L. Mocanu, T. Crawford, J. Vieira, K. Aird, M. Aravena, *et al.*, “Extragalactic millimeter-wave point source catalog, number counts and statistics from 771 square degrees of the SPT-SZ Survey,” *ArXiv 1306.3470*, 2013.
- [121] P. Phillips, “Calculation of the Kinetic Sunyaev-Zeldovich Effect from the Boltzmann Equation,” *Astrophys.J.*, vol. 455, p. 419, 1995.
- [122] S. Nozawa, N. Itoh, Y. Suda, and Y. Ohhata, “An improved formula for the relativistic corrections to the kinematical Sunyaev-Zeldovich effect for clusters of galaxies,” *Nuovo Cim.*, vol. B121, pp. 487–500, 2006.
- [123] R. Sunyaev and Y. Zeldovich, “Small-Scale Fluctuations of Relic Radiation,” *Astrophys.Space Sci.*, vol. 7, pp. 3–19, 1970.

- [124] N. Aghanim, S. Majumdar, and J. Silk, “Secondary anisotropies of the CMB,” *Reports on Progress in Physics*, vol. 71, no. 6, p. 066902, 2008.
- [125] M. Lueker, C. Reichardt, K. Schaffer, O. Zahn, P. Ade, *et al.*, “Measurements of Secondary Cosmic Microwave Background Anisotropies with the South Pole Telescope,” *Astrophys.J.*, vol. 719, pp. 1045–1066, 2010.
- [126] J. Dunkley, R. Hlozek, J. Sievers, V. Acquaviva, P. Ade, *et al.*, “The Atacama Cosmology Telescope: Cosmological Parameters from the 2008 Power Spectra,” *Astrophys.J.*, vol. 739, p. 52, 2011.
- [127] J. Puget, A. Abergel, J. Bernard, F. Boulanger, W. Burton, *et al.*, “Tentative detection of a cosmic far-infrared background with COBE,” *Astron.Astrophys.*, vol. 308, p. L5, 1996.
- [128] M. Hauser and E. Dwek, “The cosmic infrared background: measurements and implications,” *Ann.Rev.Astron.Astrophys.*, vol. 39, pp. 249–307, 2001.
- [129] H. Dole, G. Lagache, J. Puget, K. Caputi, N. Fernandez-Conde, *et al.*, “The cosmic infrared background resolved by spitzer. Contributions of mid-infrared galaxies to the far-infrared background,” *Astron.Astrophys.*, vol. 451, pp. 417–429, 2006.
- [130] N. Fernandez-Conde, G. Lagache, J.-L. Puget, and H. Dole, “Simulations of the cosmic infrared and submillimeter background for future large surveys: I. Presentation and first application to Herschel/SPIRE and Planck/HFI,” *ArXiv 0801.4299*, 2008.
- [131] M. Bethermin, H. Dole, M. Cousin, and N. Bavouzet, “Submillimeter number counts at 250  $\mu\text{m}$ , 350  $\mu\text{m}$  and 500  $\mu\text{m}$  in BLAST data,” *Astron.Astrophys.*, vol. 516, 2010.
- [132] S. Oliver, L. Wang, A. Smith, *et al.*, “HerMES: SPIRE galaxy number counts at 250, 350, and 500  $\mu\text{m}$ ,” *Astron.Astrophys.*, vol. 518, 2010.

- [133] J. Geach, E. Chapin, K. Coppin, J. Dunlop, M. Halpern, *et al.*, “The SCUBA-2 Cosmology Legacy Survey: blank-field number counts of 450 $\mu$ m-selected galaxies and their contribution to the cosmic infrared background,” *ArXiv 1211.6668*, 2012.
- [134] Planck Collaboration, “Planck 2013 results. XXX. Cosmic infrared background measurements and implications for star formation,” *ArXiv 1309.0382*, 2013.
- [135] G. Rybicki and A. Lightman, *Radiative processes in astrophysics*. Wiley-Interscience, 1979.
- [136] R. Davies, R. Watson, and C. Gutierrez, “Galactic synchrotron emission at high frequencies,” *MNRAS*, vol. 278, pp. 925–939, 1996.
- [137] W. Webber, “Cosmic ray electrons and positrons - A review of current measurements and some implications,” in *NATO ASIC Proc. 107: Composition and Origin of Cosmic Rays* (M. Shapiro, ed.), pp. 83–100, 1983.
- [138] M. Boezio, P. Carlson, T. Francke, N. Weber, M. Suffert, *et al.*, “The Cosmic-Ray Electron and Positron Spectra Measured at 1 AU during Solar Minimum Activity,” *Astrophys.J.*, vol. 532, pp. 653–669, 2000.
- [139] R. Golden, C. Grimani, B. Kimbell, S. Stephens, S. Stochaj, *et al.*, “Observations of cosmic ray electrons and positrons using an imaging calorimeter,” *Astrophys.J.*, vol. 436, pp. 769–775, 1994.
- [140] A. Strong and I. Moskalenko, “Propagation of cosmic-ray nucleons in the galaxy,” *Astrophys.J.*, vol. 509, pp. 212–228, 1998.
- [141] A. Waelkens, T. Jaffe, M. Reinecke, F. Kitaura, and T. Ensslin, “Simulating polarized Galactic synchrotron emission at all frequencies, the Hammurabi code,” *ArXiv 0807.2262*, 2008.

- [142] C. Haslam, U. Klein, C. Salter, H. Stoffel, *et al.*, “A 408 MHz all-sky continuum survey. I - Observations at southern declinations and for the North Polar region,” *Astron. Astrophys.*, vol. 100, pp. 209–219, 1981.
- [143] W. Reich, “A radio continuum survey of the northern sky at 1420 MHz. I,” *Astron. Astrophys. Suppl.*, vol. 48, pp. 219–297, 1982.
- [144] P. Reich and W. Reich, “A radio continuum survey of the northern sky at 1420 MHz. II,” *Astron. Astrophys. Suppl.*, vol. 63, pp. 205–288, 1986.
- [145] F. Bouchet and R. Gispert, “Foregrounds and CMB experiments. 1. Semianalytical estimates of contamination,” *New Astron.*, vol. 4, pp. 443–479, 1999.
- [146] G. Giardino, A. Banday, P. Fosalba, K. Gorski, J. Jonas, *et al.*, “The angular power spectrum of radio emission at 2.3 GHz,” *ArXiv 0103233*, 2001.
- [147] F. Bouchet, S. Prunet, and S. Sethi, “Multi-frequency wiener filtering of cmb data with polarisation,” *ArXiv 9809353*, 1998.
- [148] J. Cho and A. Lazarian, “MHD turbulence as a foreground for CMB studies,” *Astrophys.J.*, vol. 575, p. L63, 2002.
- [149] A. Chepurnov, “The galactic foreground angular spectra,” *Astron. Astrophys. Trans.*, vol. 17, pp. 281–300, 1999.
- [150] C. Baccigalupi, C. Burigana, F. Perrotta, G. De Zotti, L. L. Porta, *et al.*, “Power spectrum of the polarized diffuse galactic radio emission,” *ArXiv 0009135*, 2000.
- [151] M. Bruscoli, M. Tucci, V. Natale, E. Carretti, R. Fabbri, *et al.*, “The power-law behaviours of angular spectra of polarized galactic synchrotron,” *ArXiv 0202389*, 2002.

- [152] M. Tucci, E. Carretti, S. Cecchini, R. Fabbri, M. Orsini, *et al.*, “The angular power spectra of polarized galactic synchrotron,” *ArXiv 0006387*, 2000.
- [153] P. Reich and W. Reich, “A map of spectral indices of the Galactic radio continuum emission between 408 MHz and 1420 MHz for the entire northern sky,” *Astron. Astrophys. Suppl.*, vol. 74, pp. 7–20, 1988.
- [154] J. Testori, P. Reich, J. Bava, F. Colomb, E. Hurrel, *et al.*, “A radio continuum survey of the southern sky at 1420 MHz. observations and data reduction,” *ArXiv 0101322*, 2001.
- [155] K. Gorski, E. Hivon, A. Banday, B. Wandelt, F. Hansen, *et al.*, “HEALPix - A Framework for high resolution discretization, and fast analysis of data distributed on the sphere,” *Astrophys.J.*, vol. 622, pp. 759–771, 2005.
- [156] L. La Porta, P. Reich, C. Burigana, *et al.*, “Conversion of ECP maps into HEALPix maps,” *MPIfR-Memo*, vol. 1, 2005.
- [157] C. Haslam, “NOD2 A General System of Analysis for Radioastronomy,” *Astron. Astrophys.*, vol. 15, p. 333, 1974.
- [158] C. Burigana, L. La Porta, P. Reich, and W. Reich, “A statistical analysis of a Galactic all sky survey at 1.4 GHz,” *Astronomische Nachrichten*, vol. 327, p. 491, 2006.
- [159] L. La Porta, C. Burigana, W. Reich, and P. Reich, “The impact of Galactic synchrotron emission on CMB anisotropy measurements. I. Angular power spectrum analysis of total intensity all-sky surveys,” *Astron. Astrophys.*, vol. 479, 2008.
- [160] Planck Collaboration, “Planck 2013 results. II. The Low Frequency Instrument data processing,” *ArXiv 1303.5063*, 2013.

- [161] E. Keihänen, R. Keskitalo, H. Kurki-Suonio, T. Poutanen, and A.-S. Sirvio, “Making CMB temperature and polarization maps with Madam,” *Astron.Astrophys.*, vol. 510, p. A57, 2010.
- [162] R. White and S. Stemwedel, “The Quadrilateralized Spherical Cube and Quad-Tree For All Sky Data,” in *Astronomical Data Analysis Software and Systems I* (D. M. Worrall, C. Biemesderfer, and J. Barnes, eds.), vol. 25, p. 379, 1992.
- [163] P. Muciaccia, P. Natoli, and N. Vittorio, “Fast spherical harmonic analysis: a quick algorithm for generating and/or inverting full sky, high resolution cmb anisotropy maps,” *Astrophys.J.*, vol. 488, p. L63, 1997.
- [164] E. B. Saff and A. B. J. Kuijlaars, “Distributing many points on a sphere,” *Math. Intel.*, vol. 19, p. 5, 1997.
- [165] M. Tegmark, “An icosahedron-based method for pixelizing the celestial sphere,” *ArXiv 9610094*, 1996.
- [166] R. G. Crittenden and N. G. Turok, “Exactly azimuthal pixelizations of the sky,” *ArXiv 9806374*, 1998.
- [167] A. Doroshkevich, P. Naselsky, O. Verkhodanov, D. Novikov, V. Turchaninov, *et al.*, “First release of Gauss-Legendre sky pixelization (GLESP) software package for CMB analysis,” *ArXiv 0501494*, 2005.
- [168] D. Molinari and C. Burigana, “On the accuracy of map rotation for reference frame transformation in pixel and harmonic space: total intensity (temperature) maps,” *Internal Report IASF-BO*, 595/2011.
- [169] N. Jarosik, C. Bennett, J. Dunkley, B. Gold, M. Greason, *et al.*, “Seven-Year Wilkinson Microwave Anisotropy Probe (WMAP) Observations: Sky Maps, Systematic Errors, and Basic Results,” *Astrophys.J.Suppl.*, vol. 192, p. 14, 2011.

- [170] D. Spergel *et al.*, “First year Wilkinson Microwave Anisotropy Probe (WMAP) observations: Determination of cosmological parameters,” *Astrophys.J.Suppl.*, vol. 148, pp. 175–194, 2003.
- [171] N. Mandolesi, C. Burigana, A. Gruppuso, P. Procopio, and S. Ricciardi, “An overview of the Planck mission,” in *IAU Symposium* (A. Bonanno, E. de Gouveia Dal Pino, and A. Kosovichev, eds.), vol. 274, pp. 268–273, 2011.
- [172] Planck Collaboration, “Planck Early Results. I. The Planck mission,” *Astron.Astrophys.*, vol. 536, p. 16464, 2011.
- [173] B. D. Wandelt, D. L. Larson, and A. Lakshminarayanan, “Global, exact cosmic microwave background data analysis using Gibbs sampling,” *Phys.Rev.*, vol. D70, 2004.
- [174] H. Eriksen, I. O’Dwyer, J. Jewell, B. Wandelt, D. Larson, *et al.*, “Power spectrum estimation from high-resolution maps by Gibbs sampling,” *Astrophys.J.Suppl.*, vol. 155, pp. 227–241, 2004.
- [175] K. Benabed, J.-F. Cardoso, S. Prunet, and E. Hivon, “TEASING: a fast and accurate approximation for the low multipole likelihood of the Cosmic Microwave Background temperature,” *ArXiv 0901.4537*, 2009.
- [176] J. Taylor, M. Ashdown, and M. Hobson, “Fast optimal CMB power spectrum estimation with Hamiltonian sampling,” *ArXiv 0708.2989*, 2007.
- [177] G. Efstathiou, “A Maximum likelihood analysis of the low CMB multipoles from WMAP,” *MNRAS*, vol. 348, p. 885, 2004.
- [178] M. Hauser and P. Peebles, “Statistical Analysis of Catalogs of Extragalactic Objects. II. the Abell Catalog of Rich Clusters,” *Astrophys.J.*, vol. 185, pp. 757–786, 1973.

- [179] E. Hivon, K. Gorski, C. Netterfield, B. Crill, S. Prunet, *et al.*, “Master of the cosmic microwave background anisotropy power spectrum: a fast method for statistical analysis of large and complex cosmic microwave background data sets,” *Astrophys.J.*, vol. 567, p. 2, 2002.
- [180] R. Saha, P. Jain, and T. Souradeep, “A blind estimation of the power spectrum of CMB anisotropy from wmap,” *Astrophys.J.*, vol. 645, pp. L89–L92, 2006.
- [181] G. Polenta, D. Marinucci, A. Balbi, P. de Bernardis, E. Hivon, *et al.*, “Unbiased estimation of angular power spectrum,” *JCAP*, vol. 0511, p. 001, 2005.
- [182] J. Grain, M. Tristram, and R. Stompor, “Polarized CMB spectrum estimation using the pure pseudo cross-spectrum approach,” *Phys.Rev.*, vol. D79, 2009.
- [183] C.-l. Kuo *et al.*, “High resolution observations of the CMB power spectrum with ACBAR,” *Astrophys.J.*, vol. 600, pp. 32–51, 2004.
- [184] W. C. Jones, P. Ade, J. Bock, J. Bond, J. Borrill, *et al.*, “A Measurement of the angular power spectrum of the CMB temperature anisotropy from the 2003 flight of BOOMERANG,” *Astrophys.J.*, vol. 647, pp. 823–832, 2006.
- [185] J.-H. P. Wu, J. Zuntz, M. Abroe, P. Ade, J. Bock, *et al.*, “MAXIPOL: Data Analysis and Results,” *Astrophys.J.*, vol. 665, pp. 55–66, 2007.
- [186] J. Dunkley *et al.*, “Five-Year Wilkinson Microwave Anisotropy Probe (WMAP) Observations: Likelihoods and Parameters from the WMAP data,” *Astrophys.J.Suppl.*, vol. 180, pp. 306–329, 2009.
- [187] Planck Collaboration, “Planck 2013 results. XV. CMB power spectra and likelihood,” *ArXiv 1303.5075*, 2013.

- [188] . C. Pryke *et al.*, “Second and third season QUaD CMB temperature and polarization power spectra,” *Astrophys.J.*, vol. 692, pp. 1247–1270, 2009.
- [189] S. Devlin, R. Gnanadesikan, and J. Kettenring, “Robust estimation and outlier detection with correlation coefficients,” *Biometrika*, vol. 62, no. 3, pp. 531–545, 1975.
- [190] M. Tristram, J. Macias-Perez, C. Renault, and D. Santos, “Xspect, estimation of the angular power spectrum by computing cross power spectra,” *MNRAS*, vol. 358, p. 833, 2005.
- [191] M. Tegmark, “How to measure CMB power spectra without losing information,” *Phys.Rev.*, vol. D55, pp. 5895–5907, 1997.
- [192] M. Tegmark and A. de Oliveira-Costa, “How to measure CMB polarization power spectra without losing information,” *Phys.Rev.*, vol. D64, p. 063001, 2001.
- [193] M. Tegmark, A. Taylor, and A. Heavens, “Karhunen-Loeve eigenvalue problems in cosmology: How should we tackle large data sets?,” *Astrophys.J.*, vol. 480, p. 22, 1997.
- [194] A. Gruppuso, A. De Rosa, P. Cabella, F. Paci, F. Finelli, *et al.*, “New estimates of the CMB angular power spectra from the WMAP 5 yrs low resolution data,” *MNRAS*, vol. 400, pp. 463–469, 2009.
- [195] A. Gruppuso, P. Natoli, N. Mandolesi, A. De Rosa, F. Finelli, *et al.*, “WMAP 7 year constraints on CPT violation from large angle CMB anisotropies,” *JCAP*, vol. 1202, p. 023, 2012.
- [196] Planck Collaboration, “Planck 2013 results. XXIII. Isotropy and Statistics of the CMB,” *ArXiv 1303.5083*, 2013.

- [197] D. Molinari, A. Gruppuso, G. Polenta, C. Burigana, A. De Rosa, P. Natoli, F. Finelli, and F. Paci, “A comparison of cmb angular power spectrum estimators at large scales: the tt case,” *submitted to MNRAS*.
- [198] J. Kim and P. Naselsky, “Anomalous parity asymmetry of WMAP power spectrum data at low multipoles: is it cosmological or systematic?,” *Phys.Rev.*, vol. D82, 2010.
- [199] C. Monteserin, R. B. Barreiro, P. Vielva, E. Martinez-Gonzalez, M. Hobson, *et al.*, “A low CMB variance in the WMAP data,” *MNRAS*, vol. 387, pp. 209–219, 2008.
- [200] A. Gruppuso, P. Natoli, F. Paci, F. Finelli, D. Molinari, *et al.*, “Low Variance at large scales of WMAP 9 year data,” *JCAP*, vol. 1307, p. 047, 2013.
- [201] M. Greason, M. Limon, E. Wollack, *et al.*, “Wilkinson microwave anisotropy probe (wmap): Nine-year explanatory supplement,” *Greenbelt, MD: NASA/GSFC*.
- [202] A. D. Linde, “A New Inflationary Universe Scenario: A Possible Solution of the Horizon, Flatness, Homogeneity, Isotropy and Primordial Monopole Problems,” *Phys.Lett.*, vol. B108, pp. 389–393, 1982.
- [203] A. Albrecht and P. J. Steinhardt, “Cosmology for Grand Unified Theories with Radiatively Induced Symmetry Breaking,” *Phys.Rev.Lett.*, vol. 48, pp. 1220–1223, 1982.
- [204] R. Keskitalo, M. Ashdown, P. Cabella, T. Kisner, T. Poutanen, *et al.*, “Residual noise covariance for Planck low-resolution data analysis,” *Astron.Astrophys.*, vol. 522, p. A94, 2010.
- [205] A. Challinor, P. Fosalba, D. Mortlock, M. Ashdown, B. Wandelt, *et al.*, “All-sky convolution for polarimetry experiments,” *Phys.Rev.*, vol. D62, 2000.

- [206] G. Hinshaw *et al.*, “Nine-Year Wilkinson Microwave Anisotropy Probe (WMAP) Observations: Cosmological Parameter Results,” *Astrophys.J.Suppl.*, vol. 208, p. 19, 2013.
- [207] L. Page *et al.*, “First year Wilkinson Microwave Anisotropy Probe (WMAP) observations: Interpretation of the TT and TE angular power spectrum peaks,” *Astrophys.J.Suppl.*, vol. 148, p. 233, 2003.
- [208] C. Contaldi, M. Peloso, L. Kofman, and A. Linde, “Suppressing the lower multipoles in the CMB anisotropies,” *JCAP*, vol. 0307, p. 002, 2003.
- [209] C. Destri, H. de Vega, and N. Sanchez, “The pre-inflationary and inflationary fast-roll eras and their signatures in the low CMB multipoles,” *Phys.Rev.*, vol. D81, 2010.
- [210] J. Cline, P. Crotty, and J. Lesgourgues, “Does the small CMB quadrupole moment suggest new physics?,” *JCAP*, vol. 0309, p. 010, 2003.
- [211] C. Wetterich, “Cosmology and the Fate of Dilatation Symmetry,” *Nucl.Phys.*, vol. B302, p. 668, 1988.
- [212] B. Ratra and P. Peebles, “Cosmological Consequences of a Rolling Homogeneous Scalar Field,” *Phys.Rev.*, vol. D37, p. 3406, 1988.
- [213] R. Caldwell, R. Dave, and P. Steinhardt, “Quintessential cosmology: Novel models of cosmological structure formation,” *Astrophys.Space Sci.*, vol. 261, pp. 303–310, 1998.
- [214] S. Dodelson, *Modern cosmology*. Academic Press, 2003.
- [215] M. Rees and D. Sciama, “Large scale Density Inhomogeneities in the Universe,” *Nature*, vol. 217, pp. 511–516, 1968.

- [216] E. Martinez-Gonzalez, J. Sanz, and J. Silk, “Anisotropies in the microwave sky due to nonlinear structures,” *Astrophys.J.Letters*, vol. 355, pp. L5–L9, 1990.
- [217] W. Hu and N. Sugiyama, “The Small scale integrated Sachs-Wolfe effect,” *Phys.Rev.*, vol. D50, pp. 627–631, 1994.
- [218] M. Kamionkowski and D. N. Spergel, “Large angle cosmic microwave background anisotropies in an open universe,” *Astrophys.J.*, vol. 432, p. 7, 1994.
- [219] R. Crittenden and N. Turok, “Looking for Lambda with the Rees-Sciama effect,” *Phys.Rev.Lett.*, vol. 76, p. 575, 1996.
- [220] G. Efstathiou, “Hybrid estimation of cmb polarization power spectra,” *MNRAS*, vol. 370, pp. 343–362, 2006.
- [221] A. Frejsel, M. Hansen, and H. Liu, “Consistency tests for Planck and WMAP in the low multipole domain,” *JCAP*, vol. 1306, p. 005, 2013.
- [222] D. Hazra and A. Shafieloo, “Test of Consistency between Planck and WMAP,” *arXiv 1308.2911*, 2013.
- [223] M. Tegmark, A. de Oliveira-Costa, and A. Hamilton, “A high resolution foreground cleaned CMB map from WMAP,” *Phys.Rev.*, vol. D68, p. 123523, 2003.
- [224] A. de Oliveira-Costa, M. Tegmark, M. Zaldarriaga, and A. Hamilton, “The Significance of the largest scale CMB fluctuations in WMAP,” *Phys.Rev.*, vol. D69, p. 063516, 2004.
- [225] C. Copi, D. Huterer, and G. Starkman, “Multipole vectors - A New representation of the CMB sky and evidence for statistical anisotropy or non-Gaussianity at  $2 \leq \ell \leq 8$ ,” *Phys.Rev.*, vol. D70, p. 043515, 2004.

- [226] D. Schwarz, G. Starkman, D. Huterer, and C. Copi, “Is the low- $l$  microwave background cosmic?,” *Phys.Rev.Lett.*, vol. 93, p. 221301, 2004.
- [227] C. Copi, D. Huterer, D. Schwarz, and G. Starkman, “Large angle anomalies in the CMB,” *Adv.Astron.*, vol. 2010, p. 847541, 2010.
- [228] M. Maris, C. Burigana, A. Gruppuso, F. Finelli, and J. Diego, “Large-scale traces of Solar system cold dust on cosmic microwave background anisotropies,” *MNRAS*, vol. 415, pp. 2546–2552, 2011.
- [229] G. Hinshaw, A. Banday, C. Bennett, K. Gorski, A. Kogut, *et al.*, “2-point correlations in the COBE DMR 4-year anisotropy maps,” *Astrophys.J.*, vol. 464, pp. L25–L28, 1996.
- [230] M. Cruz, P. Vielva, E. Martínez-González, and R. Barreiro, “Anomalous variance in the WMAP data and Galactic foreground residuals,” *MNRAS*, vol. 412, pp. 2383–2390, 2011.
- [231] H. Eriksen, F. Hansen, A. Banday, K. Gorski, and P. Lilje, “Asymmetries in the Cosmic Microwave Background anisotropy field,” *Astrophys.J.*, vol. 605, pp. 14–20, 2004.
- [232] F. Hansen, A. Banday, and K. Gorski, “Testing the cosmological principle of isotropy: Local power spectrum estimates of the WMAP data,” *MNRAS*, vol. 354, pp. 641–665, 2004.
- [233] F. Hansen, A. Banday, K. Gorski, H. Eriksen, and P. Lilje, “Power Asymmetry in Cosmic Microwave Background Fluctuations from Full Sky to Sub-Degree Scales: Is the Universe Isotropic?,” *Astrophys.J.*, vol. 704, pp. 1448–1458, 2009.
- [234] K. Land and J. Magueijo, “The Axis of evil,” *Phys.Rev.Lett.*, vol. 95, p. 071301, 2005.
- [235] K. Land and J. Magueijo, “Is the Universe odd?,” *Phys.Rev.*, vol. D72, p. 101302, 2005.

- [236] P. Naselsky, W. Zhao, J. Kim, and S. Chen, “Is the CMB asymmetry due to the kinematic dipole?,” *Astrophys.J.*, vol. 749, p. 31, 2012.
- [237] P. Vielva, E. Martinez-Gonzalez, R. Barreiro, J. Sanz, and L. Cayon, “Detection of non-Gaussianity in the WMAP 1-year data using spherical wavelets,” *Astrophys.J.*, vol. 609, pp. 22–34, 2004.
- [238] P. Mukherjee and Y. Wang, “Wavelets and WMAP non-Gaussianity,” *Astrophys.J.*, vol. 613, pp. 51–60, 2004.
- [239] M. Cruz, M. Tucci, E. Martinez-Gonzalez, and P. Vielva, “The non-gaussian cold spot in wmap: significance, morphology and foreground contribution,” *MNRAS*, vol. 369, pp. 57–67, 2006.
- [240] P. Vielva, Y. Wiaux, E. Martinez-Gonzalez, and P. Vandergheynst, “Alignment and signed-intensity anomalies in Wilkinson Microwave Anisotropy Probe data,” *MNRAS*, vol. 381, pp. 932–942, 2007.
- [241] D. Mota, D. Shaw, and J. Silk, “On the Magnitude of Dark Energy Voids and Overdensities,” *Astrophys.J.*, vol. 675, pp. 29–48, 2008.
- [242] M. Cruz, N. Turok, P. Vielva, E. Martinez-Gonzalez, and M. Hobson, “A Cosmic Microwave Background feature consistent with a cosmic texture,” *Science*, vol. 318, pp. 1612–1614, 2007.
- [243] P. Vielva, E. Martinez-Gonzalez, M. Cruz, R. Barreiro, and M. Tucci, “Cosmic microwave background polarization as a probe of the anomalous nature of the cold spot,” *MNRAS*, vol. 410, pp. 33–38, 2011.
- [244] W. H. Press, A. Saul, W. Vetterling, and B. Flannery, *Numerical Recipes in C: The Art of Scientific Computing*. Cambridge University Press, 2nd ed., 1992.
- [245] S. Downes and B. Dutta, “Inflection Points and the Power Spectrum,” *Phys.Rev.*, vol. D87, p. 083518, 2013.

- [246] E. Dudas, N. Kitazawa, S. Patil, and A. Sagnotti, “CMB Imprints of a Pre-Inflationary Climbing Phase,” *JCAP*, vol. 1205, p. 012, 2012.
- [247] A. Sagnotti, “Brane SUSY Breaking and Inflation: Implications for Scalar Fields and CMB Distorsion,” *arXiv 1303.6685*, 2013.
- [248] Planck Collaboration, “Planck 2013 results. XXVI. Background geometry and topology of the Universe,” *arXiv 1303.5086*, 2013.
- [249] C. Gordon, W. Hu, D. Huterer, and T. Crawford, “Spontaneous isotropy breaking: a mechanism for CMB multipole alignments,” *Phys.Rev.*, vol. D72, p. 103002, 2005.
- [250] C. Copi, D. Huterer, D. Schwarz, and G. Starkman, “On the large-angle anomalies of the microwave sky,” *MNRAS*, vol. 367, pp. 79–102, 2006.
- [251] A. Rakic, S. Rasanen, and D. Schwarz, “Microwave sky and the local Rees-Sciama effect,” *MNRAS*, vol. 369, pp. L27–L31, 2006.
- [252] P. Frisch, “Tentative Identification of Interstellar Dust in the Nose of the Heliosphere,” *Astrophys.J.*, vol. 632, pp. L143–L146, 2005.
- [253] K. Inoue and J. Silk, “Local Voids as the Origin of Large-angle CMB Anomalies: The Effect of a Cosmological Constant,” *Astrophys.J.*, vol. 664, pp. 650–659, 2007.
- [254] H. Peiris and T. Smith, “CMB Isotropy Anomalies and the Local Kinetic Sunyaev-Zel’dovich Effect,” *Phys.Rev.*, vol. D81, p. 123517, 2010.
- [255] M. Hansen, J. Kim, A. Frejsel, S. Ramazanov, P. Naselsky, *et al.*, “Can residuals of the Solar system foreground explain low multipole anomalies of the CMB ?,” *JCAP*, vol. 1210, p. 059, 2012.
- [256] C. Francis and J. Peacock, “An estimate of the local ISW signal, and its impact on CMB anomalies,” *MNRAS*, vol. 406, p. 14, 2010.

- [257] G. Efstathiou, Y. Ma, and D. Hanson, “Large-angle correlations in the cosmic microwave background,” *MNRAS*, vol. 407, pp. 2530–2542, 2010.
- [258] Planck Collaboration, “Planck 2013 results. XIX. The integrated Sachs-Wolfe effect,” *arXiv 1303.5079*, 2013.
- [259] R. Battye and A. Moss, “Anisotropic dark energy and CMB anomalies,” *Phys.Rev.*, vol. D80, p. 023531, 2009.
- [260] A. Pontzen, “Rogues’ gallery: the full freedom of the Bianchi CMB anomalies,” *Phys.Rev.*, vol. D79, p. 103518, 2009.
- [261] T. Jaffe, A. Banday, H. Eriksen, K. Gorski, and F. Hansen, “Bianchi Type VII(h) Models and the WMAP 3-year Data,” *Astron.Astrophys.*, vol. 460, p. 393, 2006.
- [262] M. Cruz, E. Martinez-Gonzalez, P. Vielva, J. Diego, M. Hobson, and N. Turok, “The CMB cold spot: texture, cluster or void?,” *MNRAS*, vol. 390, pp. 913–919, 2008.
- [263] S. Das and D. Spergel, “CMB Lensing and the WMAP Cold Spot,” *Phys.Rev.*, vol. D79, p. 043007, 2009.
- [264] M. Tegmark, D. Eisenstein, W. Hu, and A. de Oliveira-Costa, “Foregrounds and forecasts for the cosmic microwave background,” *Astrophys.J.*, vol. 530, pp. 133–165, 2000.
- [265] P. Platania, C. Burigana, D. Maino, E. Caserini, M. Bersanelli, B. Capellini, and A. Mennella, “Full sky study of diffuse Galactic emission at decimeter wavelengths,” *Astron.Astrophys.*, vol. 410, pp. 847–863, 2003.
- [266] L. Toffolatti, J. Gonzalez-Nuevo, M. Negrello, G. De Zotti, L. Silva, *et al.*, “Extragalactic source contributions to arcminute-scale Cos-

- mic Microwave Background anisotropies,” *Astron.Astrophys.*, vol. 438, p. 475, 2005.
- [267] L. Fauvet, J. Macias-Perez, T. Jaffe, A. Banday, F. Desert, *et al.*, “Expected constraints on the Galactic magnetic field using PLANCK data,” *Astron.Astrophys.*, vol. 540, p. A122, 2012.
- [268] L. Fauvet, J. Macias-Perez, J. Aumont, F. Desert, T. Jaffe, *et al.*, “Joint 3D modelling of the polarized Galactic synchrotron and thermal dust foreground diffuse emission,” *Astron.Astrophys.*, vol. 526, p. A145, 2010.
- [269] T. Jaffe, K. Ferriere, A. Banday, A. Strong, E. Orlando, *et al.*, “Comparing Polarised Synchrotron and Thermal Dust Emission in the Galactic Plane,” *MNRAS*, vol. 431, pp. 683–694, 2013.
- [270] D. Prather, A. Sharkawy, S. Shi, J. Murakowski, and S. G., *Photonic Crystals: Theory, Applications and Fabrication*. Wiley, 2nd ed., 2009.
- [271] O. M.M., “Optical waveguides in the computer environment: a packaging perspective,” *Proc. SPIE*, p. 76, 1990.
- [272] S. Kawai, Y. Tashiro, H. Ichinose, and K. Kasahara, “Cascade-connective optical parallel logic processor using electrophotonic devices,” *Applied Optics*, pp. 178–185, 1992.
- [273] T. Takamori, L. Coldren, and M. J.L., “Angled etching gaas/algaas by conventional cl2 reactive ion etching,” *Appl. Phys. Lett.*, vol. 53, pp. 2549–2551, 1988.
- [274] J. Trehwella and O. M.M., “Total internal reflection mirrors fabricated in polymeric optical waveguides via excimer laser ablation,” *Proc. SPIE*, vol. 1377, p. 64, 1991.
- [275] S. Sheem, “Total internal reflection integrated-optics switch: a theoretical evaluation,” *Applied Optics*, vol. 17, pp. 3679–3687, 1978.

- [276] D. L. Perry, “Low-loss multilayer dielectric mirrors,” *Applied Optics*, vol. 4, pp. 987–991, 1965.
- [277] J. Berthold, “Computer design and fabrication techniques for a wide-band dielectric mirror,” *Applied Optics*, vol. 8, pp. 1919–1924, 1969.
- [278] E. Yablonovitch, “Inhibited spontaneous emission in solid-state physics and electronics,” *Phys. Rev. Lett.*, vol. 58, pp. 2059–2062, 1987.
- [279] S. John, “Strong localization of photons in certain disordered dielectric superlattices,” *Phys. Rev. Lett.*, vol. 58, pp. 2486–2489, 1987.
- [280] W. Haus, “A brief review of theoretical results for photonic band structures,” *J. Mod. Opt.*, vol. 41, pp. 195–207, 1994.
- [281] L. Brillouin, “Les électrons dans les métaux et le classement des ondes de de broglie correspondantes,” *Comptes Rendus Hebdomadaires des Séances de l’Académie des Sciences*, vol. 191, p. 292, 1930.
- [282] N. Ashcroft and N. Mermin, *Solid State Physics*. Saunders College, 1976.
- [283] S. Lin, E. Chow, V. Hietala, P. Villeneuve, and J. Joannopoulos, “Experimental demonstration of guiding and bending of electromagnetic waves in a photonic crystal,” *Science*, vol. 282, pp. 1259–1261, 1998.
- [284] E. Chow, S. Lin, J. Wendt, S. Johnson, and J. Joannopoulos, “Quantitative analysis of bendin efficiency in photonic crystal waveguide bends at  $\lambda = 1.55\mu\text{m}$ ,” *Opt. Lett.*, vol. 26, pp. 286–288, 2001.
- [285] M. Bayindir, B. Temelkuran, and E. Özbay, “Photonic crystal based beam splitter,” *Appl. Phys. Lett.*, vol. 77, pp. 3902–3904, 2000.
- [286] S. Fan, P. Villeneuve, and J. Joannopoulos, “Channel drop filters in photonic crystals,” *Opt. Express*, vol. 3, pp. 4–11, 1998.

- [287] A. Sharkawy, S. Shi, and D. Prather, “Multichannel wavelength division multiplexing with photonic crystals,” *Appl. Opt.*, vol. 40, pp. 2247–2252, 2001.
- [288] H. Park, S. Kim, S. Kwon, *et al.*, “Electrically driven single-cell photonic crystal laser,” *Appl. Opt.*, vol. 305, pp. 1444–1447, 2004.
- [289] H. Altug, D. Englund, and J. Vučković, “Ultrafast photonic crystal nanocavity laser,” *Nature Physics*, vol. 2, pp. 484–488, 2006.
- [290] A. Taflove and S. Hagness, *Computational Electrodynamics: The Finite-Difference Time-Domain Method*. Arthec house, 2000.
- [291] J. Berenger, “A perfectly matched layer for the absorption of electromagnetic waves,” *J. Computational Physics*, vol. 4, pp. 268–270, 1994.
- [292] A. Yariv, *Optical Electronics in Modern Communications*. Oxford University, 1997.
- [293] S. Kuchinsky, V. Golyatin, A. Kutikov, T. Pearsall, and N. D., “Coupling between photonic crystal waveguides,” *IEEE Journal of Quantum Electronics*, vol. 38, pp. 1349–1352, 2002.
- [294] T. Liu, A. Zakharian, M. Fallahi, J. Moloney, and M. M., “Design of a compact photonic-crystalbased polarizing beam splitter,” *IEEE Photonics Technology Letters*, vol. 17, pp. 1435–1437, 2005.
- [295] K. Mnaymneh, S. Frédérick, D. Dalacu, J. Lapointe, *et al.*, “Enhanced photonic crystal cavity-waveguide coupling using local slow-light engineering,” *Optics Letters*, vol. 37, pp. 280–282, 2012.
- [296] V. Zabelin, L. Dunbar, N. Le Thomas, R. Houdréand, *et al.*, “Self-collimating photonic crystal polarization beam splitter,” *Optics Letters*, vol. 32, pp. 530–532, 2007.

- [297] V. Mocella, P. Dardano, L. Moretti, and I. Rendina, “A polarizing beam splitter using negative refraction of photonic crystals,” *Optics Letters*, vol. 13, 2005.
- [298] L. Wu, M. Mazilu, J. Gallet, and T. Krauss, “Dual lattice photonic-crystal beam splitters,” *Applied Physics Letters*, vol. 86, 2005.
- [299] Y. Jiang, X. Li, Y. Zhang, and W. Xue, “Polarization beam splitter based on dielectric periodic structure with different defects for two polarizations,” *Chinese Optics Letters*, vol. 6, pp. 794–796, 2008.
- [300] L. Soldano and C. Pennings, “Optical multi-mode interference devices based on self-imaging: Principles and application,” *Journal of Light-wave Technology*, vol. 13, pp. 615–627, 1995.
- [301] M. Lu, S. Liao, and Y. Huang, “Ultracompact photonic crystal polarization beam splitter based on multimode interference,” *Applied Optics*, vol. 49, pp. 724–731, 2010.
- [302] C. Liu, A. Di Falco, D. Molinari, Y. Khan, B. Ooi, T. Krauss, and A. Fratalocchi, “Enhanced energy storage in chaotic optical resonators,” *Nature Photonics*, vol. 7, pp. 473–478, 2013.
- [303] H. Mabuchi and A. C. Doherty, “Cavity quantum electrodynamics: coherence in context,” *Science*, vol. 298, pp. 1372–1377, 2002.
- [304] K. Bourzac, “Photonic chips made easier,” *Nature*, vol. 483, p. 388, 2012.
- [305] N. Kengo *et al.*, “Ultralow-power all-optical ram based on nanocavities,” *Nature*, vol. 6, pp. 248–252, 2012.
- [306] F. Leo *et al.*, “Temporal cavity solitons in one-dimensional kerr media as bits in an all-optical buffer,” *Nature Photon.*, vol. 4, pp. 471–476, 2010.

- [307] H. A. Atwater and A. Polman, “Plasmonics for improved photovoltaic devices,” *Nature Mater.*, vol. 9, pp. 205–213, 2010.
- [308] A. Chalcraft *et al.*, “Mode structure of the l3 photonic crystal cavity,” *Appl. Phys. Lett.*, vol. 90, 2007.
- [309] A. J. Campillo, *Optical Processes in Microcavities*. World Scientific, 1995.
- [310] T. Gensty *et al.*, “Wave chaos in real-world vertical-cavity surface-emitting lasers,” *Phys. Rev. Lett.*, vol. 94, 2005.
- [311] J. U. Nöckel and A. D. Stone, “Ray and wave chaos in asymmetric resonant optical cavities,” *Nature*, vol. 385, pp. 45–47, 1997.
- [312] P. Harayama, T. Davis and K. S. Ikeda, “Stable oscillations of a spatially chaotic wave function in a microstadium laser,” *Phys. Rev. Lett.*, vol. 90, 2003.
- [313] C. Gmachl *et al.*, “High-power directional emission from microlasers with chaotic resonators,” *Science*, vol. 280, pp. 1556–1564, 1998.
- [314] C. Michel, V. Doya, O. Legrand, and F. Mortessagne, “Selective amplification of scars in a chaotic optical fiber,” *Phys. Rev. Lett.*, vol. 99, 2007.
- [315] T. Lee *et al.*, “Surface-structure-assisted chaotic mode lasing in vertical cavity surface emitting lasers,” *Phys. Rev. Lett.*, vol. 101, 2008.
- [316] C. Chen *et al.*, “Transient dynamics of coherent waves released from quantum billiards and analogous observation from free-space propagation of laser modes,” *Phys. Rev. Lett.*, vol. 102, 2009.
- [317] P. Brouwer, K. Frahm, and C. Beenakker, “Quantum mechanical timedelay matrix in chaotic scattering,” *Phys. Rev. Lett.*, vol. 78, pp. 4737–4740, 1997.

- [318] G. S. Murugan, J. S. Wilkinson, and M. N. Zervas, “Optical microdisc resonators by flattening microspheres,” *Appl. Phys. Lett.*, vol. 101, 2012.
- [319] M. Robnik, “Classical dynamics of a family of billiards with analytic boundaries,” *J. Phys. A*, vol. 16, pp. 3971–3986, 1983.
- [320] G. Boffetta, M. Cencini, M. Falcioni, and A. Vulpiani, “Predictability: a way to characterize complexity,” *Physics Reports*, vol. 356, pp. 367–474, 2002.
- [321] H. Haus, *Waves and Fields in Optoelectronics*. Prentice-Hall, 1984.
- [322] A. Tjihuis, *Electromagnetic Inverse Profiling*. VNU Science Press, 1987.
- [323] C. Beck and F. Schlögl, *Thermodynamics of Chaotic Systems*. Cambridge Univ. Press, 1993.
- [324] G. Gallavotti, *Statistical Mechanics: A Short Treatise*. Springer, 1999.
- [325] J. Li and J. Li, “Dielectric properties of silicon in terahertz wave region,” *Microw. Opt. Technol. Lett.*, vol. 50, pp. 1143–1146, 2008.
- [326] J. Dai, J. Zhang, W. Zhang, and D. Grischkowsky, “Terahertz time-domain spectroscopy characterization of the far-infrared absorption and index of refraction of high-resistivity, float-zone silicon,” *J. Opt. Soc. Am. B*, vol. 21, pp. 1379–1386, 2004.
- [327] J. McMahon, J. Beall, D. Becker, *et al.*, “Multi-chroic feed-horn coupled tes polarimeters,” *arXiv 1201.4124*, 2012.
- [328] J. Henning, P. Ade, K. Aird, A. Yefremenko, *et al.*, “Feedhorn-coupled tes polarimeter camera modules at 150 ghz for cmb polarization measurements with sptpol,” in *Society of Photo-Optical Instrumentation Engineers (SPIE) Conference Series*, 2012.